Croissance et caractérisation de nanofils de GaN et d'hétérostructures filaires de GaN/AlN

Karine Hestroffer

UNIVERSITÉ DE GRENOBLE

THÈSE

Pour obtenir le grade de

DOCTEUR DE L'UNIVERSITÉ DE GRENOBLE

Spécialité : **Physique de la matière condensée et du rayonnement**

Arrêté ministériel : 7 août 2006

Présentée par

Karine HESTROFFER

Thèse dirigée par **Bruno DAUDIN**
et codirigée par **Hubert RENEVIER**

préparée au sein de **l'équipe mixte CEA-CNRS *Nanophysique et Semiconducteurs* au CEA-Grenoble/INAC/SP2M**
et rattachée à l'**Ecole Doctorale de Physique de Grenoble**

Croissance et caractérisation de nanofils de GaN et d'hétérostructures filaires de GaN/AlN

Thèse soutenue publiquement le **25 octobre 2012**
devant le jury composé de :

Joël CIBERT
Directeur de recherche au CNRS/NPSC de Grenoble, Président
Yves GARREAU
Professeur à l'université Paris-Diderot/Paris 7, LMPQ, Rapporteur
Jean-Christophe HARMAND
Directeur de recherche au CNRS/LPN de Marcoussis, Rapporteur
Czesław SKIERBISZEWSKI
Professeur à l'institut de physique des hautes pressions de l'académie polonaise des sciences, Examinateur
Sergei NOVIKOV
Professeur à l'université de Nottingham, Examinateur
Bruno DAUDIN
Chercheur au CEA/NPSC de Grenoble, Directeur de thèse
Hubert RENEVIER
Professeur à l'institut polytechnique de Grenoble, Codirecteur de thèse

Contents

Remerciements v

Résumé en français ix

Bibliographie du résumé xxii

Acronyms xxiii

Introduction 1

1 PAMBE, III-N semiconductor properties & characterization techniques 9
- 1.1 Plasma-Assisted Molecular Beam Epitaxy . . . 11
- 1.2 Properties of III-N semiconductors . . . 15
  - 1.2.1 Structural properties . . . 15
    - 1.2.1.1 Wurtzite and zinc-blende crystal structures . . . 15
    - 1.2.1.2 Polarity . . . 17
  - 1.2.2 Elastic and plastic properties . . . 18
    - 1.2.2.1 Elastic relaxation . . . 19
    - 1.2.2.2 Plastic relaxation . . . 19
  - 1.2.3 Electronic properties . . . 20
    - 1.2.3.1 Band gap . . . 20
    - 1.2.3.2 Spontaneous and piezoelectric polarizations . . . 21
    - 1.2.3.3 Quantum-confined Stark effect . . . 23
- 1.3 Characterization techniques . . . 24
  - 1.3.1 Structural characterization . . . 24
    - 1.3.1.1 Reflection high energy electron diffraction . . . 24
    - 1.3.1.2 X-ray diffraction . . . 28
  - 1.3.2 Optical characterization . . . 31
    - 1.3.2.1 Photoluminescence . . . 32
    - 1.3.2.2 Nano-cathodoluminescence . . . 32

2 Growth and properties of self-assembled GaN nanowires on silicon 35
- 2.1 Silicon substrates . . . 37
  - 2.1.1 The assets of silicon substrates . . . 37
  - 2.1.2 Silicon substrate specifications . . . 38

2.1.3 Silicon substrate preparation . . . 38
2.1.4 Silicon substrate temperature calibration . . . 40
2.2 Self-assembled GaN nanowires on silicon . . . 42
2.2.1 State of the art of self-assembled GaN nanowires . . . 42
2.2.2 Optical properties of self-assembled GaN nanowires . . . 44
2.2.3 GaN nanowire growth conditions on bare silicon . . . 46
2.2.4 GaN nanowire density dependence on the substrate temperature . . . 47
2.2.5 GaN nanowire length and diameter versus temperature . . . 50
2.3 Conclusion of the chapter . . . 52

3 Nucleation of self-assembled GaN nanowires 53
3.1 State of the art . . . 55
3.2 Experimental details . . . 56
3.3 Nitridation of the Si surface . . . 56
3.4 Dynamics of GaN nanowire nucleation . . . 58
3.4.1 GaN nanowire nucleation on bare Si(111) . . . 58
3.4.2 GaN nanowire nucleation with an AlN buffer on Si(111) . . . 61
3.4.3 GaN nanowire nucleation on Ga-covered Si(111) . . . 62
3.5 Amorphization of the crystalline β-Si_3N_4 phase . . . 64
3.5.1 Species responsible of β-Si_3N_4 amorphization . . . 64
3.5.2 β-Si_3N_4 amorphization dependence on substrate temperature . . . 66
3.5.3 Limitation of the RHEED study in the understanding of the amorphization process . . . 67
3.6 GaN nanowire nucleation dynamics . . . 67
3.6.1 GaN nanowires nucleation dynamics on AlN/Si(111) . . . 68
3.6.2 GaN nanowires nucleation dynamics on nitrided Si(111) . . . 70
3.6.3 Comparison of the delay on AlN buffer and on bare Silicon . . . 70
3.7 Discussion and conclusion of the chapter . . . 72

4 Polarity of GaN nanowires grown by PAMBE 75
4.1 State of the art . . . 77
4.1.1 Polarity-related issues . . . 77
4.1.2 Polarity of 2D GaN layers and GaN wires . . . 77
4.2 Resonant XRD for the polarity determination of GaN NWs grown on bare Si 78
4.2.1 Principle of the method . . . 78
4.2.2 Samples preparation . . . 80
4.2.3 Results . . . 82
4.3 KOH selective etching method on GaN nanowires . . . 83
4.4 Polarity of GaN nanowires prepared in different growth conditions . . . 86
4.4.1 GaN nanowires grown on Ga-covered silicon . . . 86
4.4.2 GaN nanowires on AlN buffer on Si(111) . . . 87
4.5 Discussion and conclusion . . . 87

5 GaN-AlN core-shell nanowire heterostructures 91
5.1 Growth of the AlN shell around GaN nanowires . . . 93

5.1.1 Geometrical model . . . 94
5.1.1.1 Relation between the initial Φ_{Al}/Φ_N ratio and the effective AlN growth rate . . . 95
5.1.1.2 Growth rates along the axis and along the radius of the nanowires . . . 97
5.1.1.3 Consequence of the shadow effect . . . 99
5.1.2 Experimental observations . . . 102
5.1.2.1 GaN-AlN core-shell nanowire density . . . 102
5.1.2.2 Morphologies of the AlN shell . . . 103
5.1.2.3 AlN shell aspect ratio dependence on the atomic beams incidence angle . . . 105
5.1.2.4 Geometrical model including Al diffusion . . . 108
5.1.2.5 Discussion and conclusions on the AlN shell growth mechanisms and morphology . . . 110
5.2 Structural properties of GaN-AlN core-shell heterostructures . . . 111
5.2.1 AlN shell induced strain within GaN cores . . . 111
5.2.1.1 Resonant X-ray diffraction . . . 111
5.2.1.2 Theoretically determined strains . . . 115
5.2.1.3 Microscopic observations . . . 117
5.2.1.4 Conclusions on strains within GaN cores . . . 119
5.2.2 In-plane and out-of-plane disorientation . . . 120
5.3 Optical properties of GaN-AlN core-shell heterostructures . . . 122
5.4 Conclusion of the chapter . . . 124

6 GaN axial insertions on AlN nanowires 127
6.1 Critical GaN height on AlN for plastic relaxation in the nanowire geometry 129
6.2 Critical AlN NW diameter for strain-induced formation of GaN QDs . . . 130
6.2.1 Theoretically determined critical radius . . . 130
6.2.2 Experimentally determined critical radius . . . 131
6.3 Optical properties of GaN quantum dots in GaN-AlN core-shell nanowires 136
6.3.1 GaN axial insertion ensemble . . . 136
6.3.2 Single GaN axial insertion . . . 137
6.4 Conclusion and prospects of the chapter . . . 139

Conclusions and prospects 141

Appendices 145

A Crystallography in hexagonal systems 147

B Selective area growth of GaN nanowires on patterned silicon substrates 151
B.1 Selectivity tests . . . 152
B.2 Patterned substrates . . . 154
B.3 GaN nanowire morphology on patterned substrates . . . 155
B.4 Optical properties of GaN nanowires grown on patterned substrates . . . 157

B.5 Prospects on selective area growth of GaN nanowires 157

C Publications, conferences & workshops **159**

Bibliography **181**

Remerciements

Le 2 novembre 2009, je commençai ma thèse au CEA de Grenoble. Après près de 302 échantillons élaborés et analysés, cette grande aventure de 3 ans prend fin, non sans quelques émotions de dernières minutes...[1] Je tiens maintenant à remercier les personnes que j'ai côtoyées et qui m'ont soutenue pendant ces trois années.

Je souhaite tout d'abord témoigner ma plus profonde reconnaissance à mes deux directeurs de thèse **Bruno Daudin** et **Hubert Renevier**. Je les remercie sincèrement pour leur disponibilité, leurs conseils précieux, leur confiance et leurs encouragements. J'ai grandement apprécié leur sens de l'humour et de la dérision, qui a rendu ce travail avec eux très agréable.

Je remercie ensuite chaleureusement les membres du jury pour avoir accepté de juger mon travail de thèse. Merci donc à mes deux rapporteurs, **Yves Garreau**, professeur à l'université Paris-Diderot et **Jean-Christophe Harmand**, directeur de recherche au laboratoire de photonique et nanostructures de Marcousis. Merci aux examinateurs **Czesław Skierbiszewski**, professeur à l'académie polonaise des sciences et **Sergei Novikov**, professeur à l'université de Nottingham. Merci enfin au président **Joël Cibert**, directeur de recherche à l'institut Néel de Grenoble.

Ce travail de thèse a été effectué au sein du Laboratoire de Nanophysique et Semiconducteurs (NPSC) du Service de Physique des Matériaux et Microstructures (SP2M) de l'Institut Nanosciences et Cryogénie (INAC) au CEA de Grenoble. Je remercie **Jean-Michel Gérard** et **Henri Mariette** de m'y avoir accueillie. Quelle surprise de découvrir que le chef du laboratoire est, comme moi, originaire de Creutzwald ! Le monde est petit.

Merci du fond du cœur à **Sandrine Ferrari** de l'école doctorale de physique pour son aide précieuse, sa gentillesse et sa réactivité.

Je tiens également à remercier mes divers collaborateurs. Tout d'abord merci à mes prédécesseurs **Vincent Fellmann** et **Gabriel Tourbot** qui m'ont initiée à l'art de l'épitaxie et m'ont appris à me servir de cette grosse machine qu'est la MBE. Bon courage

[1] Comprend qui pourra!

à celle qui me succèdera dans quelques mois **Aurélie Pierret** et celui dont le tour viendra ensuite, **Thomas Auzelle**. Merci à **Yoann Cure**, toujours disponible pour nous sortir des galères relatives à la MBE et pour son super logiciel Anarheed. Merci également à **Eva Monroy**, toujours présente pour répondre à mes questions et m'aider d'une manière ou d'une autre. Côté rayons X, je souhaite exprimer ma gratitude à **Cédric Leclere** pour son travail précieux et à **Valentina Cantelli** pour son implication et pour avoir rendu les 2 semaines passées sur BM32 plus joviales. Plus généralement, merci au personnel des lignes BM02 et BM32 du synchrotron de Grenoble. Merci également à **François Rieutord** et **Vincent Favre-Nicollin** pour leur aide et leurs réponses à mes diverses questions. Passant maintenant aux spécialistes des caractérisations optiques, je tiens à remercier **Bruno Gayral** pour ses conseils divers et variés, son soutien et ses encouragements. Merci également à **Diane Sam-Giao**, ma co-bureau, pour son aide et les discussions que nous avons partagées. Merci à **Catherine Bougerol** pour ses nombreuses images de microscopie et plus largement pour son amitié. Dans le registre de la microscopie, merci à **Mathieu Kociak** de m'avoir acceuillie quelques jours au laboratoire de physique des solides d'Orsay ainsi qu'à **Luiz Tizei** pour sa patience et ses excellentes explications lors de ce séjour. Merci aux théoriciens **Yann-Michel Niquet** et **Dulce Camacho** du laboratoire de simulation de Grenoble pour leurs résultats ainsi qu'à **Frank Glas** du laboratoire de photonique et nanostructures de Marcousis pour notre collaboration. Merci aux divers protagonistes de l'ANR SINCRONE (SIlicium Nanostructuré et CRoissance Organisée de Nanofils pour l'Eclairage par LEDs) avec qui j'ai collaboré dans le but de mettre en œuvre la croissance de nanofils de GaN sur substrat patternés: **Pierre Ferret**, **François Levy**, **Philippe Gilet**, **Daniel Turover**, **Natalie Thomas**, **Stéphane Landis**, **Nicolas Chaix** et **Yohan Désières**. Plus généralement, je tiens à remercier tous mes collègues du laboratoire NPSC pour les bons moments passés au C5 : **Adrien**, **Alexander**, **Ana**, **Aparna**, **Buk**, **Christophe**, **Damien**, **Dipankar**, **Edith**, **Emmanuel**, **Fernando**, **Hervé**, **Jan-Peters**, **Jean**, **Joël B.**, **Joël E.**, **Julien**, **Kuntheak**, **Le Si Dang**, **Lionel**, **Marion**, **Mark**, **Marlène**, **Marteen**, **Moira**, **Nikos**, **Nitin**, **Pamela**, **Périne**, **Prem**, **Priyasmita**, **Régis**, **Robert E.**, **Robert K.**, **Rudee**, **Sandeep**, **Serge**, **Sirona**, **Thanh Giang**, **Thomas**, **Xiaojun**, **Yann** et **Yulia**. Merci aux deux anciens du labo que j'ai rencontré à plusieurs reprises en conférence **Mohammed** et **Lise** et qui m'ont guidée dans mes choix pour le futur. Un merci tout particulier à **Amina** pour sa bonne humeur. C'était un vrai plaisir de partager un bureau avec elle.

Durant ces trois années, j'ai également eu l'occasion de m'impliquer dans l'association des doctorants du CEA de Grenoble, AITAP. Je tiens à en remercier les différents membres avec qui j'ai passé d'excellents moments dont je garderai un souvenir impérissable : **Dayouvid** (inimitable imitation du générique des feux de l'amour), **Rara Goujat** (en cas de besoin, maintenant je sais comment tuer un morse), **Seb**, **Malek**, **Jan**, la mafia italienne et leur délicieux tiramisus **Matteo** & **Giorgio**, **Hubert** (qui fait aussi de bons gâteaux), **Alp**, **Thomas**, **Martin**, **Radek**, **Sihem**, **Raphaël**, **Larissa**, **Koceila** (sacré

partenaire de bridge), **Guillaume**, **Santiago**, **Sébastien B.**, **Sébastien G.**, **Sylvain**, **Emanuela**, **Alexis**.

Je tiens aussi à remercier mes amis de Grenoble, grâce auxquels ces trois années ont été pétillantes. D'abord, quelle bonne idée j'ai eu de m'inscrire à des cours de self-défense ! Sans ça, je n'aurais sûrement pas rencontré **Floribou** dont la folie est aussi démesurée que sa bague panda. Conclusion après 3 ans : on n'est toujours pas des expertes du maïgeri mais on s'est au moins musclé les abdos à trop rigoler (même si ça ne se voit pas encore). Merci également à **Krzysztof** et **Kavita** avec qui j'ai partagé "flowers & butterflies" pendant nos soirées-cancans autour d'un pot d'achard ! धन्यवाद् कविता क्यों की अब मैं कम् हिन्दी बोल्ती और् लिखती हूँ – Również dziękuję Ci Krzysztofie, ale to nie jest dokładnie Twoja zasługa, że mówię lepiej po polsku. **Raùl**, il faudra apprendre à cuisiner le guacamole un peu mieux. Merci aux amis de "Happy people" qui ont animé un bon nombre de mes jeudi soirs.

Ce dernier paragraphe de mes remerciements est dédié à ma famille qui m'a fait l'immense plaisir de venir en nombre à ma soutenance. Merci bien sûr à mes parents **Clément** et **Christine** qui m'ont toujours soutenue et qui ont été une grande source d'inspiration. Merci à mes deux sœurs géniales, **Magalie** et **Morgane**, pour leur soutien inconditionnel et leurs encouragements. Merci à mes grands-parents **Arlette** et **Gilbert** ainsi qu'à mes oncles, tantes, cousins et cousines **Francis**, **Cathy**, **Laurent**, **Kévin** et **Nathalie** de s'être déplacés de si loin. Je vous suis à tous, reconnaissante d'avoir gardé votre bonne humeur et votre grand humour lorsque nous avons dû prolonger la fête d'un jour alors que coincés sans électricité dans notre gite de Séchilienne après ma soutenance. Plus généralement, merci également aux membres de la famille qui n'ont pas pu venir mais qui ont pensé à moi et m'ont soutenue toutes ces années. Enfin, je remercie affectueusement **Meshkan** pour avoir relu une partie de ce manuscrit et surtout pour me supporter en (presque) toutes circonstances.

Résumé en français

Introduction

Au cours des deux dernières décennies, les matériaux semiconducteurs de la famille III-N, à savoir l'InN, le GaN, l'AlN et leurs différents alliages, ont attiré une attention croissante. Le sursaut d'intérêt suscité par ces matériaux a eu lieu vers la fin des années 90 et est couramment associé à la fabrication des premières diodes électroluminescentes et diodes lasers nitrures par les groupes japonais dirigés par le professeur Akasaki (Université de Nagoya) et S. Nakamura (Nichia Chemical Industries) [1–6]. Grâce à leur bande interdite directe et la large gamme de longueurs d'ondes couverte par les différents alliages III-N, allant de l'infrarouge proche à l'ultraviolet (UV) profond, les matériaux III-N ont été, dès lors, largement utilisés pour la fabrication de dispositifs opto-électroniques tels que les diodes électroluminescentes blanches/bleues/vertes et les diodes lasers violettes/bleues/vertes [7]. La diode laser nitrure la plus connue est d'ailleurs la diode laser bleue émettant à 405 nm, utilisée pour la technologie *blu-ray*. Les semiconducteurs III-N présentent en outre une grande stabilité chimique, une tension de seuil élevée, une grande mobilité électronique et une bonne conductivité thermique qui les rendent aptes à être utilisés dans des dispositifs fonctionnant à haute température, haute fréquence et/ou à forte puissance [8–10].

Les premières publications associées aux matériaux III-N datent du début du XX$^{\text{ième}}$ siècle et décrivent la fabrication d'AlN, de GaN et d'InN polycristallins [11–13]. Depuis cette époque, la synthèse des semiconducteurs III-N a été grandement améliorée, les premières couches épitaxiées de GaN ayant fait leur apparition dans les années 70 [14–16]. Ces couches présentaient toutefois une mauvaise qualité cristalline et un fort dopage de type n, bien que n'étant pas intentionnellement dopées. Ce n'est qu'en 1986 qu'Amano et ses collaborateurs parvinrent à améliorer de manière significative la qualité cristalline du GaN en épitaxiant celui-ci sur une couche tampon d'AlN ("buffer"), elle-même déposée sur un substrat de saphir [17]. La même équipe réalisa ensuite le premier GaN dopé p [18] qui conduisit aux succès opto-électroniques mentionnés ci-dessus. Ce qu'il est intéressant de noter, c'est qu'alors même qu'ils recherchaient les conditions de croissance favorables à la production de couches de GaN bien lisses, cette équipe décrivit la tendance du GaN à croître en formant des cristaux colonnaires coaslescés [19]. Quelques années plus tard,

les équipes des professeurs Kishino et Calleja observèrent que dans certaines conditions d'épitaxie par jets moléculaires (EJM), le GaN pouvait croître en formant de lui-même des colonnes bien séparées et de dimension nanométrique [20, 21]. Les premiers nanofils de GaN auto-assemblés ont ainsi vu le jour. Néanmoins, à cette époque, ces nanostructures furent quelque peu ignorées et il fallut une dizaine d'années supplémentaires avant qu'elles suscitent l'intérêt.

De manière plus générale, la nécessité de rendre les dispositifs toujours plus petits a stimulé, au début des années 2000, l'intérêt pour les nanofils. Comme expliqué dans les articles du groupe de Charles Lieber [22, 23], lorsque l'on atteint des dimensions inférieures à la centaine de nanomètres, les techniques de fabrications traditionnelles, dites "top-down" (du haut vers le bas), telles que la lithographie, font face à des défis à la fois fondamentaux et technologiques. Un de ces problèmes est lié aux fluctuations de taille des structures gravées qui induisent des dispersions dans les caractéristiques et les performances des dispositifs finaux. Pour dépasser cette limite de réduction des dimensions, de nouvelles stratégies, fondées sur des approches "bottom-up" (du bas vers le haut), ont été envisagées. Dans ce contexte, les objets uni-dimensionnels tels que les nanofils ou les nanotubes de carbone, sont apparus extrêmement intéressants, leur taille (et plus largement leur composition chimique, leur dopage, leur structure et leur morphologie) étant généralement déterminée par les paramètres du procédé de fabrication.

Les domaines d'application des nanofils ont, de nos jours, dépassé la nanoélectronique, se propageant à l'opto-électronique, la photonique et même la nano-détection. Ils constituent notamment les plus petits objets pouvant servir à la fois de guide optique [24] et de contact électrique [25]. D'autre part, en raison de leur géométrie anisotrope, leurs propriétés optiques et électriques dépendent de leur orientation, ce qui les rend aptes à être utilisés comme capteur sensible à la polarisation. En vertu de leur rapport surface/volume élevé, ils présentent également une meilleure interaction avec l'environnement, ce qui leur donne des propriétés de détection chimique et biologique optimales [26]. Dans le même ordre d'idées, les hétérostructures filaires radiales sont une solution intéressante pour réduire les dimensions des dispositifs sans perte d'efficacité. Ils ont en effet l'avantage de présenter, pour un volume donné de matériau déposé, une plus grande surface active que leur homologues à deux dimensions. En pratique, différents types de dispositifs basés sur des puits quantiques radiaux ont déjà été démontrés, tant en opto-électroniques [27–29], en nanoélectronique [30] que dans le domaine du photovoltaïque [31, 32]. Notons cependant que malgré ces démonstrations, un gain d'efficacité des dispositifs à base d'hétérostructures filaires par rapport aux hétérostructures 2D traditionnelles, n'a jamais été attesté.

C'est dans ce contexte qu'une partie de la recherche sur le GaN s'est orientée vers les nanostructures colonnaires de GaN. On peut ainsi se demander quels sont les avantages des nanofils GaN par rapport aux couches 2D de GaN.

- **La qualité crystalline**
  Un des problèmes majeurs des matériaux nitrures est l'absence de substrat adapté à leur croissance en épitaxie. Ainsi, de nos jours, les meilleures couches épitaxiées contiennent jusqu'à 10^7 dislocations par cm^2. Les nanofils, en revanche, présentent un rapport d'aspect (longueur/diamètre) élevé, ce qui leur permet de relaxer facilement les contraintes sur leur périphérie, et leur donne potentiellement l'avantage de croître sans contrainte et sans défaut sur n'importe quel type de substrat. Les nanofils GaN permettent donc l'utilisation de substrats ayant des paramètres de maille très différents, tout en évitant la formation de défauts dans le cristal. Naturellement, le rapport d'aspect élevé des nanofils bénéficie également aux hétérostructures filaires, à la fois axiales et radiales, puisque des matériaux très désaccordés peuvent être utilisés pour les différentes couches composant ces hétérostructures.

- **Croissance sur les surface non polaires**
  Les matériaux III-N cristallisent le plus souvent sous forme wurtzite qui est une structure non centro-symétrique. Il en résulte que la direction <0001> est polaire. En conséquence, les propriétés des hétérostructures fabriquées dans cette direction sont déterminées par la présence d'un champ électrique interne. Dans le cas d'un puits quantique, ce champ électrique induit un décalage de l'émission lumineuse vers le rouge et une augmentation du temps de vie des porteurs dans le puits. Pour contourner cette spécificité, des tentatives de croissance d'hétérostructures le long des directions non polaires du cristal, c'est-à-dire perpendiculairement à la direction <0001>, ont été effectuées. Toutefois, en raison de la forte anisotropie des propriétés des surfaces non polaires [33, 34], la croissance de couches 2D de matériaux III-N dans ces directions reste difficile et entraîne une forte densité de dislocations et de fautes d'empilement [35]. Via la fabrication de puits quantiques radiaux, les facettes des nanofils constituent une base idéale pour la croissance d'hétérostructures dans les directions non-polaires.

Objectifs et motivations de la thèse

Dans cette thèse, nous nous focalisons sur l'étude des nanofils de GaN et d'hétérostructures filaires GaN-AlN fabriqués par épitaxie par jets moléculaires assistée plasma. Depuis la parution des premières publications sur le sujet, les nanofils de GaN ont été au cœur de nombreuses études. En ce qui concerne leurs mécanismes de croissance, il est ainsi désormais admis que dès que la structure colonnaire du GaN est initiée, celle-ci est promue par la diffusion d'atomes de Ga le long des facettes du nanofil jusqu'à leur surface sommitale [36–38]. Néanmoins, les processus à l'origine de l'initiation de ces structures colonnaires (en d'autres termes, de la "nucléation" des nanofils) restent encore quelque peu incompris. Au sein de notre groupe et au cours de sa propre thèse de doctorat, O. Landré a étudié la formation des précurseurs de nanofils de GaN sur un substrat de Si(111) couvert

d'une fine couche tampon d'AlN [39, 40]. Pour ce faire, il effectua des expériences de diffraction de rayons X en incidence rasante *in situ*, au synchrotron de Grenoble (ESRF - European Synchrotron Radiation Facility) et montra que

- dans un premier temps, le GaN se dépose en une couche pseudomorphe sur la couche tampon d'AlN ;
- au-delà d'une épaisseur critique de 2.8 monocouches, le GaN subit une transition de type Stranski-Krastanov (formation de précurseurs de nanofils de GaN) ;
- ces précurseurs grossissent jusqu'à relaxer plastiquement via l'introduction d'une dislocation à l'interface GaN/AlN.

La présence d'une dislocation à l'interface GaN/AlN a également été observée par le groupe de H. Riechert (Institut Paul Drude de Berlin) [41]. Les auteurs ont montré que l'introduction de cette dislocation est corrélée à l'apparition des facettes verticales du précurseur [41] et suggèrent ainsi que la relaxation plastique signe le début de la croissance colonnaire.

C'est dans ce contexte que s'inscrit mon travail de thèse, dont le premier objectif est d'élargir notre connaissance fondamentale des mécanismes de croissance et des propriétés des nanofils de GaN auto-assemblées. Plus précisément, le travail décrit dans ce manuscrit vise à :

- étudier la nucléation des nanofils de GaN sur silicium nu, similairement à ce qui a été fait sur silicium recouvert d'une couche tampon d'AlN et à confronter les deux cas ;
- corréler les processus de nucléation à la morphologie finale des nanofils de GaN (leur densité, leur longueur, leur dispersion en longueur, leur diamètre), afin de mieux contrôler leur croissance auto-assemblée ;
- corréler la polarité des nanofils de GaN à leur processus de nucléation.

Le deuxième objectif de ce travail est d'analyser les mécanismes de croissance et les propriétés d'hétérostructures filaires originales, à savoir des hétérostructures filaires de GaN/AlN de type cœur-coquille, ainsi que des boîtes quantiques uniques de GaN dans AlN fabriquées sur nanofils de GaN. Le manuscrit de thèse est divisé en 6 chapitres dont le contenu est décrit ci-après.

Chapitre 1 - Epitaxie par jets moléculaires assistée plasma, propriétés des semiconducteurs III-N et outils de caractérisation

Dans ce premier chapitre, nous nous attachons à présenter les techniques et les matériaux au cœur de ce travail de thèse. Dans un premier temps, nous décrivons l'EJM, la technique de croissance utilisée pour la fabrication des diverses structures étudiées. Nous exposons ensuite les propriétés de base les plus significatives des semiconducteurs de la famille III-N, à savoir leur structure crystalline wurtzite, leurs propriétés élastiques et électroniques. Pour finir, nous présentons les principales techniques de caractérisation utilisées au cours de ce travail de thèse. Nous détaillons ainsi le principe de fonctionnement du RHEED (Reflection High Energy Electron Diffraction), l'outil de diffraction d'électrons rapides sous incidence rasante disponible sur le bâti d'EJM. Nous expliquons de quelle manière cette technique nous permet de suivre *in situ* et en temps réel les modifications de surface de l'échantillon en cours de croissance. Ensuite, nous nous penchons sur la technique de diffraction de rayons X qui sera utilisée à plusieurs reprises au cours du manuscrit, à savoir la diffraction anomale multi-longueurs d'onde (MAD). Dans la dernière partie, nous décrivons brièvement les deux techniques de caractérisation optique que sont la photoluminescence (à la fois à l'échelle macroscopique et à l'échelle microscopique) ainsi que la nano-cathodoluminescence.

Chapitre 2 - Croissance et propriétés des nanofils de GaN auto-assemblés sur silicium

Dans ce chapitre, nous nous focalisons sur les nanofils de GaN fabriqué par EJM sur silicium. Dans un premier temps, nous introduisons les substrats de silicium et décrivons la méthode utilisée pour calibrer leur température. Le silicium généralement utilisé est orienté [111]: cette surface présente en effet une maille surfacique hexagonale compatible avec la structure wurtzite des matériaux III-N. La surface (111) du silicium a également la particularité de se reconstruire (7×7). Dans notre groupe, nous avons mis en évidence que cette reconstruction de surface disparait lorsque le Si est exposé au gallium et réapparait lorsque tout le gallium déposé est évaporé. Le taux de désorption du gallium peut ainsi être déterminé par la mesure de la vitesse de réapparition de la reconstruction (7×7). Or il se trouve que le taux de désorption du gallium dépend de la température du substrat. De cette manière, la mesure de la vitesse de réapparition de la reconstruction (7×7) nous informe directement sur la température de la surface du silicium.

Dans la seconde partie du manuscrit, nous expliquons que sur silicium, deux possibilités de croissance de nanofils GaN auto-assemblés s'offrent à nous. La croissance peut en effet

être initiée soit directement sur silicium ou sur silicium recouvert d'une fine couche tampon d'AlN. Un bref état de l'art de la littérature nous permet de constater que l'utilisation d'une couche tampon d'AlN conduit à un ensemble de nanofils plus uniforme, c'est-à-dire présentant une faible mosaïcité dans le plan et hors du plan. Néanmoins, du fait du caractère quasi-isolant de l'AlN, il est judicieux de ne pas abandonner la piste des nanofils fabriqués sur silicium nu. Afin de mieux cerner les caractéristiques de ces derniers, nous étudions dans la dernière partie du chapitre, la dépendance de leur longueur, de leur diamètre et de leur densité à la température du substrat. Nous constatons ainsi qu'avec l'augmentation de la température du substrat, la densité des nanofils de GaN ainsi que leur longueur moyenne décroissent tandis que la dispersion de longueur entre fils augmente. Afin de mieux comprendre ces observations, une étude plus poussée de la nucléation des nanofils est entreprise au chapitre suivant.

Chapitre 3 - Nucléation des nanofils auto-assemblés de GaN

Comme mentionné ci-dessus, la nucléation des nanofils de GaN n'est pas encore complètement comprise, en particulier lorsque ceux-ci sont fabriqués sur silicium nu. Dans ce chapitre, nous combinons deux techniques de caractérisation *in situ* pour étudier la nucléation des nanofils de GaN: le RHEED et la diffraction de rayons X en incidence rasante effectuée en temps réel pendant la fabrication des nanostructures dans le bâti de la ligne BM32 de l'ESRF.

Sur silicium nu, nous identifions qu'une couche crystalline de β-Si_3N_4 se forme (nitruration du silicium) et doit être ensuite "amorphisée" (transformation du β-Si_3N_4 cristallin en Si_xN_y amorphe) avant que le GaN puisse enfin nucléer. Nous avons identifié les espèces en provenance de la cellule plasma (soit des atomes d'azote ou des ions N^+) comme étant responsables de ce dernier processus, les atomes de Ga étant quant à eux inertes. La température du substrat ne semble pas jouer de rôle dans la dynamique de nitruration-amorphisation. En revanche, sur Si_xN_y amorphe, le retard à la nucléation augmente avec l'accroissement de la température du substrat et avec la diminution du flux de gallium. Des retards de nucléation similaires sont observés pour la formation des précurseurs de GaN sur silicium nu et sur silicium couvert d'un fine couche tampon d'AlN.

Chapitre 4 - Polarité des nanofils GaN

Malgré les nombreuses études parues à leur sujet, une des caractéristiques des nanofils qui fut longtemps sujette à controverse est leur polarité. Les fils de GaN fabriqués par EJM sont-ils de polarité Ga ou N ? Dans ce chapitre, nous nous proposons d'utiliser la diffraction de rayons X résonnante pour répondre à cette question à l'échelle macroscopique.

Nous présentons ainsi dans un premier temps la méthode utilisée, avant de l'appliquer à nos nanostructures. Les résultats obtenus démontrent de manière irréfutable que les fils fabriqués sur silicium nu sont de polarité azote.

Nous testons dans un deuxième temps l'effet de la gravure chimique au KOH sur les nanofils: le KOH grave la face azote des nanofils (cette face ayant été identifiée par les rayons X) en leur donnant une forme de crayon et laisse intacte (plane) la face Ga de ces structures. Comme dans le cas des couches 2D, la sélectivité de la gravure au KOH peut donc être utilisée pour déterminer la polarité des nanofils. Nous utilisons ainsi le test KOH sur des nanofils fabriqués sur silicium recouvert d'une fine couche tampon d'AlN: toutes les colonnes se trouvent gravées en forme de crayon: ils sont de polarité N.

Parallèlement à nos recherches, le groupe dirigé par le professeur Calleja publia un article dans lequel il est montré que des nanofils d'AlGaN fabriqués sur une couche d'AlN **épaisse** sont de polarité métal [42]. Cette observation est en accord avec les résultats de Bourret et coll. qui ont montré que la polarité d'une couche d'AlN sur silicium est elle-même métal [43]. A partir de ces différentes données, nous suggérons que la polarité des nanofils est liée à leur nucléation. Sur silicium nu, il est probable que les atomes de Ga se lient avec les atomes d'azote appartenant à la couche de Si_xN_y amorphe en formant des liaisons simples (plutôt que des liaisons triples), amorçant ainsi la polarité azote. Lors de l'utilisation d'une **fine** couche tampon d'AlN, il est vraisemblable que les atomes de Ga forment le même type de liaisons avec des atomes N de "résidus" de Si_xN_y situés entre les grains du buffer d'AlN. Lors de la fabrication d'un buffer **épais**, les grains d'AlN sont coalescés. Les fils nucléent alors directement sur AlN, exhibant ainsi la même polarité que celui-ci, à savoir métal.

Chapitre 5 - Hétérostructures filaires de type cœur-coquille GaN-AlN

Après avoir étudié les nanofils de GaN, nous nous penchons dans ce chapitre sur les hétérostructures GaN-AlN de type cœur-coquille. Dans la première partie, nous étudions la croissance d'AlN sur nanofils de GaN. Plus particulièrement, nous étudions de quelle manière la morphologie (c'est-à-dire le rapport entre la longueur de la partie supérieure – le chapeau – de la coquille d'AlN et son épaisseur autour des fils de GaN) varie avec le rapport des flux Al/N et avec l'angle d'incidence des atomes. Pour cette étude, nous nous appuyons à la fois sur un modèle géométrique que j'ai développé en m'inspirant de celui proposé par Foxon en 2009 [44] et sur des observations expérimentales. Les calculs suggèrent qu'un changement de rapport de flux Al/N ne modifie pas de manière significative la morphologie des coquilles d'AlN. Cependant, en pratique, augmenter ce rapport de 0.55 à 0.86 conduit (à angles d'incidence donnés) à des épaisseurs latérales plus grandes, les

partie supérieures ayant des longueurs comparables. Les morphologies observées sont expliquées par une diffusion importante des atomes d'Al du facettes des nanofils jusqu'à leur sommet, combinée à une forte désorption des atomes de N via la formation de molécules de N_2.

Dans un deuxième temps, nous caractérisons structurellement les hétérostructures cœur-coquille. A l'aide de la technique MAD, nous mesurons l'état de contrainte des cœurs de GaN en fonction de l'épaisseur de la coquille d'AlN. En combinant cette technique macroscopique à des techniques microscopique (HRTEM) ainsi qu'à des calculs théoriques, nous montrons que l'état de contrainte des cœurs de GaN dépend en fait de la symétrie des coquilles d'AlN. En effet, lorsque la coquille croît de manière symétrique autour des nanofils de GaN, la contrainte dans le cœur de l'hétérostructure augmente avec l'épaisseur de l'AlN. Un modèle élastique décrit alors parfaitement le système. En revanche, lorsque la coquille commence à croître de manière asymétrique, le système relaxe d'abord élastiquement, mais des contraintes de cisaillement apparaissent rapidement dans le cœur de GaN aboutissant au fléchissement du nanofil. Au-delà d'une épaisseur critique d'AlN de 3 nm, le système relaxe alors plastiquement via l'introduction d'un plan c supplémentaire du côté le plus mince de la coquille.

Enfin, dans la dernière partie du chapitre, nous nous penchons sur les propriétés optiques des structures cœur-coquille GaN-AlN . La croissance d'une coquille d'AlN sur et autour des nanofils de GaN conduit à "l'extinction" de l'émission du bord de bande et à l'apparition d'un pic très large à plus basse énergie. Bien que difficile à interpréter, l'évolution avec l'épaisseur de coquille de l'intensité intégrée et de la largeur à mi-hauteur de ce pic suggère que la luminescence dépend de l'homogénéité (la symétrie) de la coquille.

Chapitre 6 - Boîtes quantiques de GaN dans des nanofils AlN

Dans ce dernier chapitre, nous tirons parti des nanostructures étudiées dans le chapitre précédent. Nous nous demandons s'il est possible de trouver des nanofils d'AlN (comprenez des nanofils cœur-coquille GaN/AlN) dont le diamètre serait suffisamment large pour permettre au GaN déposé sur cette surface de subir une transition de type Stranski-Krastanov telle qu'observée dans la formation de boîtes quantiques sur couches 2D. Tant théoriquement qu'expérimentalement, nous montrons qu'il est effectivement possible d'obtenir des insertions de GaN ayant une forme d'îlot sur des nanofils d'AlN. Expérimentalement, nous observons de tels îlots sur des nanofils d'AlN ayant un diamètre supérieur à 77 nm mais des doutes sont soulevés quant à leur composition exacte. Des analyses de microscopie révèlent en effet que le cœur des îlots contient des atomes d'Al. Il est possible que la présence de ces atomes d'Al soit une conséquence de la forme du fil d'AlN (sur GaN

toujours) lui-même, qui exhibe parfois une surface sommitale “bossue”. Lors du dépôt de GaN sur ce type de surface, le GaN envelopperait alors l’AlN en formant une sorte de “chapeau melon”.

Dans la deuxième partie du chapitre, nous étudions les propriétés optiques de ces structures originales. Grâce à des grilles spéciales et une dispersion minutieuse des fils, nous parvenons à obtenir des spectres de microphotoluminescence sur des fils uniques dont la forme de l’îlot correspondant est identifiée par microscopie en transmission. Nous détectons la présence de nombreux états localisés dans les insertions de GaN, résultats confirmés par des analyses de nano-cathodoluminescence.

Conclusion

Au cours du travail de thèse résumé ci-dessus, nous avons étudié les mécanismes de croissances et les propriétés de nanofils de GaN et d’hétérostructures filaires GaN-AlN.

En ce qui concerne les nanofils de GaN, notre attention s’est plus particulièrement portée sur les nanofils auto-assemblés sur silicium nu et sur silicium recouvert d’un fine couche tampon d’AlN. Nous avons discuté et comparé la nucléation des nanofils sur ces deux types de surfaces. Nous avons également analysé la morphologie des nanofils de GaN (densité, longueur moyenne, diamètre moyen, dispersion de longueurs) en fonction des paramètres de croissance et corrélé nos observations à la dynamique de nucléation des nanofils. Enfin, nous avons abordé la problématique de la polarité des nanofils GaN dont la croissance est initiée de différentes manières: sur silicium nu, sur silicum recouvert d’un fine couche tampon d’AlN et sur silicium dont la surface est pré-couverte de Ga. En conclusion de ce travail, nous avons pu constater que bien que les nanofils de GaN auto-assemblés aient l’avantage de croître facilement (la fenêtre de conditions de croissance étant plutôt large), le contrôle de leur morphologie est loin d’être trivial. Plus précisément, il n’est pas possible, en jouant uniquement sur la température du substrat et le rapport des flux Ga/N, d’obtenir des fils à la fois peu denses et de longueur comparable. En d’autres termes, une faible densité requiert une température élevée, qui induit une dispersion de longueur entre fils. Ceci n’est cependant vrai, que lorsque la croissance est effectuée en une seule étape. D’autres procédures, comme celle proposée dans la référence [45] peuvent aider à pallier à ce problème. Une autre possibilité est celle d’utiliser des substrats “patternés” dont la densité de trous contrôle la densité de nanofils. Cette piste est justement en cours d’étude au sein de notre groupe, l’appendice B de ce manuscrit y étant dédiée.

Nous nous sommes ensuite penchés sur les hétérostructures filaires de type GaN-AlN. Dans un premier temps, nous avons étudié la morphologie de coquilles d’AlN autour et sur les nanofils de GaN en fonction de divers paramètres de croissance. Ensuite, en utilisant une combinaison de diffraction anomale multi-longueurs d’onde, de microscopie

en transmission de haute résolution et de calculs théoriques s'appuyant sur un modèle purement élastique, l'état de contrainte des cœurs de GaN a été analysé en fonction de l'épaisseur de la coquille. Les conclusions que nous avons pu tirer de cette partie sont liées à la perspective de croître des puits quantiques radiaux. Il semble important de mieux contrôler l'homogénéité (la symétrie) des coquilles d'AlN. Ici encore, la croissance de nanofils sur substrats "patternés" pourrait être une aide précieuse. D'une part, en utilisant des trous de faible diamètre, il devrait être possible d'éliminer la "marche" à la base du pied des nanofils de GaN, pied que nous avons identifié comme étant la plus probable origine de l'asymétrie de la coquille d'AlN. D'autre part, en utilisant des trous de faible densité, nous protégerions les colonnes de "l'effet d'ombre". Néanmoins, malgré le manque d'homogénéité des coquilles d'AlN, nous avons pu synthétiser des coquilles d'AlN assez épaisses pour obtenir des structures colonnaires larges d'une centaine de nanomètres. Dans le dernier chapitre du manuscrit, nous avons donc voulu déposer quelques monocouches de GaN sur ces surface en espérant induire une transition de type Stranski-Krastanov. Nous avons effectivement pu observer des insertions ayant la forme d'îlots dans les nanofils, mais leur nature exacte peut être remise en question. Quoi qu'il en soit, ces structures ont été caractérisées optiquement et semblent présenter des états localisés. Dans le but d'identifier l'origine de ces états, des mesures de photoluminescence en température et en puissance seront prochainement réalisées sur des fils uniques.

Bibliographie du résumé

[1] I. Akasaki, H. Amano, K. Itoh, N. Koide, and K. Manabe, GaN-based ultra-violet/blue light emitting devices, *Inst. Phys. Conf. Ser.* **129**, 851 (1992).

[2] S. Nakamura, T. Mukai, and M. Senoh, Candela-class high-brightness InGaN/AlGaN double-heterostructure blue light-emitting diodes, *Appl. Phys. Lett.* **64**, 1687 (1994).

[3] S. Nakamura, M. Sehnoh, N. Iwasa, S. Nagahama, T. Yamada, and T. Mukai, Superbright green InGaN single-quantum-well-structure light emitting diode, *Jpn. J. Appl. Phys.* **34**, L1332 (1995).

[4] S. Nakamura, M. Senoh, S. Nagahama, N. Iwasa, T. Yamada, T. Matsushita, H. Kiyoku, and Y. Sugimoto, InGaN-based multi-quantum-well-structure laser diodes, *Jpn. J. Appl. Phys.* **35**, L74 (1996).

[5] S. Nakamura, M. Senoh, S. Nagahama, N. Iwasa, T. Yamada, T. Matsushita, H. Kiyoku, and Y. Sugimoto, InGaN multi-quantum-well-structure laser diodes with cleaved mirror cavity facets, *Jpn. J. Appl. Phys.* **35**, L217 (1996).

[6] S. Nakamura, M. Senoh, S. Nagahama, N. Iwasa, T. Yamada, T. Matsushita, H. Kiyoku, Y. Sugimoto, T. Kozaki, H. Umemoto, M. Sono, and K. Chocho, InGaN/GaN/AlGaN-based laser diodes with modulation doped strained-layer superlattices, *Jpn. J. Appl. Phys.* **36**, L1568 (1997).

[7] S. Nakamura, S. Pearton, and G. Fasol, The blue laser diodes - The complete story, (Springer 1997).

[8] O. Ambacher, Growth and applications of group III-nitrides, *J. Phys. D: Appl. Phys.* **31**, 2653 (1998).

[9] S. J. Pearton, J. C. Zolper, R. J. Schul, and F. Ren, GaN: Processing, defects, and devices, *J. Appl. Phys.* **86**, 1 (1999).

[10] A. Mills, Expanding horizons for nitride devices and materials, *III-Vs Review - The advanced semiconductor magazine* **19**, 25 (2006).

[11] F. Fichter, Über Aluminiumnitride, *Z. Anorg. Chem.* **54**, 322 (1907).

[12] W. C. Johson, J. B. Parsons, and M. C. Crew, Nitrogen coumponds of Gallium - III. Gallic nitride, *J. Phys. Chem.* **36**, 2651 (1932).

[13] R. Juza and H. Hahn, Über die Kristallstrukturen von Cu_3N, GaN und InN Metallamide and Metallnitride, *Z. Anorg. Allg. Chem.* **239**, 282 (1938).

[14] H. P. Maruska and J. J. Tietjen, The preparation and properties of vapour-deposited single-crystal-line GaN, *Appl. Phys. Lett.* **15**, 327 (1969).

[15] H. M. Manasevit, F. M. Erdmann, and W. I. Simpson, The use of metalorganics in the preparation of semiconductor materials - IV. The nitrides of Aluminium and Gallium, *J. Electrochem. Soc.* **118**, 1864 (1971).

[16] S. Yoshida, S. Misawa, and A. Itoh, Epitaxial growth of aluminium nitride films on sapphire by reactive evaporation, *Appl. Phys. Lett.* **26**, 461 (1975).

[17] H. Amano, N. Sawaski, I. Akasaki, and Y. Toyoda, Metalorganic vapor phase epitaxial growth of a high quality GaN film using an AlN buffer layer, *Appl. Phys. Lett.* **48**, 353 (1986).

[18] H. Amano, M. Kito, K. Hiramatsu, and I. Akasaki, P-type conduction in Mg-doped GaN treated with low-energy electron beam irradiation (LEEBI), *Jpn. J. Appl. Phys.* **48**, 353 (1989).

[19] K. Hiramatsu, S. Itoh, H. Amano, I. Akasaki, N. Kuwano, T. Shiraishi, and K. Oki, Growth mecanisms of GaN grown on sapphire with AlN buffer layer by MOVPE, *J. Cryst. Growth* **115**, 628 (1991).

[20] M. Yoshizawa, A. Kikuchi, M. Mori, N. Fujita, and K. Kishino, Growth of self-organized GaN nanostructures on Al_2O_3(0001) by RF-radical source molecular beam epitaxy, *Jpn. J. Appl. Phys.* **36**, 459 (1997).

[21] M. A. Sanchez-Garcia, E. Calleja, E. Monroy, F. J. Sanchez, F. Calle, E. Munoz, and R. Beresford, The effect of III/V ratio and substrate temperature on the morphology and properties of GaN- and AlN-layers grown by molecular beam epitaxy on Si(111), *J. Cryst. Growth* **183**, 23 (1998).

[22] W. Lu and C. M. Lieber, Semiconductor nanowires, *J. Phys. D: Appl. Phys.* **39**, R387 (2006).

[23] R. Agarwal and C. M. Lieber, Semiconductor nanowires: optics and optoelectronics, *Appl. Phys. A* **85**, 209 (2006).

[24] D. J. Sirbuly, M. Law, H. Yan, and P. Yang, Semiconductor nanowires for subwavelength photonics integration, *J. Phys. Chem. B* **109**, 15 190 (2005).

[25] Y. L. F. Qian, J. Xiang, and C. M. Lieber, Nanowire electronic and optoelectronic devices, *Mater. Today* **9**, 18 (2006).

[26] F. Patolsky and C. M. Lieber, Nanowire nanosensors, *Mater. Today* **8**, 20 (2005).

[27] F. Qian, Y. Li, S. Gradecak, D. Wang, C. J. Barrelet, and C. M. Lieber, Gallium Nitride-based nanowire radial heterostructures for nanophotonics, *Nano Lett.* **4**, 1975 (2004).

[28] F. Qian, S. Gradecak, Y. Li, C.-Y. Wen, and C. M. Lieber, Core/multishell nanowire heterostructures as multicolor, high-efficiency light-emitting diodes, *Nano Lett.* **5**, 2287 (2005).

[29] K. Tomioka, J. Motohisa, S. Hara, K. Hiruma, and T. Fukui, GaAs/AlGaAs core multishell nanowire-based light-emitting diodes on Si, *Nano Lett.* **10**, 1639 (2010).

[30] Y. Li, J. Xiang, F. Qian, S. Gradecak, Y. Wu, H. Yan, D. A. Blom, and C. M. Lieber, Dopant-free GaN/AlN/AlGaN radial nanowire heterostructures as high electron mobility transistors, *Nano Lett.* **6**, 1468 (2006).

[31] B. Tian, X. Zheng, T. J. Kempa, Y. Fang, N. Yu, G. Yu, H. Huang, and C. M. Lieber, Coaxial silicon nanowires as solar celles and nanoelectronic power sources, *Nature* **449**, 885 (2007).

[32] Y. Dong, B. Tian, T. J. Kempa, and C. M. Lieber, Coaxial group III-Nitride nanowire photovoltaics, *Nano Lett.* **9**, 2183 (2009).

[33] H. Wang, C. Chen, Z. Gong, J. Zhang, M. Gaevski, M. Su, J. Yang, and M. A. Khan, Anisotropic structural characteristics of $(11\bar{1}0)$ GaN templates and coalesced epitaxial lateral overgrown films deposited on $(10\bar{1}2)$ sapphire, *Appl. Phys. Lett.* **84**, 499 (2004).

[34] D. S. Li, H. Chen, H. B. Yu, X. H. Zheng, Q. Huang, and J. M. Zhou, Anisotropy of a-plane GaN grown on r-plane sapphire by metalorganic chemical vapor deposition, *J. Cryst. Growth* **265**, 107 (2004).

[35] T. Paskova, V. Darakchieva, P. Paskov, J. Birch, E. Valcheva, P. O. A. Persson, B. Arnaudov, S. Tungasmitta, and B. Monemar, Properties of nonpolar a-plane GaN films grown by HVPE with AlN buffers, *J. Cryst. Growth* **281**, 55 (2005).

[36] R. Meijers, T. Richter, R. Calarco, T. Stoica, H.-P. Bochem, M. Marso, and H. Lüth, GaN-nanowhiskers: MBE-growth conditions and optical properties, *J. Cryst. Growth* **289**, 381 (2006).

[37] R. Calarco, R. J. Meijers, R. K. Debnath, T. Stoica, E. Sutter, and H. Lüth, Nucleation and growth of GaN nanowires on Si(111) performed by molecular beam epitaxy, *Nano Lett.* **7**, 2248 (2007).

[38] R. K. Debnath, R. Meijers, T. Richter, T. Stoica, R. Calarco, and H. Lüth, Mechanism of molecular beam epitaxy growth of GaN nanowires on Si(111), *Appl. Phys. Lett.* **90**, 123 117 (2007).

[39] O. Landré, C. Bougerol, H. Renevier, and B. Daudin, Nucleation mechanism of GaN nanowires grown on (111) Si by molecular beam epitaxy, *Nanotechnology* **20**, 415 602 (2009).

[40] O. Landré, Etude de la nucleation et de la croissance de structures filaires GaN et AlN, Ph.D. thesis, Université de Grenoble (2010).

[41] V. Consonni, M. Knelangen, L. Geelhaar, A. Trampert, and H. Riechert, Nucleation mechnisms of epitaxial GaN nanowires: Origin of their self-induced formation and initial radius, *Phys. Rev. B* **81**, 085 310 (2010).

[42] X. Kong, J. Ristić, M. A. Sanchez-Garcia, E. Calleja, and A. Trampert, Polarity determination by electron energy-loss spectroscopy: application to ultra-small III-nitride semiconductor nanocolumns, *Nanotechnology* **22**, 415 701 (2011).

[43] A. Bourret, A. Barski, J. L. Rouvière, G. Renaud, and A. Barbier, Growth of aluminum nitride on (111) silicon: microstructure and interface structure, *J. Appl. Phys.* **83**, 2003 (1998).

[44] C. T. Foxon, S. V. Novikov, J. L. Hall, R. P. Campion, D. Cherns, I. Griffiths, and S. Khongphetsak, A complementary geometric model for the growth of GaN nanocolumns prepared by plasma-assisted molecular beam epitaxy, *J. Cryst. Growth* **311**, 3423 (2009).

[45] S. D. Carnevale, J. Yang, P. J. Phillips, M. J. Mills, and R. C. Myers, Three-dimensional GaN/AlN nanowire heterostructures by separating nucleation and growth processes, *Nano Lett.* **11**, 866 (2011).

Acronyms

2DEG	2-Dimensional Electron Gas
III-N	III-Nitride
AFM	Atomic Force Microscopy
CVD	Chemical Vapour Deposition
D_0X	Donor-bound eXciton
DAP	Donor-Acceptor Pair
ESRF	European Synchrotron Radiation Facility
FWHM	Full Width at Half Maximum
FX_A	Free eXciton A
FX_B	Free eXciton B
GIXRD	Grazing-Incidence X-Ray Diffraction
GPA	Geometrical Phase Analysis
HAADF	High-Angle Annular Dark-Field
HEMT	High Electron Mobility Transistor
HF	hydrofluoric acid
HRTEM	High Resolution Transmission Electron Microscopy
HVPE	Hybride Vapour-Phase Epitaxy
LD	Laser Diode
LED	Light-Emitting Diode
MAD	Multi-wavelength Anomalous Diffraction
MBE	Molecular Beam Epitaxy
MD	Misfit Dislocation
ML	Monolayer
MOVPE	MetalOrganic Vapour Phase Epitaxy
NW	Nanowire
PAMBE	Plasma-Assisted Molecular Beam Epitaxy
QCSE	Quantum-Confined Stark Effect
QD	Quantum Dot
Qdisk	Quantum disk
QW	Quantum Well

RF	Radio Frequency
RHEED	Reflection High Energy Electron Diffraction
SAG	Selective Area Growth
sccm	standard cubic centimetres per minute
SEM	Scanning Electron Microscopy
SF	Stacking Faults
SK	Stranski-Krastanov
TD	Threading Dislocation
TEM	Transmission Electron Microscopy
UHV	Ultra High Vacuum
VW	Volmer-Weber
WZ	Wurtzite
XRD	X-Ray Diffraction
YB	Yellow Band
ZB	Zinc Blende

Introduction

Over the past two decades, semiconductors of the III-nitride (III-N) family, namely InN, GaN, AlN and their different alloys, have been attracting increasing attention. The sudden burst of interest raised by these materials occurred in the 90s, commonly ascribed to the fabrication of the first hight brightness InGaN-based light-emitting diodes (LEDs) and laser diodes (LDs) by two Japanese groups, namely the group of Akasaki from the Nagoya University and the group of Nakamura from the Nichia Chemical Industries [1–6]. In virtue of their direct band gap and the large range of wavelengths covered by the different III-N alloys, spanning from the near infrared to the far ultraviolet over the whole visible spectrum, III-N materials have been, since then, largely used for optoelectronic devices such as white/blue/green LEDs and violet/blue/green LDs [7], in particular LDs emitting at 405 nm that are used in the *blu-ray* technology. Aside from optoelectronic applications, III-N semiconductors present a great chemical stability, high breakdown voltages, high electron mobilities and a good thermal conductivity which make them suitable for devices working at high temperature, high frequency and/or high power [8–10].

A brief history of semiconductor research that led to the interest for GaN nanowires

The first papers dealing with III-N materials date from the beginning of the 20$^{\text{th}}$ century and report growth of polycrystalline AlN [11], GaN [12] and InN [13] in 1907, 1932 and 1938, respectively. Epitaxial GaN layers were achieved no earlier than in the 70s. In particular, the first growth of epitaxial GaN on sapphire by hybrid vapour phase epitaxy (HVPE) was notified in 1969 in a paper from Maruska and Tietjen [14]. Similarly, pioneering growths of GaN by metalorganic vapour phase epitaxy (MOVPE) and by molecular beam epitaxy (MBE) were respectively reported by Manasevit *et al.* in 1971 [15] and by Yoshida *et al.* in 1975 [16]. GaN fabricated at that time exhibited a poor crystal quality and a high n-type conductivity although not purposely doped. Efforts that aimed at improving GaN crystal quality and at obtaining 2D layers as smooth as possible, were finally rewarded in 1986 when Amano *et al.* proposed the use of an intermediate AlN buffer layer on which his group successfully obtained the first high-crystalline

quality GaN film [17]. The same team achieved few years later the first GaN *p*-doping using Mg [18], which finally led to the above-mentioned III-N-based optoelectronic successes. Interestingly, during their search for GaN film growth optimized conditions, the same team reported the tendency of GaN to grow as coalesced columnar crystals [19]. Few years later, the group of Kishino and the group of Calleja concurrently observed in MBE that under specific growth conditions, GaN could form as actual nano-sized, well-separated columns [20, 21]. The first self-assembled GaN nanowires (NWs) were born. Nevertheless, at that time, such nanostructures were somewhat ignored and it took some additional 10 years for them to develop into their own research field.

More generally, interest in NWs was raised in the beginning of the 2000s by the continuous need for decrease of device dimensions (also called "scaling"). As explained in the topical reviews on semiconductor NWs published by the Lieber research group [22, 23], when reaching sub-100 nm dimensions, traditional top-down approaches, such as lithography, face both technological and fundamental challenges. One of these issues is especially related to size fluctuations of the etched structures, which induce large dispersions in device characteristics and performances. To overcome this scaling limit and sustain the well-known Moore's law, new strategies based on bottom-up approaches were considered. In this context, one-dimensional objects such as NWs and carbon nanotubes appeared as extremely interesting, their size (and more broadly their chemical composition, doping, structure and morphology) being generally determined by the growth conditions.

Application fields of NWs have since then proven to be wider than nanoelectronics, spreading to optoelectronics, photonics or even nanosensing. They for instance stand as the smallest dimension objects that permit both optical guiding [24] and electrical contacting [25]. As another example, because of their anisotropic geometry, both their optical and electrical properties depend on their orientation, which makes them suitable for use as polarization-dependent sensors. In virtue of their large surface-to-volume ratio, they also present an enhanced interaction with the environment which gives them optimal chemical and biological sensing properties [26]. Along these lines, radial NW heterostructures are expected to be an interesting solution to reduce device dimensions without loss of efficiency. They indeed have the advantage to present, for a given volume of deposited material, a larger active surface than their two-dimensional counterparts. In practice, optoelectronic devices based on radial QWs have already been demonstrated. It is for instance the case of a blue LED made with an InGaN radial QW embedded between a *n*-GaN core and an outer *p*-GaN shell obtained in 2004 [27]. No later than the next year, a color-tunable LED with III-N radial multi-QWs was achieved [28]. More recently a LED based on GaAs-AlGaAs core-multishell nanowires has also been demonstrated [29]. Radial QWs have besides been used in nanoelectronics: in 2006, Li *et al.* especially reported a successful AlN radial well-based High Electron Mobility Transistor (HEMT) [30]. Last but not the least, radial heterostructures have proven to be of interest

for photovoltaics [31, 32]. Note, however, that despite these promising results, a gain in efficiency from radial heterostructures-based compared to 2D heterostructures-based devices has not been strictly evidenced so far.

It is in this context that part of the GaN-based research developed towards GaN columnar nanostructures. Now, one key question is the following: what are the specific GaN NW features that can challenge or overtake 2D GaN layers?

- **Crystal quality**
  One of the major issues regarding the epitaxy of 2D III-N materials is the lack of suitable substrate[2]. Nowadays, the best epitaxial layers still contain up to 10^8 cm^{-2} dislocations. GaN NW high aspect ratio (length/diameter), on the other hand, allows an easy strain relaxation around their periphery, giving them the advantage to grow relaxed and defect-free, on potentially any kind of substrates. NWs hence permit the use of highly mismatched substrates while avoiding introduction of defects in the crystal. As a result GaN NWs exhibit an excellent crystalline quality[3], resulting in a stronger luminescence intensity than that of a 2D GaN layer with equivalent quantity of active material [33]. This high surface-to-volume ratio naturally also benefits to NW heterostructures, both axial and radial ones, so that highly mismatched materials may be used for the different layers composing the heterostructures.

- **Growth on non-polar surfaces**
  As we will see in chapter 1, III-N materials are usually grown as wurtzite crystals which are non-centrosymmetric: their [0001] direction is polar. As a consequence, properties of heterostructures grown in this direction are modified by the presence of an internal electric field. In particular, in the case of a QW embedded in a barrier material, the electric field induces a red-shift of the light emission and an increase of the carriers lifetime inside the well. To avoid these peculiarities, growth of heterostructures along non-polar directions of the crystal, that is perpendicularly to the [0001] direction, have been proposed. However, because of the strong anisotropy of the non-polar surface properties [34, 35], growth of III-N 2D layers along non-polar directions remains challenging, resulting in a high density of dislocations and stacking faults [36]. Through the fabrication of radial QWs, NWs then appear as an ideal base for a straightforward growth of heterostructures along non-polar directions.

Nowadays, GaN NWs can be fabricated in different ways. By MOVPE or by CVD (chemical vapour deposition), growth of GaN NWs is somewhat challenging. Catalyst-assisted approaches were primarily used in 2000 [37] but the spatial orientation as well as the epitaxial relation of the columns with the substrate appeared difficult to control. Other

[2] This will be more deeply discussed in chapter 2
[3] This will be better discussed and illustrated in chapter 2

procedures were then investigated in order to improve the column orientation such as the use of a pre-patterned substrates [38, 39] but this approach complicates the overall GaN NW growth procedure because of the patterned substrate fabrication. Only recently, self-assembled growth of catalyst-free GaN NWs was achieved in MOCVD by pre-depositing *in situ* a thin SiN_x layer on a sapphire substrate [40]. Regarding MBE, growth of GaN NWs is easier. As above-mentioned, GaN tends to self-develop with a columnar morphology under specific growth conditions. These conditions basically consist in a III/V flux ratio lower than 1 ("N-rich conditions") and a substrate temperature around 800 ℃ [21, 41–46]. Chèze and co-workers showed that it is also possible to grow catalyst-induced GaN NWs by MBE [47] but this approach does not improve the columns quality. On the contrary, catalyst-induced GaN NWs appear to contain more basal-plane stacking faults and to have a weaker photoluminescence than self-assembled ones because of contamination from the metal seed [48].

Motivations and targets

Since the first reports on their fabrication, MBE-grown self-assembled GaN NWs have been widely investigated (*e.g.* Refs. [20, 21, 33, 41–79]). Regarding their growth mechanisms, it is for instance now admitted that once GaN columnar shape is initiated, it is promoted by the diffusion of Ga adatoms along the NW facets to their top surface [42, 60, 64] rather than catalysed by a Ga droplet at the apex of the wire. The remaining issue is to understand the initiation of such columnar shape. In other words, although this GaN NW "elongation phase" is well-understood, it is not the case of mechanisms occurring at the the very first stages of the nanostructure formation (their "nucleation"). Within our group and during his own PhD thesis, O. Landré investigated the formation of GaN NW precursors (or nuclei) on a thin AlN buffer (3 nm) deposited on Si(111) [73, 80]. To do so, he performed *in situ* synchrotron-radiation-based grazing incidence X-ray diffraction (GIXRD) at the European Synchrotron Radiation Facility (ESRF) and showed that

- GaN first grows as a pseudomorphic layer on the thin AlN buffer;
- above a critical thickness of 2.8 monolayers, a Stranski-Krastanov (SK) transition occurs (formation of GaN NW nuclei);
- these nuclei ripen until relaxing by introduction of a dislocation at the GaN/AlN interface.

The main difference between SK Quantum Dots and GaN NW precursors lies in their relaxation state: the former have undergone a shape transition to elastically relax part of their strain but are still strained to some extent, while the latter have plastically relaxed [73, 80]. Plastic relaxation of GaN NW precursor is possible because of the high substrate temperature used during their growth: at high temperature, nuclei are so well-separated that they can ripen until plastic relaxation before the occurrence of coalescence.

The presence of dislocation at the GaN/AlN interface was also observed by the group of H. Riechert at the Paul Drude Institute of Berlin: in reference [76], the authors showed that the introduction of this dislocation is correlated to the apparition of vertical facets, hence suggesting that plastic relaxation signs the onset of the columnar growth.

In this context, the first aim of this thesis is to expand our fundamental knowledge of self-assembled GaN NW growth mechanisms and properties. More specifically, our objectives are

- to investigate the nucleation of GaN NWs on bare Si(111), similarly to what has been done on Si(111) covered with a thin AlN buffer and confront both cases;
- to relate nucleation processes to the final GaN NW morphology, (*i.e.* density, length, length dispersion and diameter), in order to better control their self-assembled growth;
- to correlate GaN NW polarity to their nucleation processes.

The second target of this work is to analyse the growth mechanisms and properties of novel NW-based heterostructures made of GaN-AlN by plasma-assisted MBE (PAMBE).

Organization of the manuscript

In the **first chapter** of this manuscript, we will introduce concepts necessary for the understanding of the following pages. More specifically, we will first introduce the PAMBE system and basics of the growth by PAMBE. Similarly, we will then present III-N material properties and specificities that will be useful for the reading of the rest of the manuscript. Finally, we will briefly describe the main characterization techniques used in this work: reflection high energy electron diffraction (RHEED), multiwavelength anomalous diffraction (MAD), photoluminescence and cathodoluminescence.

In **chapter 2**, we will focus on GaN NWs grown on Si(111). In a first stage, we will introduce silicon substrates and especially describe the method we will use to calibrate its temperature. This method relies on the Ga desorption rate dependence on the Si surface temperature and provides a way to ensure an excellent reproducibility of the growth temperature between samples. In a second stage, we will present the state-of-the-art of GaN NWs grown on bare Si(111) and when using a 2-3 nm thick AlN buffer on Si(111), in particular their structural and optical properties. Regarding the case of bare Si(111), we will eventually detailly analyze the dependence of GaN NW length, length dispersion, diameter and density on the substrate temperature.

Then, in **chapter 3**, in order to analyze these observations, we will use two *in situ* tools that are reflection high energy electron diffraction (RHEED) and *in situ* grazing incidence X-ray diffraction (GIXRD) at the ESRF to study GaN NW nucleation processes on both types substrates (bare Si(111) and AlN-buffered Si(111)). These experiments will provide a new insight on processes at the origin of GaN NW formation and help to clarify GaN NW morphology (*i.e.* density, mean length, length dispersion and mean diameter) dependence on the temperature observed in the previous chapter.

In **chapter 4**, we will focus on the determination of PAMBE-grown GaN NW polarity, a topic that has been controversial in the literature. Here, we propose to use a method based on resonant X-ray diffraction to reliably identify the column growth direction. In the first part of the section, the technique will be explained. Then, it will be applied to GaN NWs grown on bare Si(111). Additional chemical etching experiments will also provide information on the polarity of GaN NWs grown using a thin AlN buffer.

For the two last chapters of the manuscript, we will switch to GaN-AlN NW heterostructures. More specifically, **chapter 5** will be devoted to the deep investigation of GaN-AlN core-shell NWs. Through this chapter, we will study the influence of growth parameters such as the atomic flux incidence angles, the substrate temperature and the Al/N flux ratio on the shell morphology. In the second part, we will structurally characterize these GaN-AlN core-shell NWs. More specifically, using resonant X-ray diffraction, we will study GaN-core strain-state dependence on the AlN shell thickness. Finally in the last part, we will present a short optical characterization of these nanostructures.

In **chapter 6**, we will wonder whether it is possible to observe an elastic shape transition of GaN deposited on top of sufficiently-large AlN NWs. To address this issue, we will present preliminary results based on theoretical calculations and on experimental observations. For the experimental part, GaN-AlN core-shell NWs will be first grown and act as "AlN NWs". The top AlN segment of the AlN shell will then be used as a base for subsequent GaN deposition. In the second part of the chapter, the grown structure will be optically characterized by photoluminescence. Then, individual nanostructures will be investigated both by nano-cathodoluminescence with a very high resolution and by micro-photoluminescence.

Collaborations

To "conclude this introduction", let us emphasize that results hereafter presented are the fruit of several successful collaborations, partly with colleagues from the "Nanophysics and Semiconductors" (NPSC) group and partly with external collaborators. Here, I would like to name those who contributed the most directly to the achievement of the results used in this manuscript.

Growth by PAMBE which was performed under the supervision of my PhD advisor Dr. Bruno Daudin (NPSC) and in collaboration with former PhD students from the group.
X-ray-based characterizations were performed under the supervision of my thesis co-advisor Prof. Hubert Renevier from the "Laboratoire des Matériaux et du Génie Physique" (LMGP) of Grenoble and part of the data treatment was made with the help of Cédric Leclère (LMGP).
Dr. Catherine Bougerol (NPSC) is at the origin of the high-resolution transmission electron microscopy images and microscopy analyses shown in this manuscript.
Photoluminescence results were obtained in collaboration with Dr. Bruno Gayral (NPSC) and Diane Sam-Giao (NPSC).
Theoretical calculation on strain presented in chapter 5 were made by Dr. Dulce Camacho and Dr. Yann-Michel Niquet from the L-SIM (atomistic simulation laboratory) group of CEA Grenoble.
Theoretical calculations of chapter 6 were performed by Dr. Frank Glas from the "Laboratory of Photonics and Nanostructures" (LPN) of Marcoussis.
Nano-cathodoluminescence spectra and annular dark field images of chapter 6 were obtained by Dr. Luiz Tizei and Dr. Mathieu Kociak from the "Laboratoire de Physique des Solides" (LPS) of Orsay.

1

Plasma-assisted molecular beam epitaxy, III-N semiconductor properties & characterization techniques

This first chapter intends to give an overview of the tools relevant for the comprehension of the manuscript. Its aim is not to be exhaustive but to introduce the main concepts at stake. First, regarding its central role along this work, plasma-assisted molecular beam epitaxy will be presented. Our focus will then turn towards III-N semiconductors, the basic structural and electric properties of which will be addressed. In the last stage, we will describe the main characterization techniques used in this work, namely reflection high energy electron diffraction, resonant X-ray diffraction, photoluminescence and nanocathodoluminescence.

Contents

1.1 Plasma-Assisted Molecular Beam Epitaxy 11

1.2 Properties of III-N semiconductors 15

1.2.1 Structural properties 15

1.2.1.1 Wurtzite and zinc-blende crystal structures 15

1.2.1.2 Polarity 17

1.2.2 Elastic and plastic properties 18

1.2.2.1 Elastic relaxation 19
1.2.2.2 Plastic relaxation 19
1.2.3 Electronic properties 20
1.2.3.1 Band gap 20
1.2.3.2 Spontaneous and piezoelectric polarizations 21
1.2.3.3 Quantum-confined Stark effect 23
1.3 Characterization techniques 24
1.3.1 Structural characterization 24
1.3.1.1 Reflection high energy electron diffraction 24
1.3.1.2 X-ray diffraction 28
1.3.2 Optical characterization 31
1.3.2.1 Photoluminescence 32
1.3.2.2 Nano-cathodoluminescence 32

1.1 Plasma-Assisted Molecular Beam Epitaxy

"Molecular beam epitaxy deserves a place in the history books". So was entitled a paper written by McCray in 2007 [81], consecrating the MBE technique as one of the main roots of the whole fields of nanoscience and nanotechnology. Elaborated in the mid-1960s by B. A. Joyce and R. R. Bradley [82] for the deposition of silicon films, MBE actually found its real impulse few years later with the successful growth of GaAs crystalline layers by A. Y. Cho and J. R Arthur at the Bell Laboratories [83, 84].

As the Greek roots of the term *epitaxy* indicates ("epi" and "taxis" respectively mean "above" and "in ordered manner"), MBE belongs to the group of techniques for the growth of ordered crystalline structures in a bottom-up approach. The asset of MBE versus other epitaxy techniques lies in its slow deposition rate, typically between one and several hundreds of nanometres per hour, allowing an excellent control of the deposited material at a sub-monolayer (ML) scale. To do so, ultra-pure sources of materials are heated up in Knudsen cells facing a crystalline substrate maintained at high temperature, inside a growth chamber under ultra-high vacuum (UHV). The vaporized species are then ballistically "sprayed" towards this substrate on which they react [85]. In the specific case of III-N MBE systems, while the metallic III-elements (Ga, Al and In) as well as the doping elements (Mg and Si for instance) are obtained from solid sources, several ways of providing the N species exist. Nitrogen may for instance be obtained from the thermal dissociation of NH_3 molecules onto the substrate surface (gas-source ammonia MBE). Alternatively, N may be produced by the dissociation of N_2 molecules either by using electron cyclotron resonance (not used anymore) or a radio-frequency (RF) discharge. In both cases, the generation of the active N species is made through the lightning of a plasma, which is the reason why this two types of systems are referred to as "plasma-assisted MBE" [86, 87].

In this thesis work, the MBE used is a RF-PAMBE from the French company Meca2000. A scheme of the principle of growth in such PAMBE as well as a sketch of the Meca2000 system are depicted in figure 1.1.

More generally, in MBE the growth is led by different kinetic processes illustrated in figure 1.2. When reaching the substrate surface, impinging atoms first physisorb: they are adsorbed via Van der Waals forces onto the surface. This interaction does not involve the electronic structure of the adatoms and is therefore weak (between 10 and 100 meV). At that point, the adatoms are not yet incorporated and may diffuse on the surface and/or desorb. In a second stage, the adatoms that have not desorbed, chemisorb: they form chemical bonds with the substrate species and therefore change the chemical nature of the interface. At sufficiently high temperatures, the adatoms still diffuse until being incorporated either by forming a stable aggregate (precursor nucleation) or by bonding at a step edge (step-flow growth mode) [88]. Naturally, the occurrence and the magnitude

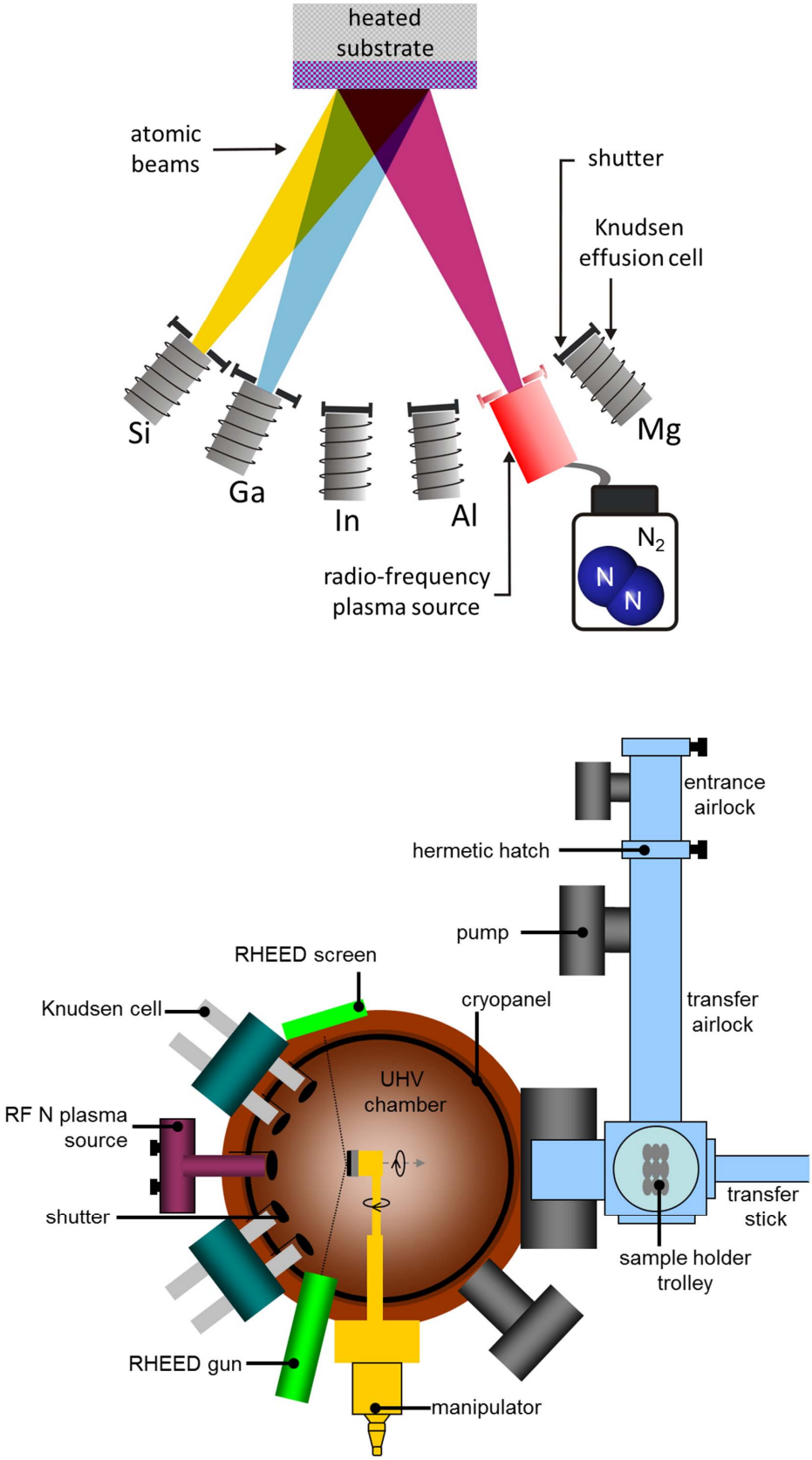

FIG. 1.1 – Scheme of the principle of growth in a PAMBE (top) and sketch of the Meca2000 PAMBE used to performed the growth of this thesis work (bottom).

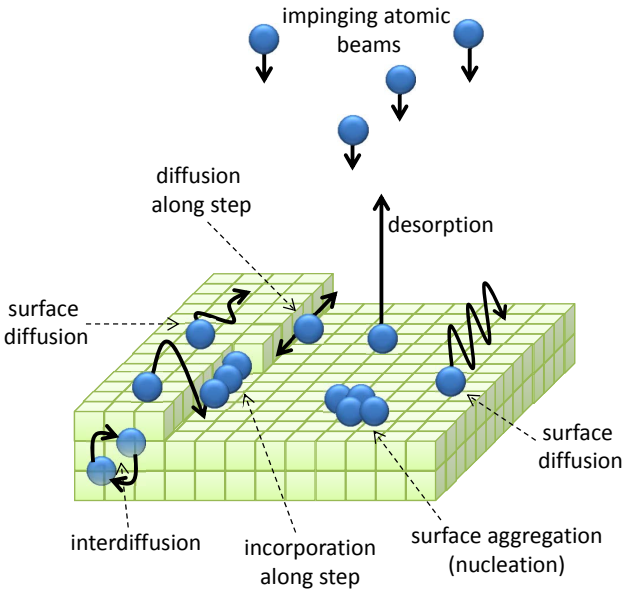

FIG. 1.2 – Scheme of the various processes involved on the substrate during MBE growth.

of these processes depend both on the nature of the impinging atoms and on their local environment on the substrate surface (chemical nature of this surface, types of sites: dangling bond, vacancy, step edge, etc.). To some extent, they can be controlled by adjusting the growth parameters hereafter described.

The substrate temperature

The adjustment of the substrate temperature depends on the substrate used, the material grown and also on the morphology that the grown material is expected to have. As an example illustrating the case of GaN, to grow a 2D layer on a GaN pseudo-substrate, the substrate temperature should be between 650 and 700 °C [89], on a Si(111) substrate around 750 °C [90], while when growing NWs on Si(111), the optimum substrate temperature is rather around 800 °C [91]. Typically, the substrate temperature influences the adatoms desorption rate (thus the effective density of adatoms on the substrate surface) and their mean diffusion length.

Under UHV conditions, measuring the substrate temperature is actually not a trivial issue. Among the various existing methods, all have pros and cons. The most widely used certainly is the pyrometer which have the advantage to be set outside the UHV chamber. Its precision is however largely dependent on the angle under which the substrate is observed and on the pyrometer calibration, as determined by the knowledge of the probed material emissivity, which is not always well established. In addition, the range of temperatures that can be measured itself depends on the emissivity of the material. For instance, in reason of the absence of infrared emission below 400 °C, it is not possible to measure the lower silicon temperatures with a pyrometer. In our PAMBE system, the substrate temperature is estimated on the backside of the substrate with a thermocouple. This method is not perfect either since the contact made by the thermocouple depends

on the molybloc used. In particular, when using a plain molybloc on which a substrate is stuck by capillarity with indium, the temperature of the backside of the molybloc is measured rather than that of the substrate itself. In addition, the thermocouple measurement can be biased by direct thermal radiation from the heater filament. Within our group, when using Si(111) substrate, an alternative solution has been used to directly estimate the effective surface temperature with an excellent accuracy and to ensure a better reproducibility of the growth conditions from sample to sample, regardless the molybloc used. This method, based on the Ga desorption rate dependence on the substrate temperature, will be detailed in chapter 2.

The N- and III- fluxes

The quantity of atoms sent towards the substrate can naturally be tuned. For the metallic species, a simple change in the Knudsen cell temperature induces a change of flux. In what concerns active N species, their amount can be controlled by tuning both the flux of N_2 delivered via a mass flow and the power of the RF plasma cell. The range of N fluxes obtainable from the RF plasma source is however not large for that the proportion of dissociated N_2 remains always quite low, around 1 %.
Regarding calibrations, the metallic fluxes can directly be measured as an equivalent pressure by a gauge placed in the chamber. This technique is however not applicable to the active N species in reason of the N_2 background in which they are generated. The alternative solution, which actually is also more accurate, is to evaluate III and N fluxes together as an equivalent III-N growth rate by mean of RHEED oscillations (the technique will be described in the last section of this chapter).

The incidence angles of the atoms

At rest, that is when no growth is going on, the base pressure in the MBE chamber is in the 10^{-11} mbar range. During growth, because of the N_2 present in the chamber, this pressure is increased to about 10^{-5} mbar. Nevertheless, even at this higher pressure, the average mean free path of the atoms is still large, about 10 metres, which implies that the atomic fluxes can be considered as ballistic. The atomic beams hence reach the substrate with given incidence angles. As we will see in chapter 5, under certain conditions, those incidence angles play a significant role in the grown material morphology. It is possible to modify the incidence angle between the atoms vaporized from a given Knudsen cell and the substrate by rotating the manipulator (Fig. 1.1).

1.2 Properties of III-N semiconductors

The objective of this section is to get now acquainted with the basic properties of the material at the center of this work: III-N semiconductors.

1.2.1 Structural properties

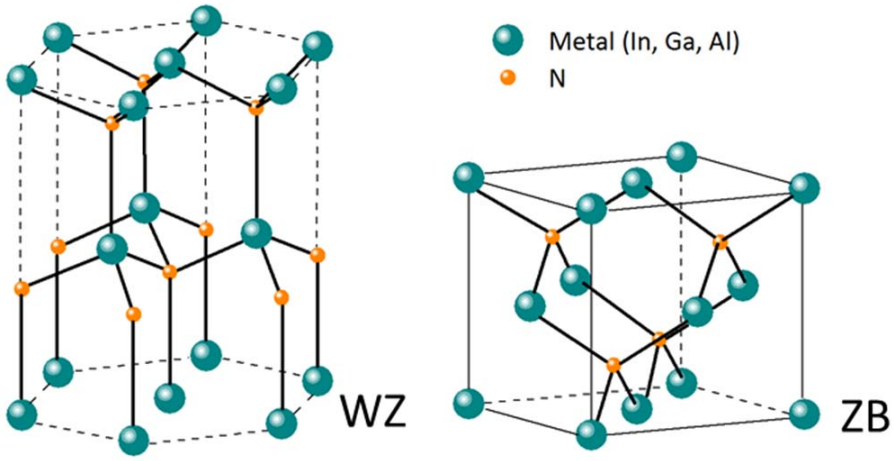

FIG. 1.3 – Wurtzite (WZ) and zinc-blende (ZB) crystal structure of III-N semiconductors

The III-N semiconductor family (InN, GaN, AlN, as well as their ternary and quaternary alloys) can take the shape of three different crystalline arrangements: the wurtzite (WZ) (α-phase), the zinc-blende (ZB) (β-phase) and the rock salt (γ-phase). As the rock salt structure can only be obtained under extreme conditions, such as very high pressures, incompatible with epitaxial growth [92], we will no longer deal with this phase in the following of the manuscript. The two other phases, WZ and ZB, are hereafter described. Their structure are presented in figure 1.3. Reminders on crystallography in hexagonal systems are given in appendix A.

1.2.1.1 Wurtzite and zinc-blende crystal structures

The wurtzite structure – whose unit cell is presented in figure 1.4 – belongs to the space group $P6_3mc$ and is composed of two interpenetrating hexagonal close-packed sublattices formed by the metallic and the N atoms respectively, ideally shifted of $u = \frac{3}{8}c$ in the [0001] direction. Equivalently, each atom is tetrahedrically coordinated with bond lengths equal to $\frac{3}{8}c$. In other words, each group-III element is bonded to four N atoms and conversely, each N atom is bonded to four group-III elements. In practice, for III-N semiconductors, the wurtzite cell is not perfect and the c/a ratio slightly differs from the ideal case ($c/a = 1.633$). As a consequence, the tetrahedrons formed by the atoms is deformed (either stretched or strained) in the [0001] direction. Lattice parameters a and c, the effective

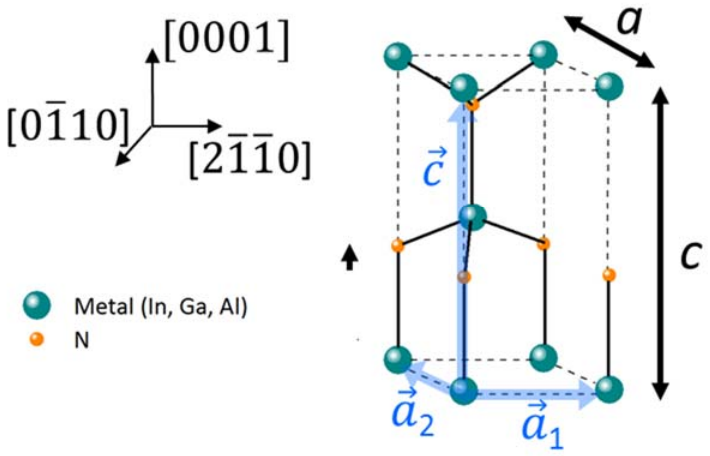

FIG. 1.4 – Wurtzite unit cell. This cell contains 4 atoms (two metal and two nitrogen atoms). a and c are the WZ lattice parameters. u is the metal-N bond length. In the ideal WZ cell $u = \frac{3}{8}c$. $\vec{a}_1$, $\vec{a}_2$ and $\vec{c}$ are the basal vectors of the hexagonal cell defined in appendix A.

c/a ratio as well as the effective u/c ratio of wurtzite InN, GaN and AlN are given in table 1.1.

	InN	GaN	AlN
a (Å) at 300 K	3.548	3.189	3.112
c (Å) at 300 K	5.760	5.185	4.982
c/a at 300 K	1.609	1.626	1.601
u/c at 300 K	0.377	0.377	0.382

TABLE 1.1 – Wurtzite InN, GaN, AlN a and c lattice parameters and u/c and c/a ratios at 300 K, taken from Ref. [93].

The primitive unit cell (Fig. 1.4) of WZ III-N compounds contains 4 atoms: 2 metallic ones and 2 nitrogen ones. Coordinates of these atoms are

$$\begin{aligned} \text{Metal}_1 : &\quad \mathbf{0}\vec{a_1} + \mathbf{0}\vec{a_2} + \mathbf{0}\vec{c} \\ \text{Metal}_2 : &\quad \tfrac{\mathbf{2}}{\mathbf{3}}\vec{a_1} + \tfrac{\mathbf{1}}{\mathbf{3}}\vec{a_2} + \tfrac{\mathbf{1}}{\mathbf{2}}\vec{c} \\ \text{N}_1 : &\quad \mathbf{0}\vec{a_1} + \mathbf{0}\vec{a_2} + \mathbf{u}\vec{c} \\ \text{N}_2 : &\quad \tfrac{\mathbf{2}}{\mathbf{3}}\vec{a_1} + \tfrac{\mathbf{1}}{\mathbf{3}}\vec{a_2} + \left(\mathbf{u} + \tfrac{\mathbf{1}}{\mathbf{2}}\right)\vec{c} \end{aligned} \tag{1.1}$$

where $\vec{a}_1$, $\vec{a}_2$ and $\vec{c}$ are the basal vectors of the hexagonal cell defined in appendix A.

As shown in figure 1.5, along the [0001] direction, the wurtzite cell is constituted of a stack ABABA of two atomic layers A and B.

The ZB phase is constituted of two face centered cubic lattice shifted of $\frac{1}{4}\sqrt{3}a$ in the [111] direction (Fig. 1.3). In this case too, each atom is tetrahedrically coordinated but the corresponding plane sequences along the [111] direction is ABCABC (Fig. 1.5) where the C plane is rotated of 60° compared to A. In other words, ZB [111] direction resembles WZ [0001] direction excepted from the 60° rotation in its tetrahedrons.

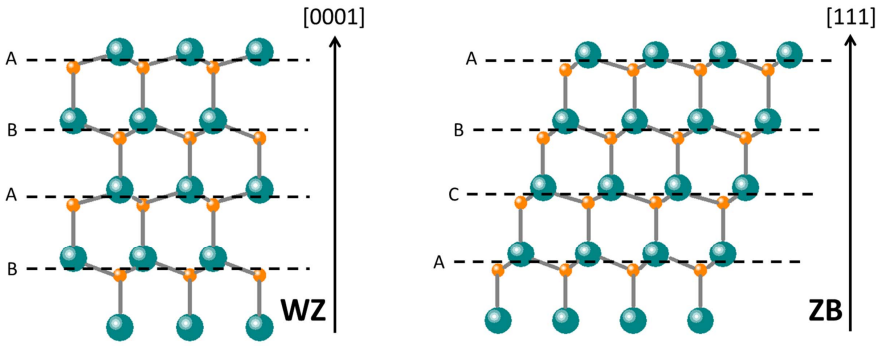

FIG. 1.5 – Wurtzite (WZ) and zinc-blende (ZB) stack sequences.

Thermodynamically, the wurtzite phase has been shown to be more stable, although the gain in energy per atom of the WZ phase compared to the ZB phase is not so large (18.4 meV for AlN, 9.9 meV for GaN and 11.4 meV for InN) [94]. It is therefore possible to grow ZB III-N either by using cubic substrates [95,96], or by introduction of one stacking fault inside a WZ segment [97].

In the following of the manuscript, substrates used as well as chosen growth conditions were such that we were not confronted to the ZB phase, only to WZ. More precisely, we will study WZ GaN NWs as well as AlN-GaN heterostructures based on GaN NWs. In this context, growth on two types of surfaces will be studied, namely m-planes and c-planes which respectively constitute the side-walls and the apex of the NWs. It is worth noting that these two types of planes do not have the same atomic surface density (Tab. 1.2). This difference of atomic surface density leads to a difference of atomic incorporation rates. More precisely, in the same growth conditions, for a given amount of supplied atoms, the incorporation rate on the m-plane is only about 0.94 times that on the c-plane (Tab. 1.2).

1.2.1.2 Polarity

The absence of centre of symmetry of the WZ structure (Fig. 1.3) involves that the [0001] and the $[000\bar{1}]$ directions are not equivalent. In order to distinguish between them, one usually considers the direction of the metal-N bond that is collinear to the c-axis of the wurtzite cell. The vector going from the metallic atom and pointing towards N conventionally defines [0001], the positive direction of the c-axis (Fig. 1.6). A structure

Plane	c-plane (0001)	m-plane ($1\bar{1}00$)
Unit cell surface	$\frac{3\sqrt{3}}{2}a^2$	ac
Number of atoms per unit cell	6	4
Surface atomic density ($atoms/cm^2$)	$\sigma_c = 2.272 \times 10^{15}$	$\sigma_m = 2.42 \times 10^{15}$
Growth rate (ML/s)	ν_c	$\frac{2.272}{2.42}\nu_c$

TABLE 1.2 – Unit cell surface, number of atoms per unit cell (metal and N), surface atomic density and relative growth rates on III-N wurtzite (0001) and ($1\bar{1}00$) planes.

is said to be metal-polar when its growth direction is [0001]. Reciprocally, a structure is said to be N-polar when its growth direction is [000$\bar{1}$].

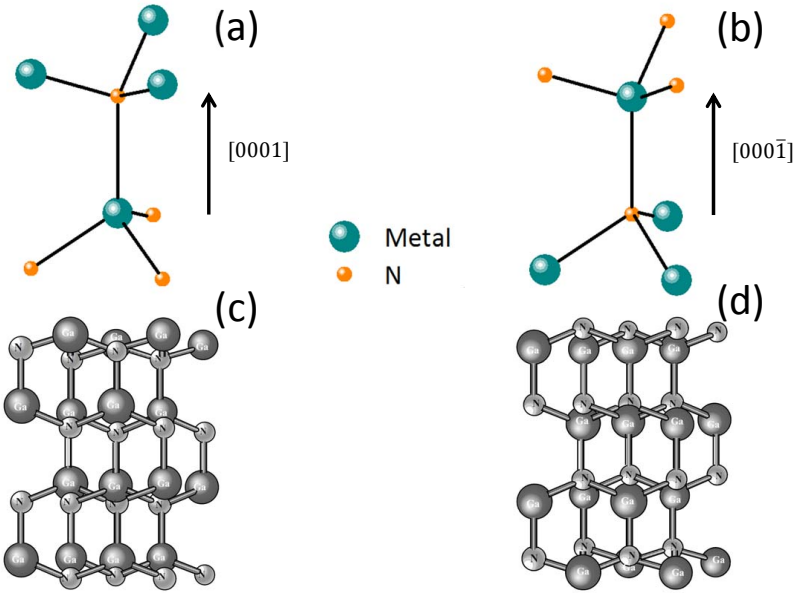

FIG. 1.6 – (a) Metal-polar and (b) N-polar directions in the III-N wurtzite cell. When the growth direction is along the [0001] direction, the structure is said to be metal-polar. Reciprocally, when the growth direction is along [000$\bar{1}$], a structure is N-polar. (c) Ga-polar and (d) N-polar stick-and-ball representations of WZ GaN, taken from Ref. [92].

Part of the work presented in this manuscript will be devoted to the determination and the understanding of PAMBE-grown GaN NW polarity. Hence more details about polarity (*i.e.* its control, its determination and its consequences) will be discussed in chapter 4.

1.2.2 Elastic and plastic properties

III-N semiconductors are generally grown in heteroepitaxy. In order to keep an epitaxial relation with the substrate, the deposited crystal hence adapts its lattice parameter

while storing elastic energy. Above a certain threshold depending on the lattice mismatch, this elastic energy must be relaxed, either elastically or plastically.

1.2.2.1 Elastic relaxation

Elastic relaxation consists in relieving the excess of stored energy through a shape transition which can be mathematically described. For small deformations, the stress σ_{ij} within the structure is indeed related to the strain ϵ_{kl} through Hooke's law:

$$\sigma_{ij} = \sum_{kl} C_{ijkl} \cdot \epsilon_{kl} \tag{1.2}$$

where C_{ijkl} is the fourth-ranked tensor of the elastic modulus which can be reduced to a 6×6 matrix (second-rank tensor) due to the symmetry of lattices belonging to the $P6_3mc$ group and by replacing the pair of indexes {xx,yy,zz,yz,zx,xy} by {1,2,3,4,5,6}. Then, equation 1.2 becomes [98]

$$\begin{pmatrix} \sigma_1 \\ \sigma_2 \\ \sigma_3 \\ \sigma_4 \\ \sigma_5 \\ \sigma_6 \end{pmatrix} = \begin{pmatrix} C_{11} & C_{12} & C_{13} & 0 & 0 & 0 \\ C_{12} & C_{11} & C_{13} & 0 & 0 & 0 \\ C_{13} & C_{13} & C_{33} & 0 & 0 & 0 \\ 0 & 0 & 0 & C_{44} & 0 & 0 \\ 0 & 0 & 0 & 0 & C_{44} & 0 \\ 0 & 0 & 0 & 0 & 0 & C_{66} \end{pmatrix} \begin{pmatrix} \epsilon_1 \\ \epsilon_2 \\ \epsilon_3 \\ \epsilon_4 \\ \epsilon_5 \\ \epsilon_6 \end{pmatrix} \tag{1.3}$$

Among the six elastic moduli, five are independent and $C_{66} = (C_{11} - C_{12})/2$. For WZ GaN, AlN, these coefficients have been both experimentally and theoretically determined. For InN, no experimental data is available so far. Theoretical values can be found in Refs. [99, 100] and experimental ones in Refs. [101–103] for instance.

1.2.2.2 Plastic relaxation

The other way of relieving the excess of stored energy is to relax plastically. This consists in either introducing dislocations or cracks in the epilayer, which both constitute defects within the crystalline arrangement. In nitrides, the most common types of dislocations are "misfit dislocations" (MD) and "threading dislocation" (TD). MDs (Fig. 1.7 (a)) are a consequence of mismatch between the substrate and the epilayer. Confined at the interface, they efficiently relieve the strain. On the other hand, TDs propagate through the whole layer and can be of three types: pure edge, pure screw or mixed. Figures 1.7 (b) and (c) respectively illustrate pure edge and pure screw threading dislocations. Edge dislocations can be seen as an extra atomic layer in the crystal. Their dislocation line vector $\vec{l}$ is perpendicular to the Burger vector $\vec{b}$. Screw dislocations on the other hand have their dislocation line vector $\vec{l}$ parallel to the Burger vector $\vec{b}$.

Sugahara *et al.* have shown that dislocations are non-radiative recombination cen-

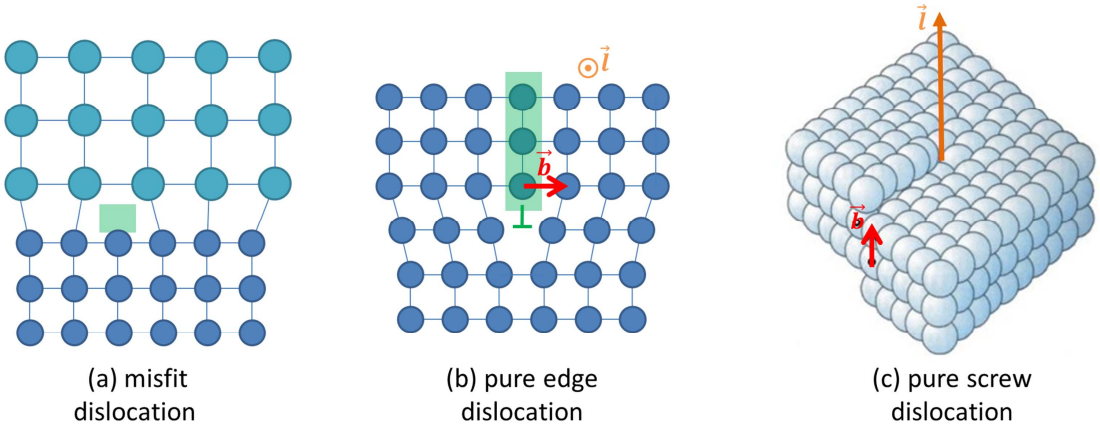

FIG. 1.7 – Scheme of (a) a misfit dislocation, (b) a pure edge threading dislocation and (c) a pure screw threading dislocation.

tres [104]. In optoelectronic devices, when the carrier diffusion length is longer than the dislocation spacing, the efficiency of the light emission is therefore lowered. With the aim of by-passing this drawback, intense efforts are made to improve the III-N structure crystalline quality. In this context, NWs constitute an alternative to the epitaxy of layers: in virtue of their high length/diameter ratio, they indeed naturally grow relaxed and defect-free (see chapter 2).

1.2.3 Electronic properties

1.2.3.1 Band gap

III-N semiconductors exhibit a direct band gap, which means that the minimum of their conduction band lies right above the maximum of their valence band (Γ point). In the WZ arrangement, strong crystal-field (CF) and spin-orbit interactions induce a splitting of the six-fold degenerated level usually associated with cubic systems. In consequence, as schemed in figure 1.8 taken from Ref. [92], the WZ structure present three valence subbands: the heavy holes (HH) band, the light holes (LH) band and the split-off band. More specifically, HH and LH subbands are lifted by the spin-orbit splitting and the split-off band by the crystal field. Values of the band-gap E_g, taken from Ref. [105] are reported in table 1.3. These values span from 0.69 eV for InN to 6.25 eV for AlN, therefore cover a large electromagnetic region going from the near infrared to the deep ultra violet.

Different intermediate band gap energies are obtained through the fabrication of ternary alloys such as $In_xGa_{1-x}N$ and $Al_xGa_{1-x}N$. For a given composition x, the band gap energy is indeed generally approached by

$$E_g(A_xB_{1-x}N) = xE_g(AN) + (1-x)E_g(BN) - x(1-x)b \tag{1.4}$$

	InN	GaN	AlN
E_g (eV) at 300 K	0.66	3.39	6.2
E_g (eV) at 0 K	0.62	3.48	6.28

TABLE 1.3 – Wurtzite InN, GaN, AlN band gap energy at 300 and 0 K, taken from Ref. [105].

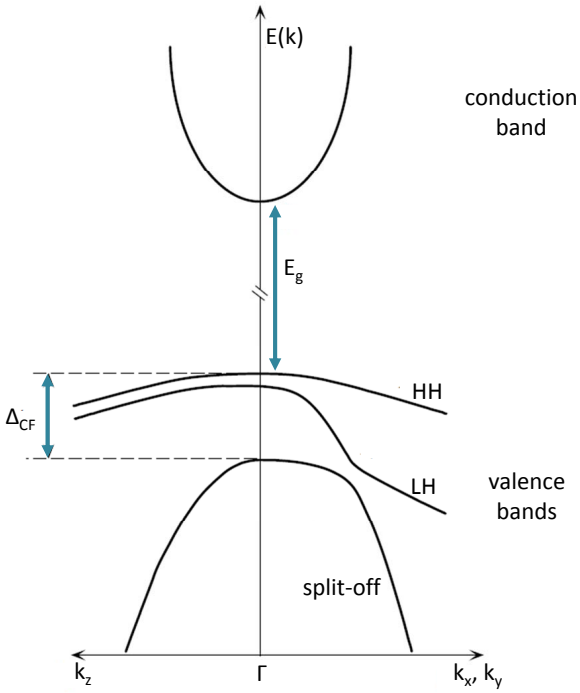

FIG. 1.8 – Sketch of the valence and conduction bands around the Γ point in WZ crystals, taken from Ref. [92].

where b is the bowing parameter which corrects the simple linear relation involving the A and B species. For $Al_xGa_{1-x}N$, this parameter can for instance be found in Refs. [106, 107] and for $In_xGa_{1-x}N$ in Refs. [105, 108–110].

1.2.3.2 Spontaneous and piezoelectric polarizations

For InN, GaN, AlN and their alloys, the difference of electronegativity between N and metal atoms induces local spontaneous polarization vectors along each III-N bond. Because of the lack of center of symmetry of their wurtzite cell, amplified by the deviation of the c/a ratio from its theoretical value, these polarization vectors do not compensate and a residual total spontaneous polarization subsists along the c-axis in the WZ cell. Values of this polarization vector were for instance theoretically determined by Bernardini *et al* in Ref. [111].

Furthermore, strains within the structure produce an additional piezoelectric polarization. In a given material, the overall polarization is therefore given by both the spontaneous and the piezoelectrical polarization. Depending on whether the material is stressed or strained, the piezoelectric component either add or subtract from the spontaneous one.

The three components P_i, where $i = x, y, z$, of the piezoelectric polarization vector can be expressed as

$$P_i = \sum_{j=1}^{3} \sum_{k=1}^{3} d_{ijk}\sigma_{jk} \tag{1.5}$$

where d_{ijk} are the 27 piezoelectric moduli and σ_{jk} is the stress tensor. Based on a change of notation and taking into account the symmetry of the WZ structure, equation 1.5 can be reduced to a matrix [98]

$$\begin{pmatrix} P_1 \\ P_2 \\ P_3 \end{pmatrix} = \begin{pmatrix} 0 & 0 & 0 & 0 & d_{15} & 0 \\ 0 & 0 & 0 & d_{15} & 0 & 0 \\ d_{13} & d_{31} & d_{33} & 0 & 0 & 0 \end{pmatrix} \begin{pmatrix} \sigma_1 \\ \sigma_2 \\ \sigma_3 \\ \sigma_4 \\ \sigma_5 \\ \sigma_6 \end{pmatrix} \tag{1.6}$$

where equation 1.3 can finally be introduced to express the piezoelectric polarization in function of the strain vector $\vec{\epsilon}$:

$$\begin{pmatrix} P_1 \\ P_2 \\ P_3 \end{pmatrix} = \begin{pmatrix} 0 & 0 & 0 & 0 & e_{15} & 0 \\ 0 & 0 & 0 & e_{15} & 0 & 0 \\ e_{13} & e_{31} & e_{33} & 0 & 0 & 0 \end{pmatrix} \begin{pmatrix} \epsilon_1 \\ \epsilon_2 \\ \epsilon_3 \\ \epsilon_4 \\ \epsilon_5 \\ \epsilon_6 \end{pmatrix} \tag{1.7}$$

Different values of the piezoelectric coefficient e_{ij} can be found in the literature [111–114]. Despite these discrepancies, the given values are always about one order of magnitude larger than for other conventional III-V or II-VI semiconductors such as GaAs or CdTe, a consequence of the strong ionic character of the III-N bond.

Regarding heterostructures, a discontinuity $\Delta\vec{P}$ of polarization appears at the interface between the two materials. The effect of this discontinuity is to create surface charge sheets σ_{surf} at the interface, expressed as

$$\sigma_{surf} = \Delta\vec{P} \cdot \vec{n} \tag{1.8}$$

where $\vec{n}$ is the normal to the interface. The sheet carrier concentration at the interface of III-N heterostructures can be of the order of 10^{14} cm^{-2} [112]. The large polarization present in III-N materials is therefore beneficial to the generation of 2-dimensional electron gas, even without intentional doping, revealing the full potential of III-N materials for transistor-like devices such as HEMTs.

1.2.3.3 Quantum-confined Stark effect

As another illustration of the peculiarity of the III-N family, let us now focus on the case of double heterostructures or more specifically on the case of a quantum well (QW) embedded in a barrier material. Here, surface charge sheets at each interface are of opposite signs. Although the type of charges confined at each interface depends on the heterostructure polarity, in both configurations the distribution of positive and negative charges induces the presence of an electric field inside the well. The effect of this electric field is to bend the conduction and the valence band inside the QW, as shown in figure 1.9. As a consequence of the resulting sawtooth potential, the first electron level in the conduction band and the first hole level in the valence band get energetically closer, resulting in a red-shift of the QW emission wavelength. In addition, the electron and the hole wavefunctions are spatially separated which diminishes their overlap, therefore reduces the transition oscillator strength. In other words, the carrier lifetime inside the QW is increased. This effect is called "quantum-confined Stark effect" (QCSE) and is schematically illustrated in figure 1.9 for a GaN QW embedded in AlN barriers.

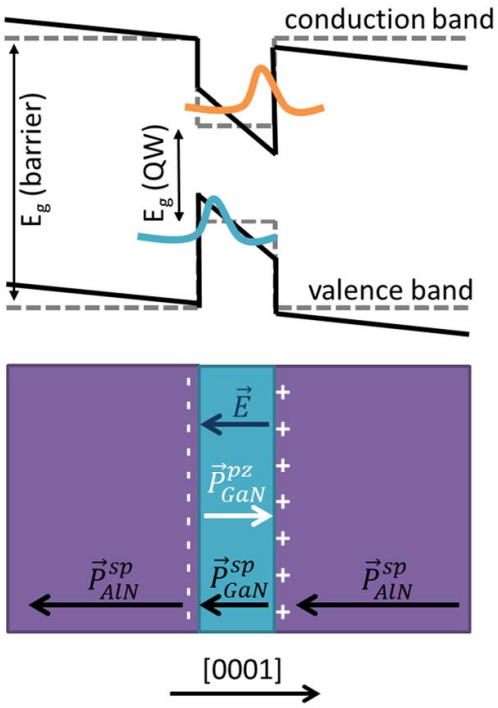

FIG. 1.9 – Illustration of the quantum-confined Stark effect for a GaN quantum well embedded in AlN barriers.

Typical values of the electric field for GaN embedded in $Al_xGa_{1-x}N$ alloys lie between 5 and 10 MV/cm. For instance, according to Ambacher *et al.*, in 2D GaN QW sandwiched between AlGaN barriers, the piezoelectric polarization can cause an electric field as high as 2 MV/cm that adds to the one induced by the spontaneous polarization, already of the order of 3 MV/cm [115]. Regarding GaN quantum dots (QDs) embedded in AlN, polarization fields of 7 MV/cm and 9 MV/cm have been reported [116, 117]. Recently, QCSE

was also observed in GaN segments (also called "quantum discs" (Qdiscs)) sandwiched in AlN barriers on top of GaN nanowires (NWs) [118]. GaN Qdisc emission appeared to shift towards lower energies with increasing thickness of this Qdisc. The thicker Qdisc probed (4.5 nm) even showed emission around 2.7 eV, well below the band gap of relaxed GaN, an evidence of QCSE. Nevertheless, the decrease in energy of the Qdisc emission with its thickness appears to be weaker than for 2D GaN QWs [119] or for GaN quantum dots (QDs) grown on a 2D AlN barrier layer [117]. Such diminution of the QCSE is attributed by the authors to a reduction of the piezoelectric field due to strain relaxation allowed by the NW geometry. A theoretical paper published in 2010 by Camacho *et al.* besides reports on GaN Qdisc emission energy shift with the thickness of the bottom and top AlN barriers. For a 4 nm thick GaN insertion, the authors expect the band gap emission to be tuned between 2.9 and 1.9 eV when changing the AlN segment heights between 4 and 16 nm.

In order to get rid of the QCSE, growth of heterostructures along non-polar directions have been attempted. However, up to now, non-polar 2D layers still contain of a large density of defects. Novel solutions aim at growth on semi-polar oriented surfaces [120]. Alternatively, the growth on non-polar surfaces is possible through the fabrication of heterostructures along NW facets. This topic will be discussed in chapter 5.

1.3 Characterization techniques

In this section, we finally give a small overview of the main techniques used to characterize and investigate the grown structures. In this thesis work, the structures were mostly structural and optically characterized.

1.3.1 Structural characterization

1.3.1.1 Reflection high energy electron diffraction

Directly positioned on the MBE chamber (see figure 1.1), reflection high energy electron diffraction (RHEED) is the first tool available for structural characterization, allowing to follow the growth *in situ* and in real time. It is constituted of an electron gun facing a phosphorus screen. As shown in figure 1.10, RHEED consists in sending a beam of electrons, emitted from this electron gun, towards the substrate with a grazing incidence (typically of the order of 2-3°) and to observe the diffracted beam pattern on the phosphorus screen.

In virtue of the wave-particle duality, the impinging electrons have a wavelength λ, associated to their momentum p by $\lambda = h/p$ where h is the Planck constant. When accelerated by a high voltage, the speed of the extracted electrons is close to the speed of light c [121]. Hence, the relativistic expression of the momentum p must be considered

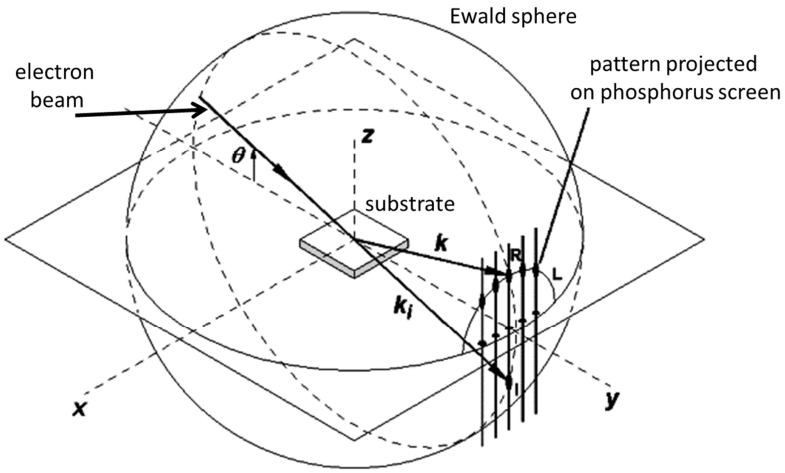

FIG. 1.10 – Principle of the RHEED

to compute λ as

$$\lambda = \frac{h}{\sqrt{2m_0eV\left(1+\frac{eV}{2m_0c^2}\right)}} \tag{1.9}$$

where m_0 is the rest mass of the electron, e its charge and V the accelerating voltage. In our case, the accelerating voltage used is 32 kV, therefore the electron wavelength is equal to 0.00675 nm. Similarly to what can be observed with X-rays, the incident electron beam is scattered by the atoms on the surface whose periodicity gives rise, under specific angles, to a diffraction pattern. This diffraction pattern is the intersection of the surface electronic density Fourier transform with the Ewald sphere of radius $k_0 = (2\pi)/\lambda$ (Fig. 1.11). Real-time analyses of such patterns permit to follow ongoing modifications of the surface during growth. Figure 1.11 illustrates some of the typical RHEED patterns observed and their corresponding surface morphology.

- In the case of a **perfect surface**, the surface electronic density Fourier transform consists in rods perpendicular to this surface. The intersection of the Ewald sphere with these rods are infinitesimal spots placed on an arc. In practice, as stated in Ref. [122], rather than spots, "streaks develop through nonidealities in the experimental arrangements". These "nonidealities" actually rise from both the substrate and the electron beam. First because of thermal agitation within the crystal, rods have a finite thickness. Second, the electron beam slightly diverges both in angle and in energy. As a result, a dispersion in k_0, the radius of the Ewald sphere, exists: the Ewald sphere is not an actual sphere but a shell with a finite thickness Δk_0. Eventually, the Ewald radius is much larger that the separation between the rods. For instance when probing the Si(111) surface, as $a_{Si} \approx 0.54\ nm$, we have $a_{Si}^{hex} = a_{Si}\sqrt{2}/2 \approx 0.38\ nm$ (see appendix A). Hence in the reciprocal space

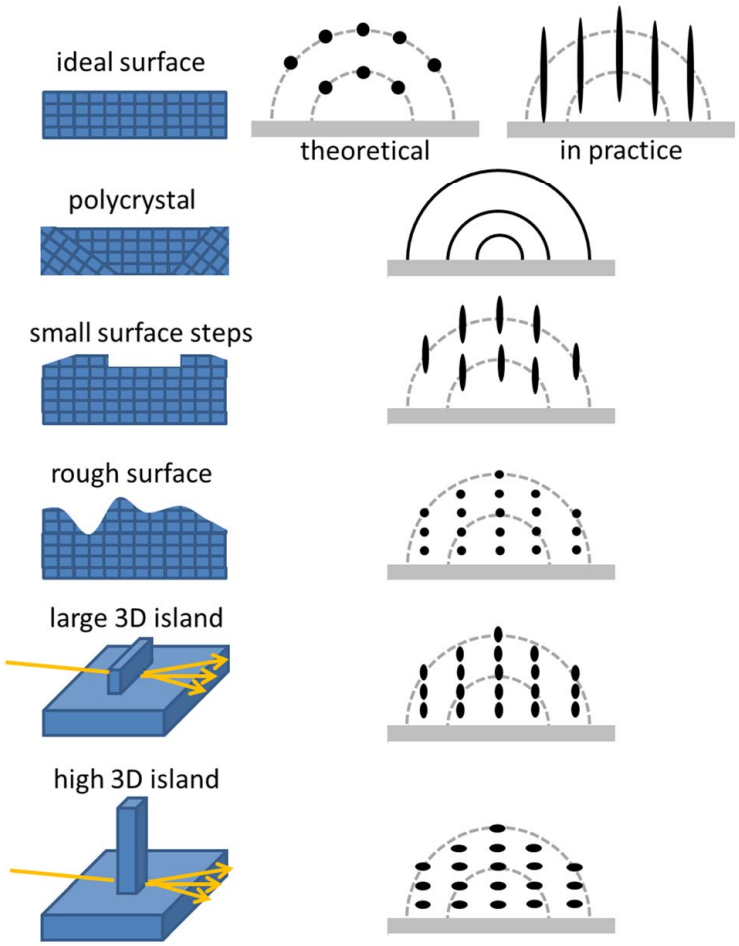

FIG. 1.11 – Typical surface morphology that one can be confronted to during a growth run and their corresponding RHEED pattern.

$a_{Si}^{hex,*} = 2\pi/a_{Si}^{hex} = 17\ nm^{-1}$ while the radius of the Ewald sphere is $k_0 = 930\ nm^{-1}$. The Ewald sphere can be imagined as "flat" in the zone where it intersects the rods. The real intersection of the thick Ewald sphere and the finite rods then happen on a certain length which explains their streaky shape [123].

- In the case of a **polycrystal**, all sorts of in-plane periodicities can be found. The surface reciprocal rods are oriented in all directions, intersecting the Ewald sphere nearly everywhere. Hence the observed pattern has a ring-shape. In terms of epitaxy, the apparition of such ring-like RHEED pattern generally signs the growth of grains with different orientations hence a poor crystal quality.

- If the surface contains **small surface steps** or a certain degree of **roughness**, the diffraction pattern is seen by transmission through the asperities. In this very case, the spots should not be confused with the intersection of infinitesimal surface rods with the Ewald sphere. Here "slashes" are "defective" streaks or in other words, modulation of intensity of the streaks one would obtain with a flat surface [124].

- If **islands** are present on the surface, diffraction on these island facets induce additional lines on the RHEED pattern. More specifically, "high" islands (*e.g.* NWs) introduce an out-of-plane periodicity, visible on the RHEED pattern by transmission of the electron beam through the other islands. RHEED spots lenghten because of the rods on the facets (atomic density Fourier transform of the facets).

Note that unlike X-rays, most electrons do not undergo single elastic scattering but multiple diffractions [125]. As a result, one usually do not draw quantitative data from the RHEED diffracted intensities. On the other hand, quantitative values can be extracted from the periodicity observed in the patterns. In fact, because of their glancing angle of incidence and their week penetration depth (typically few monolayers), mainly the in-plane atomic periodicity contributes to the formation of the diffraction pattern. For small enough incidence angles, the horizontal distance Δx between two fringes (or two arrays of spots, etc.) on the RHEED pattern can be related to the inter-planar in-plane distances d by

$$\Delta x \propto \frac{\lambda D}{d} \tag{1.10}$$

where D is the distance between the surface of the probed sample and the RHEED screen, typically of the order of 50 cm to 1 m. On the screen, the distance between two fringes is therefore inversely proportional to the d spacing.

In addition to provide indications on the surface morphology during growth, RHEED is also used to calibrate the MBE atomic fluxes by mean of RHEED oscillations [126]. In this procedure, the specular RHEED spot (or reflected spot) is observed. Figure 1.12 shows a sketch of the principle of RHEED oscillations technique. Typically, the reflected beam intensity depends on the degree of completeness of the last atomic layer. Hence, when depositing a compound on the surface, the intensity of this specular spot oscillates in time with a period Δt which corresponds to the growth duration of one complete monolayer. In this way, atomic fluxes are calibrated as monolayers per unit of time.

In the specific case of III-N compounds, the observation of the RHEED oscillations is somewhat troublesome. This method based on homoepitaxy indeed requires high quality substrates, which, as already mentioned, are still rare for GaN and AlN, and not available at all for InN. In addition, the growth should be kept in a two-dimensional layer-by-layer mode. Any step-flow growth mode, roughening of the crystal or island nucleation severely dump the oscillations. As a consequence, the window of growth conditions allowing the observation of RHEED oscillations is narrow. In particular, the requirement for GaN 2D growth in PAMBE is to keep the ratio of III/N fluxes in slight Ga excess. In practice, to tune this III/N flux ratio, the N flux is always kept constant and the Ga flux adjusted. As a consequence, oscillations observed in Ga-rich conditions always lead to the same GaN growth rate value (determined by the limiting N flux) which is useless for the Ga cell

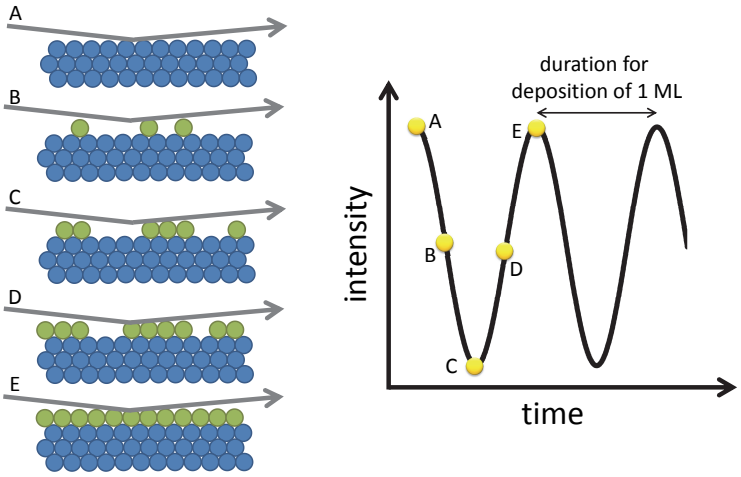

FIG. 1.12 – Principle of the RHEED oscillation technique used to calibrate the atomic fluxes.

calibration. Contradictorily, relevant oscillation measurements should be made in N-rich conditions which are unsuitable to the 2D growth mode, thus to the prolonged observation of oscillations themselves.

1.3.1.2 X-ray diffraction

In this work, most of the significant structural characterizations based on X-rays were performed at the European Synchrotron Radiation Facility (ESRF) of Grenoble. Synchrotron facility actually provides a very brilliant radiation, particularly suitable for the investigation of nanostructures. In addition, the possibility to tune the energy of the X-ray beam allows resonant diffraction to be performed. The aim of this section is to introduce one of the advanced techniques based on resonant diffraction, that will be used in the following chapters, namely multi-wavelength anomalous diffraction (MAD). In order to have a deeper insight of resonant diffraction techniques, the reader is invited to have a look at Refs. [127–132].

Resonnant scatting

Quantitative evaluations of X-ray diffraction experiments require some focus on the scattering power of the probed atoms. For a given atom, the atomic scattering factor $f\left(\vec{Q},E\right)$ is indeed generally expressed as [128]:

$$f(\vec{Q},E) = f^0(\vec{Q}) + f^{'}(E) + if^{''}(E) \tag{1.11}$$

where

- $\vec{Q} = \vec{k}' - \vec{k}$ is the scattering vector, $\vec{k}$ and $\vec{k}'$ being respectively the incident and the

outgoing wavevectors

- E is the energy of the incident wave
- $f^0\left(\vec{Q}\right)$ is the Thomson scattering which represents the elastic diffusion. This term is independent on the beam energy and is actually obtained by the Fourier transform of the electronic density in the atom. It constitutes the non-resonant term of the atomic scattering factor.
- $f^{'}(E) + if^{''}(E)$ is the complex part of the atomic scattering factor, which represents the resonant or "anomalous" scattering. More specifically, $f^{'}(E)$ is related to dispersion and $if^{''}(E)$ to absorption. The magnitude of this resonant contribution depends on the chemical nature of the scattering atom and becomes significant when the photon energy is close to one of this atom absorption edge.

Multi-wavelength anomalous diffraction

Multi-wavelength anomalous diffraction (MAD) is a technique that adds a chemical sensitivity to X-ray diffraction. In other words, it is used to characterize crystal containing at least two different atomic species. Based on resonant phenomena occurring when the energy of the incident photon is close to an absorption edge of one of these species, MAD indeed permits to chemically distinguish the contributions of the different species. To go deeper into details, we can consider that the atoms inside the crystal can be separated in two types: the anomalous atoms A (those that have an electronic edge close the chosen X-ray beam energy) and non-anomalous atoms N (all the others). Each atom type can be describe by an atomic scattering factor of the form given by equation 1.11:

$$\begin{aligned} f_A\left(\vec{Q},E\right) &= f_A^0\left(\vec{Q}\right) + f_A^{'}(E) + if_A^{''}(E) \\ f_N\left(\vec{Q},E\right) &= f_N^0\left(\vec{Q}\right) + f_N^{'}(E) + if_N^{''}(E) \end{aligned} \tag{1.12}$$

In the following, it will be considered that in the range of energy used, only $f_A^{'}(E)$ and $if_A^{''}(E)$ depend on the energy, $f_N^{'}(E)$ and $if_N^{''}(E)$ remaining constant (but non-negligible). In addition, we assume that the values of $f_A^{'}(E)$ and $if_A^{''}(E)$ at a given energy are the same for all anomalous atoms A. Then, as described by Karle in Ref. [133] and reviewed more recently in Ref. [132], the Thomson structure factor of anomalous atoms A reads

$$F_A^0\left(\vec{Q},E\right) = \sum_j^A f_A^0(\vec{Q})e^{i\vec{Q}\cdot\vec{r}_j} = \sum_j^A f_A^0(\vec{Q})e^{i\varphi_{A,j}} = |F_A|\,e^{i\varphi_A} \tag{1.13}$$

In addition, the general structure factor of non-resonant atoms N reads

$$F_N\left(\vec{Q},E\right) = \sum_j^N f_N(\vec{Q})e^{i\vec{Q}\cdot\vec{r}_j} = \sum_j^N f_N(\vec{Q})e^{i\varphi_{N,j}} = |F_N|\,e^{i\varphi_N} \tag{1.14}$$

Note that in this last expression, we have already included the resonant contribution $f'_N + if''_N$ of the non-resonant atoms. Let us now introduce the structure factor F_T as

$$F_T(\vec{Q}) = F_N + F_A^0 = \left|F_T(\vec{Q})\right| e^{i\varphi_T} \tag{1.15}$$

$F_T(\vec{Q})$ includes the non-resonant scattering of all atoms as well as the resonant contribution of non-anomalous atoms. Hence, the total structure factor $F(\vec{Q}, E)$ which takes into account the anomalous contribution of resonant atoms, can be expressed as

$$F(\vec{Q}, E) = F_T(\vec{Q}) + \frac{\left|F_A(\vec{Q})\right|}{f_A^0(\vec{Q})} \left(f'_A(E) + if''_A(E)\right) e^{i\varphi_A} \tag{1.16}$$

Finally the diffracted intensity $I(\vec{Q}, E)$ is proportional to the square modulus of the total structure factor $F(\vec{Q}, E)$:

$$\begin{aligned} I(\vec{Q}, E) &\propto \left|F(\vec{Q}, E)\right|^2 \\ &\propto |F_T|^2 + \frac{|F_A|^2}{f_A^{0\,2}} \left(f'^{\,2}_A + f''^{\,2}_A\right) + 2\frac{|F_A||F_T|}{f_A^0} \left(f'_A \cos(\varphi_T - \varphi_A) + f''_A \sin(\varphi_T - \varphi_A)\right) \end{aligned} \tag{1.17}$$

where $|F_T|$ and $|F_A|$ depend on $\vec{Q}$ (this has been omitted in equation 1.17 to lighten the notation). Equation 1.17 can finally more simply be written as

$$I(\vec{Q}, E) \propto \left[|F_T|\, cos\,(\varphi_T - \varphi_A) + \frac{|F_A|}{f_A^0} f'_A\right]^2 + \left[|F_T|\, sin\,(\varphi_T - \varphi_A) + \frac{|F_A|}{f_A^0} f''_A\right]^2 \tag{1.18}$$

In equation 1.18, the three parameters $\varphi_T - \varphi_A$, $|F_A|$ and $|F_T|$ can be experimentally determined by measuring the diffracted intensity at three different energies around the absorption edge of the anomalous specie. In practice, to ensure a better precision, the diffracted intensity is recorded at a dozen of different energies. In addition, although the values of f' and f'' are tabulated for most atoms, they can be more precisely experimentally determined. To do so, fluorescence measurements are performed to obtain f'' (the absorption contribution) and f' is afterwards obtained from f'' through the Kramers-Konig relation. The precise determination of these unknowns then allows to separately obtain the intensity of the resonant and of the non-resonant atoms. It is this distinction that adds the chemical sensitivity to X-ray diffraction [132].

GaN structure factor

Let us now go to a simpler case and forget about resonant corrections in order to derive the Thomson structure factor of WZ GaN. Relying on equation 1.13 and taking into account Ga and N atom positions in the unit WZ cell (see page 16), the Ga structure

factor reads

$$F^0_{Ga}\left(\vec{Q},E\right)=\sum_j^{Ga} f^0_{Ga}e^{2i\pi(x_jh+y_jk+z_jl)}=f^0_{Ga}\left(1+e^{2i\pi\left(\frac{2}{3}h+\frac{1}{3}k+\frac{1}{2}l\right)}\right) \tag{1.19}$$

Similarly, the N structure factor reads

$$F^0_{N}\left(\vec{Q},E\right)=\sum_j^{N} f^0_{N}e^{2i\pi(x_jh+y_jk+z_jl)}=f^0_{N}e^{2i\pi ul}\left(1+e^{2i\pi\left(\frac{2}{3}h+\frac{1}{3}k+\frac{1}{2}l\right)}\right) \tag{1.20}$$

One can remember that $u\approx 0.377\cdot c_{GaN}$ for GaN (see table 1.1). It follows that the total structure factor of equation 1.15 becomes

$$\begin{aligned} F(hkl) &= F^0_N+F^0_{Ga} \\ &= \left(f^0_{Ga}+f^0_N e^{2i\pi ul}\right)\left(1+e^{2i\pi(\frac{2}{3}h+\frac{1}{3}k+\frac{1}{2}l)}\right) \end{aligned} \tag{1.21}$$

Note that we have now expressed F as a function of hkl since $\vec{Q}=h\vec{a_1^*}+k\vec{a_2^*}+l\vec{c^*}$ (appendix A). The modulus $|F(hkl)|$ of $F(hkl)$ as well as its argument φ can then be derived providing some basic calculations on complex numbers. In particular

$$|F(hkl)|=\left|2\cos(\pi(\frac{2}{3}h+\frac{1}{3}k+\frac{1}{2}l))\right|\sqrt{{f^0_{Ga}}^2+{f^0_N}^2+2f^0_{Ga}f^0_N\cos(2\pi ul)} \tag{1.22}$$

Typically, for the $P6_3mc$ group to which WZ GaN belongs, $|F(hkl)|=\left|F(\bar{h}\bar{k}\bar{l})\right|=\left|F(hk\bar{l})\right|$ [134]. This can actually be seen in equation 1.22:

- When changing hkl into $\bar{h}\bar{k}\bar{l}$, $\cos(-2\pi ul)=\cos(2\pi ul)$ and $\cos(-\pi(\frac{2}{3}h+\frac{1}{3}k+\frac{1}{2}l))=\cos(\pi(\frac{2}{3}h+\frac{1}{3}k+\frac{1}{2}l))$. Hence $|F(hkl)|=\left|F(\bar{h}\bar{k}\bar{l})\right|$.
- When changing hkl into $hk\bar{l}$, we also have $\cos(-2\pi ul)=\cos(2\pi ul)$. We can besides write

$$\begin{aligned} \cos(\pi(\tfrac{2}{3}h+\tfrac{1}{3}k-\tfrac{1}{2}l)) &= \cos(\pi(\tfrac{2}{3}h+\tfrac{1}{3}k+\tfrac{1}{2}l-l)) \\ &= \cos(\pi(\tfrac{2}{3}h+\tfrac{1}{3}k+\tfrac{1}{2}l))\cos(\pi l) \\ &\quad +\sin(\pi(\tfrac{2}{3}h+\tfrac{1}{3}k+\tfrac{1}{2}l))\sin(\pi l) \end{aligned} \tag{1.23}$$

  l being an integer, $\sin(\pi l))=0\ \forall l$ and $\cos(\pi l)$ is equal to 1 or -1 depending on the parity of l. But whether l is odd or even, $|\cos(\pi l)|=1$. Therefore $\cos(\pi(\frac{2}{3}h+\frac{1}{3}k-\frac{1}{2}l))=\cos(\pi(\frac{2}{3}h+\frac{1}{3}k+\frac{1}{2}l)$, hence $|F(hkl)|=\left|F(hk\bar{l})\right|$.

hkl, $\bar{h}\bar{k}\bar{l}$ and $hk\bar{l}$ constitute here Bijvoet pairs which diffract with the same intensity as long as resonant effects are negligible.

1.3.2 Optical characterization

In order to optically characterize the grown structures, two types of experiments were performed in this thesis work: photoluminescence (PL) both at a macroscopic and at a

microscopic scale, and nano-cathodoluminescence (CL). These two techniques consist in exciting the investigated object above its band gap, either by mean of a laser beam (PL) or by mean of an electron beam (CL) and to detect the light subsequently re-emitted from radiative recombinations occurring within the structure. Carriers being excited above their band-gap, they first thermalize (non-radiatively) towards lower energy levels. Once the lowest energy level reached, they finally recombine radiatively. Therefore both techniques probe these lowest energy levels, which can also be impurities levels.

Transitions typically observed are related to recombination of free excitons (bound electron-hole pairs) and of excitons bound to different types of impurities present in the sample. In fact, depending on their electronic configuration and more specifically on whether they have more or less electrons than the species forming the crystal, these impurities respectively constitute "donors" or "acceptors" shallow defects.

The analysis of the collected light allows to characterize various material properties such as its crystalline quality, its purity, the type of defects it contains, or also its chemical composition in the case of ternary alloys. Deeper insights on CL and on PL can for instance be found in Refs. [135] and [136], respectively.

1.3.2.1 Photoluminescence

In this manuscript, PL spectra were obtained after excitation of the samples with a continuous-wave frequency-doubled argon laser emitting at 488 nm. The excitation wavelength was therefore 244 nm. For macro-PL, the laser spot diameter is of the order of 100 µm and the luminesced signal is collected through a Jobin-Yvon HR460 monochromator equipped with an ultraviolet-enhanced charge-coupled device camera. Regarding micro-photoluminescence (µ-PL), using a refractive microscope objective, the spot size is reduced to 1 µm.

1.3.2.2 Nano-cathodoluminescence

Nano-CL experiments were handled at the Laboratoire de Physique des Solides (LPS) of Orsay at Université Paris-Sud by L. Tizei from the group of M. Kociak. Compared to a regular CL setup, the nano-CL system has the peculiarity to enable acquisitions of luminescence spectra on regions as small as 1 nm^2. The setup has, for instance, proven the ability to distinctly measure spectra of two quantum wells separated by few nanometres [137] or the emission of individual defects in nanodiamond [138]. The increase of the resolution is due to several differences with regular systems. Typically, regular CL experiments are made in scanning electron microscopes (SEM) and focus on thick samples. The nano-CL used here relies on the use of high voltages, on small but intense beams hitting thin samples (*i.e.* absence of excitation pear) as well as on a high throughput and brightness-conserving CL detection system.

Experiments were performed on a Vacuum Generator Scanning Transmission Electron Microscope (VG STEM HB501) fitted with a Cold Field Emission Gun (CFEG) working at 60 keV and a home made nitrogen-cooled stage. The high brightness of the CFEG allows to obtain a typical current of 300 pA in an electron beam with diameter as small as 0.5 nm. As mechanical noise degrades the resolution, the effective spatial resolution is 1 nm. The CL signal was detected by a home-made, high throughput CL system. Experiments were performed in the spectral imaging mode. In this mode, the beam is scanned over the region of interest with a constant step. At each position of the scan, two types of signals are acquired:

- structural signals: light Bright Field (BF) and High Angle Annular Dark Field (HAADF)
- a spectroscopic signal: CL spectrum

At the end of the acquisition, both the images (BF and HAADF) and the spectral map are reconstructed: at each pixel of the image corresponds a given spectrum, allowing to precisely correlate both structural and spectroscopic information.

2

Growth and properties of self-assembled GaN nanowires on silicon

Focussing now our attention on GaN nanowires, the scope of this chapter is to introduce the specificities of these nanostructures as well as the substrate on which they are principally grown: silicon. In fact, the first section of the chapter will be entirely devoted to silicon. We will especially describe the procedure used for the calibration of its temperature. In the second section, we will address GaN nanowire properties, growth conditions and morphology dependence on these growth conditions with the objective of controlling their density and the homogeneity of the nanowire assembly.

Contents

2.1 Silicon substrates 37

2.1.1 The assets of silicon substrates 37

2.1.2 Silicon substrate specifications 38

2.1.3 Silicon substrate preparation 38

2.1.4 Silicon substrate temperature calibration 40

2.2 Self-assembled GaN nanowires on silicon 42

2.2.1 State of the art of self-assembled GaN nanowires 42

2.2.2 Optical properties of self-assembled GaN nanowires 44

2.2.3 GaN nanowire growth conditions on bare silicon 46
2.2.4 GaN nanowire density dependence on the substrate temperature 47
2.2.5 GaN nanowire length and diameter versus temperature 50
2.3 Conclusion of the chapter 52

2.1 Silicon substrates

2.1.1 The assets of silicon substrates

When it comes to choosing a substrate for the epitaxy of a given material, numerous parameters must be considered: lattice matching, thermal expansion compatibility, thermal conductivity, electric conductivity, crystal quality, surface finish specification, substrate size availability and naturally, cost. The main problem for the epitaxy of two-dimensional III-N layers is the lack of suitable substrate. For a long time, GaN and AlN single crystal wafers were not commercially available. Nowadays, although great progresses have been made from the point of view of elaboration of bulk GaN and AlN crystals (*e.g.* Refs. [139–142]), these structures are still cost-prohibitive to high volume production. On the other hand, GaN and AlN "templates" or "quasi-crystals" (few millimetres of GaN or AlN are grown by metal-organic chemical vapour deposition (MOCVD) or hybrid vapour-phase epitaxy (HVPE) on non-native substrates) present a large bow and still contain between 10^6 and 10^9 dislocations per cm^2. Although these substrates are already commercially used (for instance in the fabrication of optical storage media based on blue lasers (Blu-rays) or of GaN-based electronic devices), improvements in terms of device efficiency and lifetime can be expected from better quality crystals.

Regarding heteroepitaxy, often used SiC (silicon carbide) is a good thermal conductor with a lattice mismatch as low as 3 % with GaN and 0.5 % with AlN[1] but its cost is still high, between 120 and 200€ the 2-inch wafer. Sapphire is cheaper (about 50€/wafer) but its 14 % mismatch and its insulating character are a huge disadvantage for device fabrication. Silicon on the other hand combines numerous advantages. First, a 2-inch silicon wafer is as cheap as 10€. Second, its crystallization is widely mastered, especially by Czochralski process, resulting is ultra-high quality wafers. Last, both its p and n doping are perfectly controlled. These assets explain that silicon has been and still is the coumpound the most used in the microelectronic industry and that one would have great advantage to use it as a substrate for device fabrication. Unfortunately, silicon has large thermal expansion and lattice mismatches with III-N coumpounds (for instance Si(111) surface exhibit 17 % lattice mismatch with GaN and 19 % mismatch with AlN) which results in 2D layers of extremely poor quality. Nanowires (NWs) on the other hand, in virtue of their particular geometry, plastically relieve the mismatch at the interface and allow the crystal to subsequently grow with a perfect crystalline quality. Silicon therefore imposed itself as the main substrate used for the growth of GaN NWs by PAMBE.

[1] Mismatches are given in a (see appendix A), the [0001] direction being the most widely spread growth direction of wurtzite III-N materials.

2.1.2 Silicon substrate specifications

Silicon crystallizes as diamond with lattice parameter $a_{Si} = 5.431$ Å. Figure 2.1 illustrates this crystalline arrangement and highlights the [111] direction as well as the (111) plane, which constitute a basis for a reduced hexagonal cell, similar to that of the III-N WZ crystallographic phase (see appendix A). Lattice parameters of this reduced hexagonal cell are $a_{Si}^{hex} = \frac{a_{Si}\sqrt{2}}{2} = 3.840$ Å and $c_{Si}^{hex} = a_{Si}\sqrt{3} = 9.407$ Å.

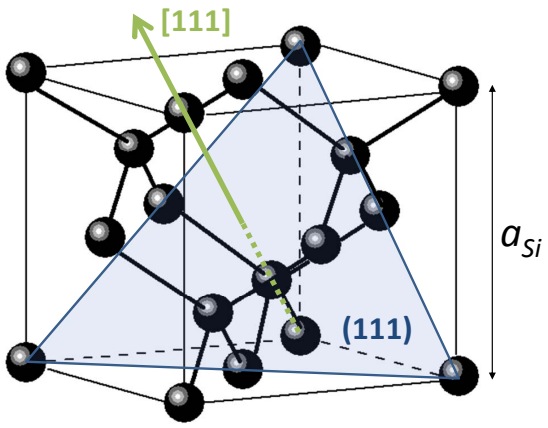

FIG. 2.1 – Silicon diamond crystalline arrangement.

Unless otherwise specified, characteristics of the wafer used are the following:

- oriented [111]
- a high n-doping (either with As or with P atoms) equivalent to a resistivity lower than 0.005 Ohm·cm
- a 2-inch diameter
- a 275-µm thickness

2.1.3 Silicon substrate preparation

Before introduction in the MBE system, the Si 2-inch wafer is dipped in HF 5 % during 40 s to remove the native SiO_2 oxide on its surface. Then, it is placed onto on the internal rim of a 2-inch hollowed substrate holder made of molybdenum (also called "molybloc") and maintained with two pinches. Once positioned onto the oven inside the growth chamber, the substrate on its molybloc is heated by radiation from the oven filament up to about 830 °C. Baking the substrate helps removing the last whiffs of SiO_2, until apparition of the typical Si(111) reconstruction by RHEED, an indication of the "cleanness" of the surface. Reconstruction (or re-arrangement) of the topmost atomic monolayer is a well-known phenomena occuring in UHV conditions to minimize the crystal energy. It is usually signed by a change of periodicity of these topmost atoms compared to the ones underneath (also called "bulk" atoms). More specifically, between 600 and 850 °C,

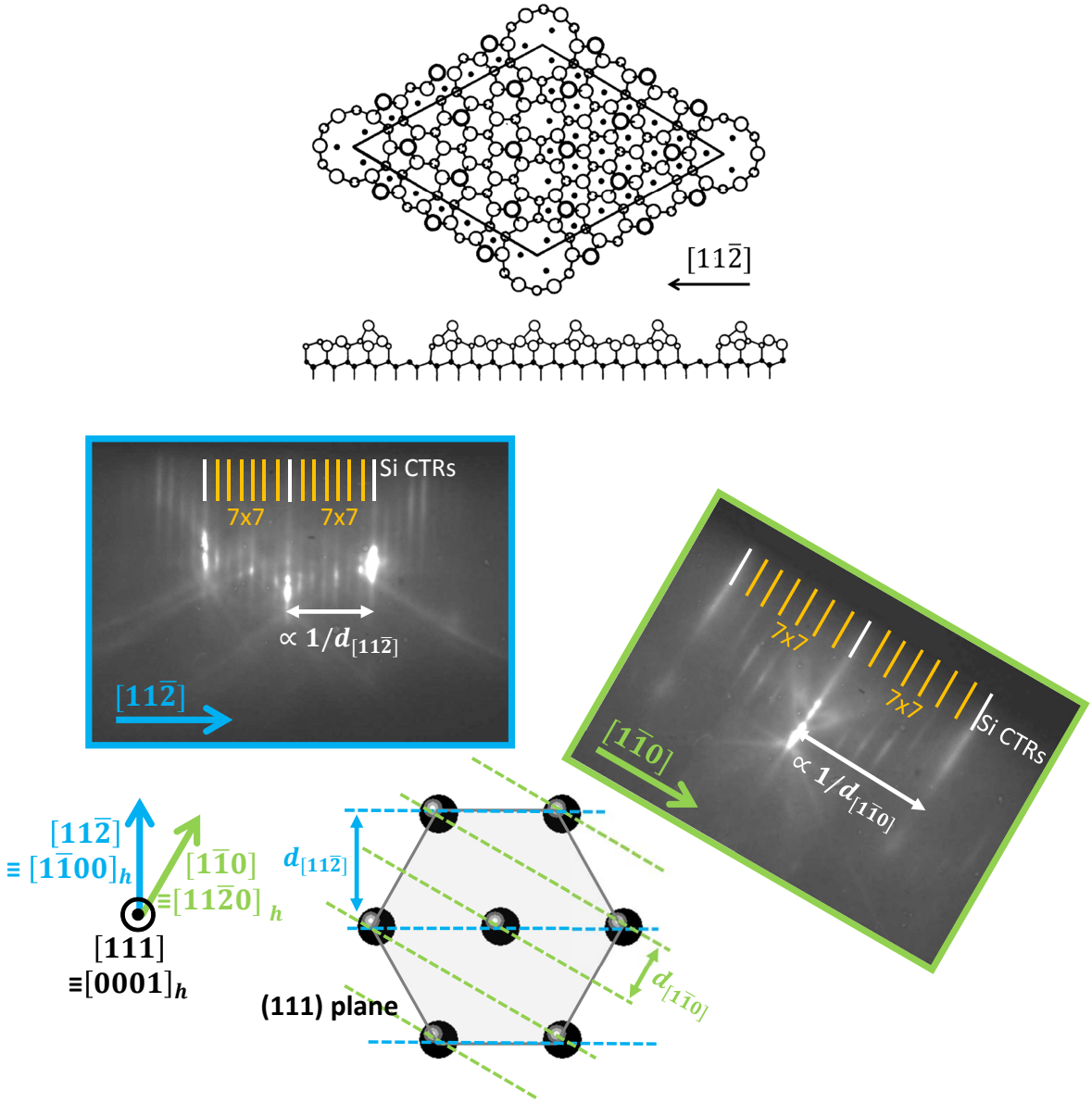

FIG. 2.2 – 7 × 7 Si(111) surface reconstruction structure taken from [147] (top) and 7 × 7 surface reconstruction observed by RHEED along [11$\bar{2}$] and [1$\bar{1}$0] azimuths (bottom).

the Si(111) surface reconstructs as 7×7 [143–148], which means that the topmost atoms have a periodicity 7 times larger than that of the bulk Si atoms. Figure 2.2 presents a scheme of the 7×7 structure, taken from Ref. [147] and its corresponding RHEED patterns along [11$\bar{2}$] and [1$\bar{1}$0] azimuths. Note that, as it is customary in the literature, RHEED-related silicon azimuts are and will be expressed with indexes belonging to the silicon cubic cell all along this manuscript. To find the equivalence in the Si reduced hexagonal cell, the reader is invited to refer to appendix A. White lines show Si(111) crystal truncation rods (CRTs), or in other terms, the streaks related to the diffraction of the silicon bulk atoms. Golden lines are related to the topmost atoms forming the

reconstruction. In the $[11\bar{2}]$ direction, the inter-atomic distance $d_{[11\bar{2}]}$ is equal to $\frac{a_{Si}\sqrt{3}}{2\sqrt{2}}$. In the $[1\bar{1}0]$ direction, the inter-atomic distance $d_{[1\bar{1}0]}$ is $\frac{a_{Si}\sqrt{2}}{4}$. Hence $d_{[11\bar{2}]} = \sqrt{3}d_{[1\bar{1}0]}$. Consistently with equation 1.10, it can be verified on figure 2.2 that the distance between two Si CRTs in the $[11\bar{2}]$ direction is $1/\sqrt{3}$ times smaller than in the $[1\bar{1}0]$ direction.

2.1.4 Silicon substrate temperature calibration

As mentioned in chapter 1, a procedure, specific to Si(111), has been used to calibrate the temperature of the substrate surface. This procedure relies on the Ga desorption time dependence on the substrate temperature. Practically, one follows the 7×7 reconstruction transient while operating the Ga shutter: as soon as the substrate temperature is stabilized, its surface is exposed to Ga flux during 10 s. As illustrated in figure 2.3 (a), which shows a typical transient obtained with this procedure, the 10-second Ga coverage (zone A) results in a drop of the 7×7 reconstruction RHEED intensity. After 10 s, the Ga shutter is closed: while Ga atoms are no longer provided, the ones already adsorbed on the silicon surface start to desorb, as observed by the rise back of the 7×7 intensity. Two stages can then be identified, distinguished by the inflexion point between zones B and C.

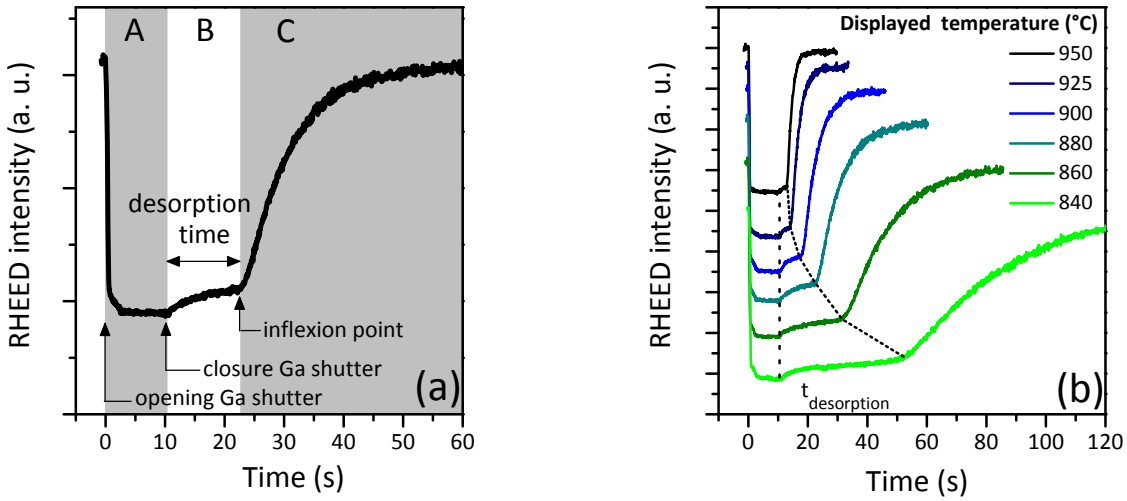

FIG. 2.3 – (a) 7×7 Si(111) reconstruction transient. At time t = 0 s, the Ga shutter is opened. Zone A corresponds to the period during which the Si(111) surface is covered with Ga adatoms (at a rate around 0.3 ML/s). At time t = 10 s, the Ga shutter is closed. The delay between the closure of the Ga shutter and the first inflexion point is defined as the Ga desorption time ($t_{desorption}$); (b) the same transients at different substrate temperatures.

Figure 2.3 (b) shows transients obtained at different substrate temperatures. It can be seen that the inflexion point delimiting zones B and C is very sensitive to the change

of temperature. It is precisely this sensitivity that can be used to calibrate the substrate temperature: the time between the closure of the Ga shutter and the inflexion point (henceforth called "desorption time") directly reflects the substrate temperature, allowing an excellent reproducibility from sample to sample. It must be noted that, as shown by G. Tourbot in Ref. [149], the strength of this procedure relies in the stability of the measured desorption time versus changes in both the Ga deposition time and the Ga flux, a consequence of the Ga auto-regulated regime.

Not only the measurement of the Ga desorption time can ensure reproducibility in the substrate temperature from sample to sample but also it can be used to evaluate the real effective Si(111) surface temperature. To do so, we used the sample from which the desorption time was determined at various substrate temperatures (Fig. 2.3 (b)). Note that temperatures given in this figure (Fig. 2.3 (b)) are the one displayed by the thermocouple and are overestimated compared to their real value. However, we already mentioned that the 7×7 reconstruction exists only up to about 850 ℃. Hence, by comparing the displayed "temperature of disappearance" of the 7×7 reconstruction to the real one, it is possible to estimate the discrepancy between displayed and real temperatures. In practice, different values of the 7×7 temperature of disappearance can be found in the literature, varying from 827 ℃ [146] to 867 ℃ [144]. More recently, Hu *et al.* have evoked a disappearance "between 840 and 870 ℃" [148]. To take account for this dispersion, we will consider that the real 7×7 reconstruction disappearance temperature is 850 ℃. Then, in order to determine the displayed 7×7 disappearance temperature, the 7×7 intensity was monitored while increasing the substrate temperature between 850 and 1025 ℃ (displayed). In order to let time to the substrate to thermalize at each step in temperature, a low ramp of 1 ℃/min was set on the oven control. Figure 2.4 shows the recorded intensity evolution versus the displayed temperature.

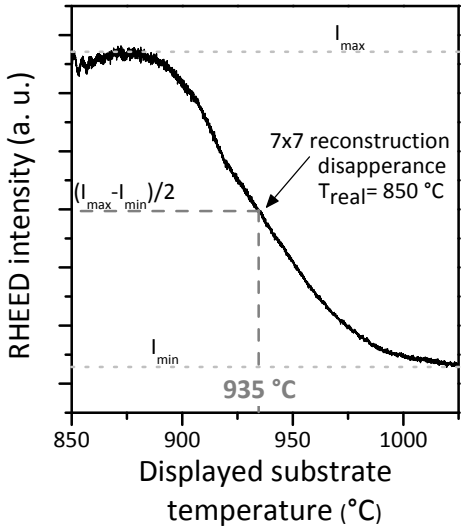

FIG. 2.4 – 7×7 Si(111) reconstruction disappearance with increasing substrate temperature. The displayed temperature of 935 ℃ corresponds to a real temperature of 850 ℃.

It can be seen that the 7×7 disappearance is progressive, which is likely due to the fact that the RHEED electron beam grazes on the surface and therefore averages the intensity over a stripe along the wafer diameter. The measured disappearance temperature was hence considered as the temperature half way between the maximum intensity recorded and the noise level. At that point, the displayed temperature of 935 ℃ corresponds to a real substrate temperature of 850 ℃. By extrapolation of this discrepancy, we then estimated that the displayed temperature was always 85 ℃ higher than the real one. This simple linear extrapolation is not perfectly accurate on a wide range of temperatures but works fine in our case, GaN NW growth temperature being close to the 7×7 disappearance temperature.

Finally, the above-described correction of 85 ℃ combined to the desorption times obtained from figure 2.3 (b) were used to determine the effective Si(111) surface temperature in function of the measured Ga desorption time (Fig. 2.5). The effective Si(111) surface substrate temperature exponentially decays with increasing desorption time. In the following of the manuscript, unless otherwise specified, the given temperature were always based on the calibration given in figure 2.5.

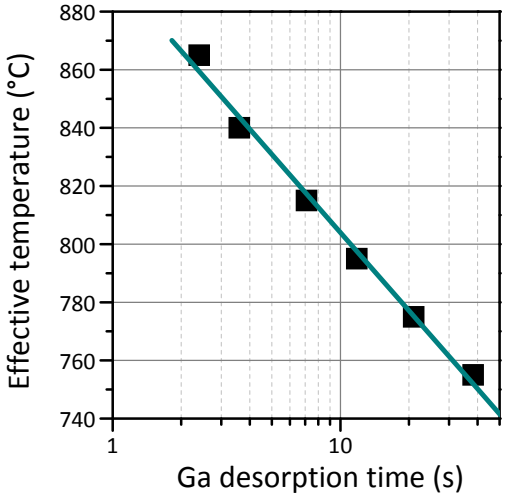

FIG. 2.5 – Effective temperature of the Si(111) surface versus measured Ga desorption time

2.2 Self-assembled GaN nanowires on silicon

2.2.1 State of the art of self-assembled GaN nanowires

Now that we have well established the procedure used to measure the effective Si(111) substrate temperature, let us focus on GaN NWs. Growth of these nanostructures by PAMBE was reported for the first time in 1997 on sapphire [20] and in 1998 on silicon [21]. On sapphire (Al_2O_3), both self- and catalyst- induced GaN NW growth are possible: while

self-assembled NWs are obtained using GaN or AlN buffer layers [43], catalyst-induced NWs form through the vapour-solid-liquid (VLS) mechanism when pre-depositing Ni seed particles directly on the sapphire surface [63]. Regarding silicon substrates, GaN NW develop without the help of any catalyst either on the bare (111) surface or on top of a thin AlN buffer layer deposited on Si(111). Figure 2.6 presents a comparison between these two types of growth.

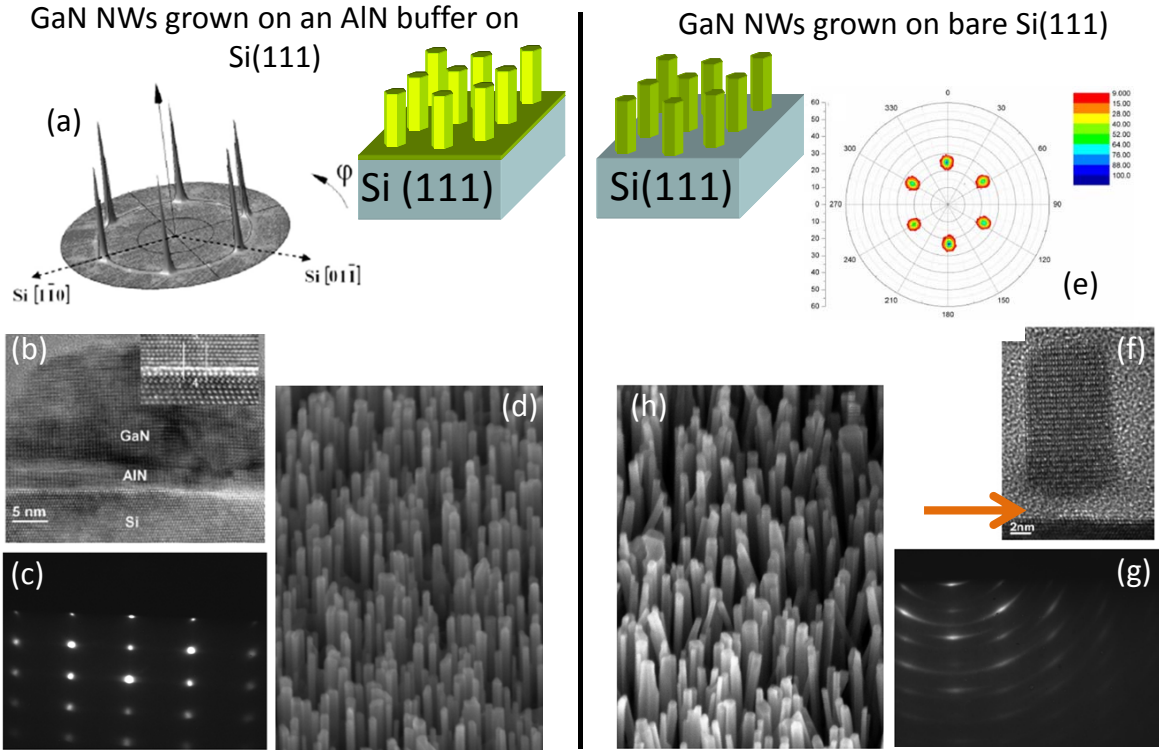

FIG. 2.6 – Morphological and structural comparison between GaN NWs, the growth of which has been initiated on top of a thin AlN layer on Si(111) and GaN NWs, the growth of which has been initiated on bare Si(111). Pole figures (a) and (e) are taken from Ref. [68] and Ref. [150], respectively; the TEM image (b) is taken from Ref. [73]; the TEM image (f) is taken from Ref. [70]; (d) and (h) are bird-eye view SEM images and (c) and (g) the corresponding RHEED patterns.

In both cases, NW facets and top surface are respectively constituted of *m*- and *c*-planes, and their growth direction is perpendicular to the substrate. Regarding NWs which growth is initiated on bare silicon, the presence of a thin amorphous Si_xN_y (pointed out by the arrow in figure 2.6 (f)) has been observed between the GaN NW feet and the Si surface [44, 49, 70, 151]. As illustrated by the pole figure in figure 2.6 (e), taken from Ref. [150], in such case, the GaN NW ensemble exhibits a six-fold symmetry. This means that all NWs have the same average in-plane orientation. However the broken-ring RHEED pattern displayed in figure 2.6 (g) illustrates a spread in this in-plane NW orientation.

Typically, based on X-ray diffraction experiments, an average twist (spread in the average in-plane orientation, also called "in-plane mosaicity") of 9° has been reported [63]. Moreover a tilt (out-of-plane mosaicity) of 3.9° was observed [63]. The presence of an amorphous Si_xN_y layer is hence associated with the presence of a non-negligible proportion of tilted and twisted NWs, as evidenced by the bird-eye view SEM image presented in figure 2.6 (h). On the other hand, the use of an AlN buffer improves the NW straightness and in-plane orientation (Figs. 2.6 (c) and (d)). In this case, Largeau *et al.* evidenced a perfect alignment between silicon $< 01\bar{1} >$ and GaN NW $< 11\bar{2}0 >$ directions (Fig. 2.6 (a), taken from Ref. [68]). The characterization of AlN buffers deposited on sapphire by MBE revealed that up to a thickness of 100 nm, AlN does not grow as a continuous film but as multiple grains with different orientations [152]. Sekiguchi and co-workers suggested than GaN NWs, grown on such grainy buffer, nucleate at the junction between the grains rather than on top of them [59]. Although growth conditions are different on silicon, the hypothesis of a grainy AlN buffer together with a nucleation at the grain junctions is also plausible. The AlN buffer would then act as a guide for GaN columns, accounting for their straightness. Moreover, Bourret *et al.* showed in Ref. [153] that for AlN deposited at temperatures above 650 °C, a single epitaxial relation exists (namely "AlN(0001) $< 2\bar{1}\bar{1}0 >$ directions aligned to Si(111) $< 02\bar{2} >$ directions") at the AlN/Si(111) interface, relieved by a 4:5 coincidence relation (illustrated in figure 2.6 (b)). The excellent in-plane orientation of the AlN buffer guide then explains the perfect in-plane alignment of GaN NWs grown with a buffer on Si(111).

Note that growth of WZ GaN NWs was also demonstrated on Si(001) surfaces [55, 63] with the growth direction perpendicular to the substrate. Geelhaar *et al.* showed that in this case, the NW in-plane orientation settles along two different azimuthal Si(001) directions [63] but the NWs present strong tilt and twist.

2.2.2 Optical properties of self-assembled GaN nanowires

Despite the observed structural improvements of GaN NWs grown on an intermediate AlN buffer layer, one should keep in mind that because of its nearly-insulating character, from the point of view of devices, the use of AlN is better to be avoided. Besides, in terms of optical properties, no difference between GaN NWs grown on an intermediate AlN buffer and GaN NWs grown on bare silicon has been observed so far. Both types of nanocolumns indeed exhibit similar excellent optical properties, as illustrated in figure 2.7 which presents a typical PL spectrum obtained from an ensemble of GaN NWs excited at 244 nm on (a) a large energy scale and (b) on a reduced zone around the GaN band-edge.

Among the characteristic GaN emission peaks that can be observed, near band-edge contributions between 3.47 and 3.50 eV are of excitonic origin [50, 154, 155]. First, the strongest peak situated at 3.472 eV is commonly attributed to excitons bound to neu-

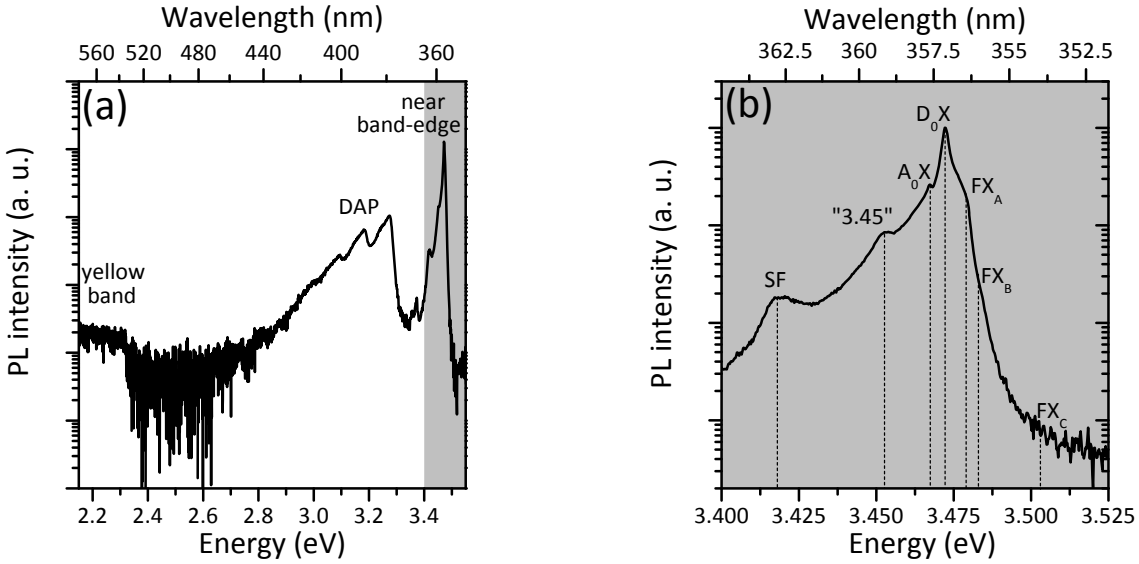

FIG. 2.7 – (a) Typical PL spectrum obtained from an ensemble of GaN NWs optically pumped at 244 nm and (b) close up of the near band-edge emission (grey area in (a)).

tral shallow donors (D_0X), such as oxygen or silicon atoms, which are typical in GaN. In the specific case of GaN NWs grown on bare silicon, Si was in fact identified as the main shallow donor [156]. In the tail of this D_0X peak, towards higher energies, the shoulder positioned at 3.479 is ascribed to free A excitons emission (FX_A), or in other words, recombinations of bound electron-heavy-hole pairs (see figure 1.8). Further away, it is sometimes also possible to observe the B and the C free exciton contributions (FX_B and FX_C), respectively at 3.483 and 3.503 eV - involving light holes and holes in the split off band [154]. Towards lower energies, another near-band-edge peak, positioned at 3.466 eV can be seen. The few papers reporting on this contribution, assigned it to an exciton bound to a shallow silicon-related acceptors (A_0X) [157–159]. Then, the peak raising at 3.45 eV has not yet been clearly identified. In the literature, its origin is still under intense discussion, alternatively attributed to recombinations of acceptor-bound excitons [154], or to a two electron satellite of the D_0X recombination [160, 161]. Further from the band edge, the contribution located around 3.42 eV is believed to be induced by recombinations of excitons bound to the stacking faults (SF) situated at the foot of the NWs [50, 151]. Further from the band-edge, the band around 3.2 eV is attributed to sharp emissions from donor-acceptor pairs (DAP) followed by several LO phonon replicas. Finally, in the lower energy range, around 2.2 eV, a large gaussian-shaped contribution called the “yellow band” (YL) is sometimes observed, the origin of which has still not been clearly established. Nevertheless, the YL is believed to be a consequence of different types of defects inside the material [162].

Typically, an intense and thin near-band-edge PL emission is indicative of a good optical quality. On the other hand, YL and DAP emission intensities reflect the amount

of impurities and defects in the crystal, thus appear to be very sensitive to the "degree of purity" inside the growth chamber itself. Regarding spectra displayed in figure 2.7, the D_0X emission is about 10 times more intense than the DAP emission, and has a full-width at half maximum (FWHM) of 2.8 meV, suggesting a good - but not the best - crystal quality. In fact, FWHM as low as 1.2 meV have already been reached within our group, which is the state of the art for GaN grown on silicon. For comparison, the smallest D_0X peak FWHM obtained with 2D GaN layers is 10 meV. However it must be emphasized that this GaN layer was as thick as 1.5 µm and grown on a GaN single-crystal [158]. Indisputably, the excellent material quality obtained from GaN on silicon is an attribute of the NW geometry and would clearly not be reached with 2D layers in reason of the large lattice mismatch between silicon and GaN. Hence, the NW geometry opens the path for combining the great properties of GaN (and other III-N compounds) to the advantageous utilization of silicon substrates. In order to make the best benefit of their potential, NWs must however be suitable to "devicization" and more particularly for contacting. It hence seems clear that the control of their morphology (*i.e.* density, length, diameter, dispersion in length and diameter between NWs, etc.) is of prime importance. In this context, the following of this section will be devoted to the analysis of GaN NWs morphology dependence on the growth conditions.

2.2.3 GaN nanowire growth conditions on bare silicon

Since the first investigations on their growth on silicon, GaN NW morphology dependence on the growth conditions (namely the substrate temperature, the III/V flux ratio and the atomic beam incidence angles) has been largely investigated [21, 41–46, 57, 61, 64, 65, 75, 78, 91, 163, 164]. It has been qualitatively established that the NW density increases with increasing III/N flux ratio and decreasing temperature. Note that because of Ga desorption these two parameters are not completely independent.

A recent paper (Ref. [46]) displays a diagram that summarizes the change in the NW morphology in function of the growth conditions (Fig. 2.8). It can be seen that the growth conditions suitable to a columnar morphology consist in a temperature around 800 °C and an effective excess of nitrogen on the surface. Because the temperature at which NWs are grown is high, the desorption of Ga species is important. Hence the nominal Ga flux may be slightly higher than the N flux. When going towards lower temperatures or higher Ga/N ratio, GaN nanocolumn density increases until coalescence to form a rough compact layer. On the other hand, when the substrate temperature is too high, Ga desorption rate is more important than its incorporation rate and no growth is observed at all.

In summary, the excess of nitrogen combined to an appropriate temperature are the key conditions for GaN NW growth: the adjustment of these two parameters allows to tune the GaN NW morphology, going from very separated NWs to a compact layer.

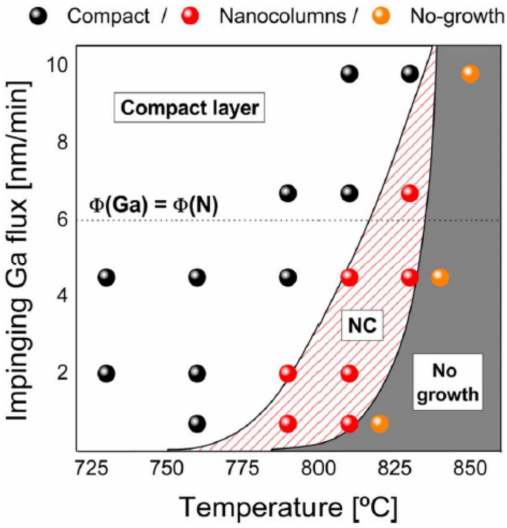

FIG. 2.8 – GaN NW growth condition diagram, taken from Ref. [46].

2.2.4 GaN nanowire density dependence on the substrate temperature

Let us now present quantitative results highlighting the dependence of GaN morphology on the substrate temperature. These results were obtained in collaboration with R. Mata and A. Cros from the university of Valencia (Spain).

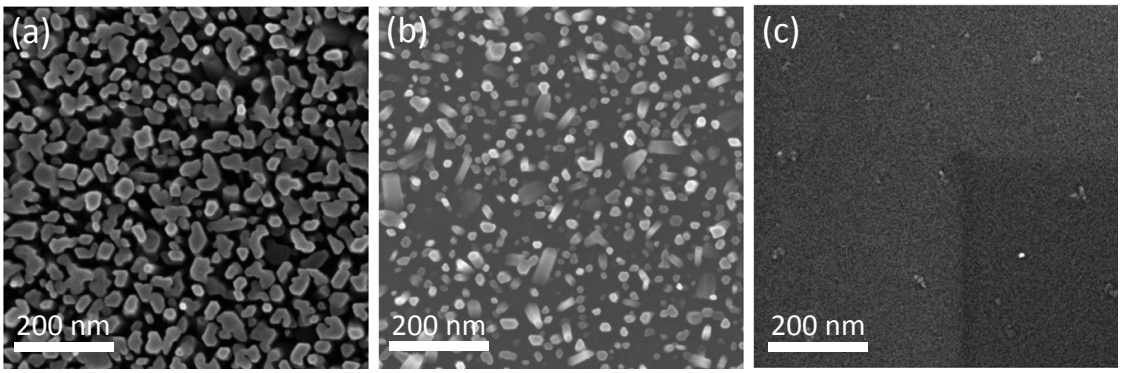

FIG. 2.9 – Top-view SEM images taken at the center of the wafer for samples grown at (a) 781 ℃, (b) 797 ℃ and (c) 812 ℃.

A series of samples was grown at various substrate temperatures estimated from the procedure previously described. In order to be precise, as growths were preformed on 2-inch substrates, caution was taken to always set the RHEED in the same way, especially ensuring that the focal point of the electron beam was at the center of the wafer. It must be noted that because of the electron glancing incidence angle, although the desorption time was measured at the center of the wafer, it is actually averaged on the stripe of wafer stridden by the beam. Growth was then undertaken during 90 minutes with a III/V ratio equal to 0.3. After growth, a stripe was cleaved along the diameter of the wafer and its center was observed by SEM. Figure 2.9 presents examples of top-view SEM images taken

at the centre of the wafer for samples grown at (a) 781 ℃, (b) 797 ℃ and (c) 812 ℃, illustrating a decrease of the NW density with the growth temperature.

Based on these top view SEM images, the NW density was then quantitatively determined, presented in figure 2.10. Let us recall that the indicated substrate temperatures were determined from the measured desorption times at the center of the wafers. It can be seen that in the range of 780-795 ℃, GaN NW density slowly decreases. From 795 ℃, this decrease becomes more drastic until falling down to 0 around 805 ℃. The absence of NW above 805 ℃ is associated to the high GaN decomposition rate in this range of temperatures, as highlighted in the work of Grandjean *et al.* [165].

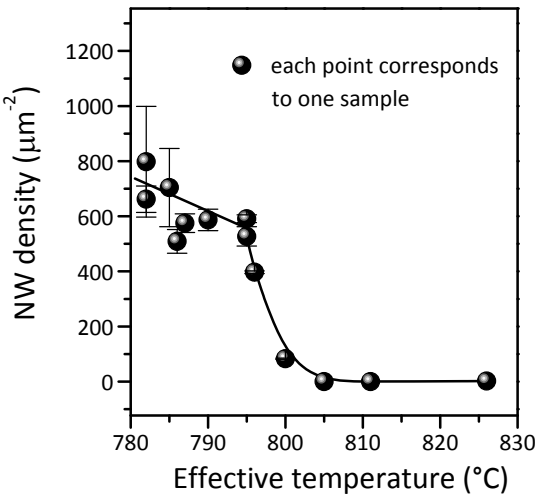

FIG. 2.10 – GaN NW density at the center of the 2-inch Si(111) wafer dependence on the substrate temperature, estimated from the Ga desorption time measured at the center of the wafer.

Such a variation of density can also be observed on a single wafer, as a consequence of the gradient of temperature existing along its 2-inch diameter. This temperature gradient results from heating inhomogeneities and partly depends on the mechanical design of the substrate holder. Figure 2.11 illustrates the evolution of GaN NW density along the wafer radius for two of the samples from the above-described series, respectively grown at 785 ℃ (squares) and 825 ℃ (circles). For the sample grown at 785 ℃ it can be seen that the density remains more or less constant in a 1.5-cm-diameter zone around the center, and then strongly increases in the 1-cm-wide peripheral ring. For the sample grown at 825 ℃, the gradient is stronger: at the center of the wafer, the temperature is higher than the GaN decomposition temperature thus no GaN was incorporated; 1 cm away from the center, the density starts to increase and this continues until the edge, more or less linearly. In order to visualize the density gradient, figure 2.12 presents schemes of both samples. The gray scale represents GaN NW density and the arrows indicate the radius along which the density evolution, displayed in figure 2.11, was evaluated.

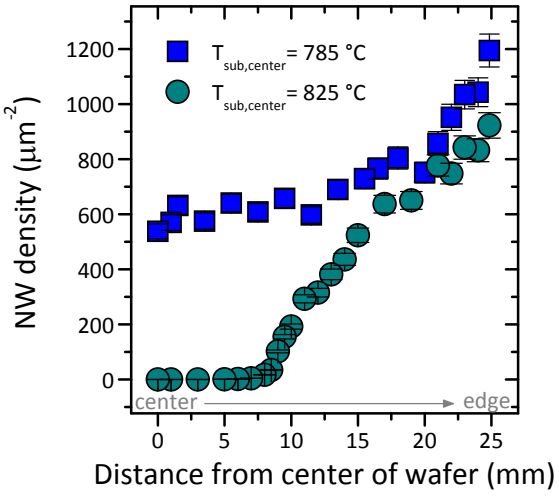

FIG. 2.11 – GaN NW density along the radius of a 2-inch Si(111) wafer for samples grown at 785 °C (full squares) and at 825 °C (full circles), as estimated from the Ga desorption time measured at the center of the wafer.

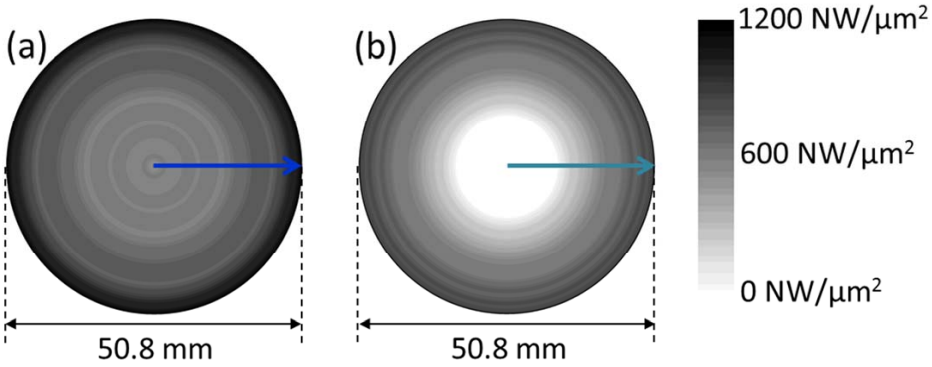

FIG. 2.12 – Representation of the GaN NW density on 2-inch Si(111) wafers heated up to (a) 785 °C and (b) 825 °C, as measured at the center of the wafer.

One can estimate that for the sample schemed in figure 2.12 (a), the temperature varies from 825 °C at the center of the wafer (given by the desorption time) to 780 °C on its periphery (obtained from figure 2.10). For the other sample, the temperature varies from 785 °C (desorption time and, consistently, figure 2.10) at the center, to about 750 °C (by extrapolation of figure 2.10) on the edge. On a 2-inch wafer, the temperature difference between the center and the periphery is therefore close to 35-45 °C, which is absolutely critical in terms of NW morphology.

It is hence possible to control, to some extent, the NW density gradient on a single growth run by simply changing the temperature measured at the center of the wafer. This procedure brings the advantage to avoid growing dozens of samples and allows to perform

density-dependent measurements on a given sample, free of other possible fluctuation between growth runs, and will reveal its full usefulness in chapter 5.

2.2.5 GaN nanowire length and diameter versus temperature

In order to observe the variation as well as the dispersion of GaN NW length and diameter in function of the growth temperature, two new samples were grown: sample A consists in GaN NWs grown during 3 hours with a Ga/N ratio equal to 0.3; sample B was grown under similar conditions but the deposition was interrupted after 20 minutes in order to obtain statistics on GaN NW precursors. Based on top and cross-sectional view SEM images, figure 2.13 illustrates the evolution of the NW density along the wafer radius of sample A, together with the corresponding NW length variation.

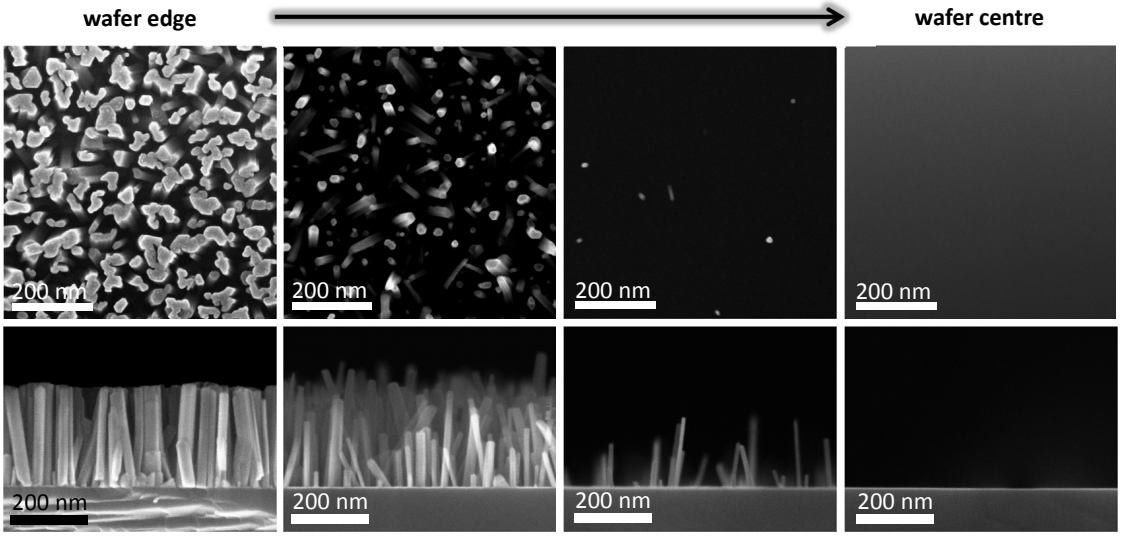

FIG. 2.13 – Top- and cross-sectional-view SEM images illustrating the evolution of the NW density and of the corresponding NW length variation along the wafer radius of sample A.

Relying on data displayed in figure 2.10, NW densities at different point along the wafer radius were "translated" into a local surface temperatures. Figure 2.14 (a) then presents the evolution of the mean NW length (circles) and of its dispersion from NW to NW (squares) as a function of this temperature. It can be seen that GaN NW mean length remains more or less constant between 775 and 790 °C but drastically decreases for temperatures higher than 790 °C, consistent with the rapid increase of GaN decomposition rate in this range of temperatures [165]. Simultaneously to the diminution of the average nanocolumn length, the length dispersion between NWs increases.

Similarly, the evolution of the average GaN NW diameter on sample A versus temperature is represented by circles in figure 2.14 (b) and is compared to the mean diameter

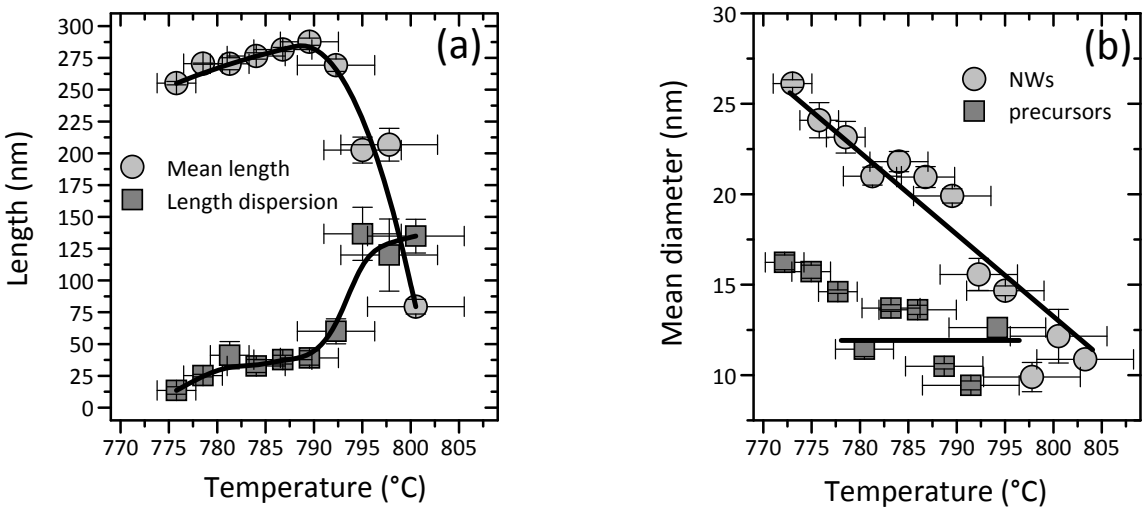

FIG. 2.14 – (a) GaN NW mean length (circles) and mean length dispersion (squares) as a function of the temperature; (b) mean diameter of GaN NWs (circles) and of GaN NW precursors (squares) in function of the temperature.

of GaN NW precursors from sample B (squares). GaN NW diameter decreases almost linearly with increasing temperature until reaching a value of about 12 nm. Interestingly, the precursor mean diameter seems to remain constant around the same value of 12 nm. Only at the lowest temperatures, their diameter is slightly larger, around 15 nm. Such a constant diameter suggests that precursors reach a critical size before turning into NWs, consistent with data reported by Consonni and co-workers [166]. The independence of their diameter on the temperature also indicates that this critical size is not governed by nucleation kinetics. It was besides recently shown that such GaN NW precursors undergo a shape transition from spherical caps nuclei to vertical-wall precursors without introduction of any dislocation at the interface between GaN and the amorphous Si_xN_y layer present on the Si(111) surface [166]. Note that, in the case of GaN NWs grown on an AlN buffer on silicon, misfit dislocations were identified at the interface GaN/AlN [73, 76]. In this case, GaN NW precursors are hence plastically relaxed. Anyway in both cases, the shape transition of GaN primary nuclei towards vertical-wall precursors likely signs the start of the vertical/axial GaN incorporation.

In order to foster these hypotheses and the interpretation of the above-described morphological observations, one now needs to go deeper into the comprehension of GaN NW nucleation, which is precisely the scope of the next chapter.

2.3 Conclusion of the chapter

In this chapter, we have introduced silicon substrates assets and temperature calibration. We have seen that relying on the Ga desorption rate dependence on the temperature, we have a powerful method for a direct estimation of the substrate temperature. In the second part of the chapter, we have presented GaN NWs. We have seen that in MBE, mainly two types of growth are performed on silicon: it is either initiated on bare Si(111) or on Si(111) covered with a thin intermediate layer. Morphologically, the thin AlN buffer improves NW straightness and in-plane orientation but its nearly insulating character makes its use inconvenient for device applications. Hence our attention focused on NWs grown on bare silicon and to the control of NW morphology through the tuning of the growth conditions. We have observed that the higher temperatures, which allow to well-separate the NWs, also bring large inhomogeneities from NW to NW. Regarding devices or more generally applications, this lack of homogeneity is a substantial issue. An alternative solution for the control of NW positioning, size and density consists in utilizing patterned substrates. This procedure, known as "selective area growth" (SAG), is one of the prospects currently investigated within our group. Preliminary results on SAG of GaN NWs on silicon are presented in appendix B. Meanwhile, in order to foster the understanding of self-assembled GaN NW morphology dependence on the growth conditions, chapter 3 will focus on NW nucleation, that is, the processes occurring at the very first stages of GaN NW growth.

3

Nucleation of self-assembled GaN nanowires

Since the first reports on their growth, GaN nanowires have been widely investigated. Although their main properties are now deeply understood, it is not the case of processes at the origin of their nucleation. This chapter therefore aims at fostering the understanding of GaN nanowire nucleation in plasma-assisted molecular beam epitaxy. After exposing a brief state of the art of GaN nanowire nucleation, we will go through the different steps of GaN nanowire formation both on bare Si(111) and on an AlN buffer deposited on Si(111).

Contents

3.1 State of the art 55

3.2 Experimental details 56

3.3 Nitridation of the Si surface 56

3.4 Dynamics of GaN nanowire nucleation 58

3.4.1 GaN nanowire nucleation on bare Si(111) 58

3.4.2 GaN nanowire nucleation with an AlN buffer on Si(111) 61

3.4.3 GaN nanowire nucleation on Ga-covered Si(111) 62

3.5 Amorphization of the crystalline β-Si_3N_4 phase 64

3.5.1 Species responsible of β-Si_3N_4 amorphization 64

3.5.2 β-Si_3N_4 amorphization dependence on substrate temperature . 66
3.5.3 Limitation of the RHEED study in the understanding of the amorphization process 67
3.6 GaN nanowire nucleation dynamics 67
3.6.1 GaN nanowires nucleation dynamics on AlN/Si(111) 68
3.6.2 GaN nanowires nucleation dynamics on nitrided Si(111) 70
3.6.3 Comparison of the delay on AlN buffer and on bare Silicon . . 70
3.7 Discussion and conclusion of the chapter 72

3.1 State of the art

As we have seen in chapter 2, GaN NW growth by PAMBE was reported for the first time in 1997 on sapphire [20] and in 1998 on silicon [21]. The main originality of these NWs resides in their growth mode which is free of catalyst, induced by diffusion processes combined to a difference of incorporation rates between the NW side-walls and their top surface [60, 61, 66]. Density, aspect ratio (length/diameter) and variation of aspect ratio from NW to NW can be tuned by adjusting both the substrate temperature and the III/N ratio, which should nevertheless not exceed 1 [41, 46, 167]. Furthermore, GaN NWs may either be grown on bare Si(111) or on top of a thin AlN buffer layer. In the former case, it was shown that a thin amorphous Si_xN_y layer forms between GaN and the Si [44, 49, 70, 151] surface resulting in a large proportion of tilted and twisted NWs. On the other hand, the use of a thin intermediate AlN buffer clearly improves NW straightness and in-plane orientation [65, 68, 70]. However, as far as devices are concerned, it is better to avoid using AlN because of its nearly insulating character (E_g = 6.2 eV).

The challenge is therefore now to improve GaN NW growth on bare Si(111), which requires a better understanding of their nucleation. On AlN/Si(111), the very first stages of GaN NWs growth have already been the center of several studies. It was for instance shown by Songmuang *et al.* that GaN first forms into islands which act as seeds for the wires [65]. Then, focusing on the dynamics of GaN NW formation on AlN/Si(111), Landré and co-workers evidenced three regimes in the growth process: a delay at nucleation, the origin of which was uncertain; a supra-linear regime corresponding to the precursor formation and their 2-dimentional ripening; and finally, a linear regime in accordance with the axial elongation of the NWs [73]. The supra-linear regime was further clarified by Consonni and co-workers who reported a shape transition of GaN NW precursors from spherical caps to pyramids, the final shape transition to vertical-wall NWs being allowed by introduction of one dislocation at the GaN/AlN interface [76]. Regarding the deposition of GaN on bare Si(111), Calleja *et al.* reported in 1999 that GaN does not actually form directly on the silicon surface but on top of an intermediate amorphous silicon nitride (a-Si_xN_y) layer [49]. Chèze and co-workers later evidenced that Ga species only start to be incorporated to form GaN [79] subsequently to the a-Si_xN_y layer formation. The following year, Consonni *et al.* investigated the mechanisms of GaN NW precursor formation on top of such a-Si_xN_y/Si(111). In this case, GaN NW precursors undergo a direct shape transition from spherical caps to vertical-wall precursors without introduction of any dislocation at the interface GaN/a-Si_xN_y. The shape transition driving force was here shown to be the lower Laplace pressure of the vertical-wall precursors together with the reduction of the surface energy through the formation of c- and m-planes [166]. It was besides evidenced that GaN NW precursors only form on a-Si_xN_y after a given delay, dependent on the growth conditions (substrate temperature and Ga flux) and that can be described by the standard island nucleation theory [168].

3.2 Experimental details

Most of the investigations described in this chapter were handled in two different systems. GIXRD was performed on the IF-BM32 beamline at the ESRF during growth in an UHV chamber (INS instrument for "In-situ growth of Nanostructures on Surfaces") described in details in Refs. [169–171] and here equipped with Ga and Al Knudsen cells and a nitrogen radio-frequency (RF) plasma source. In addition, "in-house" experiments were made in the Meca2000 PAMBE system described in chapter 1 and in which growth was followed by RHEED. In both cases, Si(111) substrates were prepared with the standard degreasing procedure and dipped into a hydrofluoric acid solution (5 %) for 40 s before growth. After introduction in their respective growth chamber, substrates were deoxidised until apparition of the typical Si(111) - 7×7 surface reconstruction. Regarding experiments made on the INS instrument, silicon substrates were aligned with the X-ray beam subsequently to the heating step. Note that in this case, silicon substrates were 0.5 µm thick, cut as squares with dimension 1×1 cm^2 and fixed onto a 1×1 cm^2 hollowed molybloc with pinches. As a result, when heating them up, they sometimes tended to bow, making the alignement with X-rays difficult. Nevertheless, unless otherwise specified, the experiments were made at a typical GaN NW growth temperature estimated to be about 820 °C. X-ray diffracted intensities were then recorded with a 2D Maxipix™ detector [171]. Let us recall that indexes related to GIXRD measurements are given in the reduced Si reciprocal space units obtained by describing the Si(111) surface by a hexagonal cell with the [111] direction parallel to the surface normal (see Fig. A.3 in appendix A). RHEED indexes, on the other hand, are given in the usual cubic Si system for consistency with the literature.

3.3 Nitridation of the Si surface

In practice, before growth starts, the substrate faces the different cells as well as the N source. N plasma is then ignited with the N shutter closed. Soon after, the growth is initiated by simultaneously opening the Ga and N shutters. Yet, in a PAMBE system, it has already been evidenced that despite the presence of the closed N shutter, a leakage of nitrogen occurs [151]. Consequently, as soon as the RF plasma source is turned on, active nitrogen reaches the silicon surface and instantly modifies its structure.

Figure 3.1 shows GIXRD h-scans taken around the Si $(10\bar{1}0)$ reflection, both before and after the RF plasma ignition (respectively top and bottom lines). The X-ray beam energy was 10 201 eV (corresponding wavelength: ≈1.216 Å) and its incidence angle was below the bulk Si critical angle $\alpha_c = 0.18°$ for which the total reflection occurs. Such conditions were chosen to enhance the weak contribution of the top Si/vacuum interface with respect to that of the bulk Si substrate. Grey areas indicate the Si(111) substrate surface crystal truncation rods (CTRs). In between these main peaks, several other extrema can

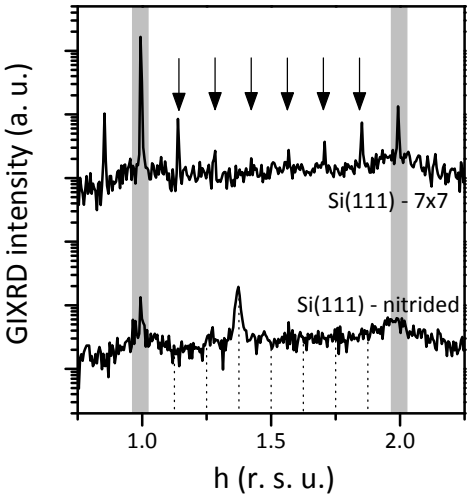

FIG. 3.1 – GIXRD h-scans spectra around the Si $(10\bar{1}0)$ reflection (given in the Si(111) hexagonal reduced cell) before (upper line) and after (bottom line) the N-plasma source was turned on. Grey zones indicate positions of the Si CTRs. Arrows and dotty lines indicate the expected positions of the 7×7 and of the 8×8 surface reconstruction-related lines, respectively.

be identified. Before the introduction of active nitrogen in the chamber (upper line), one can see, as pointed out by a series of six black arrows, peaks related to the 7×7 Si(111) surface reconstruction. Once the RF plasma is ignited and despite the closed shutter (bottom line), CTRs as well as 7×7 Si(111) surface reconstruction peaks disappear and a new peak at $h = 1.37$ (reciprocal space units) is observed.

Interestingly, a change in the RHEED pattern is also observed along the $[11\bar{2}]$ Si azimuth when turning on the RF plasma source (Fig. 3.2).

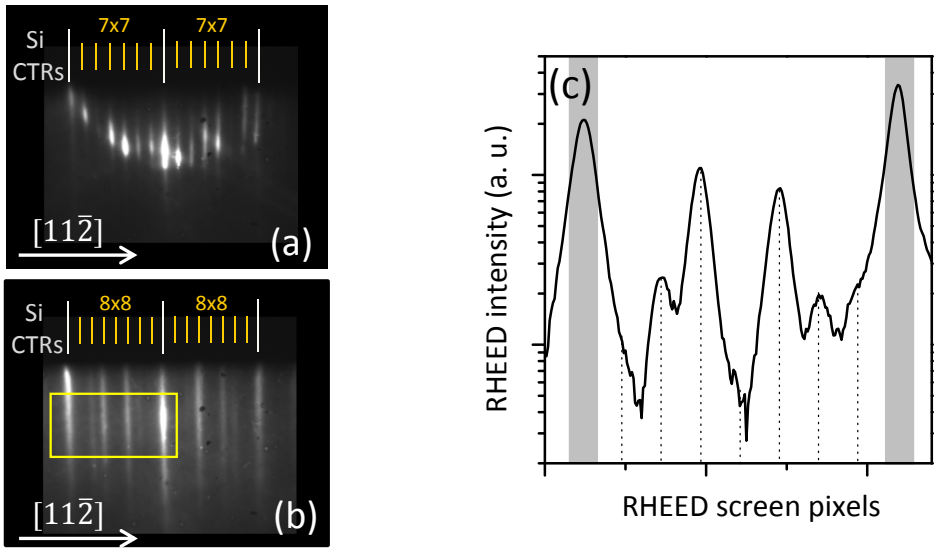

FIG. 3.2 – RHEED patterns observed along the $[11\bar{2}]$ Si azimuth (a) before and (b) after the N-plasma source is turned on, respectively displaying the typical Si(111) - 7×7 surface reconstruction and the nitrided Si(111) surface pattern. A cut view of the area delimited by the yellow box in (b) is shown in (c).

The RHEED pattern indeed evolves from the typical Si(111) - 7×7 surface reconstruction (Fig. 3.2 (a)) to the diffraction pattern displayed in figure 3.2 (b). For better clarity, a cut view of the area delimited by the rectangle in figure 3.2 (b) is reported in figure 3.2 (c).

Nitridation of Si(111) by electron-dissociated N_2 [172–174], by NH_3 [175–178], by NO [177, 179, 180] or, more recently, by a flux of atomic N generated by a RF plasma cell [181] has already been studied. In every case, it has been shown that Si(111) nitridation results in the formation of crystalline β-Si_3N_4. This β-Si_3N_4 crystal belongs to the $P6_3$ space group and presents a hexagonal structure with an in-plane lattice parameter $a_{\beta\text{-}SiN}$ = 7.61 Å [182–185], twice the length of the in-plane hexagonal Si(111) lattice parameter ($a_{Si,hex}$ = 3.84 Å). Hence a 2:1 coincidence relation exists at the interface between β-Si_3N_4 and Si(111). In addition, in the range of temperatures we are dealing with, β-Si_3N_4 has a 4 × 4 surface reconstruction, therefore reconstructs as 8 × 8 compared to the underneath bulk silicon [172, 186]. A 8/3 × 8/3 superstructure has additionally been demonstrated [177, 180], attributed by Ahn *et al.* to reorganization of the topmost N adatoms on β-Si_3N_4 [186]. In practice, the formation of β-Si_3N_4 has already been evidenced by RHEED in a PAMBE system by Wu *et al.* [187], although in their case, the surface was voluntarily exposed to active N.

In figures 3.1 and 3.2 (c), expected 8 × 8 reconstruction peak positions are indicated by dotty lines. It can be seen in the bottom GIXRD spectrum (Fig. 3.1), that the peak at h = 1.37, appearing with the supply of active nitrogen, matches the expected position of the third 8 × 8 surface reconstruction peak (h = 1.375), thus suggesting the presence of β-Si_3N_4. β-Si_3N_4 formation is also evidenced by the RHEED features that are even clearer since 4 of the nitrided Si surface peaks match those of the expected 8 × 8 surface reconstruction. In this case, note that the third peak could as well be related to the 8/3 × 8/3 superstructure. In the X-ray case, diffracted intensities are proportional to the square of the structure factor modulus. Thus, similarly to the 7 × 7 reconstruction, peaks composing the 8 × 8 reconstruction have different intensities, which may explain that they are not all visible. The better clarity of RHEED features, on the other hand, is attributed to the occurrence of strong multiple diffraction. Here, GIXRD and RHEED features appearing when turning on the RF plasma source are interpreted as the signature of the presence of β-Si_3N_4, even before the growth starts, the leakage of active N being hardly avoidable.

3.4 Dynamics of GaN nanowire nucleation

3.4.1 GaN nanowire nucleation on bare Si(111)

In order to understand to what extent the formation of β-Si_3N_4 affects GaN NW growth, h-scans around $(10\bar{1}0)$ and $(30\bar{3}0)$ reflections were recorded while exposing the

Si(111) surface to Ga and N with a III/V ratio of about 0.4 (the corresponding GaN growth rate is 0.12 ML/s). Figures 3.3 (a) and (b) show a selection of these scans, taken at different times of Ga and N deposition. In the hexagonal Si(111) reduced reciprocal lattice units, at high temperature, $(30\bar{3}0)$ reflection of relaxed GaN is expected to appear at $(3.59\ 0\ \overline{3.59}\ 0)$. For each scan, data were fitted with a pseudo-Voigt function, represented on figures 3.3 (a) and (b) as the full lines. As first sight, it seems that the β-Si_3N_4-related peak decreases and the GaN-related peak increases with the growth time going on. Note that the raise around h = 1.325 of the curve corresponding to 180 min of growth in figure 3.3 (a) is assigned to the tail of the GaN-related peak that raises at h = 1.2 simultaneously to the one at h = 3.59 in figure 3.3 (b).

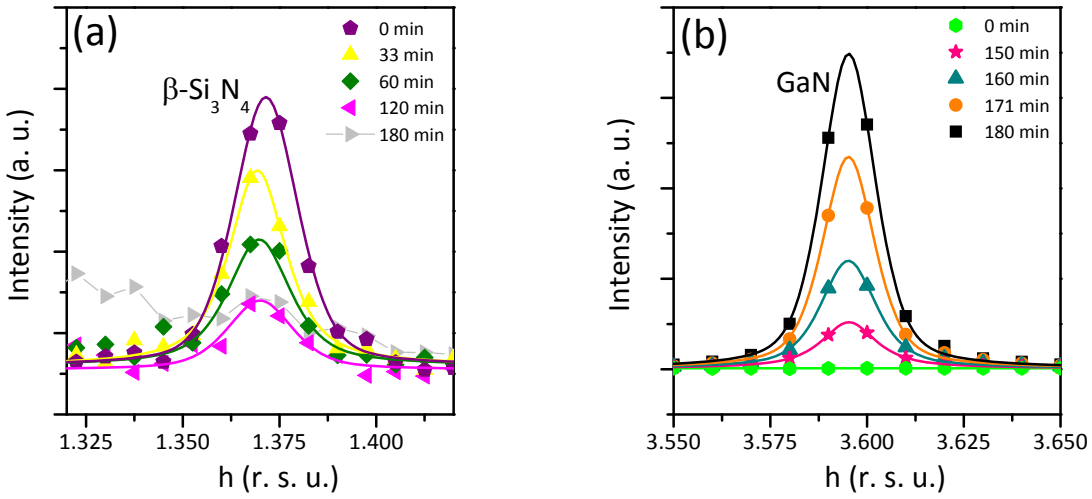

FIG. 3.3 – GIXRD h-scans taken at different times of the Ga and N deposition around (a) $(10\bar{1}0)$ and (b) $(30\bar{3}0)$ reflections.

Based on the pseudo-Voigt fits, integrated intensities of the peaks were extracted, normalized to their horizontal asymptotic value and reported in figure 3.4 (a) as a function of the growth time. Full and open circles correspond to the evolution of 8 × 8 surface reconstruction and GaN peaks, respectively. The magnitude of the β-Si_3N_4-related data being about 10 times lower than that of GaN, a close up of figure 3.4 (a) is presented in figure 3.4 (b) in order to better highlight their relative behavior.

It is important to recall that the peak at h = 1.37 is assigned to the β-Si_3N_4 surface reconstruction and not to the layer itself. The β-Si_3N_4 layer peak should indeed coincide with the 4^{th} strike of the 8 × 8 reconstruction, which is actually not observed in GIXRD nor in RHEED. The absence of $(30\bar{3}0)$ β-Si_3N_4 layer peak is however not surprising since its intensity is expected to be only 1.3 % of the intensity of its highest peak (*i.e.* $(20\bar{2}0)$). In other words, the $(30\bar{3}0)$ β-Si_3N_4 peak is at the noise level. The evolution of the peak at h = 1.37 does not provide direct information on β-Si_3N_4 behaviour but its decrease in

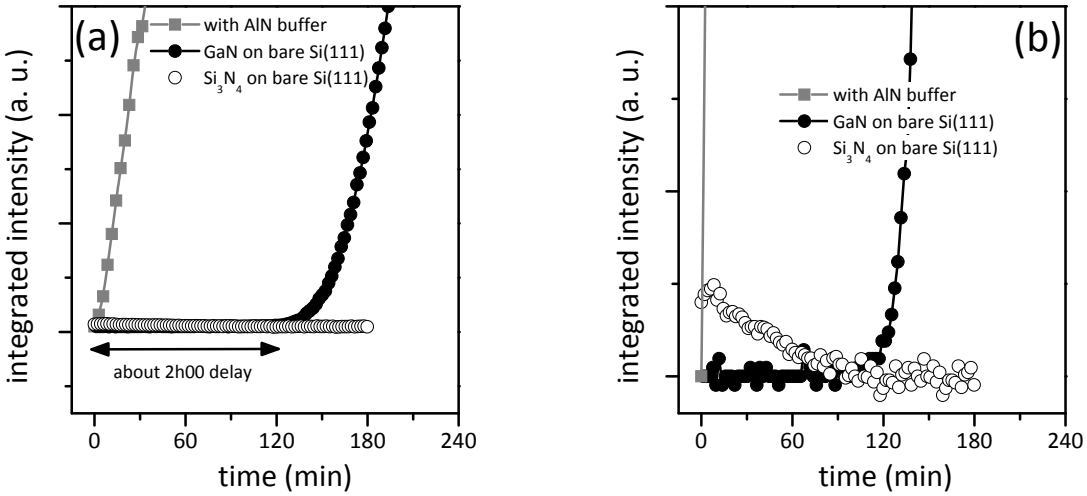

FIG. 3.4 – β-Si_3N_4 (open circle) and GaN (full circles) peaks integrated intensity evolution during deposition of Ga and N on bare Si(111). Full squares represent the evolution of the GaN peak integrated intensity when the growth is made with an AlN buffer. (b) is a close up of (a).

time shows that the 8 × 8 surface reconstruction is slowly modified when providing Ga and N species together (Fig. 3.4 (b)). More interestingly, Ga incorporation, illustrated by the increase of the peak at h = 3.59 seems to be entangled with the 8 × 8 reconstruction decline: GaN indeed only starts growing once β-Si_3N_4 reconstruction peak intensity has reached a low enough steady value. This outcome has to be correlated to high resolution transmission electron micrograph observations that exclusively report the presence of a thin (2-3 nm thick) amorphous Si_xN_y underneath the foot of the NWs [44, 49, 70, 151]. Figure 3.5 present such HRTEM image highlighting the presence of an amorphous layer between Si(111) and a GaN NW.

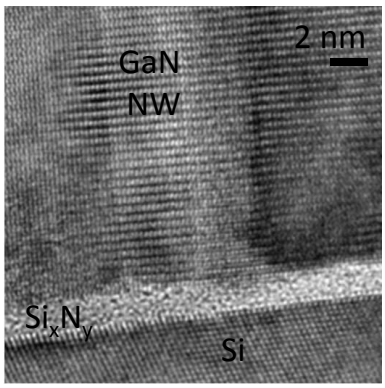

FIG. 3.5 – HRTEM image of the foot of a GaN NW grown on bare Si(111). The formation of an amorphous Si_xN_y layer is clearly visible.

Chèze and co-workers observed that a "defective crystalline layer" either composed of "disordered Si or crystalline Si_xN_y" with lattice parameter equal to 3.8 Å is amorphized before Ga starts to be incorporated [79]. In our study, we found no sign of such peri-

odicity but obtained clues of the formation of β-Si_3N_4. Present results then suggest that the decrease of the β-Si_3N_4 reconstruction peak likely reflects the amorphization of this crystalline layer which appears as a necessary step for GaN NW nucleation.

3.4.2 GaN nanowire nucleation with an AlN buffer on Si(111)

For comparison, GIXRD h-scans were also performed while growing GaN NWs in the same growth conditions, but subsequently to the deposition of a thin (2-3 nm thick) AlN buffer layer on Si(111). The energy of the X-ray beam was still 10 201 eV, the incidence angle $\alpha_i = 0.14°$, below Si and AlN critical angles (respectively 0.18 and 0.21°). To synthesize this AlN buffer, Al was deposited during 10 s on the Si(111) surface before the active nitrogen was ignited. In such a way, because of the slow Al desorption at 820 °C, the silicon surface remained protected while the plasma source was being turned on. Then, active nitrogen was provided, leading to an immediate formation of AlN. Interestingly, the peak at h = 1.37 appeared during this exposition of the Al-covered Si surface to nitrogen, but vanished after the next 10 seconds deposition of AlN. Al and N were alternately provided during 3 further cycles of 10 s each. The peak at h = 1.37 was no more observed. This is shown in figure 3.6.

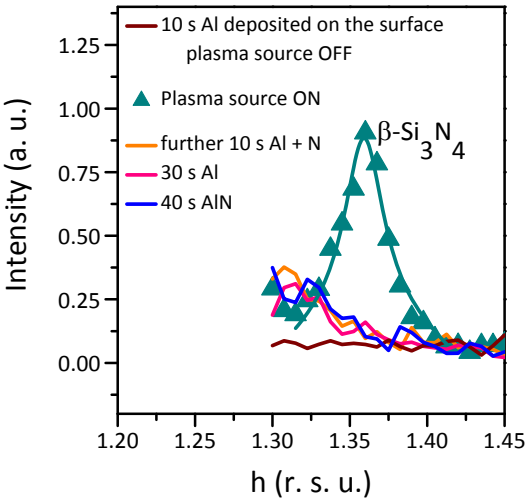

FIG. 3.6 – GIXRD h-scans taken at different stages of the AlN buffer formation around the $(10\bar{1}0)$ reflection. First, while the N plasma source has not yet been turned on, 10 seconds of Al are deposited on the surface: no β-Si_3N_4 peak is observed; then, the plasma source is turned on and even while keeping the N shutter closed, the β-Si_3N_4 peak appears; providing 10 more seconds of Al led to the disappearance of the β-Si_3N_4 peak; when further supplying N and Al alternatively, it was not recovered.

The peak intensity of GaN deposited on this AlN buffer layer is reported as a function of growth time by full squares in figures 3.4 (a) and (b). In this case, β-Si_3N_4 reconstruction peak evolution is intentionally not represented since it disappeared while making the AlN buffer itself. More interestingly, it can be seen that GaN nucleates much more quickly when using an AlN buffer layer than on bare Si, where the presence of β-Si_3N_4 has been evidenced. Although the grainy structure of the AlN buffer may act as a trap for Ga adatoms, thus favoring its incorporation, the difference in the start of nucleation appears too large (about 2 hours) to be only explained by a discrepancy of Ga diffusion on AlN

buffer and on bare Si(111) considering the high substrate temperature (820 ℃) at which we are working. The additional delay for GaN NW growth on bare Si(111) rather appears as the period during which amorphization of crystalline β-Si_3N_4 occurs, emphasizing the necessity of such process for subsequent Ga incorporation.

3.4.3 GaN nanowire nucleation on Ga-covered Si(111)

Similarly to the latter case, an attempt was made to cover the Si(111) surface with Ga before turning on the plasma source in order to protect this one from nitridation. Contrary to Al, at 820 ℃, Ga has a high desorption rate on Si(111) (see chapter 2). Therefore, in order to keep the surface covered with Ga during N plasma ignition, it was necessary to leave the Ga shutter open, that is to expose the Si(111) surface to a continuous Ga flux during the whole procedure. The substrate temperature was kept the same as before (820 ℃) and the Ga flux used here is still equal to 0.12 ML/s.

Figure 3.7 presents GIXRD h-scan around the $(10\bar{1}0)$ Si(111) reflection both before (upper line) and after (middle line) the surface coverage with Ga. The incidence angle of the X-ray beam was this time set to $\alpha_i = 0.16°$. Similarly to figure 3.1, grey areas indicate Si(111) CTRs and arrows point at the Si(111) - 7×7 surface reconstruction peaks. Here, it can be seen that when opening the Ga shutter, the Si(111) - 7×7 surface reconstruction (upper line) disappears (middle line), consistent with what is observed in RHEED when covering the Si(111) surface with Ga (see chapter 2). Despite this Ga coverage, when turning on the plasma source while keeping the N shutter closed, the peak at h = 1.37 nevertheless appeared (bottom line), indicating that the N adatoms must have diffused through the Ga coverage to form β-Si_3N_4. The strong inertness of Ga atoms with respect to silicon nitride formation is an interesting observation and will be discussed in the next section.

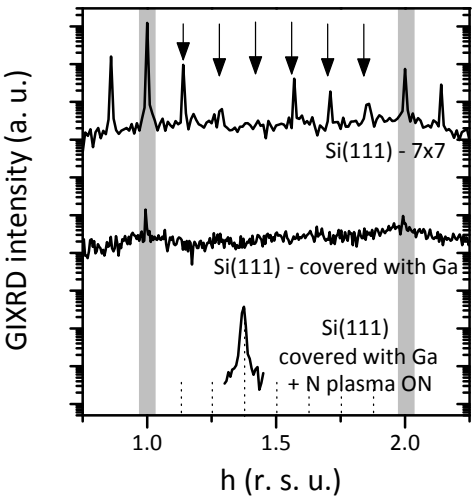

FIG. 3.7 – GIXRD h-scan around the $(10\bar{1}0)$ reflection before the Si coverage with Ga (upper line), after the Si coverage with Ga (middle line) and after turning on the N plasma source while Si(111) was still covered with Ga (bottom line). The energy of the X-Ray beam was 10 201 eV and its incidence angle $\alpha_i = 0.16°$.

Figure 3.8 presents the evolution of the peak at h = 1.37 and of the GaN peak intensities (respectively open and full rhombi) once the N shutter was opened (the Ga shutter was naturally left opened). Note that, in this case, the $(20\bar{2}0)$ GaN reflection was monitored instead of the $(30\bar{3}0)$ but the evolution of the peak integrated intensities can nevertheless be compared to that displayed in figure 3.4.

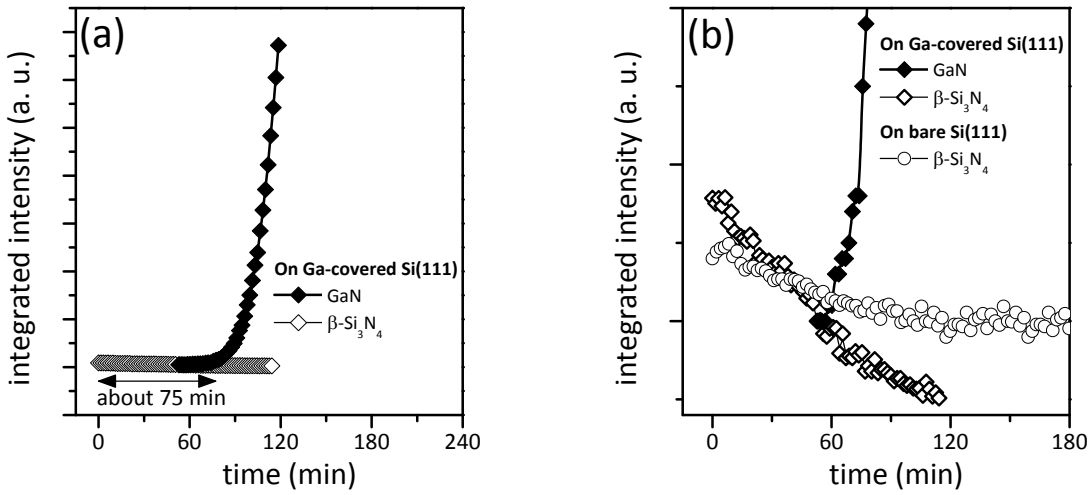

FIG. 3.8 – (a) GaN (full rhombi) and β-Si_3N_4 (open rhombi) integrated intensities evolution with Ga and N deposition time on Ga-covered Si(111) surface. (b) Close up of (a) on which the evolution of β-Si_3N_4 integrated intensity on bare silicon has been added (open circles), taken from figure 3.4

When comparing figure 3.8 (a) to figure 3.4 (a), it can be seen that the delay in the start of nucleation is now reduced of about 45 minutes (75 minutes versus 120 minutes). On figure 3.8 (b), which represents a close up of figure 3.8 (a), the integrated intensity of the β-Si_3N_4 peak on bare Si(111) has been added (open circles). The decay of the β-Si_3N_4 peak on Ga-covered Si seems to be slightly faster than on bare Si. Therefore, although the peak at h = 1.37 is observed, it is possible that the Ga coverage somewhat prevents crystalline β-Si_3N_4 to form on the whole Si(111) surface, thus explaining its faster amorphization and the reduced delay at nucleation. This hypothesis raises the question of the "shape" of the β-Si_3N_4 layer. Is it exactly an amorphous "layer" or is it constituted of sparse disordered crystallites? Does β-Si_3N_4 only partially cover the Si surface? In what concerns the amorphous Si_xN_y underneath GaN NWs, HRTEM images rather suggest a thin continuous film. Regarding crystalline β-Si_3N_4, we could not observe it so far, either because it may be too thin or because it may be unstable when taken out of the growth chamber. In this context, the aim of the next sections will be devoted to a better understanding of the β-Si_3N_4 formation and amorphization.

3.5 Amorphization of the crystalline β-Si_3N_4 phase

3.5.1 Species responsible of β-Si_3N_4 amorphization

Complementary RHEED experiments were performed in-house to further investigate the process of β-Si_3N_4 amorphization. Figure 3.9 shows RHEED pattern lines intensity related to β-Si_3N_4, monitored while operating Ga, Al, and N shutters.

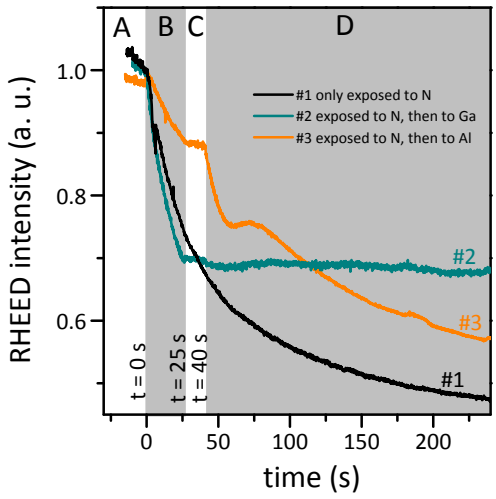

FIG. 3.9 – Evolution of the β-Si_3N_4-related RHEED lines while exposing nitrided Si(111) to N, Ga and Al. Table 3.1 summarizes the "history" of each sample.

In every case, when transients recording were started, the plasma source was already turned on, but the N shutter still closed (zone A). The N shutter was always opened at time t = 0 s, zone B corresponds to direct exposure of the Si(111) surface to active N. For sample #1, the surface was only further exposed to N (zones C and D). On the other hand, for sample #2 and sample #3, the plasma was turned off at t = 25 s and the two surfaces were left under N_2 for 15 s (zone C). Then, at t = 40 s, the surface of sample #2 was exposed to a Ga flux while the surface of sample #3 was exposed to an Al flux (zone D). This is summarized in table 3.1.

	Sample #1	Sample #2	Sample #3
t < 0 s	N plasma source already turned on, but N shutter closed		
at t = 0 s	N shutter opened: surface exposed to N		
at t = 25 s	surface left under exposure to N	N plasma source turned off	
at t = 40 s		surface exposed to Ga	surface exposed to Al

TABLE 3.1 – Summary of the actions performed on each of the sample whose RHEED pattern intensity was followed in figure 3.9.

In both cases, metallic fluxes correspond to an equivalent growth rate of 0.2 ML/s.

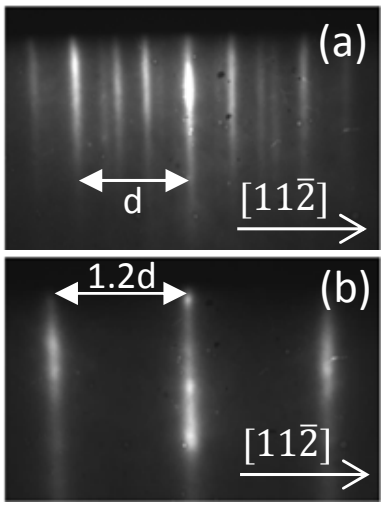

FIG. 3.10 – Nitrided Si(111) RHEED pattern (a) before and (b) after the nitrided surface is exposed to Al.

From these results, it can be seen that the presence of active N induces a decrease of the β-Si_3N_4 lines intensity, either slightly when the N shutter is still closed (zone A) or more strongly when it is opened (zone B). Interestingly, this decrease is instantaneously aborted with the turning off of the plasma (zone C). Finally, while Ga seems to have no effect on β-Si_3N_4, exposition to Al leads to a drop of the RHEED intensity. It must besides be pointed out that the slight rise up of the RHEED intensity at t = 75 s was accompanied by a clear signature of AlN formation. As a matter of fact, the RHEED changed from the diagram represented in figure 3.10 (a) to that represented in figure 3.10 (b). It can be seen that intense lines appearing with the exposition to Al have a 1.2 times higher periodicity than the Si CTR ones, consistent with the ratio a_{Si}^{hex}/a_{AlN}. Then, the general evolution of the β-Si_3N_4 reconstruction line when the surface was exposed to Al may be interpreted as the formation of AlN to the detriment of silicon nitride, followed by the coverage of this AlN by Al atoms in excess.

Regarding the drastically different behaviour of Ga and Al with β-Si_3N_4, let us note that in the literature, the favourable formation of a given compound is often justified by the lower energy per bound of the molecules it is composed of. Our case is somewhat more complex. GaN molecule energy per bound is 2.2 eV [188], lower than that of β-Si_3N_4 (4.5 eV [70]), which is consistent with such explanation. On the other hand, it is rebutted by the formation of AlN to the expense of β-Si_3N_4 since AlN energy per bound is 2.5 eV [188], lower than that of β-Si_3N_4. Reasons why β-Si_3N_4 forms to the expense of GaN and AlN forms to the expense of β-Si_3N_4 remain unclear and constitute one of the issues raised by this study. Nevertheless, a similar behavior has already been observed in ammonia-MBE by Nikishin *et al.* [189] and by Vézian and coworkers [190]. When exposed to Al atoms, β-Si_3N_4 is depleted by Al atoms to form AlN, explained by a thermodynamically favorable AlN formation versus SiN [191]. Moreover, Ga was found to be innocuous to β-Si_3N_4, consistent with our observations. From these results it can besides be understood that when growing GaN NWs on bare Si(111), nitrogen species are the only

responsible for β-Si_3N_4 amorphization. On the one hand, such amorphization is attributed by Chèze *et al.* to a roughening of the crystal [192] or a change in composition [193] induced by the low N adatom mobility [79]. On the other hand, β-Si_3N_4 is found to be sensitive, to some extent, to ion bombardment [194]. In our PAMBE system, despite the presence of deflection plates, part of N^+ ions generated together with the active N may anyway reach the surface and then play a role in the amorphization process.

3.5.2 β-Si_3N_4 amorphization dependence on substrate temperature

It is natural to wonder to what extent the nitridation process and the β-Si_3N_4 amorphization depend on the substrate temperature. In order to address this issue, the nitridation transient was monitored at different substrate temperatures, namely 770 ℃, 820 ℃, and 850 ℃. Similarly to what was previously done, the 8 × 8 reconstruction RHEED lines intensity was recorded while exposing the Si(111) surface to active N at these three temperatures. At time t = 0 s, the N shutter was opened, leading to a decrease of the β-Si_3N_4 lines intensity, similarly to what was observed for sample #1 in figure 3.9.

In order to properly compare the obtained transients, data required some processing. As a matter of fact, the recorded RHEED intensity depends both on the RHEED parameters adjustments and on the box drawn for the monitoring of the intensity on the RHEED screen, which are not entirely reproducible from experiment to experiment[1]. This slight lack of precision in the RHEED settings induces a discrepancy between the raw recorded intensities. However, the decreasing part of the curves could be well fitted with a double exponential decay function expressed as

$$I(t) = I_0 + A_1 e^{-t/t_1} + A_2 e^{-t/t_2} \tag{3.1}$$

Therefore, based on the fits, the noise level I_0 was determined for each set of raw data and subtracted from them. Finally, the curves were additionally normalized to the value of the intensity at t = 0 s. Figure 3.11 shows the processed curves, obtained at the three different substrate temperatures. The similarity of their decay dynamics suggests that a potential temperature effect on the amorphization process is negligible.

Although in the range of temperatures investigated, the temperature does not play a role in the nitridation process and the amorphization, other parameters may do. For instance, settings of the plasma cell such as the power of the RF source or the N flux. However in the whole studies described in this thesis, the same N plasma source settings were used, namely a power of 300 W and a N_2 flow of 0.6 sccm leading to an effective active N equivalent flux of about 0.3 ML/s on the surface. The investigation of the effects

[1]Note that this is also the reason why in figure 3.9, transients related to samples #1, #2 and #3 do not superimpose.

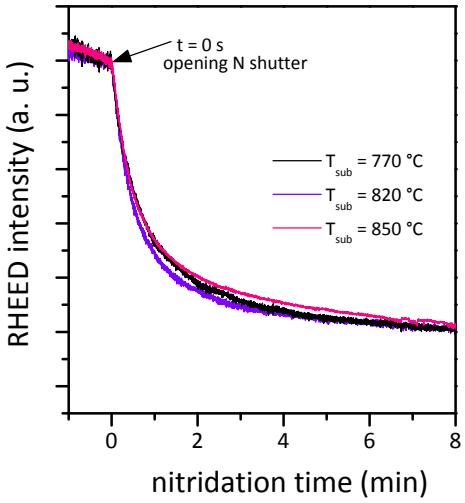

FIG. 3.11 – Evolution of RHEED line intensities during exposure of the Si(111) surface to nitrogen, at three different substrate temperatures (770 °C, 820 °C, and 850 °C)

of these parameters on the Si(111) surface nitridation goes beyond our study but such work can be found in Ref. [195] for instance.

3.5.3 Limitation of the RHEED study in the understanding of the amorphization process

The limitation of this RHEED experiment is that it was performed with N species only and it therefore does not tell us if the same happens when providing Ga and N species together. When the two species are delivered together, it is indeed possible, as suggested in section 3.4.3 that Ga are not fully inert but somehow prevent the nitridation-amorphization processes. Unfortunately, it is impossible to verify such hypothesis with RHEED since, as shown in figure 3.12 (c), when providing Ga and N together, the RHEED screen becomes blurry and the β-Si_3N_4 related intensity can not be followed anymore. On the other hand, the start of GaN NW nucleation is detectable by the transformation of this blurry RHEED pattern into a spotty one (Fig. 3.12 (d) and (e)).

3.6 GaN nanowire nucleation dynamics

As we have seen, amorphization of β-Si_3N_4 is a necessary step in the start of GaN growth and the dynamics of this amorphization does not depend on the substrate temperature (Fig. 3.11). However, the start of GaN NW nucleation may. Our study then now focuses on the role of the substrate temperature and of the Ga flux in the nucleation delay, independently from the nitridation process.

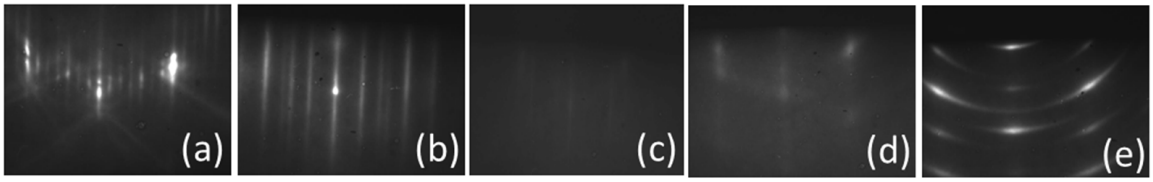

FIG. 3.12 – RHEED patterns observed along the [11$\bar{2}$] azimuth during the various steps of the growth: (a) typical 7 × 7 Si(111) surface reconstruction forming before the growth start, (b) 8 × 8 nitrided Si(111) reconstruction appearing when the N plasma source is on, (c) blurry pattern observed once Ga and N shutters are opened, (d) after few minutes, apparition of the spots related to GaN NW, indicating the start of their formation, and (e) as the growth proceeds, the spots become more distinguishable.

3.6.1 GaN nanowires nucleation dynamics on AlN/Si(111)

When using an AlN buffer, the dependence of the nucleation start on the Ga flux has already been investigated by Landré and co-workers and reported in Ref. [73]. In the INS instrument of BM32 at ESRF, they observed that the delay at nucleation increases with decreasing Ga flux. In the Meca2000 PAMBE, it is also possible to determine the nucleation start by detecting the apparition of GaN NW related spots with the RHEED. Typically, when providing Ga and N, the streaky AlN RHEED pattern (Fig. 3.13 (a)) changes to a spotty one (Fig. 3.13 (b)).

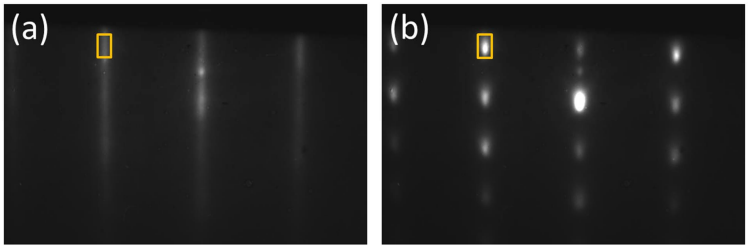

FIG. 3.13 – (a) AlN buffer RHEED pattern along the [11$\bar{2}$] azimuth, changing to (b) spotty GaN NW RHEED pattern when providing Ga and N species.

By taking advantage of the faculty to vaporize GaN at temperatures around 850 °C, it is possible to make several nucleation measurements on the same substrate. Hence, our experiment was handled as followed: GaN NW were nucleated in order to identify the zones of the RHEED pattern where the spots appear. These zones were then selected (rectangles in figures 3.13 (a) and (b)) in order to only follow the evolution of their intensity. Once the NW spots were intense enough, the substrate temperature was increased to vaporize GaN until the clean AlN buffer RHEED pattern could be observed again (Fig. 3.13 (a)). Note that, as the vaporization temperature of AlN is much higher than that of GaN, the buffer was not affected by the vaporization the NW precursors. On such clean surface, GaN NWs

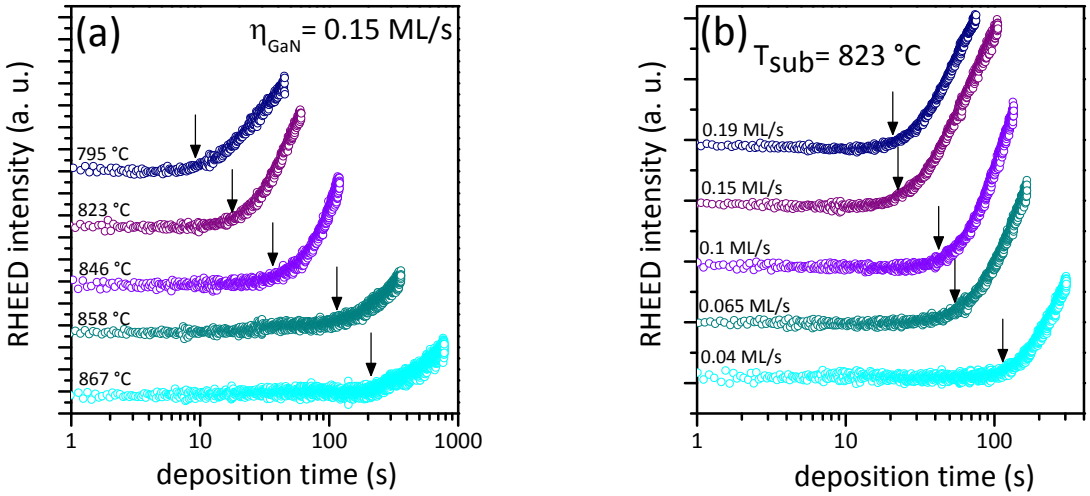

FIG. 3.14 – Evolution in time of the GaN NW related RHEED spots when providing Ga and N on an AlN buffer for different (a) substrate temperatures at constant Ga flux and (b) Ga fluxes at constant substrate temperature.

could be nucleated once more and the intensity of their related spots monitored. Several cycles of nucleation-vaporization could then be made on the same substrate, bringing the advantage of an excellent growth conditions reproducibility.

Two series of nucleation measurements were then made. First, the intensity of the spots was recorded for different substrate temperatures keeping the Ga flux constant at 0.15 ML/s (Fig. 3.14 (a)) and then at different Ga fluxes, keeping the substrate temperature constant at 823 ℃ (Fig. 3.14 (b)). The recorded spot intensities always present the same behaviour. In a first stage going from time t = 0 s (opening of the Ga and N shutters) to time t_{nucl} (black arrows), the intensity is rather constant. From time t_{nucl}, it starts to strongly increase. This inflexion point t_{nucl} is considered as the beginning of the nucleation. One can now see that t_{nucl} increases with the substrate temperature and with the decrease of the Ga flux, consistent with the observations of Landré and co-workers [73]. This supports the hypothesis of a kinetic model where the nucleation is driven by the probabilities for adatoms to meet on the surface and to form a stable precursor. When diminishing the Ga flux, less adatoms participate, which induce a lower "meeting" rate. Similarly, when increasing the substrate temperature, more Ga atoms desorb and the remaining Ga adatoms on the surface have more energy to diffuse making it more difficult to build a stable precursor.

3.6.2 GaN nanowires nucleation dynamics on nitrided Si(111)

Similar measurements were made on bare Si(111). To be more precise, as it is not possible to "denitride" the Si(111) surface and as we wanted to perform all the measurements on the same sample, the Si(111) surface was first nitrided for about 10 minutes. Transients were hence acquired on amorphized β-Si_3N_4, similarly as it was done in Ref. [168]. Figures 3.15 (a) and (b) respectively present the transients obtained for different values of the Ga flux and for different values of the substrate temperature. Similarly to the nucleation on an AlN buffer, it can be seen that the delay in the nucleation start decreases with increasing substrate temperature and increasing Ga flux.

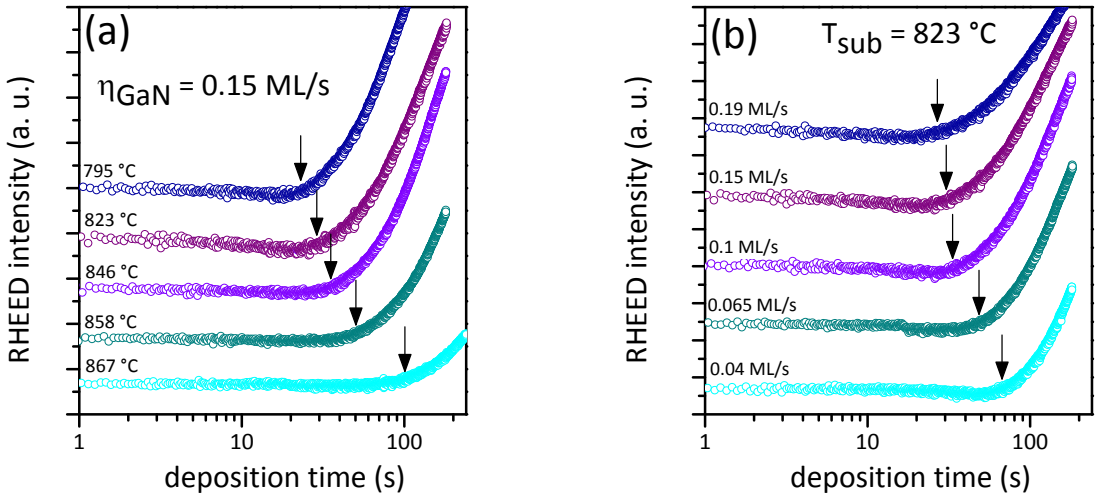

FIG. 3.15 – Evolution in time of the GaN NW related RHEED spots when providing Ga and N on nitrided Si(111) for different (a) substrate temperatures at constant Ga flux and (b) Ga fluxes at constant substrate temperature.

3.6.3 Comparison of the delay on AlN buffer and on bare Silicon

The evolution of t_{nucl} for the nucleation of GaN on AlN/Si(111) (hexagons) and on nitrided Si(111) (circles) in function of the substrate temperature and of the Ga flux are respectively displayed in figures 3.16 (a) and (b). At first sight, it seems that in the range of probed substrate temperatures and Ga fluxes, the time required for nucleation is of the same order on nitrided Si(111) and on AlN/Si(111), although the sensitivity to Ga fluxes and substrate temperature changes may be slightly stronger in the AlN/Si(111) case. Such difference may be explained by a difference of roughness of the two types of surfaces.

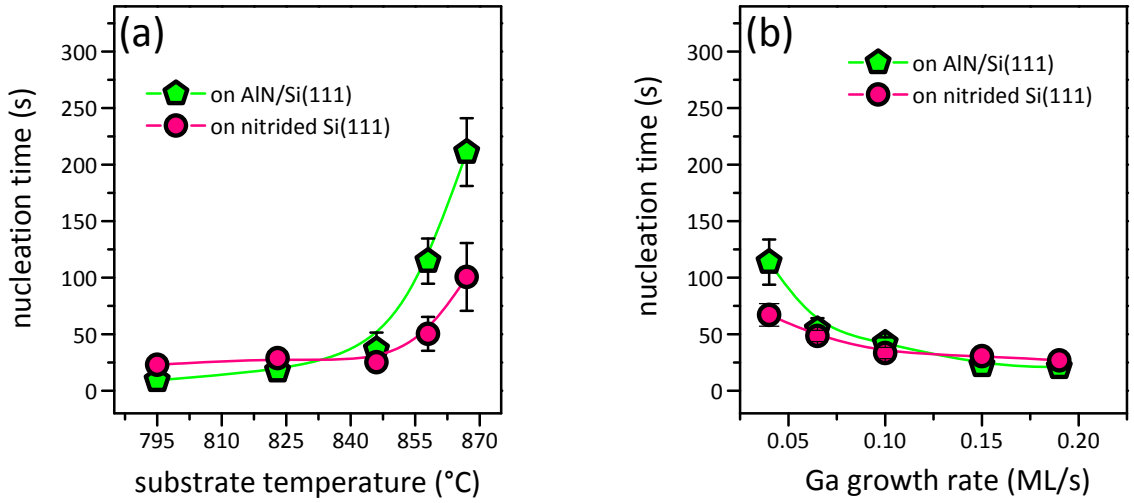

FIG. 3.16 – Evolution of t_{nucl} (a) at different temperatures and (b) for different Ga fluxes.

Now, let us recall that in the case of nitrided Si(111), an additional delay at nucleation must be taken into account. This additional delay is the time necessary for the β-Si_3N_4 to form and to be amorphized and it is possible to evaluate it. As we already described it, as long as the plasma source is off, the typical Si(111) - 7 × 7 is observed by RHEED (Fig. 3.17 (a)). As soon as the plasma source is turned on, the 7×7 surface reconstruction evolves toward a 8 × 8 surface reconstruction signing the formation of β-Si_3N_4 (Fig. 3.17 (b)). With the N shutter open all along the experiment, we then monitored the evolution of both the RHEED 8 × 8 and 7 × 7 surface reconstruction intensities (respectively violet and orange lines) while turning the plasma source on (Fig. 3.17 (c)). Between time t = 0 s and t = 42 s, the plasma is off and both the intensities of the 7 × 7 and the 8 × 8 are constant. Transients in figure 3.17 (c) have been normalized to this steady value. From time t = 42 s, the N plasma source is on (N shutter naturally still open) and we can see that while the intensity of the 7 × 7 decreases, the 8 × 8 first increases until a maximal intensity reached at time t = 57 s and then decreases. The increasing part between 42 and 57 s is interpreted as a period during which β-Si_3N_4 forms. At time t = 57 s, the amorphization process starts.

From these observations, one can evaluate the β-Si_3N_4 formation to about 15 s in the Meca2000 PAMBE we used. The amorphization time is more complex to evaluate. To do so, we considered the tangents of the decreasing part of the 8 × 8 related line at time t = 57 s and at t = ∞. These two tangents cross at t = 106 s, which is considered at the time when β-Si_3N_4 is sufficiently amorphized for GaN to start to be incorporated. It follows that the amorphization time is about 49 s. Then, the total time necessary for β-Si_3N_4 to form and be amorphized from the moment the plasma source is turned on is about 64 s. In other words, one can consider that on figure 3.16, the nucleation delay on bare Si(111) is

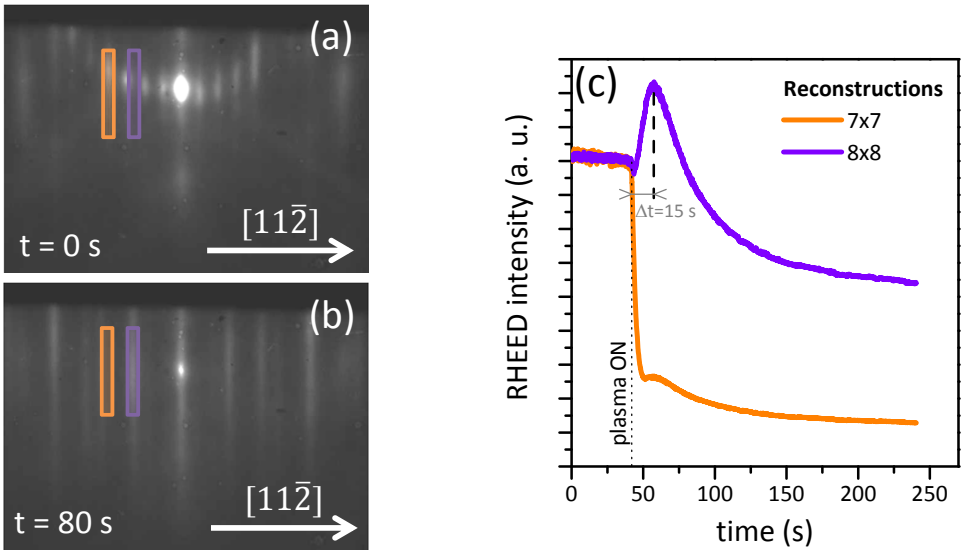

FIG. 3.17 – Si(111) - 7×7 (a) and 8×8 (b) RHEED patterns respectively observed before and after the N plasma source is turned on. By following their respective intensity (c), one can evaluate the β-Si_3N_4 formation time to about 15 s.

obtained by adding about one minute to the values of nucleation times on nitrided Si(111).

However, as we already mentioned it, the time evaluation was here made with N only, without providing Ga. In consequence, one must be careful and take the above-given values with caution. When growing NWs, both Ga and N are supplied together. It is therefore possible, as suggested by the results exposed in section 3.4.3, that Ga adatoms are not fully inert to the β-Si_3N_4 formation - nitridation processes and either catalyze or prevent the reaction.

3.7 Discussion and conclusion of the chapter

In this chapter, using a combination of *in situ* GIXRD and RHEED analyses, we have studied and compared the nucleation of GaN NWs on bare Si(111) and on AlN/Si(111). We have shown that in the case of bare Si(111), an unavoidable β-Si_3N_4 crystalline layer forms and must subsequently be amorphized to allow GaN NW to nucleate. Delays at nucleation are comparable on amorphized β-Si_3N_4 and AlN/Si(111) but because of the additional time necessary for the amorphization of β-Si_3N_4, the nucleation delay on bare Si(111) is larger than on AlN/Si(111). Nevertheless in both cases, the nucleation time increases with increasing substrate temperature and decreasing Ga flux.

Regarding the case of GaN NWs grown on bare Si(111), the increase of the nucleation time with the substrate temperature clarifies results obtained in chapter 2. In figure 2.14 (b), we indeed observed that the mean GaN NW diameter linearly decreases

with increasing temperature down to 12 nm. In parallel, the mean GaN NW precursors diameter is constant around this very same value of 12 nm in nearly the whole range of temperatures. We hence deduced that GaN precursors have to reach a critical size before turning into NWs [73, 76, 77]. Present results on nucleation show that the precursor nucleation process is governed by the substrate temperature and the Ga flux, which implies that the time necessary for the start of the GaN precursor growth increases with increasing temperature. It hence follows that the time required for the precursor critical size to be reached also increases with the substrate temperature. In other words, the start of GaN vertical/axial incorporation is delayed at the highest temperatures, which partly justifies the observed decrease of GaN NW length with temperature in figure 2.14 (a). Moreover, a recent report [196] establishes that once initiated, the axial growth rate is not constant in time but depends on the NW length itself. In fact, the authors showed that GaN axial incorporation is faster in the first stages of the column elongation in reason of a large contribution of Ga adatoms diffusing from the substrate. This substrate diffusion contribution vanishes above a certain NW height, leading to a reduced axial growth rate only determined by the directly impinging atoms and diffusion from the higher part of the NW side-walls [196]. This qualitatively supports the hypothesis that at low temperature, all precursor islands are almost simultaneously formed and reach the critical size for plastic relaxation at the same time giving place to the growth of NWs with the same length. On the contrary, at high temperature, the decrease in nucleation probabilities and the drastic increase in GaN dissociation rate both lead to a marked increase of the time laps between the formation of the first precursor having reached its critical size and the formation of the last one. The onset of GaN vertical/axial incorporation is then significantly scattered, reflecting the time duration of the precursor nucleation process and leading to the growth of wires with different lengths. This difference in length at a given time of the NW growth leads to a disparity of the local growth rate on top of each NW, which accentuates the observed NW length dispersion at the end of growth.

One issue arising from this study is related to the necessity of the amorphization process for the incorporation of Ga. In other words, one can wonder why the growth of GaN NWs on crystalline β-Si_3N_4 does not occur. To some extent, this observation is consistent with the work of Wu *et al.* who evidenced a rough and polycrystalline layer when trying to grow GaN directly on β-Si_3N_4 [187]. It is also consistent with the use of polycrystalline silicon nitride as a mask for GaN NW selective area growth [197, 198]. One possible explanation is that β-Si_3N_4 amorphization reduces the elastic stress at the interface by relieving the epitaxial constrain [79], thus allowing a nearly stress-free growth of GaN NWs. Equivalently, amorphous Si_xN_y may constitute a compliant buffer which may accommodate to the GaN lattice parameter. However, this interpretation does not satisfactorily justify the remaining in-plane orientation of GaN NWs versus silicon [150], unless a field of strain subsists through the thin amorphous Si_xN_y.

Concerning now the AlN buffer layer grown on Si, a recent article published by Largeau *et al.* reveals the formation of $Al_{1-x}Si_x$ liquid droplets on a Si(111) surface exposed to 5.6 ML of Al at 600 °C. When subsequently exposing this surface to nitrogen, the liquid droplets disappeared and hollow prints containing nanocrystals on their periphery were observed. The nanocrystals were identified as AlN with $< 11\bar{2}0 >$ directions parallel to Si $< 1\bar{1}0 >$ directions and appeared to behave as seeding pedestals for GaN NWs [199]. Although in our case the AlN buffer is made at higher temperature (*i.e.* ≈800 °C) and with a lower Al coverage (about 3 ML), a similar scenario could explain data exposed in this chapter. In particular, the formation of $Al_{1-x}Si_x$ droplets on the surface could be consistent with the observation of the β-Si_3N_4 signature when exposing the "Al-covered" surface to N (XRD peak at h = 1.37 r.s.u. in figure 3.6). In fact, such exposure to N would both induce the formation of AlN nanocrystals at the droplet positions and nitride the Si(111) surface between the droplets. Then, when providing 10 more seconds of Al, AlN would form between the nanocrystals by substitution of N atoms from β-Si_3N_4 (see section 3.5.1 and Ref. [189]). On the other hand, as discussed in section 2.2.1 of chapter 2, it is also possible that the AlN buffer has a grainy structure and that GaN NWs nucleate at the junction or between these grains. In this case, the observed β-Si_3N_4 signal could rise from tiny zones between the grains and hence be quickly amorphized when providing active nitrogen. In either way, whether GaN NWs grow on the AlN seeds or at the AlN grain junctions, AlN act as an epitaxial guide for GaN nanocolumns (either from the bottom or from the periphery) which explains their remarkable in-plane orientation versus silicon.

4

Polarity of GaN nanowires grown by PAMBE

This chapter deals with the polarity of GaN nanowires grown by plasma-assisted molecular beam epitaxy. In a first section, we discuss why polarity is important to be determined, or even controlled, and recall the knowledge that has already been established about polarity of 2D GaN layers and GaN wires, typically thicker than nanowires obtained by plasma-assisted molecular beam epitaxy. Then, based on resonant X-ray diffraction, we demonstrate that GaN nanowires grown on bare Si(111) by PAMBE are N-polar. We also show that KOH etches the N-polar face of GaN nanowires, leaving the Ga-polar face flat, similarly to what has already been observed on GaN layers. In this way, the combination of these two experiments validates the use of KOH for polarity determination on GaN NWs, which allowed us to perform further tests attempting to understand and control their polarity.

Contents

4.1 State of the art 77

4.1.1 Polarity-related issues 77

4.1.2 Polarity of 2D GaN layers and GaN wires 77

4.2 Resonant XRD for the polarity determination of GaN NWs grown on bare Si 78

4.2.1 Principle of the method 78
4.2.2 Samples preparation 80
4.2.3 Results 82
4.3 KOH selective etching method on GaN nanowires 83
4.4 Polarity of GaN nanowires prepared in different growth conditions 86
4.4.1 GaN nanowires grown on Ga-covered silicon 86
4.4.2 GaN nanowires on AlN buffer on Si(111) 87
4.5 Discussion and conclusion 87

4.1 State of the art

4.1.1 Polarity-related issues

The aim of this first section is to discuss reasons why determining polarity is important and to what extent III- and N-polar structures are different. In the case of 2D GaN layers, differences appear first of all to be significant on the morphological point of view. Ga-polar surfaces are smoother than their N-polar counterparts which exhibit pits and islands [200–203]. Ga-polar layers besides have better structural properties. For instance, it was shown that FWHM of their X-ray rocking curve around the symmetrical (0002) reflection are lower by a factor of 5 which suggests that they contain fewer screw and mixed threading dislocations [204]. From the growth point of view, the incorporation of impurities and vacancies has also been shown to differ. N-polar layers tend to incorporate more impurities [205–207], in consequence of what their optical properties are poorer [208]. Moreover, it appears that Ga-polar and N-polar layers are not equal regarding their doping, which is one of the most important issue of semiconductor materials. In particular, Mg incorporation seems to be easier in Ga-polar structures resulting in a better mastering of the *p*-type doping for this type of materials [209]. *n*-type doping, on the other hand, was shown to be comparable for both polarities [206, 210].

As already discussed in section 1.2.3.3 of chapter 1, polarity is likewise an important issue for III-N heterostructures. The electric field discontinuity raising from the difference of polarization between two materials composing an heterostructure leads to the formation of 2DEG at their interfaces. Yet, the materials polarity (hence metal- or N-) determines the polarization vector sign and therefore the type of carriers confined at each interface [115]. For instance, regarding GaN quantum wells (QWells) embedded in AlN segments, positive and negatives charges are left at the top surface of metal- and N-polar heterostructures, respectively. Both electrical [211] and optical properties of these heterostructure are then affected by the material polarity.

4.1.2 Polarity of 2D GaN layers and GaN wires

A large panel of experimental methods such as convergent beam electron diffraction [201,212], ion channeling [200], hemispherically scanned X-ray photoelectron diffraction [212, 213], X-ray standing wave technique [214], RHEED reconstruction observation [215, 216], photo-assisted Kelvin probe force microscopy [217], coaxial impact-collision ion scattering spectroscopy [218] and chemical wet etching [212,219–221] have already been used to determine the polarity of thick 2D GaN layers or large structured GaN crystals. On that account GaN layer polarity appears to depend on the growth technique (MOCVD or MBE), on the substrate (Sapphire, Si(111), SiC(0001)), on the use or not of a buffer layer and on the growth conditions of this one, leading to a wide set of

sometimes contradictory experimental results in literature [222].

Regarding layers grown by PAMBE on sapphire, polarity is determined by the surface nitridation temperature prior to the growth [223] or can be controlled by tuning the polarity of an AlN buffer layer, itself determined by the Al/N ratio during deposition [86]. On Si_3N_4/Si(111) [224] and on Si(111) [225], GaN layers turn out to be N-polar. Recently, studies have been performed on GaN wires with a diameter in the range of 1 to 5 µm, grown by MOVPE or ammonia-MBE [197, 226]. Wires grown on nitrided c-sapphire substrate exhibit a mixture of Ga- and N-polarity with a tendency to be rather N-polar while wires grown on Si(111) appear to be Ga-polar at 90 %. However, in what concerns the polarity of PAMBE GaN NWs, at the beginning of the work presented in this mansucript, literature was rather elusive and did not lead to clear conclusions [67, 79, 151, 227]. Our aim was therefore to reliably determine PAMBE-grown GaN NW polarity.

4.2 Resonant X-ray diffraction for the polarity determination of GaN nanowires grown on bare silicon

In order to unambiguously determine polarity of an ensemble of GaN NWs grown by PAMBE on bare silicon at a macroscopic scale, resonant X-ray diffraction was used [228–232]. In this section, we will explain the principle of the method and describe the sample preparation. Results are presented in the last part of the section.

4.2.1 Principle of the method

Use of resonant (or anomalous) X-ray diffraction for polarity determination has been demonstrated for the first time in the 1930s with wurtzite ZnS structures [228, 229]. This method relies on the breakdown of Friedel's law: for non-centrosymmetrical structures, when resonant effects are no longer negligible, a difference in the diffracted intensity of Friedel pairs of reflections hkl and $\bar{h}\bar{k}\bar{l}$ can be observed. In other terms, when resonant contributions are significant, $I(hkl) \neq I(\bar{h}\bar{k}\bar{l})$. Equivalently, as the intensity $I(hkl)$ of the X-ray beam diffracted by planes with Miller indexes hkl is proportional to the square of the total complex structure factor $F(hkl)$, the breakdown of Friedel's law can be written as $|F(hkl)|^2 \neq \left|F(\bar{h}\bar{k}\bar{l})\right|^2$. More generally, Bijvoet pairs, which designate symmetrically-equivalent reflections, exhibit the same properties as Friedel pairs. We have seen in chapter 1 that hkl, $\bar{h}\bar{k}\bar{l}$ and $hk\bar{l}$ constitute Bijvoet pairs for wurtzite GaN. In this specific case, the breakdown of Friedel's law can therefore be generalized to hkl and $hk\bar{l}$ pairs: $I(hkl) \neq I(hk\bar{l})$ or equivalently $|F(hkl)|^2 \neq \left|F(hk\bar{l})\right|^2$. In the following, we will explain the polarity-determination method based on Friedel pairs but one should keep in mind that the same stand for Bijvoet pairs.

Let us now recall that, as given by equation 1.16 in chapter 1, the structure factor $F(hkl)$ reads

$$F(\vec{Q},E) = F(hkl) = F_T(hkl) + \frac{|F_A|}{f_A^0}\left(f_A^{'}(E) + if_A^{''}(E)\right)e^{i\varphi_A} \tag{4.1}$$

Each term in the expression of $F(hkl)$ is a complex term which has both a modulus and a phase and which can be represented in the complex plane. Figure 4.1 (Argand diagram) shows such representation.

- The first term of equation 4.1, $F_T(hkl)$, is the sum of the resonant atom Thomson structure factor F_A^0 and of the overall non-resonant atom structure factor F_N. Its modulus is $|F_T|$ and its phase is φ_T;
- The second term $\frac{|F_A|}{f_A^0}f_A^{'}(E)e^{i\varphi_A}$ has a modulus equal to $\frac{|F_A|}{f_A^0}f_A^{'}(E)$ and a phase equal to φ_A
- The last term $i\frac{|F_A|}{f_A^0}f_A^{''}(E)e^{i\varphi_A}$ has a modulus equal to $\frac{|F_A|}{f_A^0}f_A^{''}(E)$ and a phase equal to $\varphi_A + \frac{\pi}{2}$

Now, for the reflection $\bar{h}\bar{k}\bar{l}$, each of these terms has the same modulus as for hkl. In addition, the first and the second terms have phases of opposite signs for hkl and $\bar{h}\bar{k}\bar{l}$: φ_T becomes $-\varphi_T$ and φ_A becomes $-\varphi_A$. As a consequence, if there was no third term, the resulting total structure factor would have the same modulus for hkl and $\bar{h}\bar{k}\bar{l}$ and these reflections would diffract with the same intensity. But, for $\bar{h}\bar{k}\bar{l}$, the third term has a phase equal to $-\varphi_A + \frac{\pi}{2}$ which introduces a difference in the total structure factor moduli $|F(hkl)|$ and $\left|F(\bar{h}\bar{k}\bar{l})\right|$.

In practice, we do not have experimentally access to $|F(hkl)|$ but to $|F(hkl)|^2$ which reads (see chapter 1)

$$|F(hkl)|^2 = |F_T|^2 + \frac{|F_A|^2}{f_A^{0\,2}}\left(f_A^{'\,2} + f_A^{''2}\right) + 2\frac{|F_A|\,|F_T|}{f_A^0}\left(f_A^{'}\cos(\varphi_T - \varphi_A) + f_A^{''}\sin(\varphi_T - \varphi_A)\right) \tag{4.2}$$

Following our previous reasoning, phases of $F_T(\bar{h}\bar{k}\bar{l})$ and $F_A(\bar{h}\bar{k}\bar{l})$ respectively are $-\varphi_T$ and $-\varphi_A$, therefore

$$\left|F(\bar{h}\bar{k}\bar{l})\right|^2 = |F_T|^2 + \frac{|F_A|^2}{f_A^{0\,2}}\left(f_A^{'\,2} + f_A^{''2}\right) + 2\frac{|F_A|\,|F_T|}{f_A^0}\left(f_A^{'}\cos(\varphi_T - \varphi_A) - f_A^{''}\sin(\varphi_T - \varphi_A)\right) \tag{4.3}$$

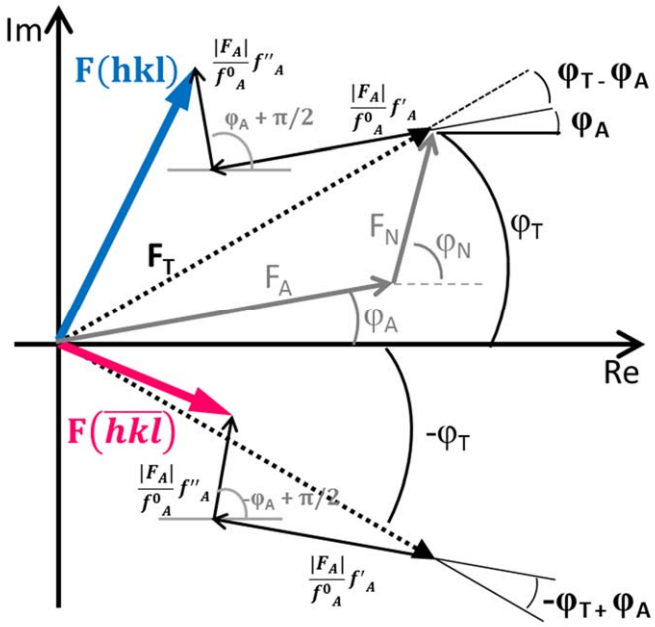

FIG. 4.1 – Argand diagram illustrating the breakdown of Friedel's law: a difference in the magnitude of the two total structure factor $|F(hkl)|$ and $\left|F(\bar{h}\bar{k}\bar{l})\right|$ moduli (thus in the diffracted intensity) occurs for non-centrosymmetrical systems when the absorption term $\frac{|F_A|}{f^0_A} f''_A(E)e^{i\varphi_A}$ of the resonant dispersive corrections is involved. F_T is the structure factor that includes the Thomson scattering of all atoms and the anomalous scattering of non-resonant atoms (*i.e.* $F_T = F_A + F_N$ where F_A corresponds to the Thomson scattering of all resonant atoms (Ga atoms in this study) and F_N gathers both Thomson and anomalous contributions of non-resonant atoms (nitrogen atoms in this study)). $\frac{|F_A|}{f^0_A} f'_A(E)e^{i\varphi_A}$ and $\frac{|F_A|}{f^0_A} f''_A(E)e^{i\varphi_A}$ are respectively related to dispersion and absorption from resonant atoms.

In consequence, the difference between the intensity of the hkl and the $\bar{h}\bar{k}\bar{l}$ reflections reads

$$\begin{aligned} I(hkl) - I(\bar{h}\bar{k}\bar{l}) &\propto |F(hkl)|^2 - \left|F(\bar{h}\bar{k}\bar{l})\right|^2 \\ &\propto 4\frac{|F_A||F_T|}{f^0_A} f''_A \sin(\varphi_T - \varphi_A) \end{aligned} \tag{4.4}$$

As the the two reflections hkl and $\bar{h}\bar{k}\bar{l}$ (or $hk\bar{l}$) diffract with distinct intensities, one can discriminate between them by comparing their experimental value to theoretically calculated intensities, and determine in this way the crystal orientation.

4.2.2 Samples preparation

The above described method requires precise measurements followed by careful data treatments. In order to rigorously establish GaN NW polarity, the only comparison of

the intensity diffracted by the NWs to its theoretical model is not enough. We actually decided to perform the measurements on both sides of the NWs and to compare each set of data to their theoretical intensity. Unfortunately, reaching the second reflection of the pair could not directly be done by diffracting through the Si substrate because if its important thickness of 250 µm. It was therefore necessary to turn over the NWs by transferring them to another substrate.

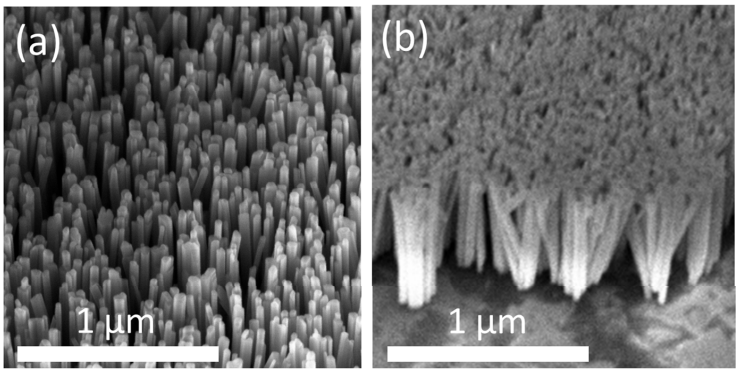

FIG. 4.2 – Bird-eye view SEM images of (a) as-grown GaN NWs and (b) upended NWs after preparation schemed in figure 4.3.

To do so, we first grew a reference sample (N1448) on bare Si(111), prepared in the usual way (see chapter 2). The substrate temperature was 800 °C and the III/V ratio equal to 0.4. The growth was initiated by simultaneously opening the Ga and N shutters. By the end of the 3.5 hour growth period, as-grown nanowires (a-NWs) were 730 nm long and had a diameter of 30 nm on average and a density of about 200 NWs/µm^2 (Fig. 4.2 (a)).

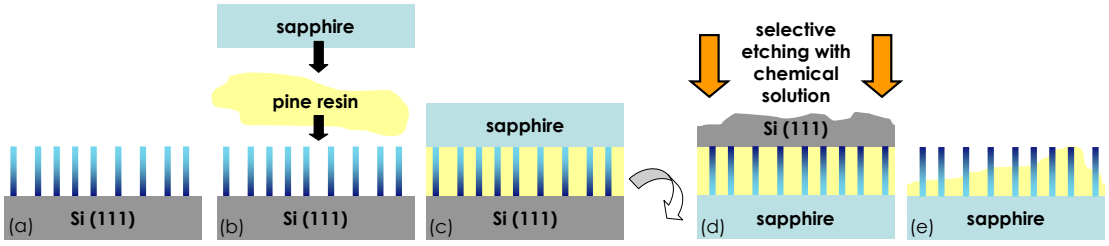

FIG. 4.3 – Scheme of the upended nanowires sample preparation

The sample with upended NWs (u-NWs) was prepared from a 5-mm^2 piece cleaved from the center of N1448. This piece (Fig. 4.3 (a)) was stuck upside down onto a sapphire lump with heated pine resin (Fig. 4.3 (b)). When cooled, the pine resin hardened, ensuring the formation of a resistant Al_2O_3/GaN NWs/Si stack (Fig. 4.3 (c)). Next, this sandwich-like assembly was plunged for several hours in a solution of 10 mL of hydrofluoric acid (49 %), 10 mL of nitric acid (65 %) and 30 mL of acetic acid (100 %). This chemical solution selectively etched the Si (Fig. 4.3 (d)), leaving the u-NWs embedded in the pine resin on top of the untouched sapphire (Fig. 4.3 (e)). The resulting up-ended NWs are presented in figure 4.2 (b).

4.2.3 Results

X-ray diffraction experiments with monochromatic synchrotron radiation were carried out on beamline BM02/D2AM at the ESRF. Intensity of symmetric Bragg reflection were measured with an 8-circle diffractometer in Euler geometry. Beam size at the focal point was about 0.3 $\times$ 0.15 mm^2 (resp. horizontally and vertically), thus illuminating a large assembly of NWs. Based on calculations, the intensity difference between the (112) and the $(\bar{1}\bar{1}\bar{2})$[1] reflections (or equivalently between (112) and $(11\bar{2})$ reflections) appeared to be significant enough, accounting for our choice to use these Bijvoet mates for the experiment. To thoroughly highlight the experimental intensity difference, extended and precise scans in energy around the Ga K-edge (10 367 eV) were recorded. The background intensity was additionally monitored to correct data from fluorescence and diffuse scattering signals. For each reflection of the Bijvoet pair, we measured and averaged three intensity spectra.

The following data treatment was performed by Cédric Leclere. First, Thomson scattering factor were calculated with the parametrized formula of D. Waasmaier and A. Kirfel [233]. Resonant scattering factors $f^{'}$ and $f^{''}$ were obtained in two different ways. For nitrogen atoms, theoretical values were obtained from the Cromer and Liberman programm [234]. On the other hand, for gallium atoms, $f^{''}_{A=Ga}$ were obtained by rescaling the fluorescence data (multiplied by the incoming beam energy) of the sample to theoretical $f^{''}_{A=Ga}$ values and $f^{'}_{A=Ga}$ were calculated from these experimental $f^{''}_{A=Ga}$ by using a difference Kramers-Kronig method implemented in the DIFFKK software [235].

The exact expression of the measured diffracted intensity is:

$$I(hkl) = KD(E)I_0\lambda^3 LPA\,|F(hkl)|^2 \tag{4.5}$$

where K is a scale factor, $D(E)$ is the detector efficiency, I_0 is the intensity of the incident X-ray beam, λ is the X-ray wavelength, L and P are the Lorentz and polarization factors, respectively, and A is the absorption factor. L and P are the same for both reflections of the Bijvoet pair, being independent of the X-ray beam energy and not contributing to the difference in intensity. The absorption term A does depend on the energy, but the effect is rather weak compared to the anomalous one. To take into account the self-absorption that reduces the diffracted intensity by about 5 - 10 %, an absorption correction was applied to theoretical spectra for symmetric Bragg geometry. A was calculated from the following formula given for a thin film of thickness τ [129]:

$$A(hkl, E) = \frac{1}{sin\alpha}\int_0^\tau exp\left(\frac{-2\mu z}{sin\alpha}\right)dz = \frac{1 - exp\left(\frac{-2\mu z}{sin\alpha}\right)}{2\mu} \tag{4.6}$$

[1] These reflections correspond to $(11\bar{2}\bar{2})$ and $(\bar{1}\bar{1}2\bar{2})$ in the four-index notation – see appendix A.

where α is the incident angle and μ is the linear absorption coefficient. The absorption correction takes into account the change of the X-ray beam footprint area, as a function of α. For reflections $(11\bar{2}2)$ and $(\bar{1}\bar{1}2\bar{2})$ measured in symmetric Bragg condition, incident and exit angles value are equal to $\alpha = 14°$ in the energy range of 10 150 - 10 650 eV. τ is the thickness of the film. In the case of NWs, τ_{eq} was used, an equivalent thickness defined by $\tau_{eq} = L \times \pi \left(D/2\right)^2 \times S = 150$ nm, where L, D and S are the length, diameter and surface density of the NWs respectively, as determined from SEM images. Finally, equation 1.16 was used to fit the background-subtracted spectrum with a Levenberg-Marquandt algorithm given by the SciPy.optimize package. Only geometrical parameters (scale factor K and $D(E)$) were fitted. Experimental data obtained from the a- and u-NWs samples as well as the best fits (solid lines) are shown in figure 4.4. Data obtained from a-NWs (pink full circles) match the simulated $(\bar{1}\bar{1}2\bar{2})$ reflection spectrum (grey upper line) and are therefore identified as N-polar. Consistently, data obtained from u-NWs (blue full circles) match the simulated $(11\bar{2}2)$ reflection spectrum (grey bottom line) and are hence identified as Ga-polar. The macroscopic size of the beam area hitting the sample together with the excellent agreement between fit and experimental data exclude the contingency of a polarity mixing.

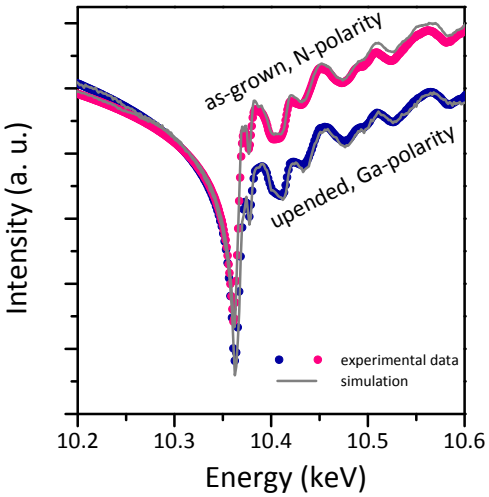

FIG. 4.4 – Evolution of the intensity of the $(11\bar{2}2)$ - $(\bar{1}\bar{1}2\bar{2})$ pair of reflections with the energy around the Ga K-edge. Pink and blue full circles stand for fluorescence-corrected experimental data obtained from a-NWs and u-NWs, respectively. Upper and bottom grey lines correspond to simulated fits obtained for $(\bar{1}\bar{1}2\bar{2})$ and $(11\bar{2}2)$ reflection, respectively.

4.3 KOH selective etching method on GaN nanowires

Regarding 2D layers, one of the most widely used method for the determination of GaN polarity consists in observing the studied surface reaction when dipped into an aqueous potassium hydroxide (KOH) solution. KOH has indeed proven to selectively etch the N-polar side of GaN (and AlN) layers while leaving untouched the Ga-polar one [221, 236–239]. According to Li *et al.*, the mechanisms of such selectivity relies on the different states of surface bonding that N- and Ga-polar surfaces present [220]. On

Ga-polar surfaces, hydroxide anions (OH^-) are strongly repelled by the electronegativity of the three N dangling bonds. In the case of N-polar surfaces, however, there is a single N dangling bond pointing in the $[000\bar{1}]$ direction (see figure 4.5 (a), taken from Ref. [220]). Figures 4.5 (b) to (d) then illustrate the processes involved in the etching: OH^- ions adsorb on the surface and react with Ga atoms by forming Ga_2O_3 which afterwards dissolves in the KOH solution.

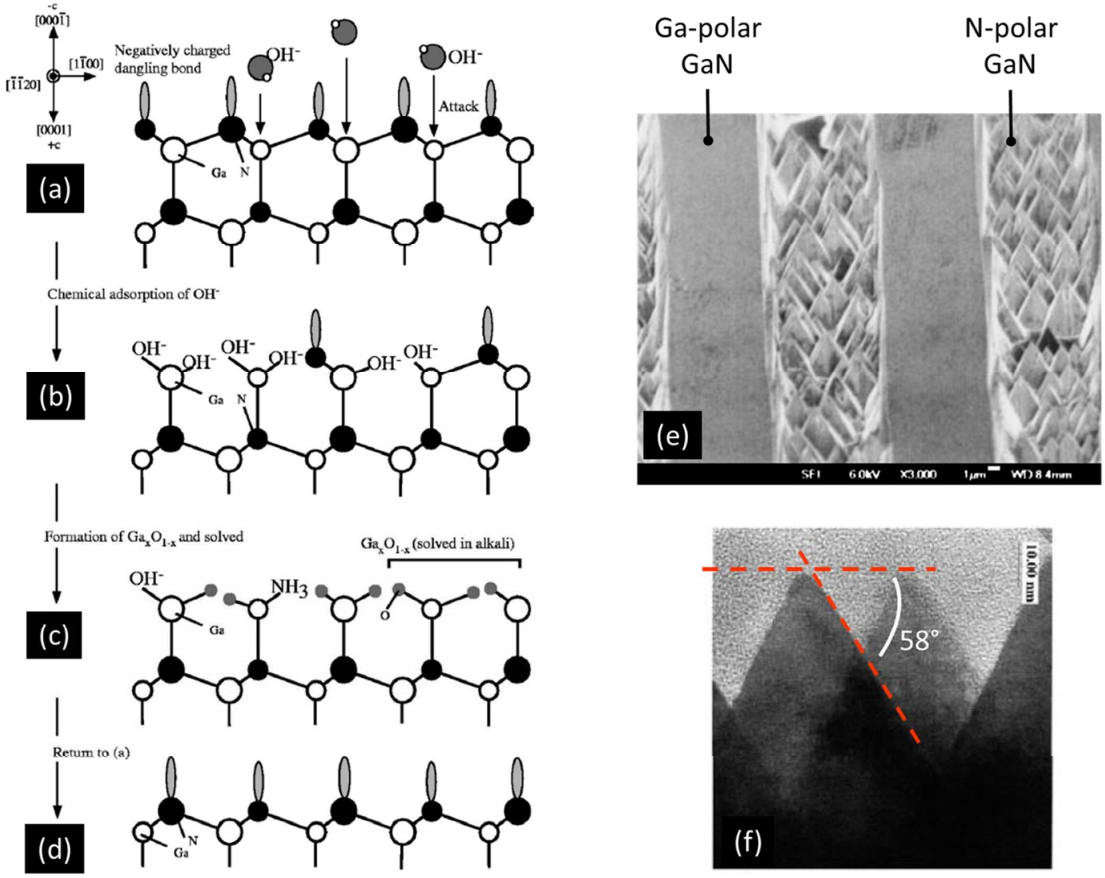

FIG. 4.5 – (a) to (d), taken from Ref. [220], illustrate the processes involved in the etching of N-polar GaN surfaces. (e), taken from Ref. [240], presents the difference of reactivity of N- and Ga-polar surface to KOH. (f), taken from Ref. [221], is a close up of pyramids formed by the KOH etching on N-polar surface. The angle between the basal plane and the pyramid facet reveals that $\{11\bar{2}\bar{2}\}$ planes most likely constitute these facets.

As a result, pyramids form on N-polar layers but Ga-polar faces remain flat. This is illustrated in figure 4.5 (e), taken from Ref. [240]: after plunging a sample having an alternation of Ga- and N-polar stripes in KOH, only the N-polar surfaces exhibit pyramidal features. Facets of these pyramids have been alternatively identified as $\{11\bar{2}\bar{2}\}$ [221] and $\{10\bar{1}\bar{1}\}$ [239] planes. As an example, figure 4.5 (f) displays one of the pyramids observed by Palacios *et al.* (taken from Ref. [221]). In this case, the angle between the basal (0001) plane and the pyramid facet is about 58° which corresponds to the angle between (0001)

and $\{11\bar{2}\bar{2}\}$ planes (table A.1 in appendix A).

As illustrated here, KOH selective etching stands as an easily-applicable method for polarity determination. In the case of NWs, however, no exhaustive investigation has been performed so far: one can therefore wonder how KOH would act on non polar facets such as those exhibited by GaN NWs, inherent to their geometry. To check the effect of KOH on GaN NW N-polar face, one piece of sample N1448 was plunged into an aqueous KOH solution for 10 minutes at room temperature. Figures 4.6 (a) and (b) show this sample respectively before and after dipping into KOH. It can clearly be seen that the top of the NWs is etched in a pencil-like shape by the KOH solution.

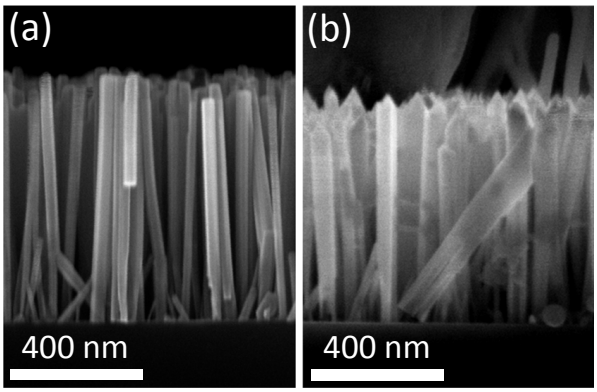

FIG. 4.6 – Cross section SEM image of sample N1448 (GaN NWs grown on bare Si(111)) before (a) and after (b) dipping into KOH.

Regarding the effect of KOH on the NW Ga-polar face, the u-NW sample appeared to be unsuitable because of the residual pine resin remaining between the NWs, making necessary the growth of a specific sample, identified as N1652 (Fig. 4.7 (a)). In this sample, in order to identify the apex from the bottom of the NWs, a thin AlN section was grown near their top surface. First, a piece of N1652 was plunged, as grown, into KOH, resulting in etched NWs (Fig. 4.7(b)). In a second stage, as shown by the SEM image taken in transmission in figure 4.7 (c), NWs from another piece of N1652 were dispersed onto a cooper grid covered with a carbon membrane. It can be seen that the nanowires are cut from the substrate in an almost perfect way and present both a flat bottom and a flat top. The carbon grid was then plunged into the KOH solution, therefore exposing both N- and Ga-polar sides of the NWs to the etchant. In figure 4.7 (d), it is clear that the top part of the NWs (identified by the position of the AlN insertion) is etched while the bottom part remains flat.

Similarly to 2D layers, KOH therefore selectively etches NW N-polar side while leaving untouched their Ga-polar face. From SEM images (cross section view as well as images taken in transmission), one can estimate that the angle between the (0001) basal plane and the pencil-like facet lies between 58 and 63°. According to the table A.1 given in appendix A, the facets are hence likely constituted of $\{10\bar{1}\bar{1}\}$ or $\{11\bar{2}\bar{2}\}$ planes, as it was

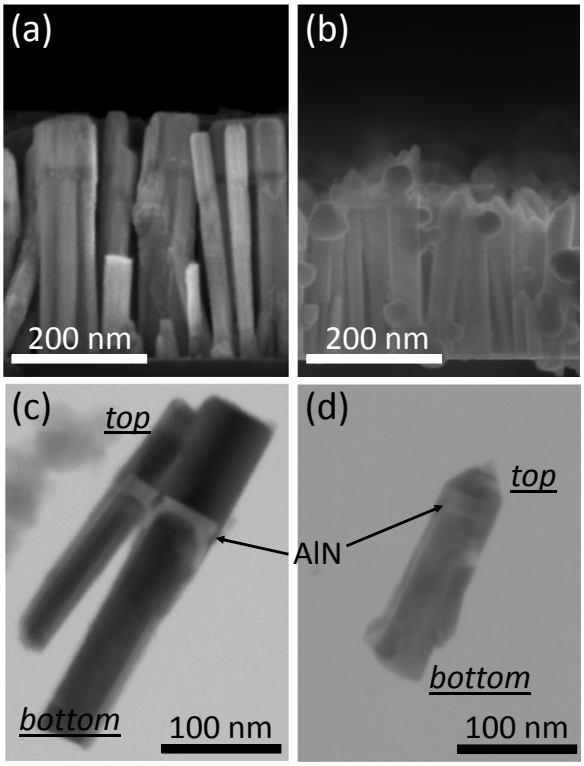

FIG. 4.7 – Cross section SEM image of sample N1652 (GaN NWs grown on bare Si(111) with an AlN insertion near their top surface) before (a) and after (b) dipping into KOH. These NWs were dispersed onto a cooper grid and observed in transmission (c). Then the grid was plunged into KOH (d). The AlN section permits to identify the top from the bottom of the NWs.

the case for 2D layers. In any ways, this evidences that KOH selective etching can be valuably used as a quick method to evaluate the polarity of GaN NWs.

4.4 Polarity of GaN nanowires prepared in different growth conditions

4.4.1 GaN nanowires grown on Ga-covered silicon

In order to foster our investigations on GaN NW polarity, two other samples were studied. First of all, similarly to the experiment described in section 3.4.3 of chapter 3, we initiated GaN NW growth on a surface covered with Ga adatoms. To do so, the Si(111) surface was exposed to a constant Ga flux before, during and after turning on the N plasma source. This means that when active N species started to be provided, either in a first stage with the N shutter close (leakage) or subsequently, with the N shutter open, the surface was already covered with gallium atoms, attested by the absence of the 7×7 Si(111) surface reconstruction. Figures 4.8 (a) and (b) show SEM images of this sample (N1567) respectively before and after dipping into KOH. It can be seen that NWs grown on such Ga-covered surface are still N-polar.

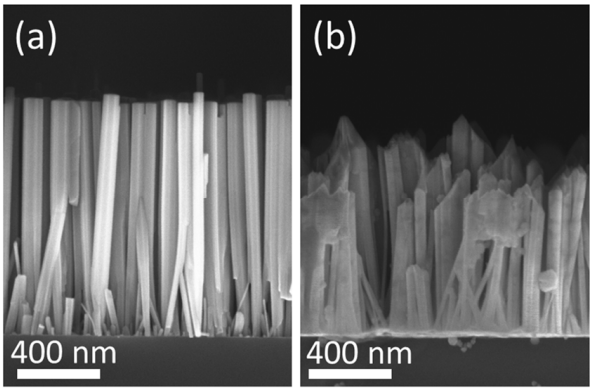

FIG. 4.8 – Cross section SEM image of sample N1567 (GaN NWs grown on Ga-protected Si(111)) before (a) and after (b) dipping into KOH.

4.4.2 GaN nanowires on AlN buffer on Si(111)

Polarity was then tested with KOH on sample N1011, fabricated with an AlN buffer layer on Si(111). This thin AlN buffer was made at 830 ℃ by first depositing Al on the Si(111) surface during 10 s, resulting in a 3 ML coverage. Next, the plasma source was turned on and N was provided to consume the Al on the surface. Al and N were alternatively supplied for 2 more cycles of 10 s each. The corresponding buffer is hence about 2.3 nm thick. Growth conditions for the subsequent fabrication of GaN NWs were comparable to those used for N1448. Figures 4.9 (a) and (b) show a piece of N1011 respectively before and after it was plunged into the KOH solution. It can be seen that, similarly to the case of GaN NWs grown on bare Si(111), nanocolumns were also etched by KOH, revealing their N-polar character.

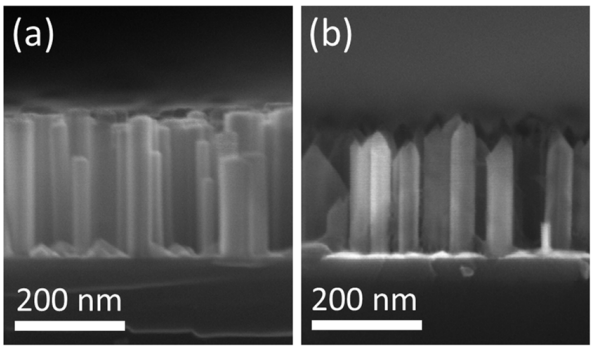

FIG. 4.9 – Cross section SEM image of sample N1011 (GaN NWs grown on AlN/Si(111)) before (a) and after (b) dipping into KOH.

4.5 Discussion and conclusion

In chapter 3, we have evidenced that GaN NWs do not grow directly on bare silicon but on an amorphous Si_xN_y layer that forms on the Si(111) surface. We have also shown that even when attempting to protect the Si(111) surface with Ga adatoms, active nitrogen atoms diffuse through the Ga coverage to form Si_xN_y. In both cases, the resulting GaN NW N-polar character is hence certainly induced by the presence of this amorphous Si_xN_y. In a recent article, Kong *et al.* used electron energy loss spectroscopy to demonstrate

that PAMBE-grown GaN NWs on Si(111) are N-polar [241]. The authors suggested that this N-polarity is induced by the way Ga atoms bind to the N-rich Si_xN_y layer. More specifically, to achieve a N-polarity, the first Ga atom on the Si_xN_y/Si(111) surface must bind to a single N atom from Si_xN_y (configuration A in figure 4.10) rather than to three N atoms (configuration B in figure 4.10).

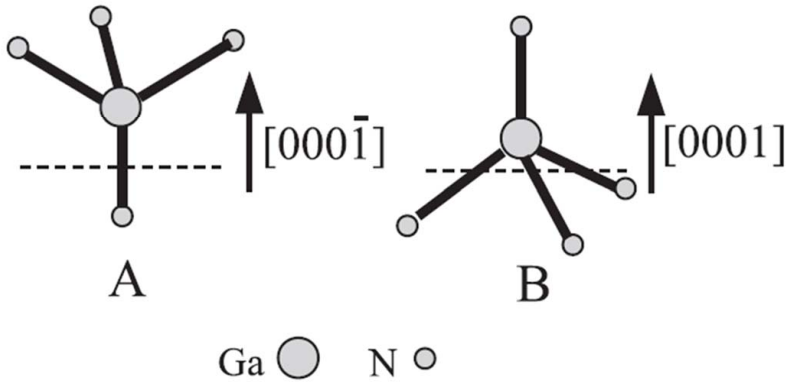

FIG. 4.10 – Illustration of the two ways Ga can bind to N atoms from the amorphous Si_xN_y layer, taken from Ref. [241]. Configuration A induces the N-polarity while configuration B induces the Ga-polarity

The case of GaN deposited on an AlN buffer layer is more complex. Regarding 2D layers on Si(111), it has already been established that GaN polarity depends on the AlN buffer thickness. Palacios *et al.* indeed showed that the use of a thin AlN buffer layer on Si(111) results in N- or mixed-polarities and the use of a thicker AlN buffer (> 30 nm) leads to a Ga- polar GaN layer [221]. Consistently, GaN NWs observed in our study were grown on a 2-3 nm thick AlN buffer and exhibit a N-polarity. On thick AlN buffer, no polarity determination of PAMBE-grown GaN NWs has been reported so far. This lack of data may have to do with the difficulty to obtain GaN NWs on thick AlN layers. Indeed, we showed in our group that the columnar growth is inhibited for thick AlN buffers [80]. Kong *et al.* nevertheless successfully obtained AlGaN NWs on a 30 nm thick AlN buffer and reported a metal-polarity of the columns. Interestingly, AlN grown on Si(111) has been shown to be Al-polar [242]. Considering the hypothesis that AlN grows as grains and that GaN NWs nucleate between these grains rather than on top of them (see discussion in section 2.2.1), one can argue that Ga atoms bind with single N atoms (configuration A in figure 4.10) from residual Si_xN_y between the grains, inducing the NW N-polarity. On the other hand, increasing the buffer thickness enhances its smoothness, hence prevents a columnar nucleation at the grain junctions. On such a smoother AlN, GaN then nucleates as a Ga-polar rough layer.

Alternatively, with the AlN buffer growth conditions they used (see discussion of chap-

ter 3), Largeau *et al.* suggested the presence of N-polar AlN nanocrystals surrounded by an Al-polar AlN layer [199]. The authors attribute the nanocrystal potential N-polar character to the formation of Al-Si bonds at the interface, induced by the abundance of Al atoms in $Al_{1-x}Si_x$ droplets. These nanocrystal then act as a pedestal for GaN NWs which grew with a N-polarity. On the surrounding Al-polar layer, no NW nucleated but a rough Ga-polar GaN layer was observed. Back to our case, although the AlN buffer was grown in different conditions (at higher temperature and with a lower primary Al coverage of the Si(111) surface), the formation of N-polar AlN pedestal and subsequent nucleation of GaN NWs on these pedestals could also possibly explain their N-polarity.

These two pictures hence suggest that N-polar GaN NWs either grow between AlN grains or on top of N-polar AlN nanocrystals. On the other hand, results published in Ref. [241] show that III-N NWs nucleating **on top of** Al-polar AlN are themselves metal-polar. This observation allows to use the polarity as a indication of the zone where the corresponding NWs have nucleated. In our case, SEM images obtained after dipping N1011 in KOH exhibit NWs that are all N-polar (they are all etched in a pencil-like shape) thus revealing that no NW nucleation occurred on the Al-polar AlN layer. Such absence of NW nucleated on the Al-polar AlN is in fact one of the issue raised by this study and which will be fostered in our group in the near future. Is it precisely a matter of polarity or rather a question of smoothness of the AlN layer? Is it possible and in which conditions, to nucleate GaN NWs on top of Al-polar AlN grains or layer?

In conclusion, based on resonant XRD and KOH selective etching, we have established that GaN NWs grown on bare Si(111), on Ga-covered Si(111) and using a thin AlN buffer layer on Si(111) all exhibit a N-polarity. In the two former cases, we attribute the N-polarity to the binding of Ga atoms with single N atoms from Si_xN_y that inevitably forms on the Si(111) surface before the ignition of GaN NWs. In the latter case, the N-polarity is either a consequence of the same Ga-N bound occurring with Si_xN_y present between AlN buffer grains or – but this is less probable – may be directed by the polarity of N-polar AlN nanocrystals possibly formed on the Si surface and acting as a pedestal for GaN NWs.

5

GaN-AlN core-shell nanowire heterostructures

After investigating GaN nanowires, we will now focus on the fabrication and properties of GaN-AlN nanowire heterostructures. In this context, two types of heterostructures can be distinguished: GaN/AlN ***axial heterostructures****, grown on top of GaN nanowires or in others words along the* [0001] *direction, and GaN/AlN* ***radial heterostructures****, grown on the GaN nanowire periphery, that is along* $< 10\bar{1}0 >$ *directions. As an initial step towards the realization of either type of heterostructures, its is necessary to deposit AlN on GaN nanowire bases. The aim of this chapter precisely is to investigate GaN radial quantum wells and axial insertion common building blocks, namely GaN-AlN core-shell nanowires. In a first stage, we will focus on the growth of GaN-AlN core-shell nanowires and describe the resulting structures by a geometrical model based on the one demonstrated by Foxon et al. [243]. Then, GaN-AlN core-shell nanowire heterostructures will be structurally and optically characterized.*

Contents

5.1 Growth of the AlN shell around GaN nanowires 93

5.1.1 Geometrical model 94

5.1.1.1 Relation between the initial Φ_{Al}/Φ_N ratio and the effective AlN growth rate 95

5.1.1.2 Growth rates along the axis and along the radius of the nanowires 97
5.1.1.3 Consequence of the shadow effect 99
5.1.2 Experimental observations 102
5.1.2.1 GaN-AlN core-shell nanowire density 102
5.1.2.2 Morphologies of the AlN shell 103
5.1.2.3 AlN shell aspect ratio dependence on the atomic beams incidence angle 105
5.1.2.4 Geometrical model including Al diffusion 108
5.1.2.5 Discussion and conclusions on the AlN shell growth mechanisms and morphology 110
5.2 Structural properties of GaN-AlN core-shell heterostructures 111
5.2.1 AlN shell induced strain within GaN cores 111
5.2.1.1 Resonant X-ray diffraction 111
5.2.1.2 Theoretically determined strains 115
5.2.1.3 Microscopic observations 117
5.2.1.4 Conclusions on strains within GaN cores 119
5.2.2 In-plane and out-of-plane disorientation 120
5.3 Optical properties of GaN-AlN core-shell heterostructures . 122
5.4 Conclusion of the chapter 124

5.1 Growth of the AlN shell around GaN nanowires

In PAMBE, an AlN shell can be fabricated around GaN NWs by taking advantage of the significant lateral AlN growth rate. Al and N atomic fluxes Φ_{Al} and Φ_N (given in atoms/cm^2/s), which can be considered as ballistic beams, impinge GaN nanocolumns with incidence angles α_{Al} and α_N typically between 20 and 30° (Fig. 5.1), giving rise to both an AlN cap **on top of** GaN nanocolumns and an AlN contribution **around** GaN nanocolumns, respectively on the GaN c-plane ((0001) plane) and m-plane ($(1\bar{1}00)$ plane) surfaces (see appendix A).

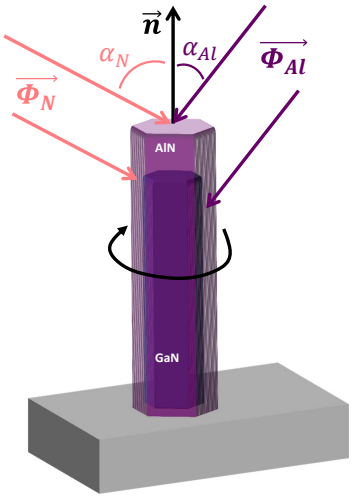

FIG. 5.1 – Geometry of the system for the growth of the AlN shell around GaN NWs. The Al and N atoms impinge the nanocolumns with incidence angles α_{Al} and α_N, respectively.

The axial (on top) and the lateral contributions are therefore intrinsically linked and their ratio is directed by the choice of growth conditions. One can hence wonder which parameters of the growth are the most appropriate to influence either of the contributions. To our knowledge, no detailed analysis of the shell morphology dependence on the growth conditions has been reported so far. In this first part of the chapter dedicated to GaN-AlN core-shell NWs, we intend to study the change of the AlN shell morphology as a function of two growth parameters that are the Al to N flux ratio (Φ_{Al}/Φ_N) and the incidence angles α_{Al} and α_N. We will compare experimental data statistically obtained from core-shell NWs grown in various conditions to a geometrical model hereafter described. But first of all, it is important to clarify the background of this experiment.

In our PAMBE system, as shown in figure 5.2, α_{Al} and α_N cannot be separately changed since the only free parameter available is the rotation of the manipulator θ. One can define $\vec{n}_\theta$ as the vector normal to the substrate when the manipulator is in the position θ. Note that $\vec{n}_\theta$ also defines the growth direction of the columns. The position $\theta = 0$ corresponds to an optimal situation such as, by construction of the machine, the angle of each impinging flux with respect to $\vec{n}_0$ is minimal. In this position, the RHEED beam grazes the substrate surface. Following geometrical considerations, when the monitor is

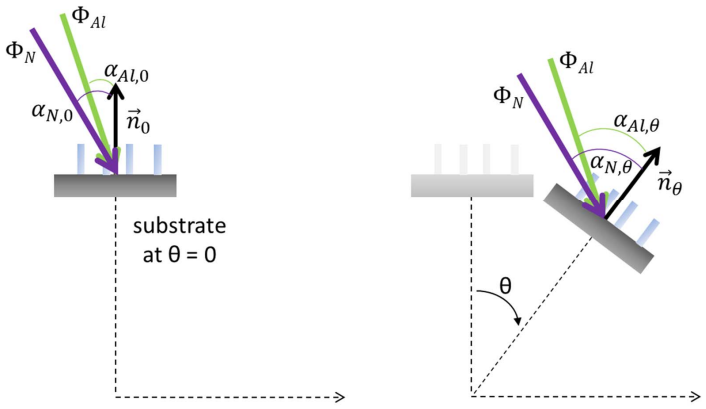

FIG. 5.2 – Geometry of the system and relation between the manipulator position θ and the incidence angles of Al and N fluxes (respectively $\alpha_{Al,\theta}$ and $\alpha_{N,\theta}$).

rotated to position $\theta \neq 0$, $\vec{n}_\theta$ is itself rotated of θ compared to $\vec{n}_0$. α_{Al} and α_N are naturally dependent on θ and can be determined by considering the positions of the Al and N cells. In particular, table 5.1 gives the angles α_{Al} and α_N determined as a function of θ for several θ used in this study. In order to distinguish between the different α_{Al} and α_N at stake, let us rename them $\alpha_{Al,\theta}$ and $\alpha_{N,\theta}$, respectively.

	$\theta(°)$						
	0	8	15	20	25	30	35
$\alpha_{Al,\theta}$ (°)	28	37	45	50	56	61	67
$\alpha_{N,\theta}$ (°)	20	27	34	39	45	50	55

TABLE 5.1 – Equivalence between the manipulator positions θ and the incidence angles $\alpha_{Al,\theta}$ (respectively $\alpha_{N,\theta}$) between the normal to the surface $\vec{n}_\theta$ and the Al flux Φ_{Al} (respectively N flux Φ_N) considered as ballistic beams.

5.1.1 Geometrical model

Based on the model demonstrated by Foxon *et al.* [243] for GaN NWs, and assuming, as a first approach, that Al and N adatoms neither desorb nor diffuse, the AlN shell morphology can be described by considering the geometry of the system. As a matter of fact, GaN NW top surface and side-walls are not impinged by the same flux of atoms, which gives rise to a difference of growth rate along the NW axis compared to the growth rate along its radius.

First, considering the incidence angles $\alpha_{Al,\theta}$ and $\alpha_{N,\theta}$, one can write that a point of the top surface is reached by a total atomic flux given by

$$\Phi_{Al} cos\left(\alpha_{Al,\theta}\right) + \Phi_N cos\left(\alpha_{N,\theta}\right) \quad \text{atoms/cm}^2\text{/s}. \tag{5.1}$$

Meanwhile, a point on the side-walls is reached by

$$\frac{1}{\pi}(\Phi_{Al} sin\left(\alpha_{Al,\theta}\right) + \Phi_N sin\left(\alpha_{N,\theta}\right)) \text{ atoms/cm}^2\text{/s}. \tag{5.2}$$

The $\frac{1}{\pi}$ factor raises from that the column is rotated during growth. Now, on each surface (*i.e.* *c*-plane surface and *m*-plane surfaces), impinging atoms are not all incorporated. Two parameters actually control the incorporation of Al and N atoms or in other terms, the AlN growth rate: the effective ratio of Al and N atoms available on the considered surface which itself depends on the initial Φ_{Al}/Φ_N ratio, and the AlN atomic surface density. Both these parameters differ on the top surface and on the side-walls (Tab. 1.2 in chapter 1).

5.1.1.1 Relation between the initial Φ_{Al}/Φ_N ratio and the effective AlN growth rate

Let us first focus on the effective ratio of Al and N atomic fluxes on a given surface and how it is related to the initial Φ_{Al}/Φ_N ratio. The problem in a PAMBE system is that active N atoms are initiated within a N_2 background and it is therefore not possible to determine Φ_N out of Φ_{N_2} with a gauge. Nevertheless, the effective ratio of Al and N atomic fluxes on the surface can be deduced from the AlN growth rate, expressed in monolayer per second (ML/s). This is possible because to incorporate 1 complete ML of AlN on a given surface, one needs σ atoms/cm^2 where σ is the atomic surface density of this surface. Then, if one provides an atomic density d_{at} atoms/cm^2, one can grow

$$x = \frac{d_{at}}{\sigma} \tag{5.3}$$

monolayers of AlN on this surface. The atomic flux Φ is then simply obtained by divided d_{at} by the time. Therefore the corresponding growth rate $\eta_{growth-rate}$ reads

$$\eta_{growth-rate} = \frac{\Phi}{\sigma} \text{ ML/s}. \tag{5.4}$$

The advantage of transforming fluxes in growth rates lies in the fact that the growth rate can be precisely determined by mean of RHEED oscillations (Fig. 1.12 of chapter 1). Yet, RHEED measurements are performed on AlN pseudo-substrates oriented [0001] and thus give the AlN growth rate on the *c*-plane at $\theta = 0$. At stoichiometry, that is when the same fluxes of N and Al impinge the surface ($\Phi_{Al} cos\left(\alpha_{Al,0}\right) = \Phi_N cos\left(\alpha_{N,0}\right)$), the measured growth rate is $\eta_{AlN,stoichio}$. The total amount of atoms contributing to the growth rate $\eta_{AlN,stoichio}$ is $2\Phi_N cos\left(\alpha_{N,0}\right)$ atoms/cm^2/s. Therefore, following equation 5.4, $\eta_{AlN,stoichio}$ reads

$$\eta_{AlN,stoichio} = \frac{2\Phi_N cos\left(\alpha_{N,0}\right)}{\sigma_c} \text{ ML/s} \tag{5.5}$$

In non-stoichiometric conditions, that is when the Al flux on the surface is different from the N flux, the AlN growth rate η_{AlN} depends on the limiting species. More precisely,

in our MBE, the N flux provided is always the same and only the Al flux is changed. In the "N-rich" conditions typically used for the growth of NWs, the effective Al flux on the surface is inferior to the effective N flux on the surface and therefore determines the growth rate (or equivalently the quantity of incorporated atoms). In this case, η_{AlN} then writes

$$\eta_{AlN} = \frac{2\Phi_{Al} cos\left(\alpha_{Al,0}\right)}{\sigma_c} \tag{5.6}$$

As the nominal N flux Φ_N is always the same, let us now express Φ_{Al} in function of Φ_N as $\Phi_{Al} = \gamma\Phi_N$. Equation 5.6 then becomes

$$\eta_{AlN} = \frac{2\gamma\Phi_N cos\left(\alpha_{Al,0}\right)}{\sigma_c} \tag{5.7}$$

Then, when dividing equation 5.7 by equation 5.5, we get that

$$\gamma = \eta \frac{cos(\alpha_{N,0})}{cos(\alpha_{Al,0})} \tag{5.8}$$

where $\eta = \eta_{AlN}/\eta_{AlN,stoichio}$. In other terms, equation 5.8 gives the proportionality coefficient γ between the initial fluxes Φ_{Al} and Φ_N leading to a given growth rate η_{AlN} in the [0001] direction at $\theta = 0$. Relying on γ it is thus now possible to switch to the NWs case and determine AlN growth rates $\nu_{ax}(\theta)$ and $\nu_{rad}(\theta)$, along the axis and along the radius of the NWs, respectively.

The case of NWs nevertheless requires some caution. Although in this experiment, η was always chosen to be inferior to 1, one can not straightforwardly conclude that "N-rich" conditions occur at every θ, both on the side-walls and on the top facets. In other words, although the initial values of Φ_{Al} and Φ_N were such that the effective N flux on the c-surface was always superior or equal to the Al one at $\theta = 0$, proportions between the two species change at different θ.

In order to clarify the effective Al to N fluxes ratio on the side-walls and on the top surface as a function of θ, one can reason as follows: on the top surface of the NWs, "N-rich conditions" are synonym of

$$\Phi_N cos\left(\alpha_{N,\theta}\right) > \Phi_{Al} cos\left(\alpha_{Al,\theta}\right) \tag{5.9}$$

In the range of θ we take into account, $\alpha_{N,\theta}$ and $\alpha_{Al,\theta}$ belong to $]0; \frac{\pi}{2}[$ (Table 5.1), therefore all the terms of equation 5.9 are positive. Taking into account equation 5.8, it thus comes that to be N-rich on top of the NWs, the following inequality must be fulfilled

$$f_{axial}(\theta) = \frac{1}{\eta} \frac{cos\left(\alpha_{N,\theta}\right)}{cos\left(\alpha_{Al,\theta}\right)} \frac{cos\left(\alpha_{N,0}\right)}{cos\left(\alpha_{Al,0}\right)} > 1 \tag{5.10}$$

Similarly, on the nanowires side-walls, to be N-rich, one must have

$$\Phi_N sin\left(\alpha_{N,\theta}\right) > \Phi_{Al} sin\left(\alpha_{Al,\theta}\right) \tag{5.11}$$

Therefore, the following equation must be fulfilled

$$f_{radial}(\theta) = \frac{1}{\eta} \frac{sin\left(\alpha_{N,\theta}\right)}{sin\left(\alpha_{Al,\theta}\right)} \frac{cos\left(\alpha_{N,0}\right)}{cos\left(\alpha_{Al,0}\right)} > 1 \tag{5.12}$$

Figures 5.3 (a) and (b) respectively present variations of f_{axial} and f_{radial} as a function of θ for different values of η. It can be seen that on the NW apex, when η is chosen inferior or equal to 1 (N-rich conditions on the top surface at $\theta = 0$), the conditions remain N-rich at all higher values of θ. On the other hand, this is not the case on the side-walls. Figure 5.3 (b) clearly shows that for the higher values of η, the sides-walls become Al-rich. For the later comparison to experiments, the two values of η that have been retained are $\eta = 0.55$ and $\eta = 0.86$. These two values lead to two different cases. For $\eta = 0.55$, both the top surface and the sides-walls are N-rich for all the probed angles θ. In the latter case, that is when $\eta = 0.86$, only the top surface is N-rich. The side-walls, on the other hand, are Al-rich for all the values of θ.

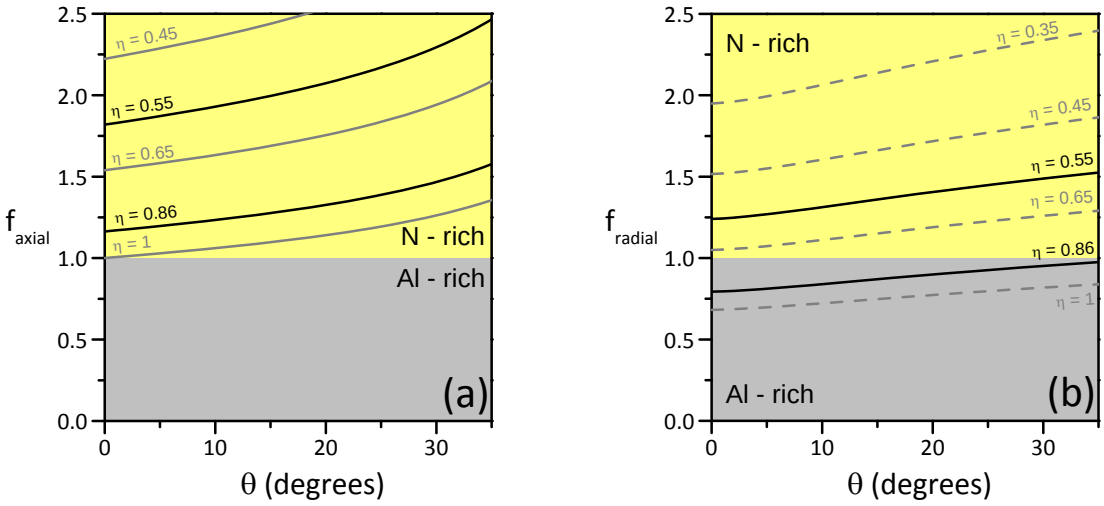

FIG. 5.3 – f_{axial} and f_{radial} (see equations 5.10 and 5.12) as a function of θ for different values of η.

5.1.1.2 Growth rates along the axis and along the radius of the nanowires

Along the axis, as we are always in N-rich conditions for all the investigated values of θ, the limiting species are Al and thus, the growth rate $\nu_{ax}(\theta)$ is similar to the 2D case:

$$\nu_{ax}(\theta) = \frac{2\Phi_{Al} cos(\alpha_{Al,\theta})}{\sigma_c} \tag{5.13}$$

which gives, when introducing equation 5.8

$$\nu_{ax}(\theta) = \Phi_N \frac{2\eta}{\sigma_c} \frac{cos(\alpha_{N,0})}{cos(\alpha_{Al,0})} cos(\alpha_{Al,\theta}) \tag{5.14}$$

Similarly to our previous reasoning, the growth rate along the radius $\nu_{rad}(\theta)$ is given by dividing the amount of impinging atoms on the m-planes by the m-plane atomic surface density σ_m. Its expression depends on the case in which we are. If we are N-rich on the side-walls, then $\nu_{rad}(\theta)$ writes

$$\nu_{rad}(\theta) = \frac{1}{\pi} \frac{1}{\sigma_m} 2\Phi_{Al} sin(\alpha_{Al,\theta}) \tag{5.15}$$

or in other terms, ν_{rad} can be now be expressed in function of η, the measured ratio of growth rates along the [0001] direction as

$$\nu_{rad}(\theta) = \Phi_N \frac{1}{\pi} \frac{2\eta}{\sigma_m} \frac{cos(\alpha_{N,0})}{cos(\alpha_{Al,0)}} sin(\alpha_{Al,\theta}) \tag{5.16}$$

On the other hand, when Al-rich conditions happen on the side-walls, then nitrogen atoms are the limiting species and $\nu_{rad}(\theta)$ reads

$$\nu_{rad}(\theta) = \Phi_N \frac{1}{\pi} \frac{2}{\sigma_m} sin(\alpha_{N,\theta}) \tag{5.17}$$

Finally, the ratio ν_{ax}/ν_{rad} itself depends on whether N-rich or Al-rich conditions occurs on the sides-walls. In the former case

$$\frac{\nu_{ax}}{\nu_{rad}}(\theta) = \pi \frac{\sigma_m}{\sigma_c} \frac{1}{tan(\alpha_{Al,\theta})} \tag{5.18}$$

and in the latter case

$$\frac{\nu_{ax}}{\nu_{rad}}(\theta) = \pi\eta \frac{\sigma_m}{\sigma_c} \frac{cos(\alpha_{N,0})}{cos(\alpha_{Al,0})} \frac{cos(\alpha_{Al,\theta})}{sin(\alpha_{N,\theta})} \tag{5.19}$$

In addition, let us note that in the two other possible cases that are, Al-rich conditions both on the top surface and on the sidewalls, and Al-rich rich top surface combined with N-rich side-walls, the ratio of growth rates would respectively be

$$\frac{\nu_{ax}}{\nu_{rad}}(\theta) = \pi \frac{\sigma_m}{\sigma_c} \frac{1}{tan(\alpha_{N,\theta})} \tag{5.20}$$

and

$$\frac{\nu_{ax}}{\nu_{rad}}(\theta) = \frac{\pi}{\eta} \frac{\sigma_m}{\sigma_c} \frac{cos(\alpha_{Al,0})}{cos(\alpha_{N,0})} \frac{cos(\alpha_{N,\theta})}{sin(\alpha_{Al,\theta})} \tag{5.21}$$

but these two cases will not be further investigated in this study. As one can expect, when the atomic incorporation is limited by the same species on both the top surface and the

side-walls (for instance Al), the ratio of growth rates do not depend on the ratio between the two species η (Eq. 5.18).

Equations 5.18 to 5.21 give ratios of growth rates, each being expressed in monolayers per second. Yet, the formation of one AlN monolayer does not contribute the same way on top of the NW and on its facets. On the (0001) surface, that is along the axis, one monolayer is proportional to $c_{AlN} = 0.498\ nm$ while on the m-planes (along the radius) it is proportional to $a_{AlN}\sqrt{3} = 0.539\ nm$. When both the top surface and the side walls are N-rich, the ratio of the axial over radial lengths then writes

$$\frac{L_{ax}}{L_{rad}} = \pi \frac{c_{AlN}}{a_{AlN}\sqrt{3}} \frac{\sigma_m}{\sigma_c} \frac{1}{tan(\alpha_{Al,\theta})} \tag{5.22}$$

whereas when the side-walls are Al-rich and the top surface is N-rich

$$\frac{L_{ax}}{L_{rad}} = \pi\eta \frac{c_{AlN}}{a_{AlN}\sqrt{3}} \frac{\sigma_m}{\sigma_c} \frac{cos(\alpha_{N,0})}{cos(\alpha_{Al,0})} \frac{cos(\alpha_{Al,\theta})}{sin(\alpha_{N,\theta})} \tag{5.23}$$

Eventually, $\frac{\sigma_m}{a_{AlN}\sqrt{3}} = \frac{\sigma_c}{c_{AlN}} = \rho_{AlN}$, the atomic volume density of wurtzite AlN[1]. Therefore equations 5.22 and 5.23 can respectively be simplified as

$$\frac{L_{ax}}{L_{rad}} = \frac{\pi}{tan(\alpha_{Al,\theta})} \tag{5.24}$$

and

$$\frac{L_{ax}}{L_{rad}} = \pi\eta \frac{cos(\alpha_{N,0})}{cos(\alpha_{Al,0})} \frac{cos(\alpha_{Al,\theta})}{sin(\alpha_{N,\theta})} \tag{5.25}$$

L_{ax}/L_{rad} is a function of $1/\tan(\alpha_{Al,\theta}, \alpha_{N,\theta})$. In the range of θ we have used for the growths, $\alpha_{Al,\theta}$ and $\alpha_{N,\theta}$ increase respectively from 28 to 60° and from 20 to 55° (table 5.1). As in this range of angles, tangent is a decreasing function, one can expect that the ratio L_{ax}/L_{rad} will decrease with increasing θ.

5.1.1.3 Consequence of the shadow effect

Depending on the atomic flux incidence angle, the NW density, their mean diameter and length, screening by neighbouring NW may become important. It is particularly the case when thickening the nanocolumn with the AlN shell. Figure 5.4 illustrates this issue.

Let us consider that time t = 0 s corresponds to the start of the AlN shell deposition (Fig. 5.4 (a)). At that moment, the average length of the GaN NW bases is $h(t_0)$, their average diameter is δ and the mean distance between two neighbouring NWs is d. If we focus on a single atomic specie (for instance Al), the length $z_{impinged}(t_0)$ of the column which is actually impinged by these atoms is determined by this mean distance between

[1] $\rho_{AlN} \approx 9.6$ atoms/cm^3

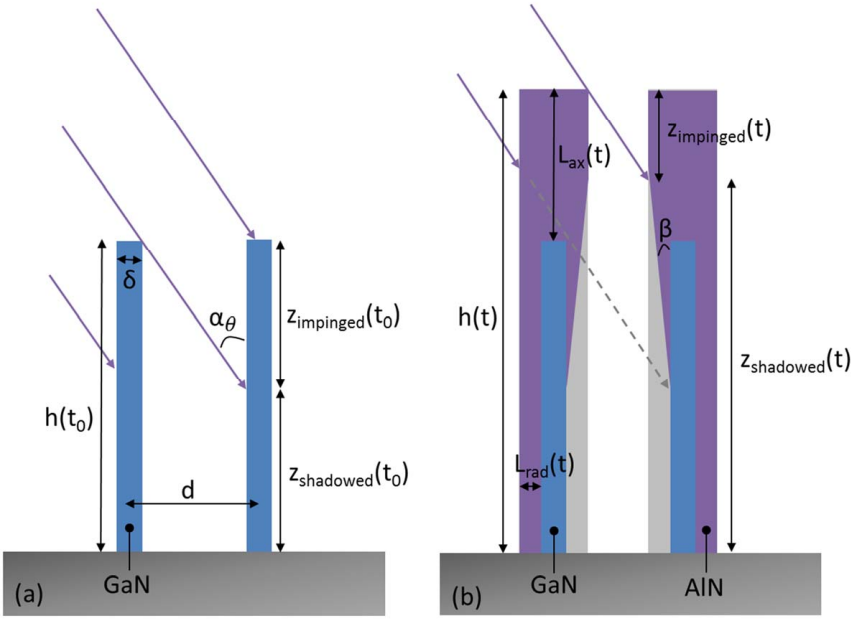

FIG. 5.4 – Illustration of the shadow effect: (a) schemes GaN NW cores at time t_0, that is the time of AlN deposition start; (b) schemes GaN-AlN core-shell NWs at time t of the AlN deposition. $h(t_0)$ is the height of GaN NW cores, δ their diameter and d, the distance between two of these columns. The considered atomic flux (for instance Al) impinge the NWs with an angle α_θ. $z_{shadowed}(t)$ is the height of the nanocolumn that is shadowed by its neighbour, at time t. Equivalently, $z_{impinged}(t)$ is the height of the nanocolumn that is not shadowed by its neighbour (*i.e.* that is impinged) at time t.

GaN NW basis (d), their mean diameter (δ) and the incidence angle α_θ of these atoms. One can easily see that

$$z_{impinged}(t_0) = \frac{d - \delta}{tan(\alpha_\theta)} \tag{5.26}$$

Similarly, as illustrated by figure 5.4 (b), at an arbitrary time t of the AlN shell deposition

$$z_{impinged}(t) = \frac{d - \delta - 2L_{rad}(t)}{tan(\alpha_\theta)} \tag{5.27}$$

Now the length of the NW that is shadowed may be expressed as

$$z_{shadowed}(t) = h(t) - z_{impinged}(t) \tag{5.28}$$

where $h(t)$ is the total length of the column composed of GaN and AlN at time t, hence

$$z_{shadowed}(t) = h(t_0) + L_{ax}(t) - z_{impinged}(t) \tag{5.29}$$

Then, inserting equation 5.27 and considering that $\nu_{ax,rad} = L_{ax,rad}(t)/t$, one get

$$z_{shadowed}(t) = h(t_0) - \frac{d-\delta}{tan(\alpha_\theta)} + \left(\nu_{ax} + \frac{2\nu_{rad}}{tan(\alpha_\theta)}\right) \cdot t \tag{5.30}$$

where ν_{rad} is here the nominal radial growth rate, that is, the growth rate that one would expect when no shadow effect occurs and which can be considered as constant in time. In practice, the radial growth at a given height z of $h(t)$ is aborted once this height becomes shadowed. In other words, the effective shell thickness during growth at the height z is determined by the time $t_{shadowed}(z)$ at which Al stops reaching this height, which can be expressed as

$$L_{rad}(z,t) = \begin{cases} \nu_{rad} \cdot t & t \leq t_{shadowed} \\ 0 & t \geq t_{shadowed} \end{cases} \tag{5.31}$$

At the end of the growth, that is after a deposition time t_{growth} the final shell thickness at a height z is therefore given by

$$L_{rad}(z) = \begin{cases} \nu_{rad} \cdot t_{shadowed}(z) & z < z_{shadowed}(t_{growth}) \\ \nu_{rad} \cdot t_{growth} & z > z_{shadowed}(t_{growth}) \end{cases} \tag{5.32}$$

where $z_{shadowed}(t_{growth})$ is the boundary height below which the NW is shadowed at the end of the shell deposition and above which the column is free of shadowing. Based on equation 5.30, we can expressed $t_{shadowed}(z)$ as

$$t_{shadowed}(z) = \left(z - h(t_0) + \frac{d-\delta}{tan\,(\alpha_\theta)}\right) \frac{tan\,(\alpha_\theta)}{\nu_{ax} tan\,(\alpha_\theta) + 2\nu_{rad}} \tag{5.33}$$

to finally get that

$$L_{rad}(z) = \begin{cases} \left(z - h(t_0) + \frac{d-\delta}{tan(\alpha_\theta)}\right) \frac{tan(\alpha_\theta)\nu_{rad}}{\nu_{ax} tan(\alpha_\theta) + 2\nu_{rad}} & z < z_{shadowed}(t_{growth}) \\ \nu_{rad} \cdot t_{growth} & z > z_{shadowed}(t_{growth}) \end{cases} \tag{5.34}$$

From equation 5.34, it can be seen that L_{rad} increases linearly with the NW height z in the zone where $z < z_{shadowed}(t_{growth})$ and is constant at the apex of the NW when $z > z_{shadowed}(t_{growth})$. This means that, as depicted in figure 5.4 (b), when a column is shadowed by its neighbours, the AlN shell grows with a conical shape around the GaN NW basis. This conic geometry is however interrupted in the upper NW portion which is not affected by shadow effects: the core-shell nanowire retrieves there its vertical facets. The splay angle β of the cone-like shell can be estimated as

$$tan(\beta) = \frac{\nu_{rad} \cdot t_{growth}}{z_{shadowed}(t_{growth}) - z_{shadowed}(t_0)} \tag{5.35}$$

Typically, if we consider $h(t_0) = 400$ nm, $d = 100$ nm, $\delta = 30$ nm, $\alpha_\theta = 30°$, $\nu_{ax} = 0.0625$ nm/s, $\nu_{rad} = 0.00625$ nm/s, $t_{growth} = 7200$ s, we get that β is of the order of 2-3°.

5.1.2 Experimental observations

For the experimental part of this study, two series of samples were elaborated. For all the samples, GaN NWs were first grown using the same conditions of temperatures, fluxes and deposition time on top of a thin AlN buffer layer. In order to well separate the nanocolumns, thus avoiding as much as possible shadow effects and coalescence between NWs, a high substrate temperature of 845 ℃ was used. As a result, no GaN was incorporated at the center of the wafer but thanks to the temperature gradient along the wafer radius, a suitable GaN NW density could be achieved near the wafer periphery (see chapter 2 and details hereafter). On top of these GaN NW bases, AlN was subsequently deposited for 2 hours, using different manipulator angles θ for each sample. The difference between the two series stands in the choice of the nominal AlN growth rates of 0.25 ML/s and 0.16 ML/s for the first and the second series, respectively. These growth rates respectively correspond to η values of 0.86 and 0.55. Table 5.2 summarizes the samples grown for each series.

		Manipulator position			
		$\theta = 0°$	$\theta = 8°$	$\theta = 15°$	$\theta = 30°$
Al/N ratio	η=0.55	N1840	N1832	N1842	N1844
	η=0.86	N1838	N1834	N1843	N1846

TABLE 5.2 – Samples grown for the study of the AlN shell morphology dependence on the growth conditions.

5.1.2.1 GaN-AlN core-shell nanowire density

As explored in chapter 2, a gradient of temperature exists on the 2-inch silicon substrates that we use. A consequence of this temperature gradient is a density gradient along the substrate radius. Typically at 845 ℃, the GaN NW density spans from nearly coalesced nanocolumns to nearly no nanocolumns at all. Naturally, in the zones where the density is the highest, the above described consequences of shadow effects are expected to be observed. On the other hand, both the desorption rate and diffusion of Al adatoms are expected to remain low, even at 845 ℃. Hence, when depositing AlN on top of a zone where the GaN NW density is low, AlN also grows on the substrate, between the NWs and bury them.

Figure 5.5 illustrates this issue. These SEM images were taken near the peripheral ring, along the substrate radius of sample N1834 grown at a manipulator angle $\theta = 8°$ with an η value of 0.86 and highlight the density gradient. It can be seen that for the highest NW density (top view SEM image in figure 5.5 (a) and corresponding cross sectional view in figure 5.5 (d)), the AlN can not reach the side-walls, because these surfaces are shadowed by the neighbouring NWs. AlN thus nearly fully incorporates on the top

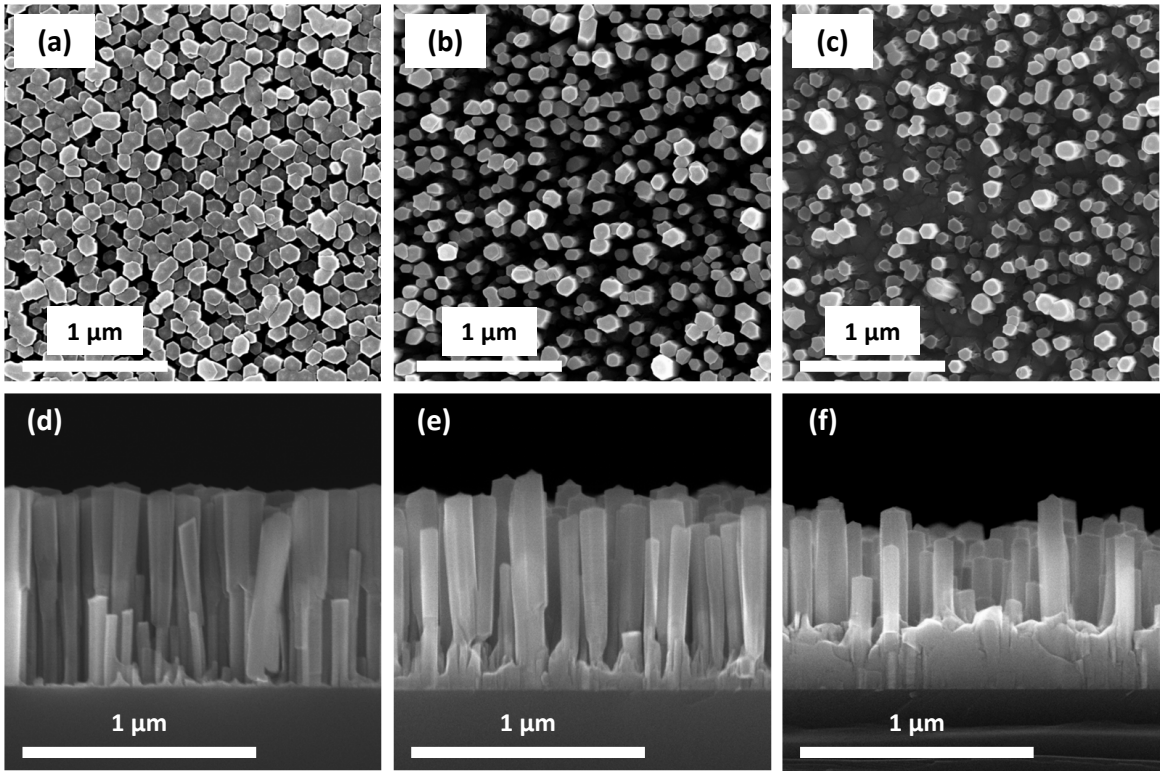

FIG. 5.5 – SEM top view and corresponding cross-sectional view images of GaN-AlN core-shells NWs taken along the radius of the 2-inch silicon substrate of sample N1834. If the NWs are too dense ((a) and (d)), shadow effects occur. If the NWs density is too low ((c) and (f)), a thick AlN layer forms on the silicon substrate, burying the NWs. NWs investigated in transmission in the following part of the section, were therefore taken from zones where the density was the most suitable, as shown in (b) and (e).

surface. Conversely, figures 5.5 (c) and (f) present NWs whose density is too low and where the core-shell structures have literally been buried to half of their length. The compromise between these two situations is a density of the order of that presented in figures 5.5 (b) and (e). In this case, the NWs are sufficiently separated to avoid shadow effects but not too distant either, so that the rough surface 2D layer remains thin enough not to bury the NWs.

5.1.2.2 Morphologies of the AlN shell

It must be noted that although NWs are better separated in the zone corresponding to figures 5.5 (b) and (e) than in the zone corresponding to figures 5.5 (a) and (d), they are still not perfectly distributed. In consequence, even if it is possible to find some sufficiently isolated NWs, they are not all fully spared by shadow effects and display various morphologies. Figure 5.6 illustrates some of these different morphologies. Typically, most of the NWs resemble NWs ❶ and ❸ whose AlN shell does not have a constant thickness

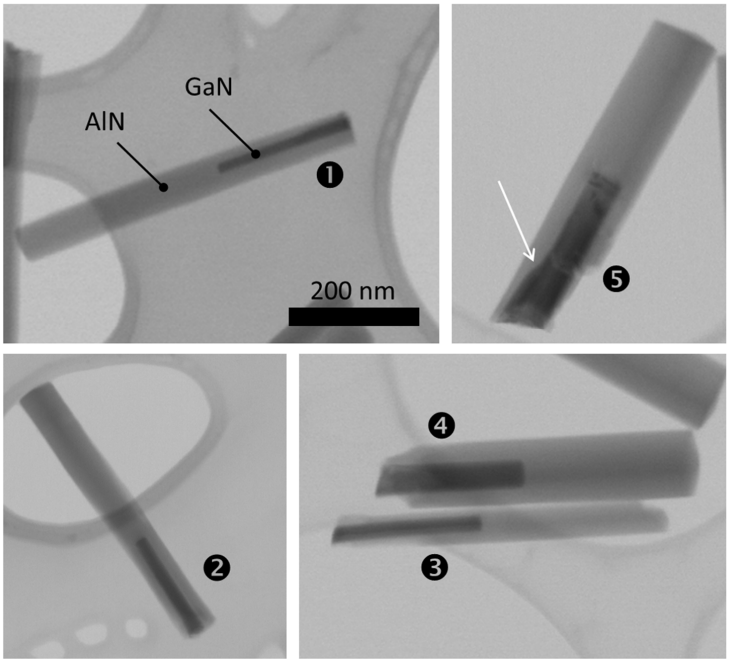

FIG. 5.6 – SEM images taken in transmission of GaN-AlN core-shells NW heterostructures displaying various characteristic morphologies. The NWs originate from the same sample and were scrapped off from a zone where their density was adapted, as shown in figures 5.5 (b) and (e). The scale bar stands for all the images.

along the whole periphery of the GaN core. NWs with a more symmetrical AlN shell, such as NW ❷ and ❹, can also be found, but more rarely. The inhomogeneity of the AlN shell thickness may be due to the proximity of another NW near the thinner side of the shell, inducing shadow effect. On the other hand, an homogeneous shell does not guarantee that no shadow effect took place. This can be seen when comparing the thickness of the shell of NW ❷ and ❹. The thicker shell exhibited by NW ❹ proves that a higher lateral growth rate than that of NW ❷ is possible. In other words, one can consider that NW ❷ was also subjected to shadow effects but only on one of its sides. Consequently, for the subsequent analysis of SEM images taken in transmission, only the thicker shells were measured. Conversely, it sometimes happens that a thick AlN shell is not a real shell. It is typically the case of NW ❺, which displays a step at the foot of the GaN core (pointed out by a white arrow). In this case, AlN incorporation on top of the step may be confused with incorporation on the side-walls above the step.

Interestingly, when focusing on some NWs, the conical shape of the AlN shell, expected from calculation presented in section 5.1.1.3, is observable, highlighting the occurrence of shadow effects (Fig. 5.7).

Based on these observations, the analysis of SEM images taken in transmission described in the following section were made with an extreme care. First, NWs scrapped off from a given sample were taken from the zone with the suitable NW density. Then, the investigated NWs were not randomly taken into account but were selected from the whole scrapped off bunch: only the thicker shells were measured, excluding those grown on/around GaN cores having a step at their foot.

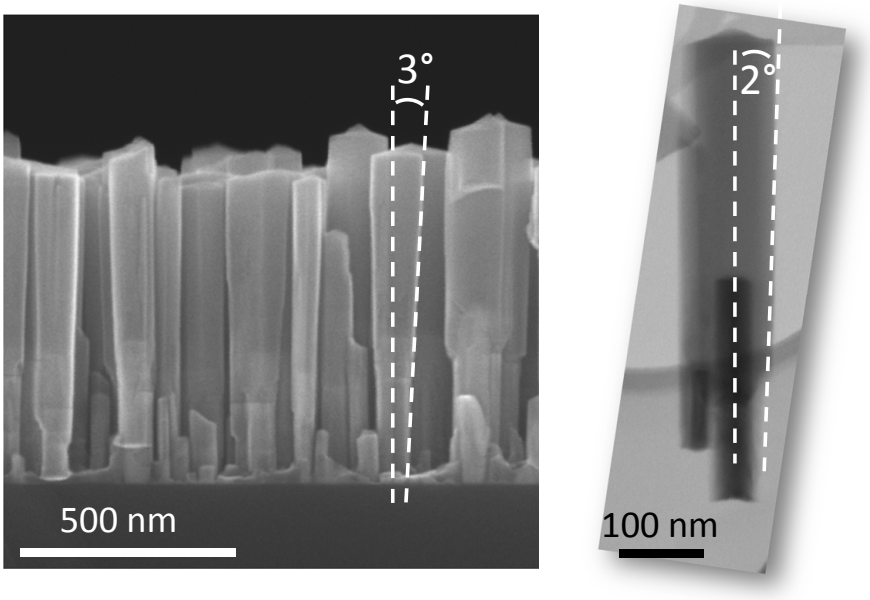

FIG. 5.7 – Cross-section view SEM image and SEM image taken in transmission of core-shell NWs having a conical AlN shell due to shadowing from neighbouring NWs.

5.1.2.3 AlN shell aspect ratio dependence on the atomic beams incidence angle

Figure 5.8 shows SEM images taken in transmission of one homogeneous, representative NW from each sample. A difference in the shell morphology can clearly be observed. At first sight, this change in morphology seems to be induced by the variation of θ rather than by the change of η. In addition, an increase in θ seems to diminish the length of the top AlN segment but does not noticeably thicken the shell.

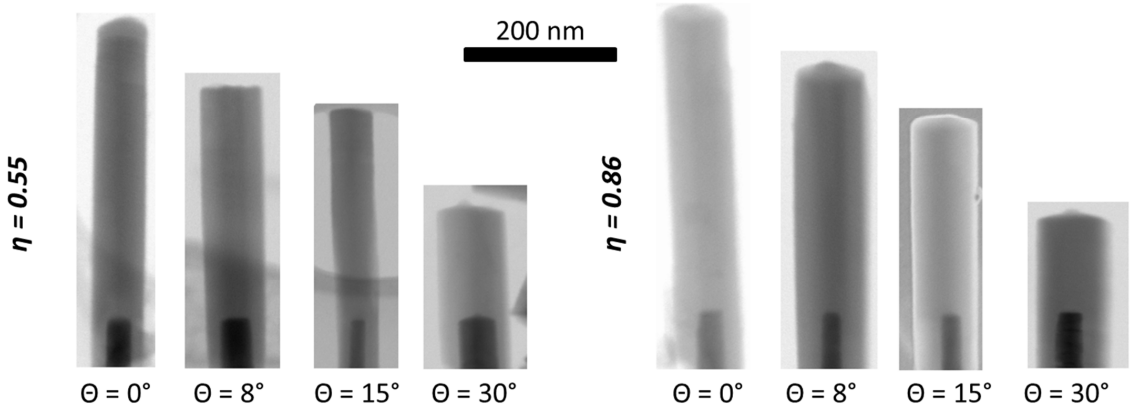

FIG. 5.8 – SEM images taken in transmission of GaN-AlN core-shell NWs grown in various conditions of η and θ. The darker material is the GaN core and the lighter material is AlN.

With the aim of quantifying these observations, SEM images taken in transmission

were used to measure the length of the AlN top segment and the thickness of the AlN shell. For sake of statistical relevancy, about 30 NWs were investigated for each sample. Figure 5.9 presents the evolution of the ratio L_{ax}/L_{rad} versus θ for shells grown with $\eta = 0.86$ (full squares) and with $\eta = 0.55$ (full circles). The error on θ is estimated to be about 2° because of play in the manipulator rotation. The dispersion in L_{ax}/L_{rad} is the standard deviation from the mean value. In addition, the dashed and the dotted lines represent equations 5.24 and 5.25, respectively calculated for $\eta = 0.55$ and $\eta = 0.86$.

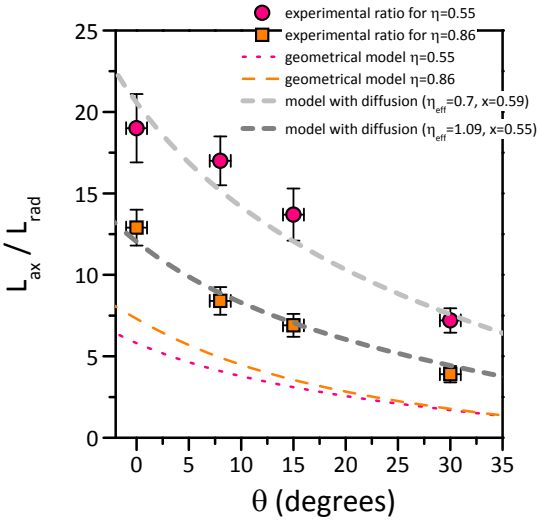

FIG. 5.9 – Variation of L_{ax}/L_{rad} as a function of θ and comparison to the geometric model described in section 5.1.1.

As expected, for a given η, L_{ax}/L_{rad} decreases with increasing θ. However, one can see that for both values of η, the geometrical model underestimates L_{ax}/L_{rad}. Let us recall that in our geometric model, we assumed that neither Al nor N atoms diffuse nor desorb. The discrepancy observed between the model and the actual AlN shell shape suggests that at least one of these assumptions does not reflect the reality.

In order to further investigate this issue, let us have a look at L_{ax} and L_{rad} separately and compare them to their expected values $L_{ax,expected}$ and $L_{rad,expected}$, respectively. Based on the AlN growth rate (η_{AlN}), given in monolayers per second (ML/s) and measured by mean of RHEED oscillations, the expected length $L_{ax,expected}$ of the AlN top segment may be estimated as

$$L_{ax,expected} = 0.25 \cdot \eta_{AlN} \cdot t_{growth} \cdot cos(\theta) \tag{5.36}$$

where t_{growth} is the duration of the AlN deposition, 0.25 is the proportionality coefficient between monolayers and nanometres (one AlN wurtzite cell is composed of two monolayers and $c_{AlN} \approx 0.5\ nm$) and $cos(\theta)$ takes into account the angle at which the AlN is deposited since the determination of the growth rate is itself always made at $\theta = 0$. $L_{rad,expected}$ is then determined as $L_{ax,expected}$ divided by the theoretical L_{ax}/L_{rad} ratio displayed in figure 5.9.

Figures 5.10 (a) and (b) respectively show the variation of L_{ax} and L_{rad} as a function of θ for shells grown with $\eta = 0.55$ (circles) and $\eta = 0.86$ (squares). For both values of η, $L_{ax,expected}$ and $L_{rad,expected}$ are represented by the dashed and dotted lines. In addition, the black line represents $L_{ax,max}$ and $L_{rad,max}$, that is the maximal length that the top segment and the shell can have, as fixed by the AlN growth rate at stoichiometry, or in other words, as fixed by the N flux.

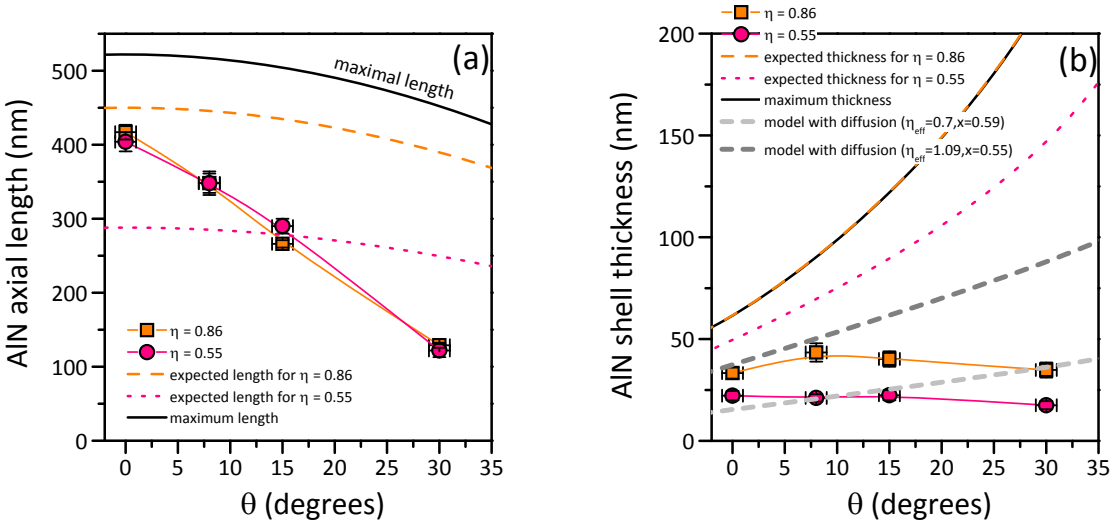

FIG. 5.10 – Variation of (a) L_{ax}, the length of the AlN top segment and (b) L_{rad}, the thickness of the AlN shell as a function of θ.

Now, if we want to analyze these data more quantitatively, one must be careful and consider only the values determined at $\theta = 0$. As a matter of facts, at $\theta = 0$, the position of the substrate is optimized to be at the "focal point" of all the Knudsen cells. In this position, the center of the wafer therefore receives the maximum quantity of atoms. Now, when rotating the manipulator to another position, as shown in figure 5.11, the center of the wafer (which is about 10 cm ahead from the manipulator center of rotation) no longer is at the focal point of the Knudsen cells. In this new position, the wafer is thus reached by less atoms than the value one would find when simply applying an angular correction. The study of the fluxes gradient going beyond this study, we will only focus on values determined at $\theta = 0$ for quantitative analysis of L_{ax} and L_{rad}. Note that the ratio L_{ax}/L_{rad}, on the other hand, should not be affected by the "loss of atoms" occurring at $\theta > 0$.

Considering now data at $\theta = 0$ on figures 5.10 (a) and (b), one can note that for $\eta = 0.55$, the axial AlN segment is 40 % longer than expected (400 nm instead of 288 nm) while the thickness of the shell is only about half that predicted by the geometrical model.

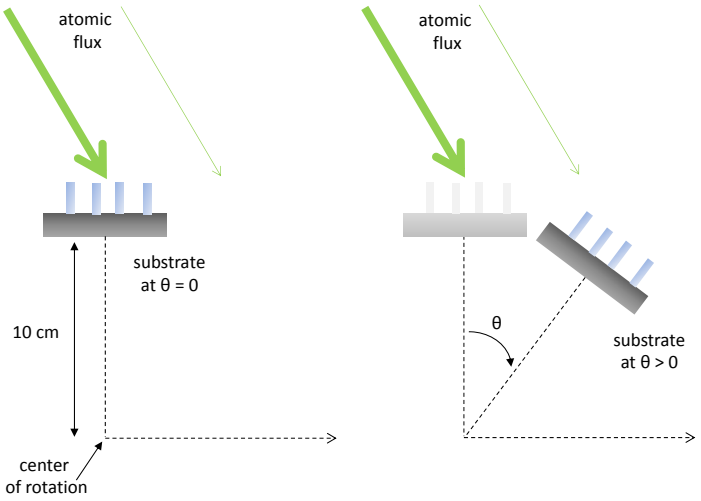

FIG. 5.11 – Scheme of the system. As the center of rotation is about 10 cm away from the center of the substrate, when rotating the manipulator to $\theta > 0$, the substrate is not anymore at the "focal point" of the Knudsen cells. The amount of atoms reaching the substrate is therefore less important than at $\theta = 0$.

These observations strongly suggest that part of the Al atoms impinging on the NW side-walls has diffused to the top surface and incorporated there. For $\eta = 0.86$, the case is somewhat different. Although the thickness of the shell is also only half that predicted by the geometrical model, L_{ax} is 7 % **lower** than its expected value. To understand this, a striking feature deserves to be pointed out: the evolution of L_{ax} with θ is similar for both values of η (Fig. 5.10 (a)). Both sets of data indeed completely overlap, as if the growth rate along the axis was independent from the nominal growth rate, or in other words, from the Al fluxes used. The similarity of L_{ax} evolution when using $\eta = 0.55$ and $\eta = 0.86$ is therefore a strong indication that the axial growth rate is actually not limited by Al but by N atoms. Nevertheless, at $\theta = 0$, experimental values of L_{ax} are about 21 % lower than the value they should exhibit with a growth limited by these N species (maximal value depicted by the black line). This suggests that a large proportion of N species have desorbed. Such hypothesis is reasonably justified by the fact that the growth rate determination by mean of RHEED oscillations is made at a much lower temperature (about 790 °C) than that used for the growth the AlN shell. Moreover, nitrogen desorption is known to be possible via re-formation of N_2 molecules. It has been calculated by Lymperakis that the N deorption rate is high at 845 °C [244]. In summary, the analysis of figures 5.10 (a) and (b) tends to indicate that a large proportion of Al atoms impinging on the NW side-walls diffuse to the top surface where the AlN growth rate is then limited by N atoms, part of which have desorbed. Regarding Al atoms in excess on the top surface, one can venture the hypothesis that they eventually desorb.

5.1.2.4 Geometrical model including Al diffusion

Let us now try to incorporate Al diffusion in our model. If part of the Al atoms reaching the side-walls diffuse towards the top surface where the growth is then limited by N atoms, it means that the growth conditions are *de facto* different from those considered in our preliminary hypotheses. More specifically, the top surface is Al-rich rather than N-rich

(as previously thought based on figure 5.3 (a)). In addition, as 21 % of N atoms desorb on the top surface, the effective growth rate at stoichiometry is only 0.79 times the one previsouly considered:

$$\eta_{AlN,stoichio,eff} = 0.79 \cdot \eta_{AlN,stoichio} \tag{5.37}$$

Hence

$$\eta_{eff} = \frac{\eta_{AlN}}{\eta_{AlN,stoichio,eff}} = \frac{\eta}{0.79} \tag{5.38}$$

In other words

$$\begin{cases} \eta_{eff,0.55} = 0.7 \\ \eta_{eff,0.86} = 1.09 \end{cases} \tag{5.39}$$

Let us name χ_{Al} the quantity of Al atoms diffusing from the side-walls to the top surface. Then χ_{Al} is a proportion x of the Al atoms on the side-walls $\frac{\Phi_{Al} sin(\alpha_{Al,\theta})}{\pi}$, which can be written as $\chi_{Al} = x\frac{\Phi_{Al} sin(\alpha_{Al,\theta})}{\pi}$ where $x \leq 1$. This quantity χ_{Al} must be subtracted from the atoms incorporated on the side-walls and added to the atoms incorporated on the top surface. In the end, on the Al-rich top surface, the axial growth rate limited by N species reads

$$\nu_{ax} = \frac{2\Phi_N}{\sigma_c} cos(\alpha_{N,\theta}) \tag{5.40}$$

and on the side-walls, although N likely also desorb there, because a large quantity of Al has diffused to the top surface, we consider a N-rich environment. Hence, the radial growth rate reads

$$\nu_{rad} = \Phi_N \frac{1}{\pi} \frac{2\eta_{eff}}{\sigma_m} \frac{cos(\alpha_{N,0})}{cos(\alpha_{Al,0})} sin(\alpha_{Al,\theta})(1-x) \tag{5.41}$$

hence it comes that the ratio $\frac{L_{ax}}{L_{rad}}$ reads

$$\frac{L_{ax}}{L_{rad}} = \frac{\pi}{\eta_{eff}} \frac{cos(\alpha_{Al,0})}{cos(\alpha_{N,0})} \frac{cos(\alpha_{N,\theta})}{sin(\alpha_{Al,\theta})} \frac{1}{(1-x)} \tag{5.42}$$

Equation 5.42 is reported as the gray dashed lines in figure 5.9 for $\{\eta_{eff} = 0.7, x = 0.59\}$ (light grey) and for $\{\eta_{eff} = 1.09, x = 0.55\}$ (dark grey). Each set of points is quite well fitted by its corresponding function. The same equation was used to compute the new $L_{rad,expected}$ taking into account Al diffusion. Those new $L_{rad,expected}$ are displayed in figure 5.10 (b) as the grey dashed lines. At $\theta = 0$, the model including Al diffusion reasonably fits the measured shell thicknesses. One can hence deduce from these fits that about 55–60 % of the Al atoms impinging on the side-walls are not incorporated there and diffuse to the top surface where the AlN axial growth rate is eventually limited by N species.

5.1.2.5 Discussion and conclusions on the AlN shell growth mechanisms and morphology

The comparison between our model and experimental data shows that the morphology of AlN shells cannot be described by simple geometrical considerations, only, but its understanding requires taking into account that a large proportion of Al atoms diffuse from the side-walls of the NWs to their top surface. To our knowledge, this is the first time that the diffusion of Al on "AlN NW" facets is experimentally evidenced. Interestingly, it is possible to draw a parallel between the diffusion of Al along AlN NW facets and Ga on GaN NW facets, system which has been already more widely studied and described in the litterature. Jindal and Shahedipour-Sandvik actually calculated that on $(1\bar{1}00)$ AlN surfaces, the energy barrier for Al to diffuse in the [0001] direction is 2.79 eV, about 25 times larger than in the $[11\bar{2}0]$ direction (0.11 eV) [245]. Regarding the Ga/GaN system, Lymperakis calculated that the diffusion barrier energy of Ga on $(1\bar{1}00)$ GaN surfaces is 0.93 eV in the [0001] direction and 0.21 eV in the $[11\bar{2}0]$ direction [244]. These data are summarized in table 5.3.

	directions		reference
	[0001]	$[11\bar{2}0]$	
Ga on GaN	0.93 eV	0.21 eV	[244]
Al on AlN	2.79 eV	0.11 eV	[245]

TABLE 5.3 – Diffusion barrier energies of Ga on GaN and Al on AlN $(1\bar{1}00)$ surfaces, taken from [244] and from [245].

For both Ga on GaN and Al on AlN, the diffusion barrier energy is larger in the [0001] direction than in the $[11\bar{2}0]$ direction. This suggests that Ga (resp. Al) on GaN (resp. AlN) do not diffuse along the NW length but sort of "zigzag" on the NW facets to the top surface. Regarding GaN, its has already been established that diffusing Ga atoms contribute noticeably to the axial growth rate [78, 196, 246], despite the "non-straightforward" path followed by these species. Likely, in the case of AlN, the large diffusion barrier of 2.79 eV in the [0001] direction somewhat hinders the diffusion of Al species, despite the low diffusion barrier of 0.11 eV in the $[11\bar{2}0]$ direction. These hypotheses are consistent with the non-negligible NW lateral growth rate achievable with AlN and with the difficulties to thicken GaN NWs.

Regarding the control of the AlN shell morphology, although the geometrical model predicts that at given η, increasing θ permits to thicken the lateral contribution, one can see that, it is not the case experimentally. For the grown core-shell structures, the lateral contribution thickness actually remains more or less constant for all θ at given η. On the other hand, the axial segment length drastically decreases with increasing θ, a consequence of the "out-of-focus" position of the sample at $\theta > 0$. Hence, although the shell is not effectively thickened, the ratio between the top and the lateral AlN contributions

of the shell decreases with increasing θ down to 5 at theta $\theta = 30°$ (this corresponds to atomic incidence angles of 50 and 60°), following the trend given by our geometrical model including diffusion. Further decrease of this ratio at larger θ would certainly be compromised by severe shadow effects. One alternative to foster the thickening of the lateral contribution while limiting the lengthening of the top contribution could focus on the reduction of Al diffusion, which could for instance be attempted by lowering the growth temperature.

5.2 Structural properties of GaN-AlN core-shell heterostructures

The aim of this section is to investigate the structural properties of GaN-AlN core-shell heterostructures and more particularly, the effect of the shell thickness on the strain of GaN cores and on the strain relaxation mechanisms. To do so, a series of core-shell nanowires was studied. In this series, only the AlN deposition time was varied, resulting in core-shell samples with identical GaN cores and different AlN shell thicknesses, ranging from 0.8 nm to 12.0 nm as verified by SEM images taken in transmission. The AlN growth rate used for this series is such that $\eta = 0.55$ and the manipulator was kept at its usual position (*i.e.* $\theta = 0°$) resulting is a large L_{ax}/L_{rad} of 21.5 ± 1.6 (the Al Knudsen cell is different from the one used in the previous section and the angle $\alpha_{Al',0}$ is here equal to 20°).

5.2.1 AlN shell induced strain within GaN cores

5.2.1.1 Resonant X-ray diffraction

Samples were investigated by resonant X-ray diffraction at the BM02 beamline of the ESRF with the eight-circle diffractometer equipment. Reciprocal space maps around the $(10\bar{1}5)$ and around the $(30\bar{3}2)$ Bragg reflections of relaxed AlN were measured with a Vantec^{TM} linear detector at different energies of the incident X-ray beam, close to the Ga K-edge (10.367 keV). Figures 5.12 (a) and (d) present such maps obtained around the $(10\bar{1}5)$ reflection of core-shell nanowires having an average AlN shell thickness of 1.9 nm and 12 nm, respectively. Similarly, figures 5.13 (a) and (d) present those maps for the $(30\bar{3}2)$ reflection. These reciprocal spaces were taken large enough to cover also the Bragg reflection of the GaN core. Stars, added on the maps, indicate the position of relaxed GaN and AlN in the reciprocal space.

Ga scattering contribution (modulus of the Ga partial structure factor) and {Al+N} scattering contributions (modulus of the {Al+N} partial structure factor) were extracted by C. Leclere through the analysis of MAD measurements (see chapter 1). Figures 5.12 (b) and (e) as well as figures 5.13 (b) and (e) show such extracted maps of the Ga contribution

$|F_{Ga}|^2$. In addition, figures 5.12 (c) and (f) as well as figures 5.13 (c) and (f) show maps of the non-resonant ({Al+N}) contributions. Note that these maps are given in the reciprocal space of relaxed AlN. This choice was made because the large AlN top segment of the shell (referred to as "axial segment" in the previous section) above GaN cores is relaxed (this will be discussed and illustrated later – see for instance figure 5.16). However, because of a recurring data acquisition problem on the setup used, maps of figures 5.12 and 5.13 are slightly shifted compared to the position they should have. This can for instance be seen in figure 5.12 (d): the maximum of the AlN peak is not exactly located at $(10\bar{1}5)$ (indicated by the star) where the relaxed contribution of the AlN shell is expected to appear. Nevertheless, in the following, when reciprocal space coordinates will be given, they will already be shift-corrected.

For the sample with the thinner shell (Fig. 5.12 (a)), one peak is located very near the relaxed GaN position while nearly no signal is detectable at the relaxed AlN position. This is consistent with the fact that in this case, very little AlN has been deposited and that the small amount of deposited AlN is lattice-matched to GaN. Now, concerning the total contributions detected for the sample with the larger shell (Fig. 5.12 (d)), two peaks are observed: a strong one at the relaxed AlN position and another one, shifted from relaxed GaN position towards AlN. Interestingly, the GaN peak seems to shift towards AlN with the thickening of the shell. The same is observable on the $(30\bar{3}2)$ maps (Figs. 5.13 (a) and (d)), although the GaN shift is less pronounced than with the $(10\bar{1}5)$ reflection.

Although it is not possible to distinguish between Al and N contributions, a precise estimation of the GaN strain level can be determined from the Ga contribution maps. More specifically, $(10\bar{1}5)$ reflections being more sensitive to the out-of-plane parameter c, the related Ga contribution $|F_{Ga}|^2$ maps were used to extract informations on ϵ_c, the strain component along the <0001> direction, as

$$\epsilon_c = \frac{c_{GaN} - c^0_{GaN}}{c^0_{GaN}} = \frac{l^0_{GaN} - l_{GaN}}{l_{GaN}} \tag{5.43}$$

where c^0_{GaN} is the relaxed c parameter of GaN, c_{GaN} is the strained one, l^0_{GaN} is the value of the Miller index l of relaxed GaN in the relaxed AlN reciprocal space and l_{GaN} is the (corrected) value obtained from the $(10\bar{1}5)$ $|F_{Ga}|^2$ contribution maps of the strained GaN core. On the other hand, maps taken around the $(30\bar{3}2)$ reflection rather provide informations about the in-plane parameter a and thus are used to estimate the in-plane strain ϵ_a as

$$\epsilon_a = \frac{a_{GaN} - a^0_{GaN}}{a^0_{GaN}} = \frac{h^0_{GaN} - h_{GaN}}{h_{GaN}} \tag{5.44}$$

a^0_{GaN} being the relaxed a parameter of GaN, a_{GaN} is the strained one, h^0_{GaN} is the value of the Miller index h of relaxed GaN in the relaxed AlN reciprocal space and h_{GaN} is

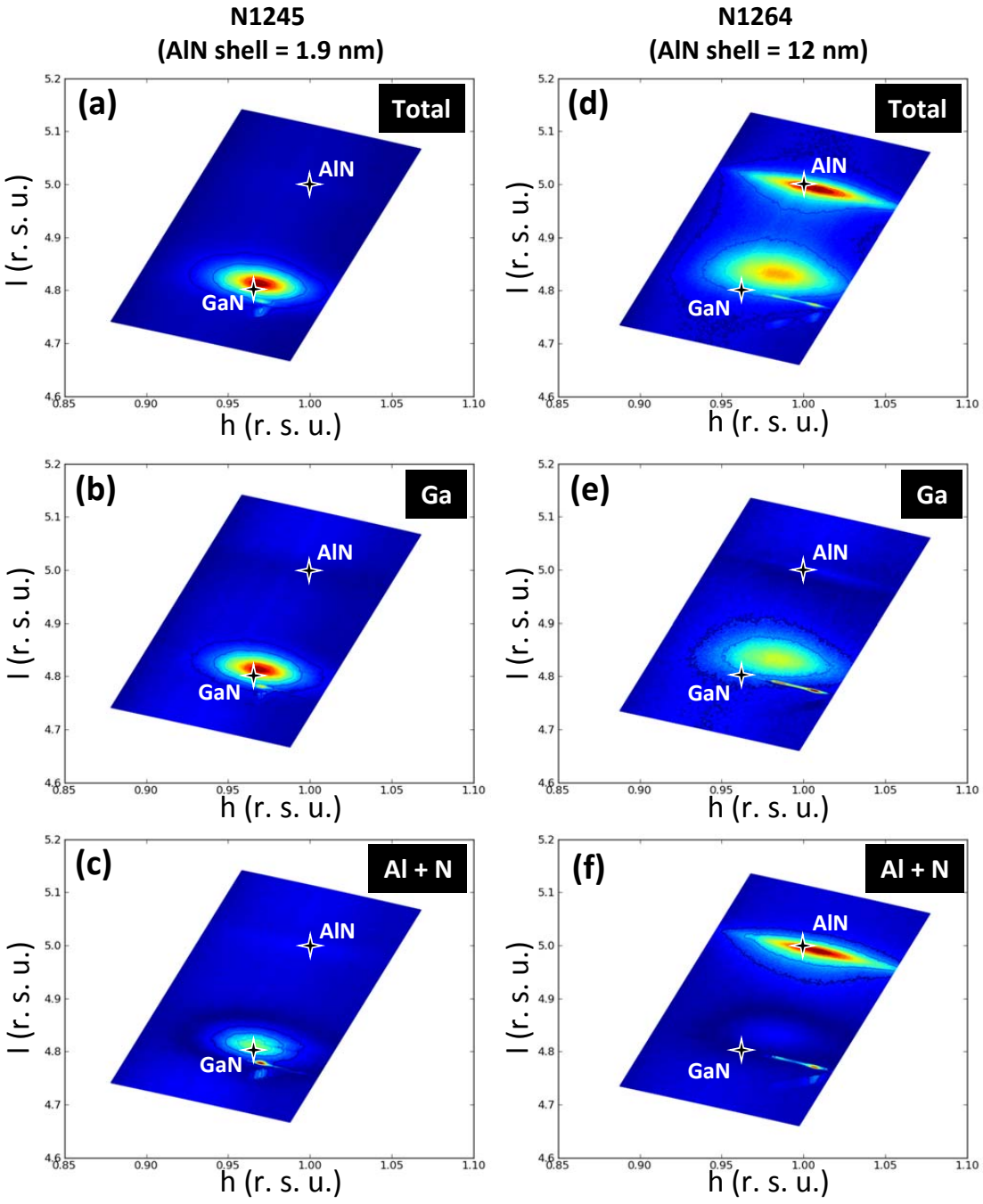

FIG. 5.12 – Reciprocal space maps taken around the $(10\bar{1}5)$ AlN Bragg reflection. (a) and (d) $|F_T|^2$ total Thomson scattering maps; (b) and (e) $|F_{Ga}|^2$ extracted resonant atoms scattering contribution; (c) and (f) non-resonant atoms {Al+N} scattering contribution obtained on sample N1245 (thin AlN shell) and sample N1264 (thicker AlN shell). Stars show positions of relaxed AlN and GaN.

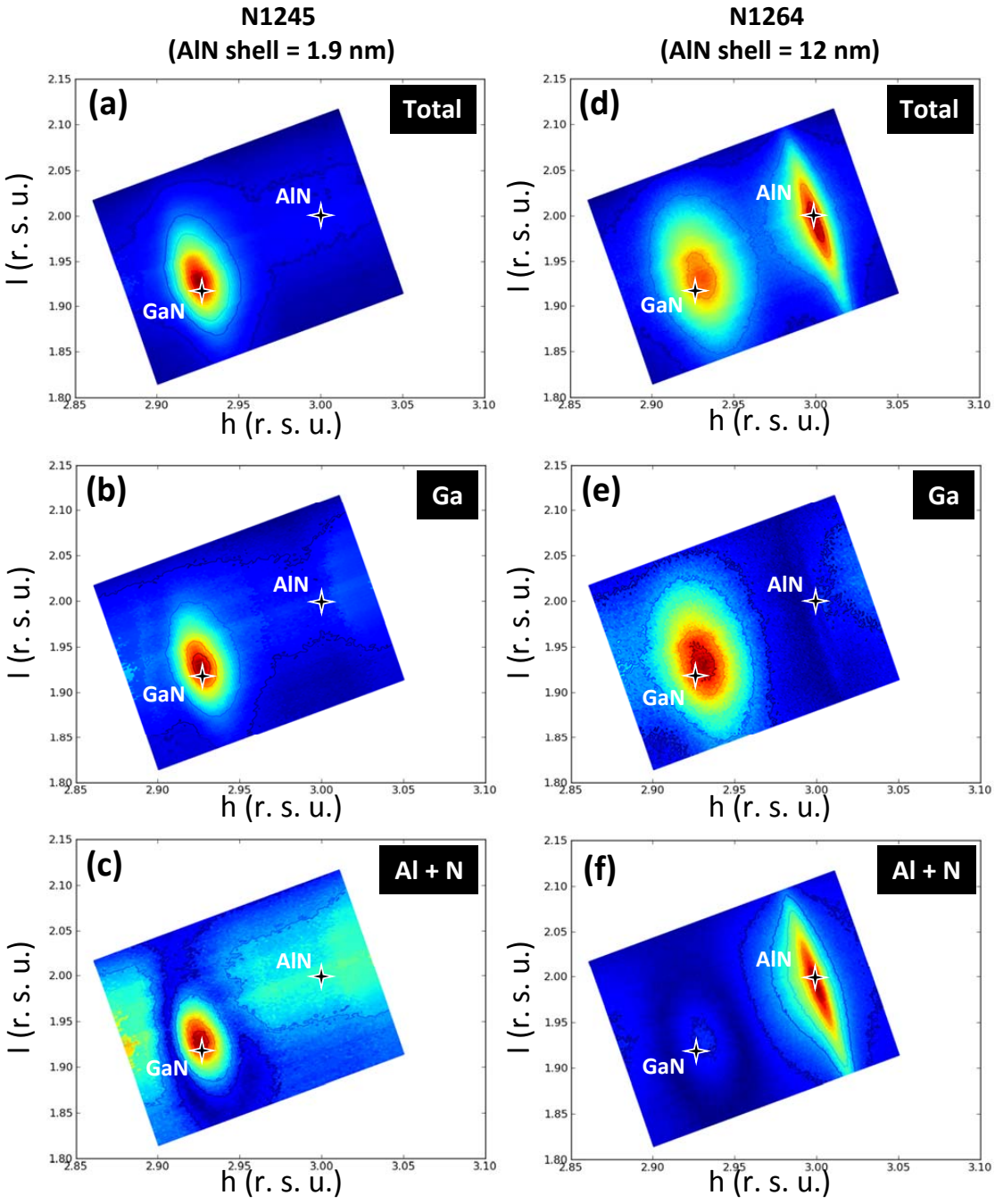

FIG. 5.13 – Reciprocal space maps taken around the $(30\bar{3}2)$ AlN Bragg reflection. (a) and (d) $|F_T|^2$ total Thomson scattering maps; (b) and (e) $|F_{Ga}|^2$ extracted resonant atoms scattering contribution; (c) and (f) non-resonant atoms ({Al+N}) scattering contribution obtained on sample N1245 (thin AlN shell) and sample N1264 (thicker AlN shell). Stars show positions of relaxed AlN and GaN.

the value obtained from the $(30\bar{3}2)$ reciprocal space maps of the strained GaN core. The strains ϵ_a and ϵ_c are plotted in figure 5.14 as a function of the shell thickness (open and full triangles, respectively) for all the investigated samples.

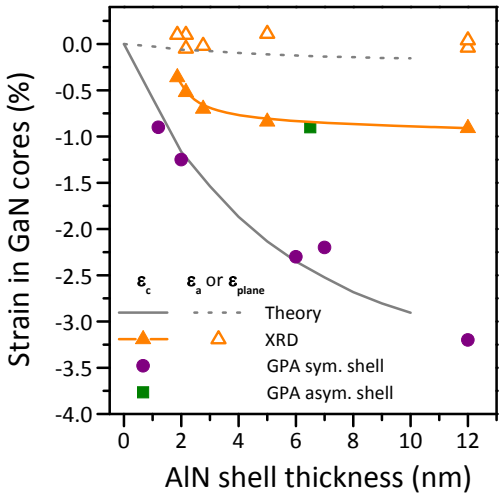

FIG. 5.14 – In-plane (open triangles) and out-of-plane strains (full triangles) $\epsilon_a = \frac{h^0_{GaN} - h_{GaN}}{h_{GaN}}$ and $\epsilon_c = \frac{l^0_{GaN} - l_{GaN}}{l_{GaN}}$ within GaN cores obtained from resonant XRD experiments. Full circles and the full square represent the out-of plain strain values obtained from GPA analyses of HRTEM images taken on NWs with symmetrical and asymmetrical AlN shells, respectively. The dotty line and the full line are theoretically calculated strains $\epsilon_{plane} = \frac{\epsilon_{xx}+\epsilon_{yy}}{2}$ and ϵ_c for a GaN core diameter of 20 nm.

5.2.1.2 Theoretically determined strains

In order to compare these experimental strains to their theoretical evolution, Y. M. Niquet and D. Camacho, from the L-SIM group at Grenoble, simulated GaN-AlN core-shell heterostructures based on an atomistic valence force field model adapted to WZ materials [247]. To do so, they minimized the elastic energy of the system with respect to the atomic positions and without introducing dislocations. In other words, only the elastic relaxation was considered. Then, based on the equilibrium atomic positions, in-plane and out-plane strains were determined with respect to relaxed parameter value of each material.

Figures 5.15 (a), (b), (c) and (d) present maps of the strains ϵ_{xx}, ϵ_{yy}, $\epsilon_{plane} = \frac{\epsilon_{xx}+\epsilon_{yy}}{2}$ and ϵ_c within the cross section of a heterostructure with a GaN core diameter of 20 nm and an AlN shell thickness of 3 nm. Regarding the chosen set of axis (x, y), ϵ_{xx} gives the strain along $< 11\bar{2}0 >$ directions and ϵ_{yy} along $< 1\bar{1}00 >$ directions. The strain ϵ_{yy} is therefore equivalent to the one previously determined by X-rays.

Qualitatively, ϵ_{xx} and ϵ_{yy} maps indicate that the deformation of the AlN cell on the facets (m-planes) is such that a_{AlN} is stretched in parallel to the facet, that is along the $< 11\bar{2}0 >$ direction ($\epsilon_{xx} > 0$) and stressed, or compressively strained, perpendicularly to the facet, that is along the $< 1\bar{1}00 >$ direction ($\epsilon_{yy} < 0$). On the other hand, the GaN core is only weakly compressively strained. The out-of-plane strain ϵ_c is homogeneously

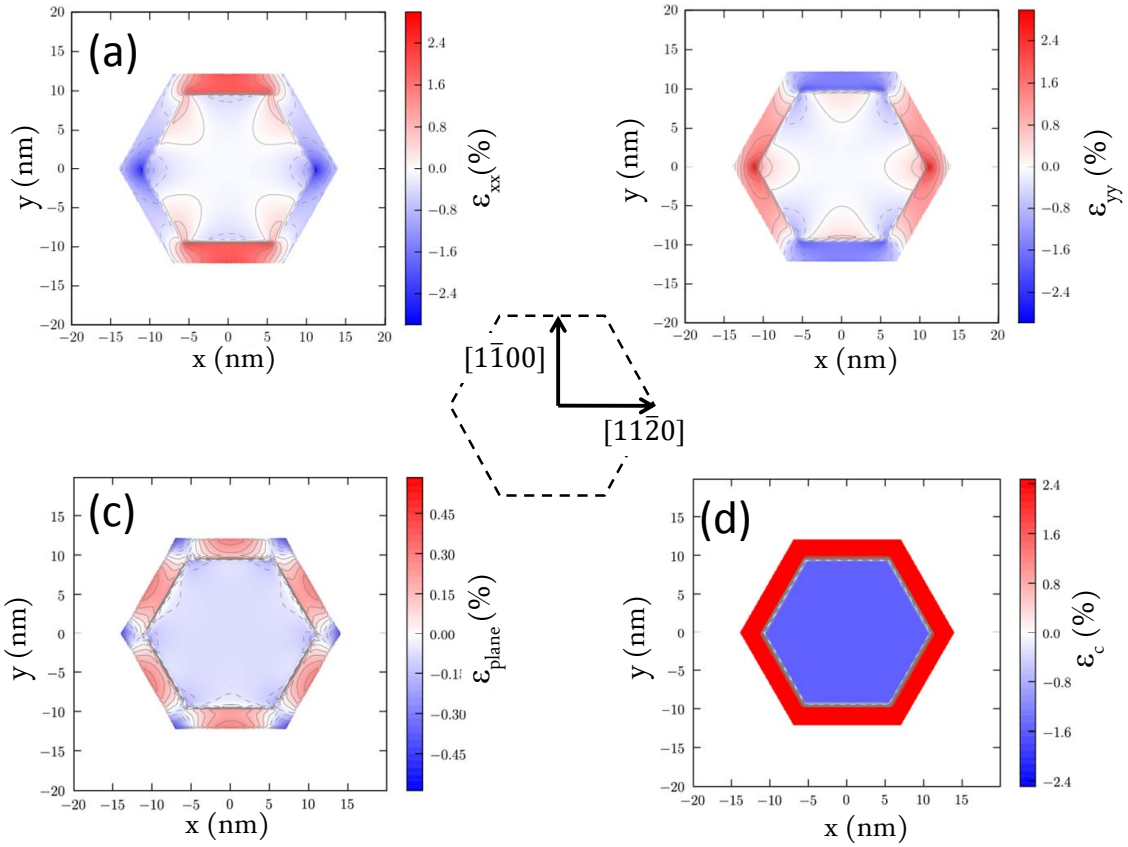

FIG. 5.15 – Theoretically calculated maps of (a) the in-plane strain ϵ_{xx}, along the [11$\bar{2}$0] direction, (b) the in-plane strain ϵ_{yy}, along the [1$\bar{1}$00] direction (c) the average in-plane strain $\epsilon_{plane} = \frac{\epsilon_{xx}+\epsilon_{yy}}{2}$ and (c) the out-of-plane strain ϵ_c of a GaN/AlN core-shell NW cross-section with a GaN core diameter of 20 nm and an AlN shell thickness of 3 nm.

distributed within the cross section and has a magnitude about 10 times larger than the in-plane strain, whether we take into account ϵ_{xx}, ϵ_{yy} or ϵ_{plane}.

Now coming back to figure 5.14, theoretically obtained ϵ_{plane}[2] and ϵ_c are represented by dotty and full lines, respectively. One can see that despite small fluctuations and following the theoretical trend, the in-plane strain ϵ_{plane} determined by X-rays is close to zero, which means that the a lattice parameter of the GaN core is not or weakly strained by the AlN shell. On the other hand, ϵ_c increases with increasing shell thickness up to about 3 nm, and seems to keep constant at -0.8 % for AlN shells thicknesses above 3 nm. This behaviour drastically differs from the theory, which predicts an out-of-plane strain value up to -2.9 % for a 10 nm-thick AlN shell.

[2]When integrated over the cross-section of the core, ϵ_{xx}, ϵ_{yy} and ϵ_{plane} are equivalent. In particular considering the low magnitude of the in-plane strain compared to the out-of-plane one.

The same model was used to plot strain maps in cross section along the length of the core-shell NW (Fig. 5.16). Here, it can be observed that the AlN top segment relaxes quickly above the GaN/AlN axial interface to retrieve its own lattice parameter. This elastic relaxation is besides consistent with the calculations of F. Glas who showed that in virtue of the NW geometry, an infinite AlN axial segment may be deposited on top of a 20 nm diameter GaN NW, without introduction of dislocation (the misfit between relaxed GaN and AlN is about 2.4 % in a) [248]. For comparison, according to calculations performed by Kioseoglou *et al.*, the critical thickness for plastic relaxation of a 2D AlN layer on a 2D GaN layer lies between 40 and 300 Å, depending on the heterostructure polarity and on the way AlN and GaN adapt their in-plane lattice parameter to one another [249].

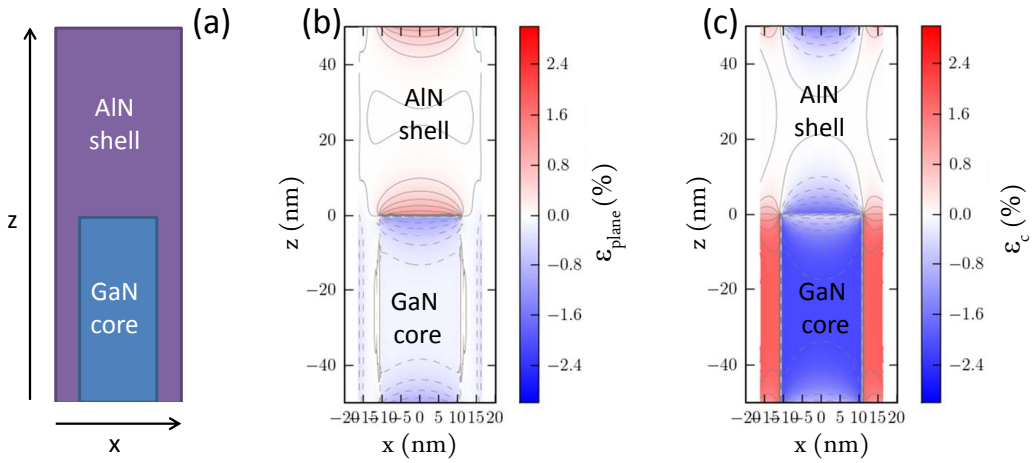

FIG. 5.16 – (a) Sketch of the cross-section along GaN-AlN core-shell NW length, (b) in-plane ϵ_{plane} and (c) out-of-plane ϵ_c strains map within this cross-section.

5.2.1.3 Microscopic observations

At this point, it has to be underlined that whereas XRD technique provides averaged information on an ensemble of NWs, calculation were performed for ideal (perfect) NW heterostructures. Yet, SEM in transmission mode have already revealed that the wires present various morphologies (Fig. 5.6) and especially often exhibit an asymmetrical AlN shell and a bent GaN core (Fig. 5.17).

In order to study the effect of the AlN shell asymmetry on the GaN core strain, HRTEM experiments were carried out on samples having different shell homogeneities by C. Bougerol. In this way, it was possible to analyze both straight and bent heterostructures by choosing in each case a proper set of single NWs.

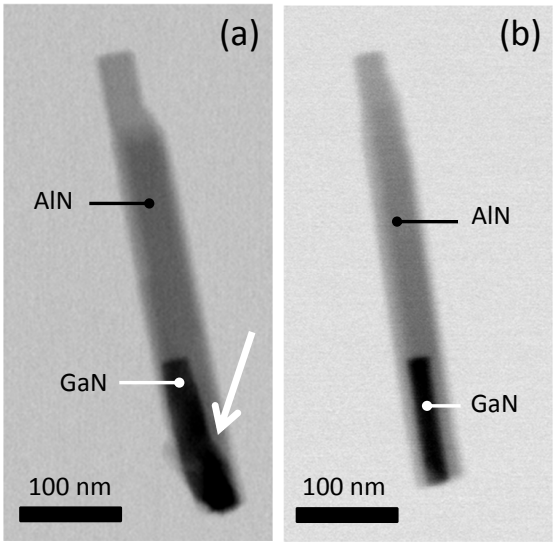

FIG. 5.17 – SEM images taken in transmission of NW heterostructures with (a) an asymmetrical and (b) a symmetrical AlN shell (lighter material) around GaN core (darker material). A step on the side of the GaN core is clearly visible in the case of the asymmetrical shell (pointed out by the white arrow).

HRTEM micrographs were analyzed by the geometrical phase analysis method [250] using the $(10\bar{1}0)$ and the (0002) reflections in the Fourier transform to get maps of the a and c lattice parameters, respectively. Figures 5.18 (a) and (d) present HTREM images obtained from NW heterostructures with a symmetrical thin and a thicker shell, respectively. Figures 5.18 (b) and (e) display the a- parameter maps obtained from the GPA analysis. It can clearly be seen that for both the thinner and the thicker shell samples, the AlN top segment and its shell have the same a- parameter, different from that of the GaN core. On the c-maps (Figs. 5.18 (c) and (f)), however, the AlN shell (both in the thin and the thick cases) is matched to the GaN core but has a different parameter than the AlN capping (top segment). This difference is accentuated in the case of the thinner shell.

Given that the AlN top segment is relaxed (Fig. 5.16), and thus has relaxed a^0_{AlN} and c^0_{AlN} lattice parameters, quantitative values of the strained GaN core parameters were extracted, allowing the determination of the strain value within the cores, based on equation 5.43. Here, only the out-of plane strain was determined. A precise extraction of the in-plane lattice parameter would actually suffer from the variation of thickness along the NW diameter. The analysis was spread to several NWs with different symmetrical AlN shell thicknesses. The obtained strain values are reported on figure 5.14 as full circles and appear to be in remarkable agreement with theory.

The same analysis was performed on a core-shell NW with an asymmetrical shell. Reported in figure 5.14 as the full square, the out-of-plane strain determined in this case drastically differs from theory but matches the values obtained by resonant XRD. Obviously, the theory well-describes the strain in GaN cores for "ideal", perfect NWs but overestimates the strain in GaN-AlN core-shell heterostructures with asymmetrical AlN shells. Figure 5.19 (a) presents a HRTEM image of such asymmetrical shell NW.

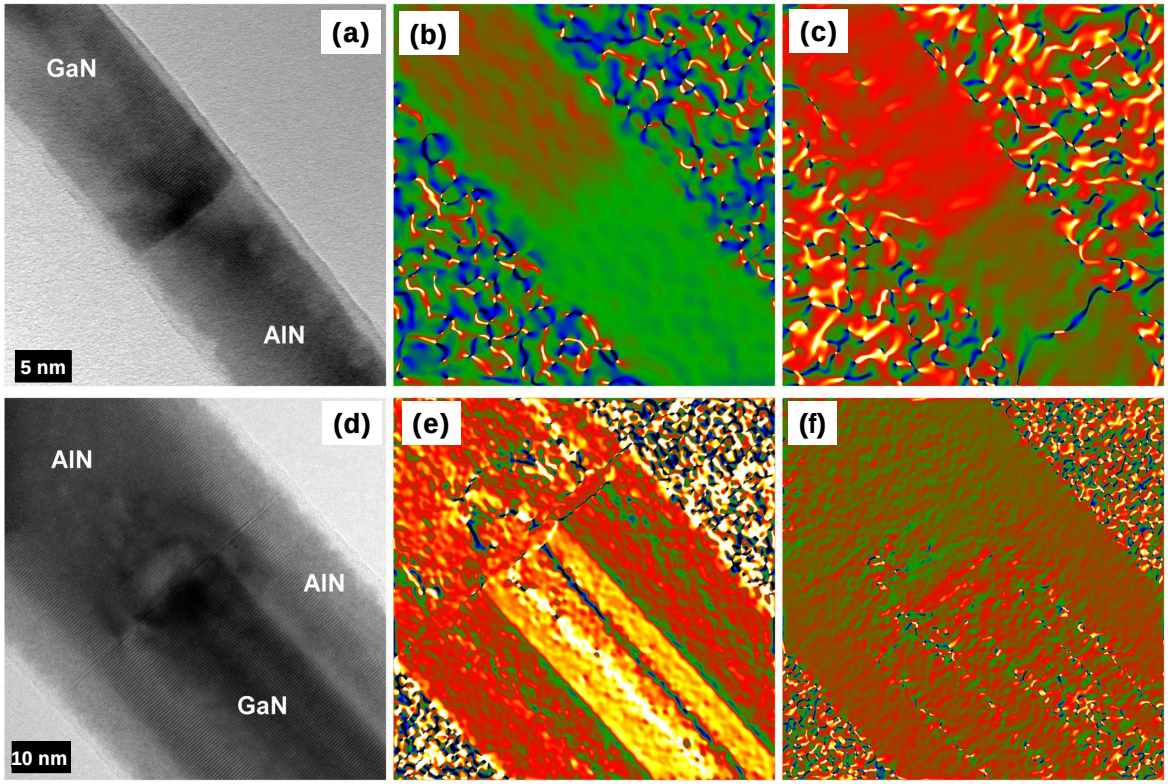

FIG. 5.18 – Geometrical phase analysis of core-shell NW heterostructures with symmetrical AlN shells. (a) and (d) are HRTEM images, (b) and (e) the corresponding a parameter maps and (c) and (d) the corresponding c parameter maps.

An enlarged view of the shell thinner side is exhibited in Fig. 5.19 (b). On this side, the formation of an edge dislocation (introduction of an extra c-plane) is clearly observed, suggesting that the lower strain value measured in GaN cores surrounded by asymmetrical AlN shell is a consequence of plastic relaxation.

5.2.1.4 Conclusions on strains within GaN cores

These results establish that the asymmetry in the AlN shell plays a determining role in the structural properties of the core-shell NWs. On a macroscopic sample, two GaN NW populations are present: some GaN NWs have a symmetrical AlN shell and some have an asymmetrical one. As measured by GPA analysis and observed on HRTEM images, in the former case, the system responds elastically, resulting in a large out-of plane strain. This strain increases as a function of the shell thickness without plastic relaxation and in the absence of significant in-plane strain. The extrapolation of the results of Ref. [251] for a 10 nm radius GaN core and an AlN shell actually suggests that plastic relaxation would occur even for a shell as thin as 1 nm through the introduction of "line dislocations" (dislocations propagating along [0001] with Burgers vector in the $[11\bar{2}0]$ direction, tangential

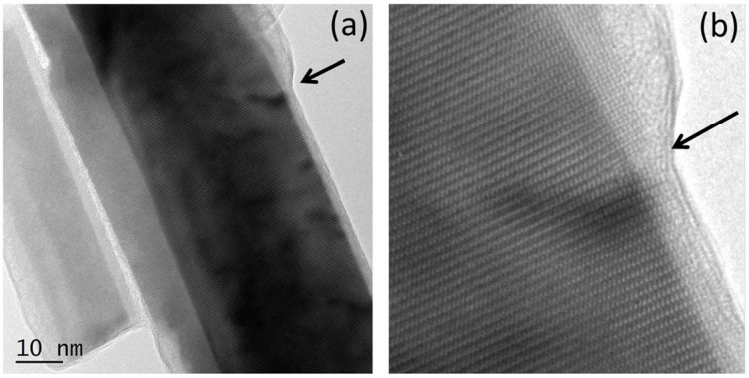

FIG. 5.19 – (a) HRTEM image of a GaN-AlN core-shell NW having an asymmetrical shell and (b) close up of (a) on the shell thinner side, highlighting the formation of an edge dislocation.

to the radial heterointerface). Nevertheless, HRTEM analysis performed on our NWs did not lead to any observation of such dislocations and their presence is still under questioning. We presume that their existence at the GaN/AlN interface could partly account for the GaN in-plane relaxation put in evidence by the resonant XRD data. Concerning the out-of-plane relaxation mechanism, the possibility of the formation of "loop dislocations" (dislocations with a Burgers vector oriented along the *c*-axis of the NWs) has been examined in Refs. [251, 252] and should lead to an AlN critical shell thickness of the order of some tens of nanometres. This is consistent with the experimental observation that the critical shell thickness, if any, would be beyond 12 nm.

In addition, SEM in transmission mode and HRTEM analysis of a statistically significant number of NWs revealed that inhomogeneous AlN shells are most often associated with the presence of a step (such as the one pointed out by a white arrow in figure 5.17 (a)) at the base of the GaN NW. Likely, AlN preferentially incorporate on top of these steps which signs the onset of the shell asymmetry and induce a strain gradient in the GaN core: on the side of the step, the GaN core undergoes a compressive strain induced by the incorporated AlN; on the opposite side, the GaN core is left free. Such strain unbalance leads to the bending of the GaN-AlN column until the formation of edge dislocations (extra *c*-plane) in the AlN shell, as evidenced by HRTEM. In this context, the change of regime around a shell thickness of about 3 nm, put in evidence by resonant XRD experiments, which, as we already underlined, is a macroscopic characterization method, may be interpreted as the amount of AlN above which shear-strained GaN/AlN heterostructures can easily relax by formation of dislocations in AlN.

5.2.2 In-plane and out-of-plane disorientation

As a complementary experiment, we wanted to observe the effect of the AlN shell on the GaN NW in plane and out-of-plane mosaicity. It has already been shown that GaN NWs grown on an AlN buffer layer have a perfect in-plane orientation, the GaN $<11\bar{2}0>$

directions being aligned to the <01$\bar{1}$> directions of Si [68] (or equivalently GaN <11$\bar{1}$0> directions are aligned with <11$\bar{2}$> Si directions). One can then wonder to what extent the deposition of the AlN shell affects this alignment or in other words, if the asymmetry in the AlN shell causes a disorder in the crystal. To address this issue, pole figures were recorded around the (10$\bar{1}$5) reflection of GaN. Figures 5.20 (a) and (b) show half pole figures respectively obtained from sample N1280 (nominal shell thickness 2.3 nm) and N1264 (nominal shell thickness 12 nm). Note that the Si directions are purely indicative as we did not extend the pole figures to the Si-related reflections.

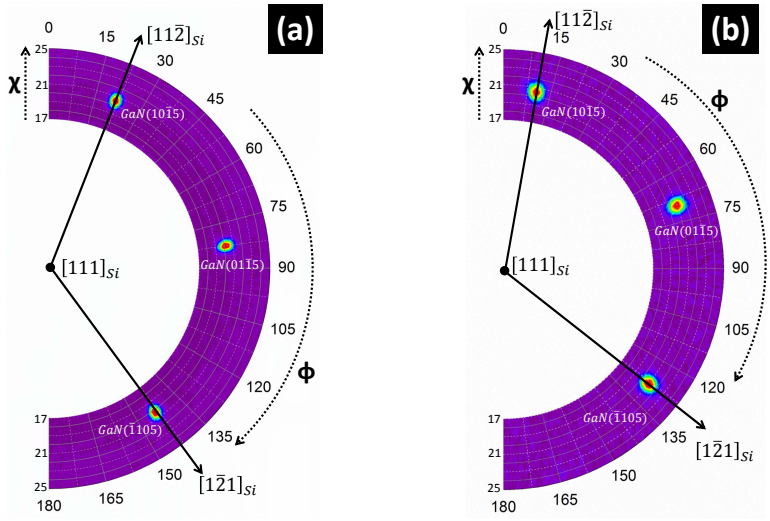

FIG. 5.20 – Half pole figures around the (10$\bar{1}$5) GaN reflection for (a) sample N1280 and (b) sample N1264 with respective nominal shell thickness of 2.3 nm and 12 nm. Si directions have been added as an indication.

On these half pole figures, Φ is the azimuthal angle. In both cases, three distinct Bragg spots can be observed, distinctly separated by 60°. The absence of signal between these peaks indicates that the in-plane mosaicity is negligible. From the epitaxial point of view, such result could have been expected. As GaN NWs are perfectly aligned to silicon and to one against each other, there is no reason why the deposition of an AlN shell could induce an in-plane mosaicity. On the other hand, considering the bending of the GaN cores observed by SEM in transmission and induced by the AlN shell, out-of plane mosaicity may occur. Here χ represents the sample inclination. (10$\bar{1}$5) Bragg spots appear at $\chi \approx 20.5°$, that is close to value expected from the angle between the [0001] and the [10$\bar{1}$5] directions (see equation A.6). This χ value indicates that, on average, GaN NWs embedded in an AlN shell are quite straight. However, in order to better quantify the out-of-plane mosaicity, we performed ω-scans around the (0002) Bragg reflection. Figure 5.21 displays the scans obtained on a reference sample (GaN NWs without any AlN shell) as well as on samples N1280 and N1264.

It can be seen on figure 5.21 that the FWHM of the reference sample spectrum is about 0.68°. This FWHM can be seen as the disorientation of the [0001] direction around its mean value or in other words as the distribution describing the bending of GaN NWs

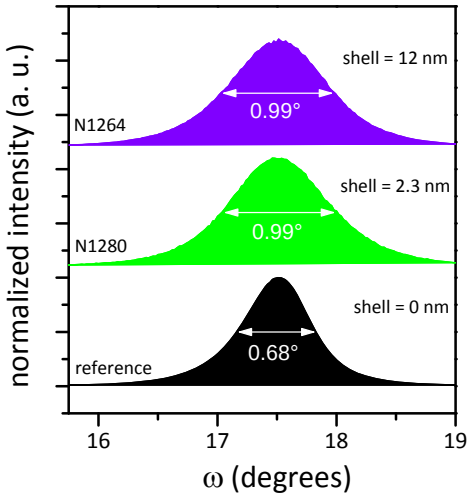

FIG. 5.21 – ω-scans around (0002) Bragg reflection of a reference sample (GaN NWs without AlN shell) and samples N1280 and N1264, GaN NWs with AlN shell with respective thickness 2.2 nm and 11.3 nm.

around their mean value. For both shelled samples, the FWHM value has increased to 0.99°. This 46 % rise in the FWHM value suggests that the deposition of the AlN shell around GaN NWs increases the distribution of tilts (the distribution gets widers, the NWs are more bended). On the other hand, a thicker shell does not involved a larger disparity in the NWs orientation. This is consistent with the fact that above 3 nm shell thickess, the strain is relaxed by the dislocation and the NWs do not need to further accomodate their strain by accentuating their bending.

5.3 Optical properties of GaN-AlN core-shell heterostructures

Capping a NW by another material has often been shown to optimize the optical properties of the NW itself. Deposition of a shell around and above a nanocolumn in fact spatially pushes surfaces states away from the active core area. It has for instance been observed that capping GaAs NWs with AlGaAs or InGaP shells increases the intensity of the core material [253, 254] luminescence. In addition, the shell-induced strain inside the core may be used to tune the emission wavelength of this core [255, 256]. Concurrently to our investigations, Rigutti *et al.* correlated the structure of GaN/AlN core-shell NWs to their optical properties. The authors showed that, for coherent core-shell NWs, GaN excitonic emission is blueshifted proportionally to the magnitude of the compressive strain ϵ_{zz} induced by the AlN shell [257]. Typically for 3 nm-thick shells, they reported an emission shift of about 60 meV compared to shell-free GaN NWs.

In our case however, the optical characterization of GaN-AlN core-shell NWs do not lead to the same conclusions. Figure 5.22 (a) presents the macro-PL spectra obtained at 7 K from ensemble of NWs grown with various nominal AlN shell thicknesses. The typical

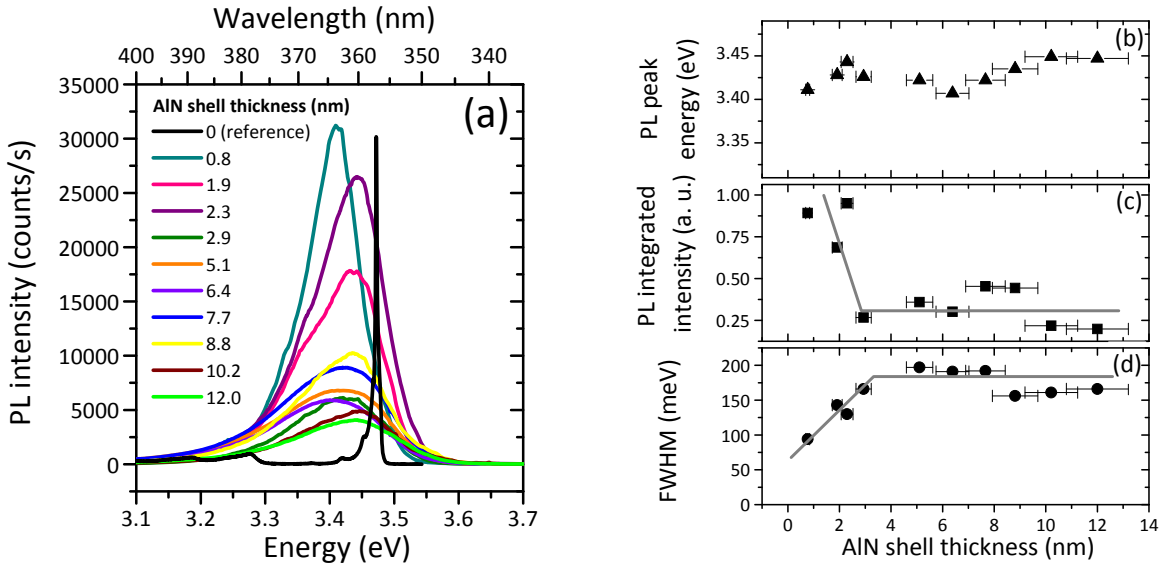

FIG. 5.22 – (a) macro-PL spectra of GaN-AlN core-shell NWs with different shell thicknesses, taken at 7 K; (b), (c) and (d) respectively are the peak position, integrated intensity and FWHM evolution versus the shell thickness.

spectrum of "bare" GaN NWs (without shell) has been added for qualitative comparison (black line). It can be seen that, here, the deposition of an AlN shell induces a quenching of the GaN near band-edge emission around 3.47 eV and the emergence of a broad peak in the lower energy range, around 3.42 eV. Figure 5.22 (b) shows the position of this peak in function of the AlN shell thickness but no clear tendency can be drawn. In fact, the peak apparently raises at different positions between 3.41 and 3.45 eV, independently from the shell thickness. In his PhD thesis, J. Renard performed time-resolved PL on a GaN-AlN core-shell NW ensemble and observed that this broad peak is in fact composed of several contributions [258]. The main part of these contributions has a very large decay time and was therefore attributed to carriers strongly localized on shallow defects. On the other hand, another contribution emerging at higher energy appears to have a short decay time, about 50 ps, that is much shorter than the typical decay time of excitons in shell-free GaN NWs (about 130 ps). This high energy contribution was then assumed to have an excitonic origin but to recombine non-radiatively because of the possible existence of easy paths towards non-radiative channels. This hypothesis in fact justifies the short decay time of this high energy contribution and therefore its absence in the continuous-wave PL spectra of figure 5.22 (a).

Regarding now figure 5.22 (c), data suggest that the broad peak integrated intensity decreases up to shell thicknesses about 3 nm and remains constant above this critical value. In parallel, the peak FWHM (Fig. 5.22 (d)) increases with the shell thickness up to 3 nm thick shells and then stabilizes around 200 meV. In both figure 5.22 (c) and figure 5.22 (d), grey lines are hand-drawn guides for the eyes. Although difficult to inter-

pret, these luminescence-related changes of regime are possibly correlated to the plastic relaxation observed in NW ensembles with AlN shell thicker than 3 nm. Dislocations introduced in asymmetrical shells may indeed act as additional non-radiative centres. One could then hypothesize that for samples with shell thicknesses larger than 3 nm, the observed luminescence nearly solely originates from NWs with a homogeneous shell. As a next stage of this study, it would be interesting to explore this possibility by performing micro-PL measurements on single core-shell NWs dispersed on a TEM grid that would allow to correlate the structure of the NW – or more specifically the homogeneity of its shell – to the recorded spectrum. Nevertheless, at that point, results do not permit to strictly conclude on the behaviour and the origin of the luminescence of our GaN-AlN core-shell NWs.

5.4 Conclusion of the chapter

This chapter devoted to GaN-AlN core-shell NW heterostructures was constituted of three parts: in a first stage, we focused on the growth of the AlN shell around GaN NWs and on the dependence of its aspect ratio on the growth conditions (namely the Al flux, the substrate temperature and the atomic beam incidence angles); in a second stage we investigated the structural properties of these heterostructures; finally, in the last section we dealt with their optical properties.

We have hence first shown that it is possible, to some extent, to control the morphology of the AlN shell around GaN NWs by tuning the atomic flux incidence angles. More specifically, increasing this incidence angle favors AlN radial incorporation against AlN axial incorporation. Based on calculations, a change in the Φ_{Al}/Φ_N ratio was not expected to significantly modify the AlN shell morphology. However, in practice, increasing the effective Al/N flux ratio on the surface from 0.55 to 0.86 led to thicker shells and comparable axial AlN lengths. The observed shell morphologies are explained by a strong Al diffusion from the NW side-walls to the top of the NWs, combined to desorption of part of the impinging N atoms via N_2 formation.

In the two first sections of this study, we have besides evidenced the frequent formation of AlN shells with an inhomogeneous shape. Structural characterization results have established that such asymmetry in the AlN shell plays a determinant role in the structural properties of the core-shell NWs. On the one hand, when the shell grows homogeneously, the system responds elastically, which results in a large uniaxial out-of-plane strain within GaN cores. This strain increases as a function of the shell thickness without plastic relaxation and in the absence of significant in-plane strain. On the other hand, when the shell is asymmetrical, the system first relaxes elastically: shear strains are expected to appear in the GaN cores, resulting in the bending of the NWs. Above a critical shell thickness of about 3 nm, it eventually relaxes plastically by introducing an extra *c*-plane in the shell

thinner side. Likely, the asymmetry in the shell is due to the presence of steps at the base of the GaN NWs, as seen in figure 5.17 (a), known to be preferential incorporation sites.

Regarding optical properties, depositing an AlN shell around GaN NWs leads to a quenching of the near band-edge emission and to the emergence of a broad peak at lower energy. The quenching of the near-band edge emission is attributed to the creation of non-radiative channels at the GaN-AlN interface and the broad peak is assigned to the emission of carriers trapped on shallow defects. Although clear conclusions are hardly drawn from the obtained results, the evolution of the broad peak integrated intensity and FWHM tends to suggest that the luminescence itself depends on the homogeneity of the shell.

As a consequence, our results indicate that the full potential of core-shell NW heterostructures for applications strongly depends on the control of the shell growth process, possibly driven by the presence of steps on the GaN NW sides, and of its homogeneity. In order to better master the fabrication of the AlN and subsequent GaN shells, Carnevale and coworkers used a growth temperature as low as 500 ℃ and restrained themselves to shell thicknesses below 3 nm [259]. Although this method recently resulted in the successful fabrication of resonant tunnelling diodes based on GaN-AlN core-shell NW heterostructures [260], lowering the temperature to 500 ℃ presents some disadvantages. Regarding GaN, it is known that low temperatures may lead to a change of phase from WZ to ZB, thus inducing stacking faults [261]. In addition, for both GaN and AlN, the use of such a low temperature leads to the formation of a rough layer between the nanocolumns. As future alternatives, we propose to use an adapted patterned substrate in order to avoid both the formation of this rough layer and the emergence of steps at the GaN NW feet and to tune the atomic beam incidence angle in order to favour the lateral incorporation.

6

GaN axial insertions on AlN nanowires

Focussing now our attention on axial GaN/AlN nanowire heterostructures, the aim of this last chapter is to present preliminary results on GaN quantum dots formed on top of GaN-AlN core-shell nanowires. In fact, we have seen in the previous chapter that it is possible to thicken the AlN shell around GaN nanowire cores. One can hence wonder whether the thicker shells have a sufficiently large top c-surface for subsequently-deposited-GaN to undergo an elastic shape transition. Considering this issue, the first part of this chapter will consists in comparing theoretical calculations of the critical AlN shell diameter above which the GaN elastic shape transition is likely to occur to the experimentally observed critical diameter. Then, optical properties of these original nanostructures will be addressed both by photo- and cathodoluminescence.

Contents

6.1 Critical GaN height on AlN for plastic relaxation in the nanowire geometry 129

6.2 Critical AlN NW diameter for strain-induced formation of GaN QDs 130

6.2.1 Theoretically determined critical radius 130

6.2.2 Experimentally determined critical radius 131

6.3 Optical properties of GaN quantum dots in GaN-AlN core-shell nanowires 136

6.3.1 GaN axial insertion ensemble 136
6.3.2 Single GaN axial insertion 137
6.4 Conclusion and prospects of the chapter 139

6.1 Critical GaN height on AlN for plastic relaxation in the nanowire geometry

In his article published in 2006, F. Glas showed that when depositing a given material on top of a nanowire, there exists a critical height of this deposited material below which no misfit dislocation is introduced. The author calculated the dependence of this critical height on the NW radius for different values of the misfit between the base nanowire material and the deposited one [248]. As an illustration, we explained in section 5.2.1.2 of chapter 5 that the critical height of the axial AlN segment is infinite on GaN NWs having a diameter of 20 nm.

We have also seen in chapter 5 that it is possible to thicken the AlN shell around the GaN bases and obtain AlN diameters as large as hundreds of nanometers. According to calculations of F. Glas, even on such large diameters, the critical height of a GaN axial segment is infinite. To have a better overview of the dependence of the critical height on the NW radius, figure 6.1 represents the graph published by F. Glas in Ref. [248]. On this graph, the grey zone represents the range of radii we are concerned with.

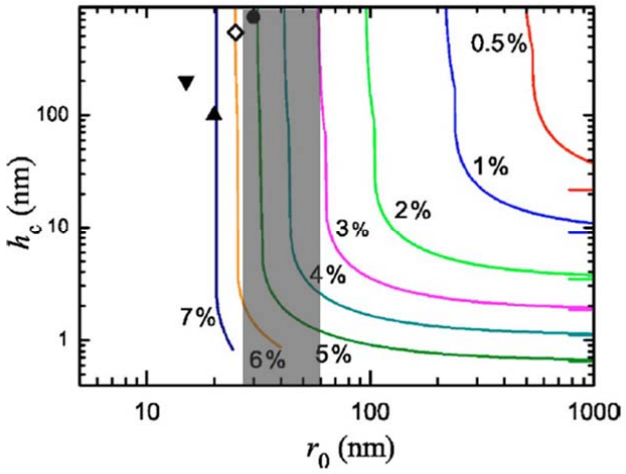

FIG. 6.1 – Graph taken from Ref. [248] and illustrating the dependence of the critical thickness h_c for plastic relaxation in the NW geometry on the NW radius r_0 for different values of the mismatch between the base and the deposited material. The grey zone indicates the range of radii we are dealing with in this study. The in-plane mismatch between AlN and GaN is about 2.4 %.

Although in the range of diameters we are dealing with, no plastic relaxation is expected to occur, it is clear that for the largest radii, the critical thickness becomes close to that determined in the 2D case [249]. In other words, when increasing their diameter, nanocolumns tend to behave like 2D layers. One can then naturally expect that on sufficiently large NWs, similarly to the 2D case, for a given amount of deposited material

below the critical thickness for plastic relaxation, a shape transition may take place. Even if no plastic relaxation occurs, one can wonder whether an elastic shape transition would not be favorable for the systems. Would it be possible to grow Stranski-Krastanov (SK) or Volmer-Weber (VW) quantum dots (QDs) on top of AlN NWs and if so, above which critical diameter?

In the following, we will differentiate quantum disc (Qdisc) from quantum dot (QD) types of axial insertions: the former consists in a pseudomorphic segment inserted in the axis of the NW without shape transition while the latter has undergone a shape transition towards an island.

6.2 Critical AlN nanowire diameter for strain-induced formation of GaN quantum dots

6.2.1 Theoretically determined critical radius

To address the issue of the critical diameter for an elastic shape transition, our collaborator F. Glas from LPN (Laboratoire de photonique et de nanostructures) of Marcoussis performed theoretical calculations. The calculations are of the same type of those handled for the InGaN/GaN NW system, recently published in Ref. [262]. F. Glas in fact considered an AlN NW having a cylindrical shape with a radius R_{NW} and a cylindrical island of GaN with a radius $R < R_{NW}$ deposited on this AlN column (Fig. 6.2 (a)).

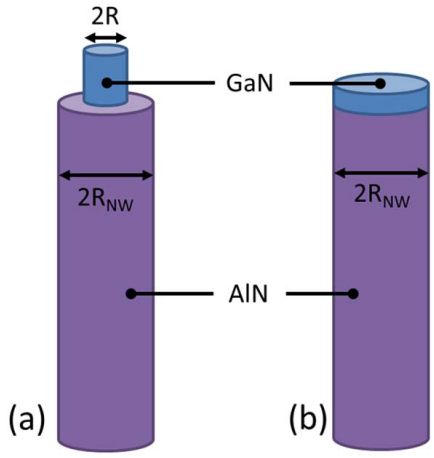

FIG. 6.2 – Scheme of the two possible shapes GaN may take on top of AlN/GaN NWs: (a) SK or WV QD and (b) Qdisc.

Based on finite elements and leaving the radius R of the GaN island free to vary, he computed E_{island}, the total energy of the system, as the sum of the elastic energy corresponding to the coherent relaxation of the whole system and of the surface energy of the island side-walls. The energy of the most favorable configuration was then compared to the energy E_{disc} of a GaN disc with the same volume as the corresponding island,

but whose diameter was fixed by the diameter of the underneath AlN base (Fig. 6.2 (b)). Figure 6.3 presents a map of E_{island}/E_{disc}, the ratio between these two energies for different AlN NW base radii and normalized deposited GaN volumes. In other terms, the island volume is given in MLs of the radius R_{NW}. As these calculus were made considering an isotropic elasticity of the materials, only one mismatch could be taken into account. For the map displayed in figure 6.3, the 2.5 % mismatch in a between GaN and AlN was used.

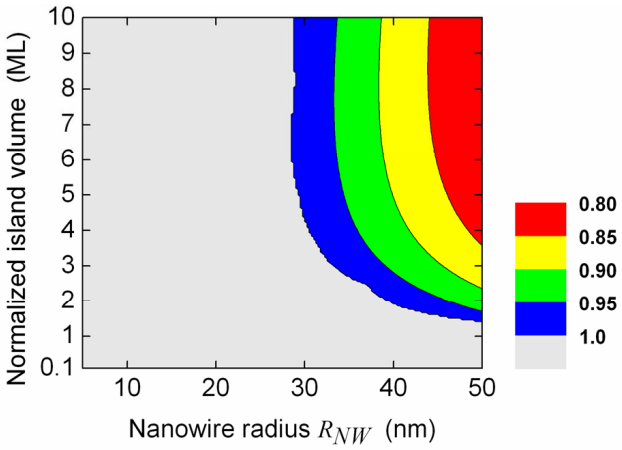

FIG. 6.3 – Map of the ratio E_{island}/E_{disc} in function of the AlN bases radius R_{NW} and of the deposited GaN volume (expressed in MLs of the radius R_{NW}. The grey zone and the coloured zones respectively indicate parameters favorable to the formation of a Qdisc with radius $R = R_{NW}$ and of an island with radius $R < R_{NW}$.

Naturally, for the shape transition to be favourable, the energy of the island should be lower than the energy of the corresponding disc. This means that, on the map of figure 6.3, the coloured zones which correspond to E_{island}/E_{disc} ratios lower than one, indicate the parameters favorable to the emergence of GaN QDs while the grey zone (ratio equal to one) indicates the parameters favorable to the constitution of a Qdisc. Hence, for given amounts of deposited GaN, the frontier between the grey and the coloured zones gives the critical AlN radius above which QDs are likely to appear. As an example, when depositing 4.4 ML of GaN, the critical AlN diameter is around 60 nm.

6.2.2 Experimentally determined critical radius

In order to compare this theoretical prediction to experiments, two samples were grown and investigated. Rather than pure AlN NWs whose growth is still not well mastered to date, we used AlN deposited on GaN NWs as bases for the subsequent deposition of GaN insertions. This is illustrated in figure 6.4. In the following, "AlN NWs" will therefore refer to "AlN-GaN core-shell NWs", similar to those described in chapter 5. For both grown samples, GaN-AlN core-shell NWs were hence first fabricated. Then, for sample N1772 a

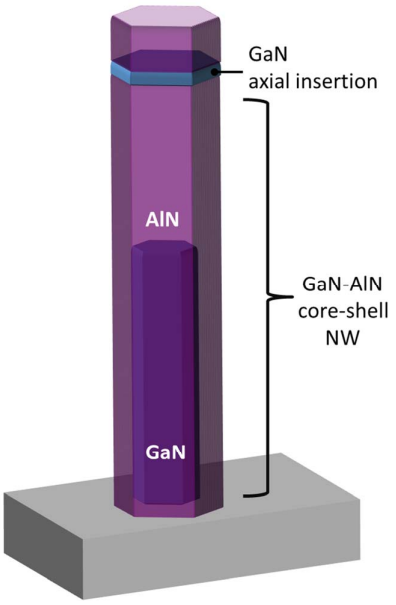

FIG. 6.4 – Sheme of the grown structures. GaN-AlN core-shells NWs were used as a basis for the subsequent deposition of the GaN axial insertion.

single GaN insertion was deposited during 17 s with a Ga equivalent flux of 0.26 ML/s. The quantity of Ga deposited was therefore equal to 4.4 ML. Sample N1875 contains four GaN axial insertions also made of 4.4 ML of Ga. For this sample, apart from the last insertion which remained uncapped, each GaN deposition was followed by the deposition of 30 nm of AlN. As observed in figure 6.5 which displays HRTEM images of NWs from sample N1772, taken by C. Bougerol, both axial insertions with an island-like shape (a) and with a disc shape (b) could be found in the population of NWs.

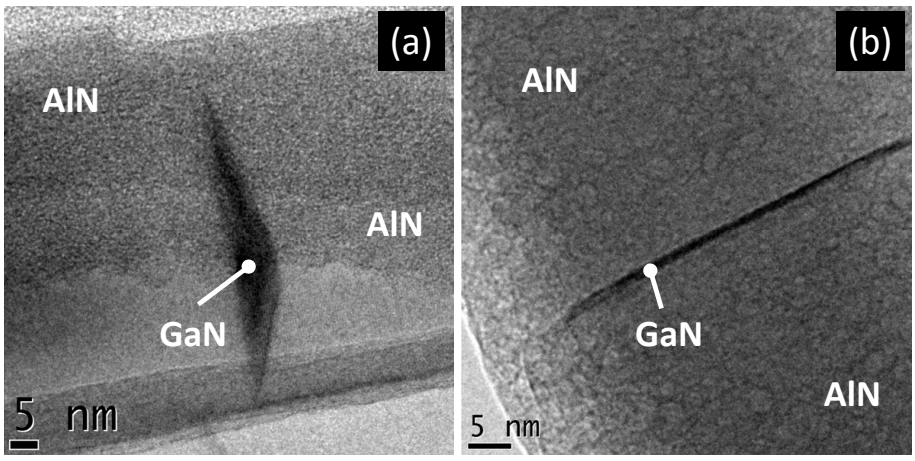

FIG. 6.5 – HRTEM images taken by C. Bougerol of two NWs from sample N1772 presenting (a) an island-like and (b) a disc-like axial insertion.

Qualitatively, Qdiscs are observed on thin AlN NWs and QDs on the large ones. In order to determine the experimental critical diameter above which QDs are more likely to

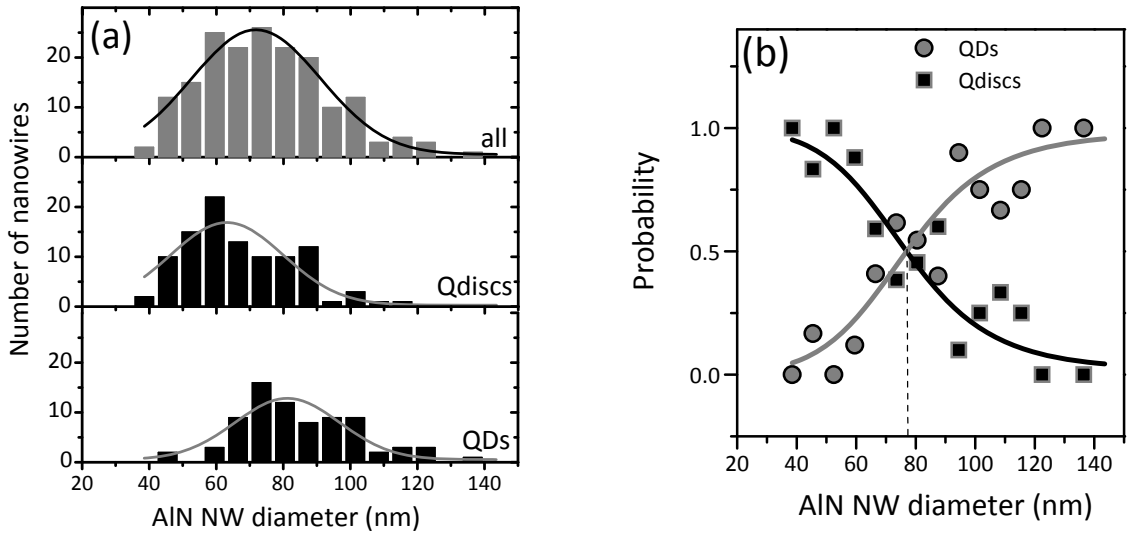

FIG. 6.6 – (a) Statistical distributions of the overall AlN NW diameters, of the AlN NW diameters on which Qdiscs are observed and of the AlN NW diameters on which QDs are observed (b) Probabilities $\mathbb{P}_{QDs}$ (circles) and $\mathcal{G}_{QDs}$ (gray line) to observed a QD and probabilities $\mathbb{P}_{Qdisc}$ (squares) and $\mathcal{G}_{Qdisc}$ (black line) to have a Qdisc, as a function of the AlN nanowire diameter.

be formed than Qdiscs, we observed the shape of the first GaN axial insertion of nearly 200 nanocolumns from sample N1875 and measured the corresponding underneath AlN diameter. Figure 6.6 (a) presents the distributions of the overall AlN NW diameters, of the AlN NW diameters on which Qdiscs are observed and of the AlN NW diameters on which QDs are observed.

These histograms were fitted with Gaussian functions $\mathcal{G}_{all}$, $\mathcal{G}_{Qdiscs}$, $\mathcal{G}_{QDs}$ which revealed that on sample N1875, the AlN NW average diameter is about 72 nm with a broad distribution of 39 nm around this value. The mean diameter of NWs on which Qdiscs are found is about 63 nm while that of NWs on which QDs are found is about 81 nm. The critical diameter d_c above which the probability to observe a QD is higher than the probability to observe a Qdisc lies between these two values and can be considered as the intersection of the two Gaussian fits. Another way to depict this intersection is to calculate the probability to find either one or the other type of structure for given NW diameters d. Based on the histograms, such probabilities $\mathbb{P}$ were calculated as

$$\mathbb{P}_{QDs}(d) = \frac{N_{QDs}(d)}{N(d)} \tag{6.1}$$

and

$$\mathbb{P}_{Qdisc}(d) = \frac{N_{Qdisc}(d)}{N(d)} \tag{6.2}$$

where $N_{QDs}(d)$, $N_{Qdisc}(d)$ and $N(d)$ are respectively the number of wires with diameter

d on which QDs are observed, the number of wires with diameter d on which Qdiscs are observed and the total number of wires with diameter d listed. Figure 6.6 (b) displays the evolution of $\mathbb{P}_{QDs}$ (circles) and $\mathbb{P}_{Qdisc}$ (squares) in function of the NW diameters. Lines correspond to probabilities calculated from the Gaussian fits of figure 6.6 (a) as

$$\frac{\mathcal{G}_{QDs}}{\mathcal{G}_{Qdiscs} + \mathcal{G}_{QDs}} \tag{6.3}$$

and

$$\frac{\mathcal{G}_{Qdiscs}}{\mathcal{G}_{Qdiscs} + \mathcal{G}_{QDs}} \tag{6.4}$$

Based on these probabilities, the critical diameter d_c is then estimated as 77 nm. Clearly, above this value, it is more probable to find a QD than a Qdisc and the chances of observing a QD further increase with increasing NW diameters. Conversely, for the smallest diameters the probability of finding a QD tends towards 0: Qdiscs are then more likely to be formed.

On figure 6.3, the theoretical experimental value of the critical NW diameter for 4.4 ML of GaN was around 60 nm which is in quite good agreement with the experimental d_c of 77 nm, considering that the model used should be taken with caution. The theoretical model is actually "simple" and does not account for the actual hexagonal symmetry of the NW and for the potential asymmetry of the AlN top c-surface. In addition, the calculated energy of the system might not only depend on the $|a_{GaN} - a_{AlN}|/a_{AlN}$ ratio but on a more complex expression of the misfit which includes the contribution of GaN and AlN c-parameters. The considered mismatch would then lie somewhere between $|a_{GaN} - a_{AlN}|/a_{AlN}$ and $|c_{GaN} - c_{AlN}|/c_{AlN}$ (that is between 2.5 % and 4.1 %). Nevertheless, maps, such as the one displayed in figure 6.3, obtained for mismatch values larger than 2.5 % revealed a shift of critical AlN NW radii towards lower values, which does not better fit our experiment critical diameter. F. Glas also performed his calculations after introducing a difference between the horizontal surface energy of the AlN NW and that of the GaN insertion. It appears that when the horizontal surface energy of the AlN NW is smaller than that of the GaN insertion, the island formation is favoured: critical radii shift towards lower values, and conversely [263]. This illustrates that values of the theoretical critical diameter are largely dependent on the calculus input parameters and should not be taken with too much attention.

Besides, in figures 6.5, the quantity of material incorporated in the island-like insertion seems to be larger than in the Qdisc. The deposited quantity of GaN is equal to 4.4 ML, which is consistent with the observed thickness of the Qdisc (about 1.5 nm) but which is much lower than the quantity of material required to fill the volume of the island in figure 6.5 (a). More specifically, based on simple geometrical considerations, the volume of this island is equivalent to the volume of a disc with height equal to 2.7 nm, that is

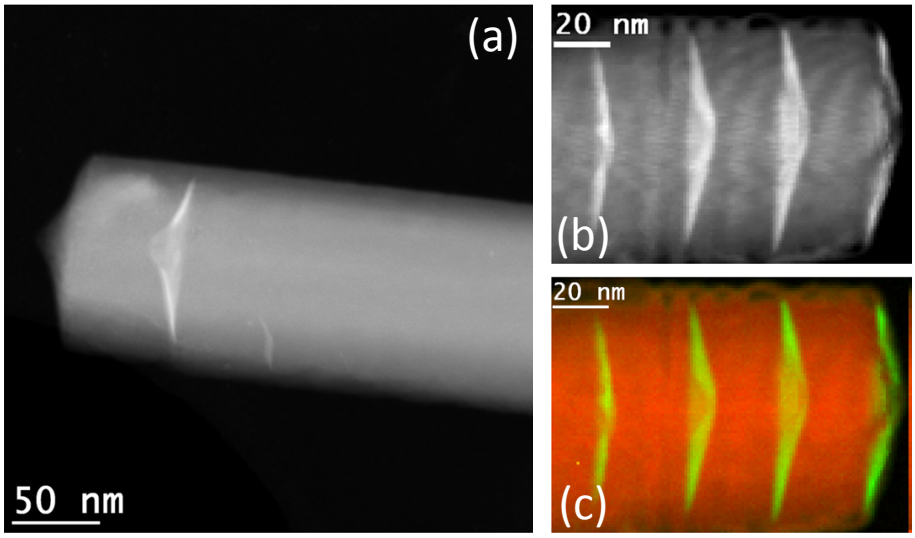

FIG. 6.7 – (a) ADF image of a GaN island embedded in AlN NWs taken from sample N1772, (b) HAADF image of the GaN islands from sample N1875 and (c) compositional EELS map of (b), treated using the "principal component analysis" method in order to enhance the signal-to-noise ratio. Ga atoms are in green and Al in red. These images were all obtained on a USTEM 200 Cs corrected STEM, by L. Tizei from the LPS group of Orsay.

nearly twice the height expected from directly impinging Ga atoms. It is hence possible that the effective quantity of incorporated material is partly due to Ga atoms diffusing from the facets on some NWs. If this is the case, one could wonder why such Ga diffusion occurs only on some NWs and not on the whole ensemble. Surprisingly, STEM HAADF images such as the one displayed in figure 6.7 (a) sometimes exhibit unexpected contrasts inside the GaN QD. The same contrasts were often observed in GaN islands of sample N1875 (Fig. 6.7 (b)). Our collaborator L. Tizei further performed EELS (Electron Energy Loss Spectroscopy) analysis on this 4-QD NW (Fig. 6.7 (c)). The presence of Ga atoms (in green) was detected via images taken at the Ga M-edge and the Al presence (in red) via images taken at the Al K-edge. It seems that a certain quantity of Al atoms lies in the core the GaN island. If those contrasts are not artefacts, one can then hypothesize on a possible diffusion of Al atoms inside GaN islands. Regarding GaN QDs grown on a 2D AlN layer, Arlery *et al.* showed that no significant Ga/Al intermixing occurs [264]. However, Gogneau and coworkers later observed that overgrowing 2D GaN QDs with AlN induces an isotropic reduction of about 1 ML of the GaN island size because of a thermally activated exchange between Al atoms from the cap layer and Ga atoms from the QD [265]. If we consider that typical growth temperatures for 2D QDs range from 680 to 750 °C [265, 266] and that the temperature at which GaN axial insertions of samples N1772 and N1875 were deposited was 820 °C, one can imagine that the exchange between Al and Ga goes beyond a single ML and may become comparable to an actual intermixing of the two species. Nevertheless, if such process would occur, the gradient of contrast in figures 6.7 (a) and (b) would be opposite: the white zone (with the highest Ga content)

should be at the bottom of the island and reciprocally. On the other hand, as evidenced in figures 5.5, 5.6, 5.7 or even 5.8 of chapter 5 and recalled hereafter in figure 6.8, AlN shells themselves do not always exhibit a totally flat top *c*-surface but sometimes present a hill-like prominence in their center. One can then imagine that on such a surface, GaN deposits as a sort of "bowler hat" coating the AlN hill. Clearly, further experiments are required to clarify the issue. In particular, performing electron tomography on these NWs would allow to obtain 3D representations of their structure and may lead to a better understanding of the origin of their shape. In the future, we also intend to grow new samples on which the GaN axial insertion will be deposited at a lower temperature, comparable to the 2D case. In addition, regarding sample N1875, it would be interesting to determine whether each dot contains the same amount of Al and if/how this amount is correlated to the strain state of the corresponding QD.

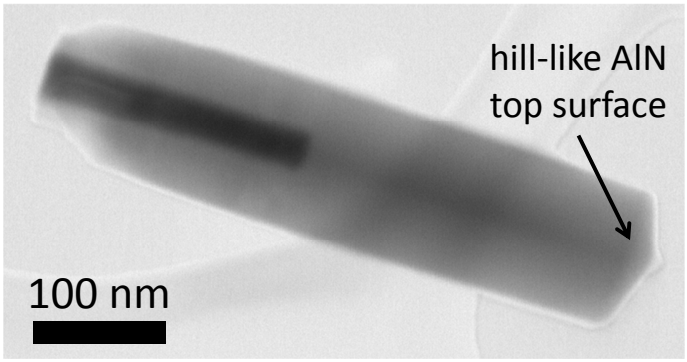

FIG. 6.8 – SEM image taken in transmission of a GaN-AlN core-shell NW from sample N1843 exhibiting a hill-like top AlN surface.

6.3 Optical properties of GaN quantum dots in GaN-AlN core-shell nanowires

6.3.1 GaN axial insertion ensemble

Despite our doubts on the morphological details of GaN QDs, we found interesting to optically characterize the grown structures. Macro-PL was hence first performed on sample N1772. Figure 6.9 (a) presents spectra obtained at different temperatures. At low temperature, one can identify one main peak about 3.47 eV attributed to excitonic recombinations in the GaN NW core. The shoulder at higher energy is related to the GaN axial insertions. Its positions is about 3.71 eV. Although it seems that this shoulder is composed of several contributions, we measured its integrated intensity and plotted it versus temperature in figure 6.9 (b) (black balls). For comparison, other data have been added, namely the PL intensity obtained by J. Renard (Ref. [258]) from 2D GaN QWells embedded in AlN (triangles), 2D GaN QDs embedded in AlN (hexagons) and

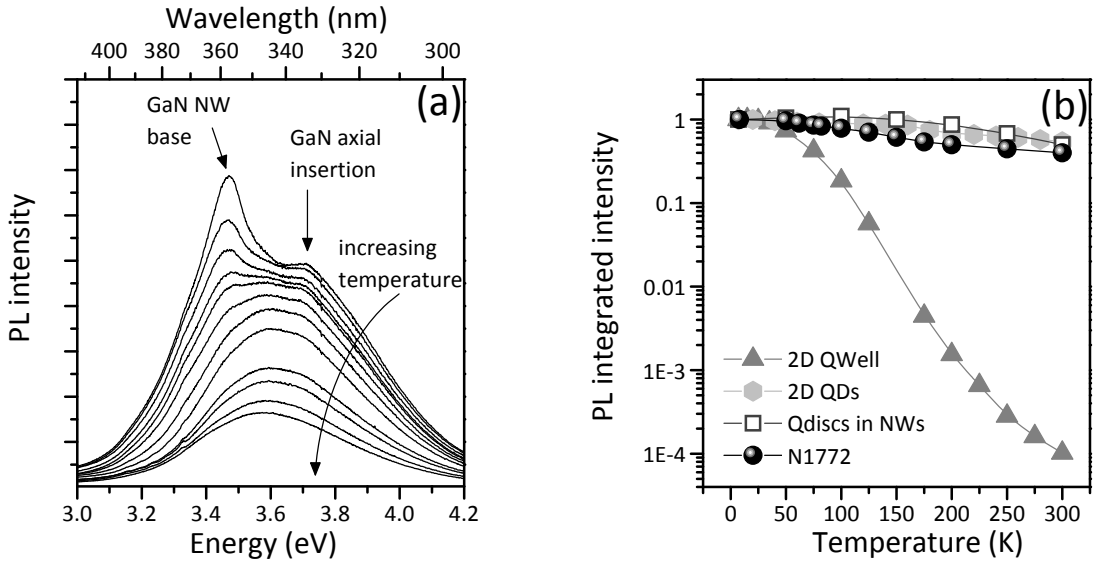

FIG. 6.9 – (a) Macro-PL spectra obtained at different temperatures of an ensemble of GaN QDs and Qdiscs embedded in AlN on GaN NWs (sample N1772) and (b) dependence of the GaN axial insertion integrated intensity on temperature (black balls) compared to that of 2D GaN QWells in AlN (triangles), 2D QDs in AlN (hexagons) and of GaN Qdiscs (exclusively) in AlN on GaN NWs (open squares).

from an ensemble of GaN axial insertions exclusively composed of Qdiscs embedded in AlN on top of GaN NWs (squares). Similarly to what is observed with QDs-like structures, our ensemble of axial insertions composed of both QDs and Qdiscs well survive at high temperature. Its luminescence intensity is only reduced by a factor 2 between 4 and 300 K, which is much better that what is obtained with QWells. However, as mentioned, the probed NWs are composed of both QDs and Qdiscs and in order to investigate their respective behaviour one must go to a microscopic scale.

6.3.2 Single GaN axial insertion

In order to investigate the properties of single quantum dots, two microscopic techniques were used, namely micro-PL and nano-CL. For micro-PL experiment, NWs from sample N1772 were dispersed with ethanol onto a marked Si_3N_4 thin membrane fabricated by our collaborator M. den Hertog. NWs were separated enough to allow probing single wires or single "bunches" of wires. Markers on the grid permitted to identify the investigated NW on both the micro-PL camera and the SEM, allowing to match the spectrum with its corresponding nanostructure. Figure 6.10 shows example of spectra obtained from single NWs with single insertions (❶, ❷ and ❸) and from bunches of NWs with single insertions (❹, ❺ and ❻).

One can see that every spectrum is composed of many narrow lines, including those

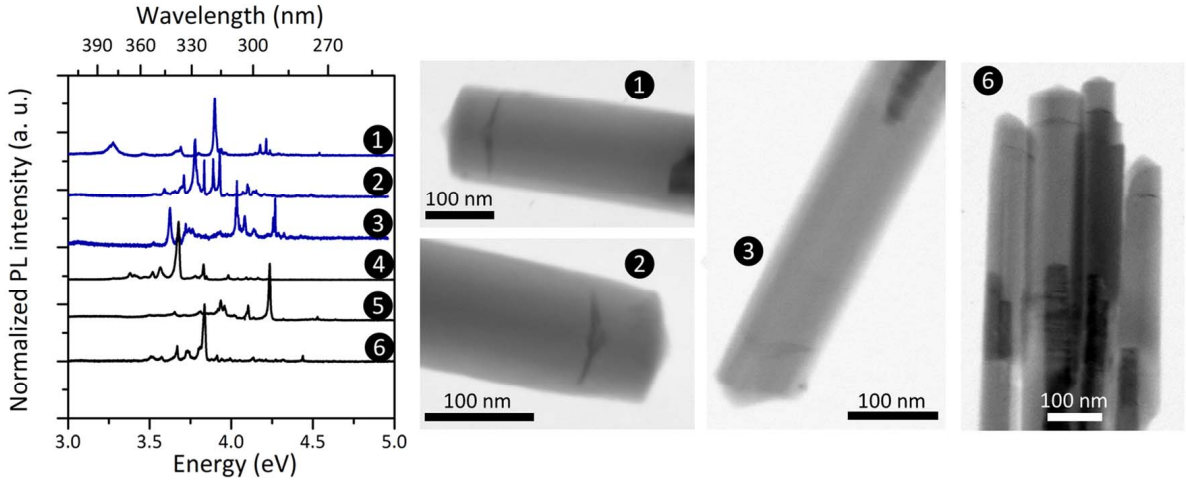

FIG. 6.10 – Micro-PL spectra obtained at 4 K from single NWs of sample N1772 with single GaN axial insertions (❶, ❷ and ❸) and from bunches of NWs containing single GaN insertions (❹, ❺ and ❻).

related to single NWs. In addition, the number of narrow lines does not seem to be proportional to the number of NWs probed. Most of them raise above the GaN band edge where nearly no signal is detected. This observation is somewhat surprising: considering that the laser spot had a diameter of about 100 µm, its is unlikely that, when exciting the GaN axial insertion, we did not excite the GaN NW base. The band edge emission was on the other hand observed in the macro-PL spectra of figure 6.9 (a). Besides these considerations, note that among all acquired spectra, no peak was recurrently observed but most of the randomly-raising lines present a narrow FWHM below 5 meV.

The presence of these multiple peaks was besides confirmed by nano-CL experiments performed by L. Tizei in the STEM group at the Laboratoire de Physique du Solide (LPS) of Orsay. Figure 6.11 (a) shows the CL spectrum (the inset is a close up of the large-scale spectrum presented on the main axis) acquired on the GaN insertion of figure 6.11 (b). Figure 6.11 (c) is a lower resolution ADF image of the same insertion, rescaled to match the size of figures 6.11 ①, ②, ③ and ④. Those images in fact present maps of the CL luminescence integrated over the ranges of wavelengths indicated by the corresponding grey zones in figure 6.11 (a). A striking feature is that different wavelengths are emitted when different zones of the GaN island are excited by the electron beam. In particular, luminescence centered around 3.69 eV (336 nm) and that centered around 3.99 eV (311 nm) arise from the two opposite sides of the nanostructure.

Both the presence of multiple peaks and their emergence at various energies when different zones of the axial insertions are excited suggest the presence of localized states inside island-like GaN nanostructures. The origin of these localized states is however difficult to identify. On the one hand, one can hypothesize on the presence of donors that

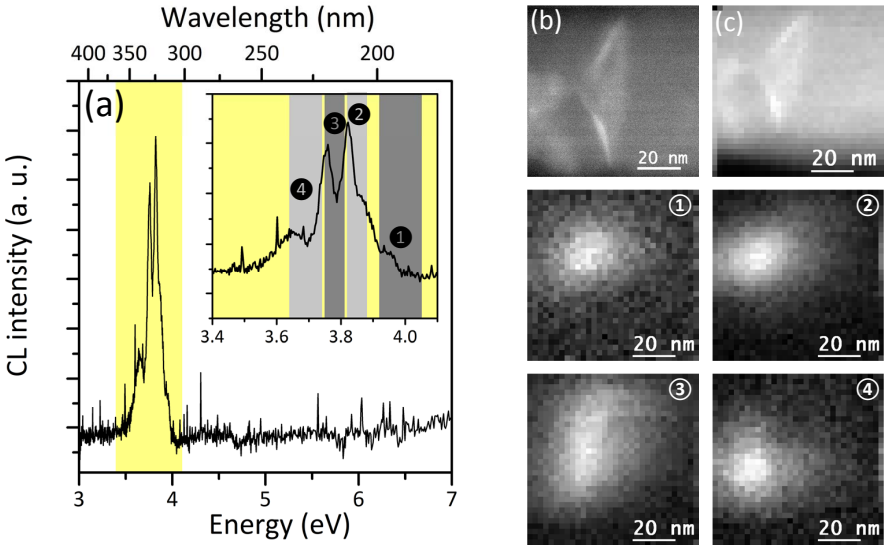

FIG. 6.11 – (a) CL spectrum (the inset is a close-up of the large-scale spectrum presented on the main axis) acquired on the GaN insertion of figure 6.11 (b); (c) low resolution ADF image of the same insertion, rescaled to match the size of figures 6.11 ①, ②, ③ and ④ which present maps of the CL luminescence integrated over the ranges of wavelengths indicated by the corresponding gray zones in (a).

would trap the carriers in the nanostructure. The typical residual donor background in GaN grown by MBE is about 10^{16} atoms/cm^3. Considering this value and a GaN axial insertion volume of about 4×10^{-18} cm^3, a simple calculus leads to the conclusion that only one donor should be found inside the GaN nanostructure every 40 NWs. This result is absolutely inconsistent with the observation of several peaks in each NW. In fact, for residual donors to be at the origin of the observed peaks, one should have an impurity residual background of 10^{18} atoms/cm^3, which is unrealistically high for GaN. On the other hand, as evoked in the previous section, if Al and Ga atoms inter-diffuse during the deposition of the GaN axial insertion or of the subsequent AlN barrier, one can imagine that AlGaN alloys with different contents create different strained states which give rise to the several peaks observed. It would be interesting to further explore this lead by correlating the strain distribution inside GaN islands to the emission spot of each peak.

6.4 Conclusion and prospects of the chapter

In this chapter, we addressed the issue of GaN axial insertions on AlN NWs from an original point of view. GaN axial insertions are usually grown on thin AlN NWs and keep the diameter of the underneath column, which owe them to be called “Qdiscs”. Here, we wondered whether it would be possible to observe a shape transition of GaN, from such Qdisc towards islands, on sufficiently large AlN NWs.

Theoretical calculations performed by F. Glas predicts that such shape transition would be favorable to the GaN/AlN system above a given critical AlN NW diameter, the value of which depends on the input parameters of the calculus. In particular, considering a mismatch of 2.5 % between GaN and AlN, the AlN NW critical diameter was estimated to be around 60 nm. Experimentally, we observed island-like GaN axial insertions on AlN NW diameters larger than 77 nm but doubts exist on the composition and the exact shape of these islands. Microscopy analyses actually revealed that GaN island cores contain Al atoms. Likely, the presence of these Al atoms is a consequence of the shape of the AlN NW itself. In fact, rather than pure AlN NW (the growth of which is not yet fully mastered) we used AlN deposited on GaN NWs, *i.e.* GaN-AlN core-shell heterostructure NWs. In the previous chapter, we observed that such heterostructures sometimes exhibit a hill-like top AlN surface. As a result, it is possible that when depositing GaN on such surface, GaN coats the hill and form a "bowler hat" around AlN. Optical characterization (both by photoluminescence and by cathodoluminescence) of these original nanostructures revealed the presence of localized states inside GaN axial insertions, the origin of which is not yet determined.

Data and discussions presented in this chapter constitute preliminary results of an ongoing work. Clearly, in virtue of their novelty, structures hereby presented are interesting and deserve to be further investigated. In particular, taking advantage of our faculty to isolate a single NW, we plan to perform temperature-dependent and power-dependent micro-PL experiments which may give us more insight on the origin of the localized states. Ideally, we would then correlate micro-PL results with the structure of the corresponding island by observing the very same NW in HRTEM. We eventually plan to grow new GaN island in AlN NW samples with the aim of first flattening the AlN shell top surface by changing the Al/N flux ratio.

Conclusions and prospects

The objective of the work presented in this manuscript was to investigate the growth mechanisms as well as the fundamental properties of GaN NWs and GaN-AlN heterostructures based on GaN NWs. To do so, nanostructures were elaborated by plasma-assisted molecular beam epitaxy and a combination of structural and optical characterization techniques was used, namely RHEED, X-ray diffraction-based techniques, microscopy, photoluminescence and cathodoluminescence.

Self-assembled GaN nanowires

Regarding GaN NWs, our attention focused on the self-assembled growth mode both on bare Si(111) and when using a 2-3 nm thick AlN buffer on Si(111).

In the former case, that is **the case of bare silicon**, whether Ga or N species are provided first, N inevitably bond with silicon atoms from the substrate. The resulting structure was identified as crystalline β-Si_3N_4 from the 8×8 surface reconstruction it forms with Si(111). Interestingly, it appears that this crystalline β-Si_3N_4 layer must be amorphized before GaN can start to form. Species responsible from the transformation of crystalline β-Si_3N_4 into amorphous Si_xN_y were evidenced to be provided by the plasma source and could be either N atoms themselves or N^+ ions generated together with N atoms from the plasma source. In other words, on bare Si(111), when providing Ga and N species together, processes occurring on the surface are the following:

- Si(111) surface **nitridation** (despite the potential presence of Ga atoms), resulting in the formation of crystalline β-Si_3N_4 which reconstructs as 8×8 compared to Si(111)
- **Amorphization** of β-Si_3N_4 into Si_xN_y
- Formation of GaN precursors (**nucleation**) on amorphous Si_xN_y

GaN nucleation is then followed by the precursor ripening and by the axial GaN incorporation corresponding to the nanocolumn **elongation phase**. Investigation of the elongation phase goes beyond this study but more insight about it can be found in Ref. [196] for

instance.

The case of GaN NWs grown using a thin AlN buffer is somewhat different. Unlike Ga atoms, Al in fact strongly bind with N species. AlN then forms directly on Si(111) without intermediate silicon nitride phase. As a consequence, when subsequently delivering Ga and N atoms to initiate GaN NWs growth on such surface, there is no process of β-Si_3N_4 formation and amorphization before GaN actually nucleates.

In chapter 4, we besides showed that **both GaN NWs grown on bare Si(111) and on Si(111) covered by a thin AlN buffer** are **N-polar**.

AlN buffers on silicon, fabricated in the same conditions as the one we used, have already been identified in the literature as Al-polar [242]. In addition, AlGaN NWs grown on a 30 nm-thick AlN buffer were shown to be metal-polar [241]. Based on these informations and on our own results, we proposed a model to describe the growth of GaN NWs on Si(111) covered by a thin AlN buffer. First, it is likely that AlN do not deposit as a continuous layer but as grains [80], similarly to what has already been observed on sapphire [152]. Then, for the thinnest AlN buffers, these grains may not overlay the entire silicon surface, leaving small areas between the AlN grains uncovered. The nucleation of subsequently deposited GaN likely occurs between the grains, on nitrided Si(111), analogously to what happens on bare Si(111). GaN NW polarity is then directed by the way Ga bind to N atoms from Si_xN_y rather than guided by the polarity of the AlN buffer itself. When the AlN buffer is thicker, it covers the entire silicon surface. On such surface, GaN has no choice than to grow on top of AlN and most likely with the same polarity: metal. Several puzzling points need, however, to be mentioned:

- If, when using a thin AlN buffer, GaN NW nucleate on Si_xN_y as it is the case on bare silicon, one should be able to observe this Si_xN_y layer underneath the column feet by cross-sectional HRTEM. Yet, up to now, the presence of Si_xN_y between AlN buffer grains and under GaN nanocolumns has not been evidenced.
- In our group, our numerous attempts to grow GaN NWs on thick AlN buffers remained unsuccessful. It seems that no matter the growth conditions we use, we end up with a rough GaN layer. If GaN columnar growth is initiated by a Stranski-Krastanov-like transition, as observed in Refs. [73, 80] on thin AlN buffers, then we should be able to induce it even on thick AlN layers. Are we not using "extreme-enough" growth conditions, such as ultra-low Ga fluxes? It would be interesting to test such unusual growth conditions. Alternatively, grazing-incidence X-ray diffraction performed *in situ* while depositing GaN on a thick AlN buffer could help clarifying this issue.

Regarding now dynamics of the different growth steps above-described, the time necessary for the two first stages, that are nitridation and amorphization, was found to be

independent from the substrate temperature, at least between 770 and 850 °C. On the other hand, raising the substrate temperature increases both the diffusion and the desorption of Ga adatoms on amorphous Si_xN_y, thus lowers the probability of GaN precursors to form: the average time necessary for the precursor formation (for the elongation phase to start) as well as the delay between the formation of the first and the last of these precursors and also the mean distance between two precursors are extended. In other terms, the highest substrate temperatures generate a low NW density and a large disparity of their final length. The same mechanisms stand for the nucleation of GaN NW precursors on a thin AlN buffer.

In conclusion, although self-assembled GaN NWs have the advantage to be easily grown, the control of their morphology (density, length, length dispersion, diameter) is not trivial. In particular, a compromise must be done between the NW mean separation distance and the homogeneity of the NW ensemble, the lowest densities bringing the largest NW length disparity and conversely. This statement is however only true when performing GaN NW growth in a single step. In Ref. [259], the authors proposed to separate the nucleation and the growth phases. With such method, it is possible to first use a high substrate temperature in order to nucleate precursors with a low density. In a second stage, one can decrease the temperature in order to achieve a more homogeneous elongation of the nanocolumns. Nevertheless, when lowering the temperature for the second phase, some new precursors may likely nucleate between the precursors from the first phase and one would face the same issue as with a single-step growth. As length homogeneity between NWs is intrinsically linked to their density, it would be nice to get rid of one of these two parameters for a better control of the NW morphology. In this context, selective area growth (SAG) could permit to control the column density through the hole density in the mask, so that low densities could be achieved even at low temperatures allowing, in parallel, to reach a better homogeneity of the column length. In our group, we are currently exploring this lead. Preliminary results of SAG of GaN NWs on patterned silicon substrates can be found in appendix B.

GaN-AlN nanowire heterostructures

Regarding now the second part of the manuscript, our attention focused on GaN-AlN heterostructures based on GaN NWs. Investigating first GaN-AlN core-shells NWs, we showed that it is possible to increase the ratio between the AlN shell thickness and its length by tuning both the Al/N flux ratio and the incidence angle of these two species. The observed shell morphologies are explained by a strong Al diffusion from the NW sidewalls to the top of the NWs, combined to desorption of part of the impinging N atoms via N_2 formation.

We besides studied the evolution of the strain inside GaN cores as a function of the

AlN shell thickness. Up to a thickness of 3 nm, experimental results based on X-rays follow the theoretical trend drawn within a purely elastic model but drastically differ from this one for larger shells. Microscopy analyses revealed that **the strain within GaN cores is in fact governed by the homogeneity of the AlN shell** they are surrounded of. On the one hand, when the shell grows homogeneously, the system responds elastically, which results in a large uniaxial out-of-plane strain within GaN cores. This strain increases as a function of the shell thickness without plastic relaxation and in the absence of significant in-plane strain, at least up to 12 nm which was the thicker shell investigated in this study. On the other hand, when the shell is asymmetrical, the system first relaxes elastically: shear strains are expected to appear in the GaN cores, resulting in the bending of the NWs. Above a critical shell thickness of about 3 nm, it eventually relaxes plastically by introducing an extra *c*-plane in the shell thinner side. Likely, the asymmetry in the shell is due to the presence of steps at the base of the GaN NWs.

With the perspective of growing GaN radial QWs based on such GaN-AlN core-shell NWs, it therefore seems necessary to better master the symmetry of the AlN shell. This could possibly be managed by improving the morphology of the GaN cores themselves: in particular, by performing SAG on patterned substrate with sufficiently small holes, we should be able to get rid of the step at the foot of the columns. SAG would besides bring the advantage to well separate GaN columns, thus to avoid shadow effects when subsequently depositing the shells. Naturally, another prospect is to perform a study analogous to the one handled in chapter 5 for the deposition of GaN "over-shell" on GaN-AlN core-shell NWs. Such study would provide further precious informations for the fabrication of GaN radial QWs.

On the other hand, the possibility to build AlN shells as large as a hundred of nanometres opened the path to the last chapter of this thesis (chapter 6). When depositing GaN on sufficiently large AlN shells, namely above 77 nm, we observed the formation of island-like GaN insertions. The exact composition of these novel nanostructures is still under questioning, as we detected the presence of Al atoms in their cores. The structures were nevertheless optically characterized and highlighted the presence of localized states, the origin of which has not been yet strictly identified but is likely due to the formation of AlGaN alloys. In the future, temperature-dependent and power-dependent micro-PL experiments on such single nanostructures should help clarifying their origin.

Appendices

A

Crystallography in hexagonal systems

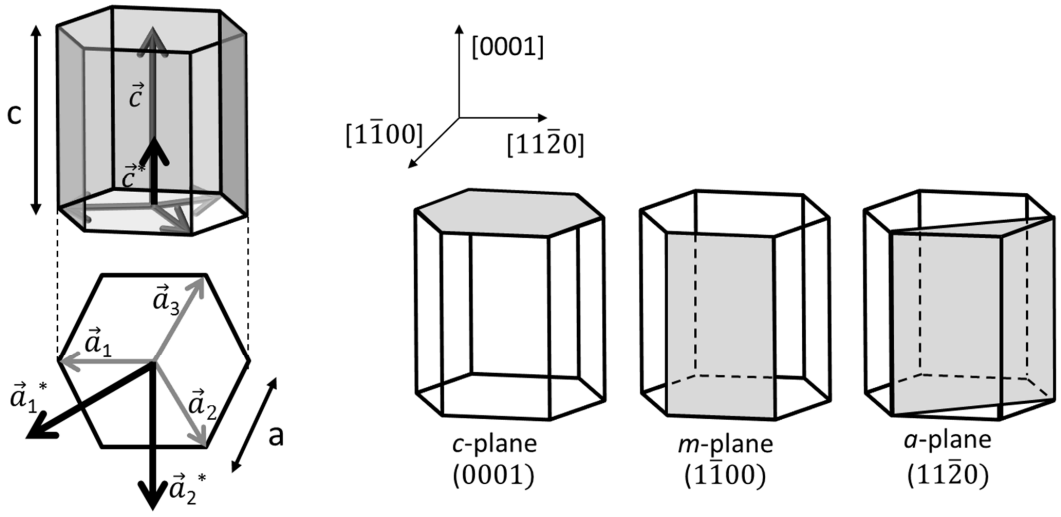

FIG. A.1 – Direct and reciprocal space vectors of hexagonal structures, and most common planes.

In cubic systems, the different permutations of the (h, k, l) Miller indexes describe the whole family of symmetrically equivalent planes. Those indexes are however not appropriate for the hexagonal symmetry. To overcome this issue, a fourth index i defined as $i = -h - k$ has been introduced (Bravais-Miller notation). A thorough description of the hexagonal crystal is then made using the four-index notation (h, k, i, l): when permuting the 3 indexes h, k, and i, one describes the whole family of equivalent planes. For instance the plane (0001) (also called c-plane) illustrated in figure A.1 has no symmetric equivalent. The plane $(1\bar{1}00)$ has five equivalents: $(01\bar{1}0)$, $(\bar{1}010)$, $(\bar{1}100)$, $(0\bar{1}10)$, and $(10\bar{1}0)$, referred

to as "m-planes". Similarly the plane $(11\bar{2}0)$ (a-plane) also has five equivalents. Traditionally, planes in hexagonal system are either expressed in the three- or in the four-index notation. The relation between the two notations is the following:

$$\begin{array}{lcl} (hkil) & \rightarrow & (h,k,l) \\ (stu) & \rightarrow & (s,t,(-s-t),u) \end{array} \tag{A.1}$$

Although convenient for the description of planes, the four-index notation should be taken with caution in what concerns directions. h, k, i, and l are indeed given in the referential defined by the four basis vectors $(\vec{a_1}, \vec{a_2}, \vec{a_3}, \vec{c})$ shown in figure A.1. As it can be observed, $\vec{a_1}$, $\vec{a_2}$ and $\vec{a_3}$ form angles equal to 120 ° and therefore do not constitute an **independent** basis. More specifically, $\vec{a_3} = -\vec{a_1} - \vec{a_2}$. Hence in this case, the relation between the three- and the four-index notation is not as straightforward as for planes [267, 268]:

$$\begin{array}{lcl} [vwxy] & \rightarrow & \left[\frac{(v-x)}{3}, \frac{(w-x)}{3}, \frac{y}{3}\right] \\ [stu] & \rightarrow & [(2s-t),(-s+2t),(-s-t),u] \end{array} \tag{A.2}$$

The conversion between three- and four-index directions can be better seen through the scheme displayed in figure A.2

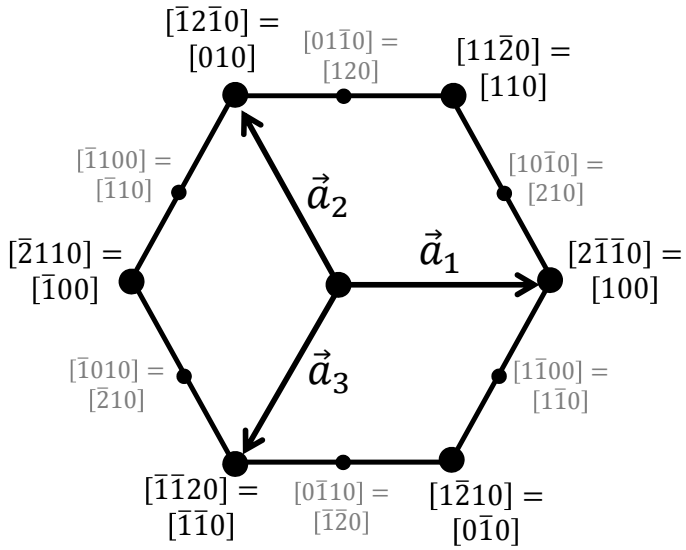

FIG. A.2 – Representation of the equivalence between three- and four- index notations for some specific directions of the hexagonal crystal. This scheme is copied from Ref. [269].

The reciprocal space vectors $(\vec{a_1^*}, \vec{a_2^*}, \vec{c^*})$ are also displayed on figure A.1. The basal reciprocal space vectors $\vec{a_1^*}$ and $\vec{a_2^*}$ are rotated of 30° compared to $\vec{a_1}$ and $\vec{a_2}$, respectively counterclockwise and clockwise. They therefore form an angle equal to 60° and are perpendicular to $\vec{c^*}$. Norms of the reciprocal space vectors are

$$\left\|\vec{a_1^*}\right\| = \left\|\vec{a_2^*}\right\| = \frac{2}{a\sqrt{3}} \tag{A.3}$$

and

$$\left\|\vec{c^*}\right\| = \frac{1}{c} \tag{A.4}$$

Following the definition of Miller indexes, the reciprocal space vector $\vec{q} = h\vec{a_1^*} + k\vec{a_2^*} + l\vec{c^*}$ is perpendicular to the plane $(hkil)$ which cuts the direct space vectors $(\vec{a_1}, \vec{a_2}, \vec{c})$ at $(1/h, 1/k, 1/l)$. Note that in the hexagonal geometry, excepted in some special cases, the direct space vector $\vec{r} = h\vec{a}_1 + k\vec{a}_2 + l\vec{c}$ is however not perpendicular to the the plane $(hkil)$ but $h\vec{a}_1 + k\vec{a}_2 + \frac{3}{2}\frac{a^2}{c^2}l\vec{c}$ is.

In the hexagonal symmetry, the interreticular distance between 2 planes of the $\{hkil\}$ family is given by

$$d_{hkl} = \frac{1}{\sqrt{\frac{4}{3a^2}\left(h^2 + k^2 + hk\right) + \frac{l^2}{c^2}}} \tag{A.5}$$

and the angle α between two planes $(hkil)$ and $(h'k'i'l')$ is

$$\cos\alpha = \frac{hh' + kk' + \frac{1}{2}\left(hk' + h'k\right) + \frac{3a^2}{4c^2}ll'}{\sqrt{\left(h^2 + k^2 + hk + \frac{3a^2}{4c^2}l^2\right)\left(h'^2 + k'^2 + h'k' + \frac{3a^2}{4c^2}l'^2\right)}} \tag{A.6}$$

As an illustration, table A.1 gives the values of the angle between the c-planes ((0001) and $(000\bar{1})$) and other common planes of the GaN WZ cell.

		Plane family					
		$\{1\bar{1}00\}$ *m-planes*	$\{11\bar{2}0\}$ *a-planes*	$\{10\bar{1}\bar{1}\}$	$\{10\bar{1}1\}$	$\{11\bar{2}\bar{2}\}$	$\{11\bar{2}2\}$
c-planes	(0001)	90	90	118.1	62.0	121.7	58.4
	$(000\bar{1})$	90	90	62.0	118.1	58.4	121.7

TABLE A.1 – Angles (given in degrees) between the c-planes ((0001) and $(000\bar{1})$) and other common planes of the GaN WZ cell.

Finally, let us mention that ZB structures as well as diamond structures can be described by a hexagonal cell. Figure A.3 shows how the hexagonal framework is build, based on the cubic one.

Lattice parameters of the reduced hexagonal cell can then be expressed as $a^{hex} = a\sqrt{2}/2$ and $c^{hex} = a\sqrt{3}$. For instance regarding silicon, as $a_{Si} = 5.431$ Å, we get $a_{Si}^{hex} = 3.840$ Å and $c_{Si}^{hex} = 9.459$ Å.

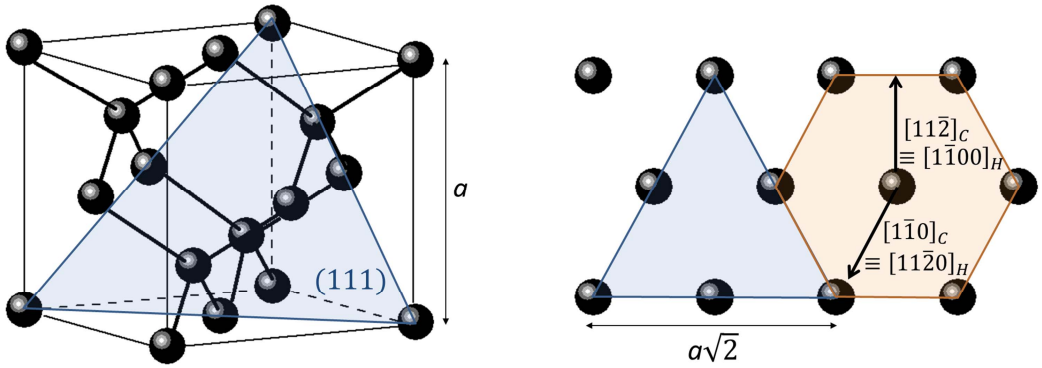

FIG. A.3 – Diamond cell structure in 3D (left) and atomic arrangement in the (111) plane (right). The (111) plane in the cubic frame serves as a basis for the definition of the hexagonal framework.

Considering the matrix

$$M = \begin{pmatrix} -1/2 & 1/2 & 0 \\ 0 & -1/2 & 1/2 \\ 1 & 1 & 1 \end{pmatrix} \tag{A.7}$$

Vectors $\vec{u}_H = (h, k, i, l)$ in the four-index notation of the hexagonal framework are obtained by first calculating

$$\vec{v} = (v_1, v_2, v_3) = M \cdot \vec{u}_C \tag{A.8}$$

where $\vec{u}_C$ is the vector expressed in the three-index notation. Then one must normalize $\vec{v}$ to its smaller integer. Finally $h = v_1$, $k = v_2$, $i = v_1 - v_2$ and $l = v_3$.

B

Selective area growth of GaN nanowires on patterned silicon substrates

Selective area growth (SAG) consists in controlling the incorporation of the deposited material within well-defined zones on the substrate. This method hence requires a specific processing of the substrate prior to the growth, which embrace the deposition and the patterning of a mask layer. The material used for the mask is chosen in function of its selectivity versus the nucleation layer, itself determined by the contrast of mean diffusion lengths and incorporation coefficients of the deposited material between the mask and the nucleation layer. Then, patterns etched in the mask layer define the NW positioning, size and density.

In MBE, few papers on SAG of III-N semiconductors report either homoepitaxy of GaN on GaN substrates [270] or on an AlGaN nucleation layer [271] using SiO_2 as a mask. The first successful SAG of GaN NWs on GaN substrate by PAMBE was realized by the team of K. Kishino, using a Ti mask [272]. This group also attempted growth on bare Si(111) masked with Ti [273] but obtained bunches of NWs rather than well-separated single nanowires. More recently, and simultaneously to the period during which the results hereafter described were obtained, the team of R. Calarco successfully grew well-separated GaN NWs using a SiO_x [274] or a Si [275] mask on an AlN nucleation layer deposited on Si(111).

Here, our aim is to address SAG of GaN NWs on bare silicon with the objective of obtaining well-separated single nanowires. The preliminary work presented hereby has

been made within the ANR SINCRONE. The patterned substrates have been prepared by the teams of S. Landis and P. Ferret using nanoimprint lithography.

B.1 Selectivity tests

In a first stage, we tested the selectivity of three different potential materials to be used as a mask versus bare silicon, namely titanium nitride (TiN), tungsten (W) and vitreous (or glassy) carbon (C). To perform the tests, $3/4^{\text{th}}$ of 2-inch Si(111) wafers were covered with each material to be tested while the other $1/4^{\text{th}}$ was keep uncovered.

The incorporation of a deposited material on a surface depends on its faculty to diffuse on this surface and to desorb before it nucleates. It is hence clear that the roughness of the surface if of prime importance: if the mask is rough, adatoms will be more easily trapped on its surface, resulting in a reduced selectivity of the mask layer. Before attempting any growth on the masked substrates, we therefore checked their surface roughness. Figure B.1 presents $1{\times}1$ µm^2 atomic force microscopy images acquired on each surface.

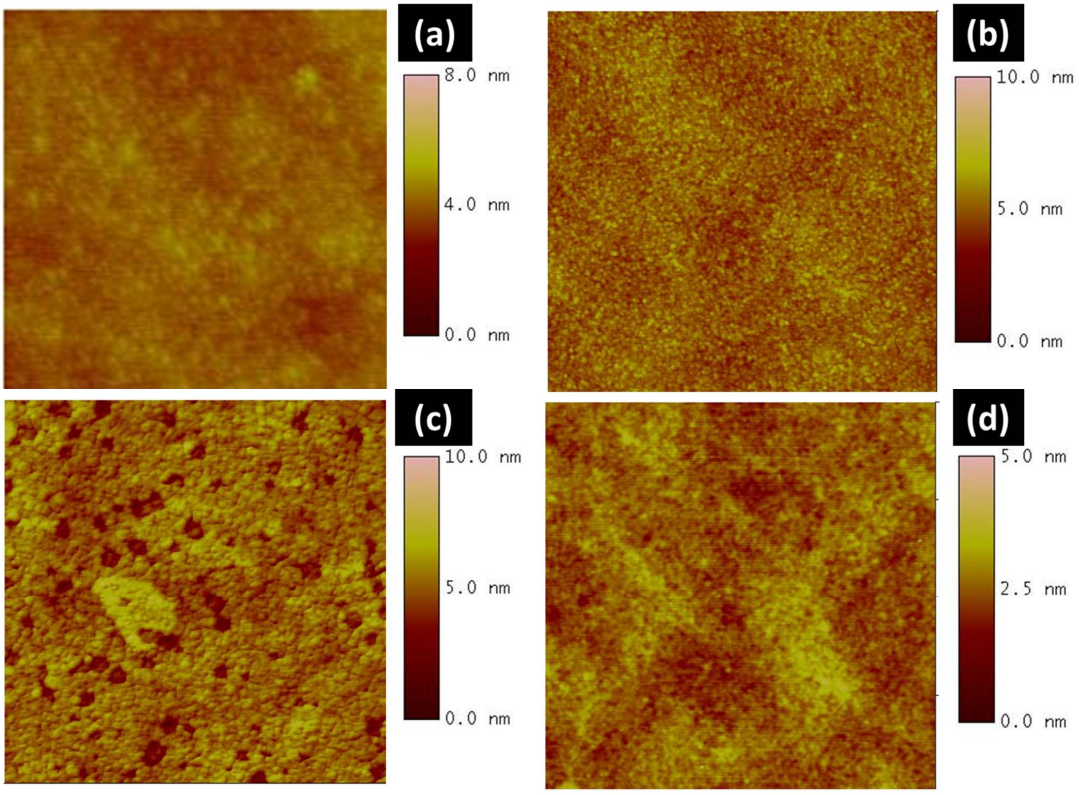

FIG. B.1 – AFM micrographs of (a) the Si(111) surface before mask material depostion, (b) deposited TiN mask, (c) deposited W mask and (d) deposited vitreous C mask. The micrographs are $1 \times 1\ \mu m^2$. The roughness RMS determined from these images are (a) 0.34 nm, (b) 0.53 nm, (c) 0.85 nm and (d) 0.35 nm.

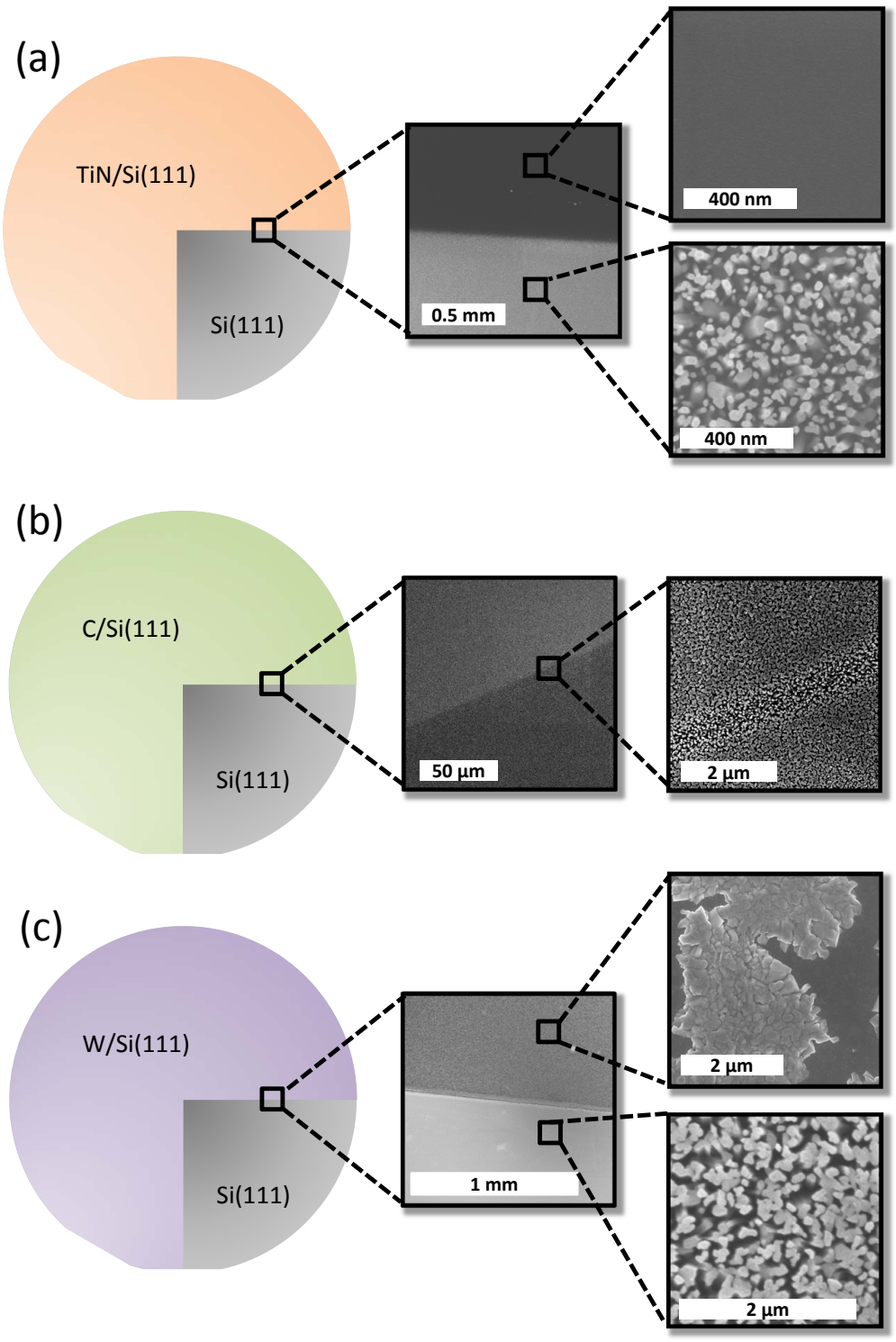

FIG. B.2 – Selectivity tests performed at 795 °C on 2-inch Si(111) wafers covered to $3/4^{th}$ with different materials. (a) TiN mask shows a good selectivity (b) vitreous carbon mask shows no selectivity at all and (c) tungsten mask shows a bad selectivity at this temperature.

Figure B.1 (a) exhibits a micrograph of the Si(111) surface before its processing. Based on the tools available with the AFM acquisition software, the roughness of this surface was estimated to be equal to 0.34 nm. After deposition of the mask materials, TiN (Fig. B.1 (b)), W (Fig. B.1 (c)) and C (Fig. B.1 (d)), surfaces have respective roughnesses of 0.53 nm, 0.85 nm and 0.35 nm. In every case, the roughness of the mask is only slightly higher than that of the Si(111) surface, hence should not play a substantial role is the trapping of the adatoms.

GaN was then deposited on each of the masked substrate at a temperature of 795 °C and with a growth rate of 0.11ML/s (Ga/N flux ratio equal to 0.6). Figure B.2 presents top view SEM images obtained on each side of the border between the mask material and the Si(111) substrate. It appears that in this set of growth conditions, TiN (Fig. B.2 (a)) exhibits an excellent selectivity: GaN NWs indeed exclusively grew on the bare Si(111) side of the border leaving the TiN side uncovered. Vitreous carbon (Fig. B.2 (b)), on the other hand, shows no selectivity at all: GaN NWs grew on both the bare Si(111) surface and the mask. Finally, tungsten (Fig. B.2 (c)) exhibits a poor selectivity. Likely in this case, it could have been possible to improve the selectivity by adjusting the growth conditions. Nevertheless, considering the promising result obtained from TiN, our choice went towards this material for use as a mask in patterned substrates.

B.2 Patterned substrates

The patterned substrates we used were fabricated as follows:

- First, 20 nm of SiO_2 were deposited on the silicon surface. This layer is used in the third step as an etch-stop.
- Second, 20 nm of TiN were deposited on top of the SiO_2 layer.
- Third, holes with a specific design – hereafter described – were etched in the TiN layer by nanoimprint lithography.
- Last, SiO_2 was removed from the holes by CHF_3 plasma etching down to the silicon.

This is illustrated in figure B.3.

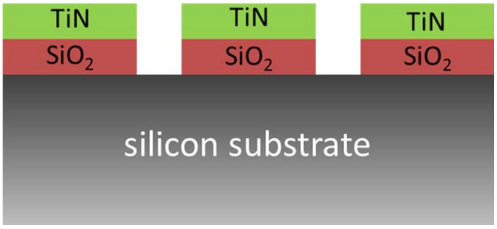

Fig. B.3 – Scheme of patterned substrates we used in this study.

The resulting patterned substrates contain different squares (named S_i) gathering holes with different diameters and spacing. Figure B.4 displays a scheme of this substrate. Numbers inside the squares indicate the hole diameter (without bracket) and the spacing between the holes (inside brackets). Crossed squares mask those that were not etched during the nanoimprint lithography.

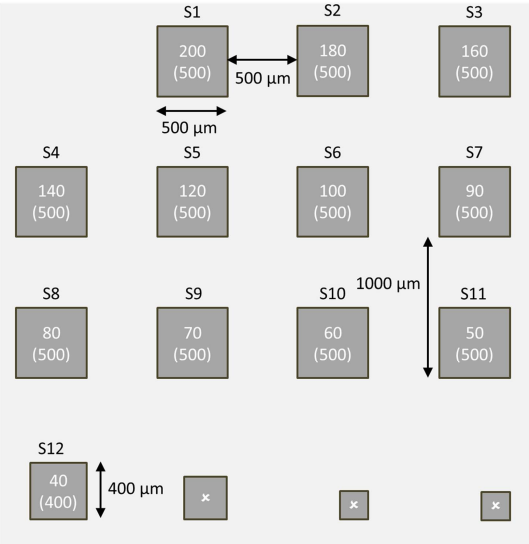

FIG. B.4 – Sketch of type B patterned substrates. Numbers inside the squares indicate the hole diameter (without bracket) and the spacing between the holes (inside brackets). Crossed squares mask those that were not properly etched during the nanoimprint lithography.

B.3 GaN nanowire morphology on patterned substrates

Figure B.5 presents bird-eye view SEM images of each square of sample N1686, grown during 3 hours at 815 ℃ with a Ga/N ratio of 0.8. While zones S1 to S3 with the larger holes present a bad selectivity, nearly no trace of GaN is observed on the TiN mask of zones S4 to S12. In these zones, GaN NWs have indeed grown as bunches within the holes but exhibit a certain degree of bending compared to the normal to the substrate.

Qualitatively, by tuning the growth conditions we were observed that

- the selectivity of the mask is debased when going to lower substrate temperatures and/or to higher Ga fluxes ;
- NW density inside the holes is reduced when going to higher substrate temperatures and/or lower Ga fluxes. GaN growth is sometimes even inhibited (too high substrate temperature or too little Ga provided).

It is difficult to quantify these observations. We noticed that aside from the growth conditions themselves, the NW eventual morphology largely depends on the substrate quality and preparation. From sample to sample, these two features are not always reproducible. Nevertheless, although we tested a large set of growth conditions, we could not achieve

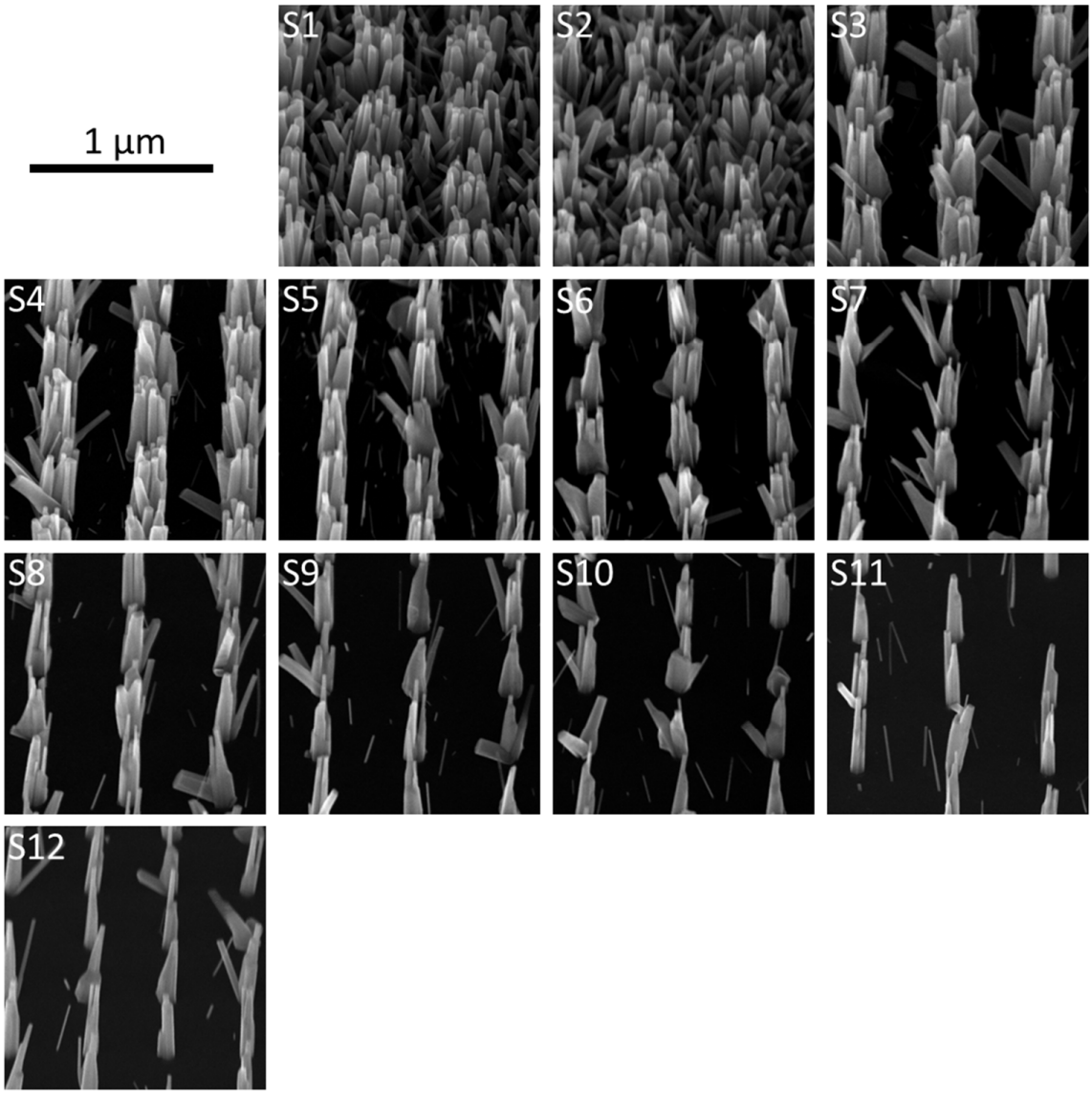

Fig. B.5 – Bird-eye view SEM images taken in each square of sample N1686 grown during 3 hours at 815 ℃ with a Ga/N ratio of 0.8.

"morphologically nicer" NWs: some of them (mostly those located at the periphery of the mask holes) always exhibit a tendency to grow askew. Likely, such bending is induced by the nucleation of GaN NWs on the irregular side-wall surface of the mask holes.

B.4 Optical properties of GaN nanowires grown on patterned substrates

Despite their lack of straightness, GaN NWs grown on such patterned substrates showed very promising optical properties. This is true even on squares S1 to S3 where the mask was not perfectly selective. Figure B.6 displays PL spectra obtained from each square of sample N1686 (a) on a large energy scale and (b) around the GaN band-edge.

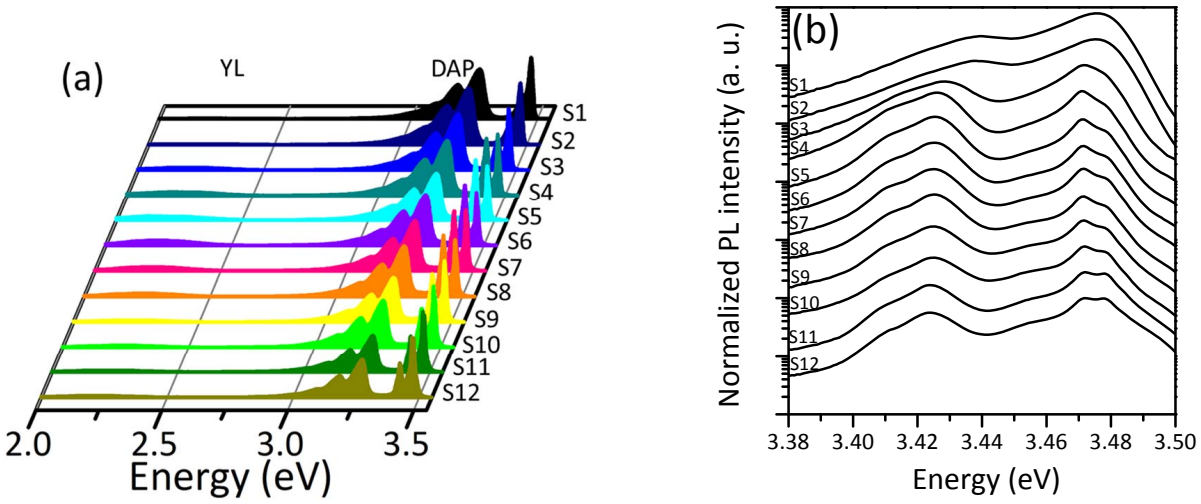

FIG. B.6 – PL spectra acquired from each square on sample N1686
(a) on a large scale and (b) around the GaN band-edge.

The first thing that deserves to be pointed out is the quasi-absence of yellow band (YL). Then, another striking feature is the thinness of the GaN band-edge. A FWHM of about 1.8 meV has been measured on the spectrum from S1, which is of the same order than that of the best self-assembled GaN NWs. When going towards smaller holes (S12 for instance), one can even distinguish the D_0X and the FX_A contributions at 3.482 and 3.489, respectively. These results indicate that although not "morphologically nice", GaN NWs grown on patterned substrate have a good crystal quality.

B.5 Prospects on selective area growth of GaN nanowires

Difficulties we face to obtain well-separated straight GaN NWs on patterned silicon substrate raise some questions. Why does nucleation of GaN NWs occur on the side-walls

of the holes? Is it a problem related to the fabrication of the substrate? Could we prevent GaN NWs to grow askew? For the moment, it seems difficult to improve SAG of GaN NWs on bare silicon. In this context, we are currently putting aside this type of substrates. The new leads we are investigating rely on the use of different patterned substrates which have the disadvantage to require more preparation steps but which will hopefully result in more successful localized GaN NW growths.

C

Publications, conferences & workshops

So far, the work presented in this manuscript led to the following publications and presentations:

Publications

- D. Jalabert, Y. Curé, K. Hestroffer, Y. M. Niquet, and B. Daudin
  Strain state in GaN nanodisks in AlN nanowires studied by medium energy ion spectroscopy.
  Nanotechnology **23**, 425703 (2012).

- K. Hestroffer, C. Leclere, V. Cantelli, C. Bougerol, H. Renevier, and B. Daudin
  In situ study of self assembled GaN nanowires nucleation on Si(111) by Plasma-Assisted Molecular Beam Epitaxy.
  Appl. Phys. Lett. **100**, 212107 (2012).

- R. Mata, A. Cros, K. Hestroffer, and B. Daudin
  Surface optical phonon modes in GaN nanowire arrays: Dependence on nanowire density and diameter.
  Phys. Rev. B **85**, 035322 (2012).

- K. Hestroffer, C. Leclere, C. Bougerol, H. Renevier, and B. Daudin
  Polarity of GaN nanowires grown by plasma-assisted molecular beam epitaxy on Si(111).
  Phys. Rev. B **84**, 245302 (2011).

- R. Mata, K. Hestroffer, J. Budagosky, A. Cros, C. Bougerol, H. Renevier, and B. Daudin
  Nucleation of GaN nanowires grown by plasma-assisted molecular beam epitaxy: the effect of temperature.
  J. Cryst. Growth **334**, 177 (2011).

- K. Hestroffer, R. Mata, D. Camacho, C. Leclere, G. Tourbot, Y. M. Niquet, A. Cros, C. Bougerol, H. Renevier, and B. Daudin
  The structural properties of GaN/AlN core-shell nanocolumn heterostructure.
  Nanotechnology **21**, 415702 (2010).

Conferences and workshops

2012

- *Nucleation of GaN nanowires on silicon.*
  K. Hestroffer, C. Leclere, V. Cantelli, C. Bougerol, H. Renevier, B Daudin
  Nanowires2012, Berlin, Germany (Poster)

- *Nucleation of GaN nanowires on silicon.*
  K. Hestroffer, C. Leclere, V. Cantelli, C. Bougerol, H. Renevier, B Daudin
  13$^{\text{ème}}$ journées de la matière condensée, Montpellier, France (Poster)

- *Growth of quantum wire III-N nanostructures.*
  B. Daudin, C. Bougerol, B. Gayral, K. Hestroffer, M. Kociak, C. Leclere, Z. Mahfoud, H. Renevier, D. Sam-Giao, G. Tourbot
  4$^{\text{th}}$ International Symposium on Growth of III-Nitrides, St. Petersburg, Russia (Invited oral presentation)

2011

- *Polarity of GaN nanowires grown by Plasma-Assisted Molecular Beam Epitaxy.*
  K. Hestroffer, C. Bougerol, C. Leclere, H. Renevier, J. L. Rouvière, B. Daudin
  ICNS-9, Glasgow, Scotland (Oral presentation)

- *Anomalous X-Ray scattering for nanostructure characterisation: GaN nanowires polarity.*
  C. Leclere, K. Hestroffer, C. Bougerol, B. Daudin, H. Renevier
  REXS 2011, Aussois, France (Poster)

- *Nucleation of GaN nanowires grown by molecular beam epitaxy: its relation to length distribution.*
  R. Mata, J. Budagosky, A. Cros, A. Garcia-Cristobal, K. Hestroffer, B. Gayral,

C. Bougerol, **B. Daudin**, H. Renevier
EMRS 2011, Nice, France (Invited oral presentation)

- *Polarity of GaN nanowires grown by Plasma-Assisted Molecular Beam Epitaxy.*
  K. Hestroffer, C. Bougerol, C. Leclere, H. Renevier, J. L. Rouvière, B. Daudin
  EMRS 2011, Nice, France (Oral presentation)

- *Growth, structural and optical properties of GaN/AlN and GaN/GaInN nanowire heterostructures.*
  G. Tourbot, K. Hestroffer, B. Gayral, **B. Daudin**, C. Bougerol, C. Leclere, H. Renevier, P. Gilet
  BWSP-15, Juiz de Fora, Brazil (Invited oral presentation)

- *Polarity of GaN nanowires grown by Plasma-Assisted Molecular Beam Epitaxy.*
  K. Hestroffer, C. Bougerol, C. Leclere, H. Renevier, J. L. Rouvière, B. Daudin
  Euro-MBE 2011, Alpe d'Huez, France (Oral presentation)

- *GaN nanowires nucleation and growth mechanisms: the input of in-situ X-rays diffraction.*
  C. Bougerol, **B. Daudin**, K. Hestroffer, O. Landré, C. Leclere, G. Renaud, H. Renevier, G. Tourbot
  ESRF User's Meeting 2011, Grenoble, France (Invited oral presentation)

- *Structural Properties of GaN/AlN Core-Shell Nanocolumn Heterostructures.*
  K. Hestroffer, R. Mata, D. Camacho, C. Leclere, G. Tourbot, Y. M. Niquet, A. Cros, C. Bougerol, H. Renevier, B. Daudin
  ESRF User's Meeting 2011, Grenoble, France (Poster)

2010

- *Nucleation Kinetics of GaN Nanowires Grown by Molecular Beam Epitaxy.*
  R. Mata, J. Budagosky, K. Hestroffer, A. Cros, A. Garcia-Cristobal, B. Gayral, C. Bougerol, H. Renevier, B. Daudin
  IWN 2010, Tampa, USA (Oral presentation)

- *Structural Properties of GaN/AlN Core-Shell Nanowire Heterostructures.*
  K. Hestroffer, R. Mata, D. Camacho, C. Leclere, G. Tourbot, Y. M. Niquet, A. Cros, C. Bougerol, H. Renevier, B. Daudin
  IWN 2010, Tampa, USA (Oral presentation)

Bibliography

[1] I. Akasaki, H. Amano, K. Itoh, N. Koide, and K. Manabe, GaN-based ultraviolet/blue light emitting devices, *Inst. Phys. Conf. Ser.* **129**, 851 (1992).

[2] S. Nakamura, T. Mukai, and M. Senoh, Candela-class high-brightness InGaN/AlGaN double-heterostructure blue light-emitting diodes, *Appl. Phys. Lett.* **64**, 1687 (1994).

[3] S. Nakamura, M. Sehnoh, N. Iwasa, S. Nagahama, T. Yamada, and T. Mukai, Superbright green InGaN single-quantum-well-structure light emitting diode, *Jpn. J. Appl. Phys.* **34**, L1332 (1995).

[4] S. Nakamura, M. Senoh, S. Nagahama, N. Iwasa, T. Yamada, T. Matsushita, H. Kiyoku, and Y. Sugimoto, InGaN-based multi-quantum-well-structure laser diodes, *Jpn. J. Appl. Phys.* **35**, L74 (1996).

[5] S. Nakamura, M. Senoh, S. Nagahama, N. Iwasa, T. Yamada, T. Matsushita, H. Kiyoku, and Y. Sugimoto, InGaN multi-quantum-well-structure laser diodes with cleaved mirror cavity facets, *Jpn. J. Appl. Phys.* **35**, L217 (1996).

[6] S. Nakamura, M. Senoh, S. Nagahama, N. Iwasa, T. Yamada, T. Matsushita, H. Kiyoku, Y. Sugimoto, T. Kozaki, H. Umemoto, M. Sono, and K. Chocho, InGaN/GaN/AlGaN-based laser diodes with modulation doped strained-layer superlattices, *Jpn. J. Appl. Phys.* **36**, L1568 (1997).

[7] S. Nakamura, S. Pearton, and G. Fasol, The blue laser diodes - The complete story, (Springer 1997).

[8] O. Ambacher, Growth and applications of group III-nitrides, *J. Phys. D: Appl. Phys.* **31**, 2653 (1998).

[9] S. J. Pearton, J. C. Zolper, R. J. Schul, and F. Ren, GaN: Processing, defects, and devices, *J. Appl. Phys.* **86**, 1 (1999).

[10] A. Mills, Expanding horizons for nitride devices and materials, *III-Vs Review - The advanced semiconductor magazine* **19**, 25 (2006).

[11] F. Fichter, Über Aluminiumnitride, *Z. Anorg. Chem.* **54**, 322 (1907).

[12] W. C. Johson, J. B. Parsons, and M. C. Crew, Nitrogen coumponds of Gallium - III. Gallic nitride, *J. Phys. Chem.* **36**, 2651 (1932).

[13] R. Juza and H. Hahn, Über die Kristallstrukturen von Cu_3N, GaN und InN Metallamide and Metallnitride, *Z. Anorg. Allg. Chem.* **239**, 282 (1938).

[14] H. P. Maruska and J. J. Tietjen, The preparation and properties of vapour-deposited single-crystal-line GaN, *Appl. Phys. Lett.* **15**, 327 (1969).

[15] H. M. Manasevit, F. M. Erdmann, and W. I. Simpson, The use of metalorganics in the preparation of semiconductor materials - IV. The nitrides of Aluminium and Gallium, *J. Electrochem. Soc.* **118**, 1864 (1971).

[16] S. Yoshida, S. Misawa, and A. Itoh, Epitaxial growth of aluminium nitride films on sapphire by reactive evaporation, *Appl. Phys. Lett.* **26**, 461 (1975).

[17] H. Amano, N. Sawaski, I. Akasaki, and Y. Toyoda, Metalorganic vapor phase epitaxial growth of a high quality GaN film using an AlN buffer layer, *Appl. Phys. Lett.* **48**, 353 (1986).

[18] H. Amano, M. Kito, K. Hiramatsu, and I. Akasaki, P-type conduction in Mg-doped GaN treated with low-energy electron beam irradiation (LEEBI), *Jpn. J. Appl. Phys.* **48**, 353 (1989).

[19] K. Hiramatsu, S. Itoh, H. Amano, I. Akasaki, N. Kuwano, T. Shiraishi, and K. Oki, Growth mecanisms of GaN grown on sapphire with AlN buffer layer by MOVPE, *J. Cryst. Growth* **115**, 628 (1991).

[20] M. Yoshizawa, A. Kikuchi, M. Mori, N. Fujita, and K. Kishino, Growth of self-organized GaN nanostructures on Al_2O_3(0001) by RF-radical source molecular beam epitaxy, *Jpn. J. Appl. Phys.* **36**, 459 (1997).

[21] M. A. Sanchez-Garcia, E. Calleja, E. Monroy, F. J. Sanchez, F. Calle, E. Munoz, and R. Beresford, The effect of III/V ratio and substrate temperature on the morphology and properties of GaN- and AlN-layers grown by molecular beam epitaxy on Si(111), *J. Cryst. Growth* **183**, 23 (1998).

[22] W. Lu and C. M. Lieber, Semiconductor nanowires, *J. Phys. D: Appl. Phys.* **39**, R387 (2006).

[23] R. Agarwal and C. M. Lieber, Semiconductor nanowires: optics and optoelectronics, *Appl. Phys. A* **85**, 209 (2006).

[24] D. J. Sirbuly, M. Law, H. Yan, and P. Yang, Semiconductor nanowires for subwavelength photonics integration, *J. Phys. Chem. B* **109**, 15 190 (2005).

[25] Y. L. F. Qian, J. Xiang, and C. M. Lieber, Nanowire electronic and optoelectronic devices, *Mater. Today* **9**, 18 (2006).

[26] F. Patolsky and C. M. Lieber, Nanowire nanosensors, *Mater. Today* **8**, 20 (2005).

[27] F. Qian, Y. Li, S. Gradecak, D. Wang, C. J. Barrelet, and C. M. Lieber, Gallium Nitride-based nanowire radial heterostructures for nanophotonics, *Nano Lett.* **4**, 1975 (2004).

[28] F. Qian, S. Gradecak, Y. Li, C.-Y. Wen, and C. M. Lieber, Core/multishell nanowire heterostructures as multicolor, high-efficiency light-emitting diodes, *Nano Lett.* **5**, 2287 (2005).

[29] K. Tomioka, J. Motohisa, S. Hara, K. Hiruma, and T. Fukui, GaAs/AlGaAs core multishell nanowire-based light-emitting diodes on Si, *Nano Lett.* **10**, 1639 (2010).

[30] Y. Li, J. Xiang, F. Qian, S. Gradecak, Y. Wu, H. Yan, D. A. Blom, and C. M. Lieber, Dopant-free GaN/AlN/AlGaN radial nanowire heterostructures as high electron mobility transistors, *Nano Lett.* **6**, 1468 (2006).

[31] B. Tian, X. Zheng, T. J. Kempa, Y. Fang, N. Yu, G. Yu, H. Huang, and C. M. Lieber, Coaxial silicon nanowires as solar celles and nanoelectronic power sources, *Nature* **449**, 885 (2007).

[32] Y. Dong, B. Tian, T. J. Kempa, and C. M. Lieber, Coaxial group III-Nitride nanowire photovoltaics, *Nano Lett.* **9**, 2183 (2009).

[33] M. Tchernycheva, C. Sartel, G. Cirlin, L. Travers, G. Patriarche, J.-C. Harmand, L. S. Dang, J. Renard, B. Gayral, L. Nevou, and F. Julien, Growth of GaN free-standing nanowires by plasma-assisted molecular beam epitaxy: structural and optical characterization, *Nanotechnology* **18**, 385 306 (2007).

[34] H. Wang, C. Chen, Z. Gong, J. Zhang, M. Gaevski, M. Su, J. Yang, and M. A. Khan, Anisotropic structural characteristics of $(11\bar{2}0)$ GaN templates and coalesced epitaxial lateral overgrown films deposited on $(10\bar{1}2)$ sapphire, *Appl. Phys. Lett.* **84**, 499 (2004).

[35] D. S. Li, H. Chen, H. B. Yu, X. H. Zheng, Q. Huang, and J. M. Zhou, Anisotropy of a-plane GaN grown on r-plane sapphire by metalorganic chemical vapor deposition, *J. Cryst. Growth* **265**, 107 (2004).

[36] T. Paskova, V. Darakchieva, P. Paskov, J. Birch, E. Valcheva, P. O. A. Persson, B. Arnaudov, S. Tungasmitta, and B. Monemar, Properties of nonpolar a-plane GaN films grown by HVPE with AlN buffers, *J. Cryst. Growth* **281**, 55 (2005).

[37] X. F. Duan and C. M. Lieber, Laser-assisted caralytic growth of single crystal GaN nanowires, *J. Am. Chem. Soc.* **122**, 189 (2000).

[38] P. Deb, H. Kim, V. Rawat, M. Olivier, S. Kim, M. Marshall, E. Stach, and T. Sands, Faceted and vertically aligned GaN nano-rod arrays fabricated without catalysts or lithography, *Nano Lett.* **5**, 1847 (2005).

[39] S. D. Hersee, X. Sun, and X. Wang, The controlled growth of GaN nanowires, *Nano Lett.* **6**, 1808 (2006).

[40] R. Koester, J. S. Hwang, C. Durand, D. L. S. Dang, and J. Eymery, Self-assembled growth of catalyst-free GaN wires by metal-organic vapour phase epitaxy, *Nanotechnology* **21**, 015 602 (2010).

[41] Y. S. Park, S.-H. Lee, J.-E. Oh, C.-M. Park, and T.-W. Kang, Self-assembled GaN nano-rods grown directly on (111)Si substrates: dependance on growth conditions, *J. Cryst. Growth* **282**, 313 (2005).

[42] R. Meijers, T. Richter, R. Calarco, T. Stoica, H.-P. Bochem, M. Marso, and H. Lüth, GaN-nanowhiskers: MBE-growth conditions and optical properties, *J. Cryst. Growth* **289**, 381 (2006).

[43] E. Calleja, J. Ristic, S. Fernancez-Garrido, L. Cerutti, M. A. Sanchez-Garcia, J. Grandal, A. Trampert, U. Jahn, G. Sanchez, A. Griol, and B. Sanchez, Growth, morphology, and structural properties of group III-nitride nanocolumns and nanodisks, *phys. stat. sol. (b)* **244**, 2816 (2007).

[44] J. Ristic, E. Calleja, S. Fernancez-Garrido, L. Cerutti, A. Trampert, U. Jahn, and K. H. Ploog, On the mechanisms of spontaneous growth of III-nitride nanocolumns by plasma-assisted molecular beam epitaxy, *J. Cryst. Growth* **310**, 4035 (2008).

[45] A. P. Vajpeyi, G. Tsiakatouras, K. Tsagaraki, M. Androulidaki, A. Georgakilas, S.Tripathy, and S. J. Chua, Effect of substrate temperature on spontaneous GaN nanowires growth and optoelectronic properties, *Physica* **41**, 427 (2009).

[46] S. Fernandez-Garrido, J. Grandal, E. Calleja, M. Sanchez-Garcia, and D. Lopez-Romero, A growth diagram for plasma-assisted molecular beam epitaxy of GaN nanocolumns on Si(111), *J. Appl. Phys* **106**, 126 102 (2009).

[47] C. Chèze, L. Geelhaar, B. Jenichen, and H. Riechert, Different growth rates for catalyst-induced and self-induced GaN nanowires, *Appl. Phys. Lett.* **97**, 153 105 (2010).

[48] C. Chèze, L. Geelhaar, O. Brandt, W. M. Weber, H. Riechert, S. Münch, R. Rothemund, S. Reitzenstein, A. Forchel, T. Kehagias, P. Komniou, G. P. Dimitrakopulos, and T. Karakostas, Direct comparison of catalyst-free and catalyst-induced GaN nanowires, *Nano Res.* **3**, 528 (2010).

[49] E. Calleja, M. A. Sanchez-Garcia, F. J. Sanchez, F. Calle, F. B. Naranjo, E. Munoz, S. I. Molina, A. M. Sanchez, F. J. Pacheco, and R. Garcia, Growth of III-nitrides on Si(1 1 1) by molecular beam epitaxy. Doping, optical, and electrical properties, *J. Cryst. Growth* **201**, 296 (1999).

[50] E. Calleja, M. A. Sanchez-Garcia, F. J. Sanchez, F. Calle, F. B. Naranjo, E. Munoz, U. Jahn, and K. Ploog, Luminescence properties and defects in GaN nanocolumns grown by molecular beam epitaxy, *Phys. Rev. B* **62**, 16 826 (2000).

[51] G. Koblmueller, P. Pongratz, R. Averbeck, and H. Richert, Delayed nucleation during molecular beam epitaxy growth of GaN observed by line-of-sight quadrupole mass spectroscopy, *Appl. Phys. Lett.* **80**, 2281–2283 (2002).

[52] J. Sanchez-Paramo, J. M. Calleja, M. A. Sanchez-Garcia, E. Calleja, and U. Jahn, Structural and optical characterization of intrinsic GaN nanocolumns, *Physica E* **13**, 1070 (2002).

[53] R. Averbeck, G. Koblmueller, H. Riechert, and P. Pongratz, Nucleation and growth of GaN observed by in situ line-of-sight mass spectrometry, *J. Cryst. Growth* **251**, 505 (2003).

[54] K. A. Bertness, A. Roshko, N. A. Sanford, J. B. Schlager, and M. H. Gray, Formation of AlN and GaN nanocolumns on Si(111) using molecular beam epitaxy with amonia as a nitrogen source, *phys. stat. sol. (c)* **2**, 2369 (2005).

[55] L. Cerutti, J. Ristic, S. Fernandez-Garrido, E. Calleja, A. Trampert, K. H. Ploog, S. Lazic, and J. M. Calleja, Wurtzite GaN nanocolumns grown on Si(001) by molecular beam epitaxy, *Appl. Phys. Lett* **88**, 213 114 (2006).

[56] K. A. Bertness, N. A. Sanford, J. M. Barker, J. B. Schlager, A. Roshko, A. V. Davydov, and I. Levin, Catalyst-free growth of GaN nanowires, *J. Electron. Matter.* **35**, 576 (2006).

[57] K. A. Bertness, A. Roshko, N. A. Sanford, J. M. Barker, and A. V. Davydov, Spontaneously grown GaN and AlGaN nanowires, *J. Cryst. Growth* **287**, 522 (2006).

[58] N. Thillosen, K. Sebald, H. Hardtdegen, R. Meijers, R. Callarco, S. Montanari, N. Kaluza, J. Gutowski, and H. Lüth, The state of strain in single GaN nanocolumns as derived from micro-photoluminescence measurements, *Nano Lett.* **6**, 704 (2006).

[59] H. Sekiguchi, T. Nakazato, A. Kikuchi, and K. Kishino, Structural and optical properties of GaN nanocolumns grown on (0001) sapphire substrates by rf-plasma-assisted molecular-beam epitaxy, *J. Cryst. Growth* **300**, 259 (2007).

[60] R. K. Debnath, R. Meijers, T. Richter, T. Stoica, R. Calarco, and H. Lüth, Mechanism of molecular beam epitaxy growth of GaN nanowires on Si(111), *Appl. Phys. Lett.* **90**, 123 117 (2007).

[61] K. A. Bertness, A. Roshko, L. M. Mansfield, T. Harvey, and N. A. Sanford, Nucleation conditions for catalyst-free GaN nanowires, *J. Cryst. Growth* **300**, 94 (2007).

[62] L. H. Robins, K. A. Bertness, J. M. Baker, N. A. Sanford, and J. B. Schlager, Optical and structural study of GaN nanowires grown by catalyst-free molecular beam epitaxy. I. Near-band-edge luminescence and strain defects, *J. Appl. Phys.* **101**, 113 505 (2007).

[63] L. Geelhaar, C. Chèze, W. M. Weber, R. Averbeck, H. Riechert, T. Kehagias, P. Komninou, G. P. Dimitrakopulos, and T. Karakostas, Axial and radial growth of Ni-induced GaN nanowires, *Appl. Phys. Lett.* **91**, 093 113 (2007).

[64] R. Calarco, R. J. Meijers, R. K. Debnath, T. Stoica, E. Sutter, and H. Lüth, Nucleation and growth of GaN nanowires on Si(111) performed by molecular beam epitaxy, *Nano Lett.* **7**, 2248 (2007).

[65] R. Songmuang, O. Landré, and B. Daudin, From nucleation to growth of catalyst-free GaN nanowires on thin AlN buffer layer, *Appl. Phys. Lett.* **91**, 251 902 (2007).

[66] K. A. Bertness, A. Roshko, L. M. Mansfield, T. E. Harvey, and N. A. Sanford, Mechanism for spontaneous growth of GaN nanowires with molecular beam epitaxy, *J. Cryst. Growth* **310**, 3154 (2008).

[67] D. Cherns, L. Meshi, I. Griffiths, S. Khongphetsak, S. V. Novikov, N. Farley, R. P. Campion, and C. T. Foxon, Defect reduction in GaN/(0001)sapphire films grown by molecular beam epitaxy using nanocolumn intermediate layers, *Appl. Phys. Lett.* **92**, 121 902 (2008).

[68] L. Largeau, D. L. Dheeraj, M. Tchernycheva, G. E. Cirlin, and J. C. Harmand, Facet and in-plane crystallographic orientations of GaN nanowires grown on Si(111), *Nanotechnology* **19**, 155 704 (2008).

[69] M. Tchernycheva, C. Sartel, G. Cirlin, L. Travers, G. Patriarche, L. Largeau, O. Mauguin, J.-C. Harmand, L. S. Dang, J. Renard, B. Gayral, L. Nevou, and F. Julien, GaN/AlN free-standing nanowires grown by molecular beam epitaxy, *phys. stat. sol. (c)* **5**, 1556 (2008).

[70] T. Stoica, E. Sutter, R. J. Meijers, R. K. Debnath, R. Calarco, H. Lüth, and D. Grützmacher, Interface and wetting layer effect on the catalyst-free nucleation and growth of GaN nanowires, *Small* **4**, 751 (2008).

[71] A. P. Vajpeyi, G. Tsiakatouras, K. Tsagaraki, M. Androulidaki, and A. Georgakilas, High optical quality GaN nanopillars grown on (111) Si using molecular beam epitaxy, *Mater. Res. Soc. Symp. Proc.* **1068**, C06–08 (2008).

[72] O. Landré, R. Songmuang, J. Renard, E. Bellet-Amalric, H. Renevier, and B. Daudin, Plasma-assisted molecular beam epitaxy growth of GaN nanowires using indium-enhanced diffusion, *Appl. Phys. Lett.* **93**, 183 109 (2008).

[73] O. Landré, C. Bougerol, H. Renevier, and B. Daudin, Nucleation mechanism of GaN nanowires grown on (111) Si by molecular beam epitaxy, *Nanotechnology* **20**, 415 602 (2009).

[74] T. Aschenbrenner, C. Kruse, G. Kunert, S. Figge, K. Sebald, J. Kalden, T. Voss, J. Gutowski, and D. Hommel, Highly ordered catalyst-free and mask-free GaN nanorods on *r*-plane sapphire, *Nanotechnology* **20**, 075 604 (2009).

[75] A. P. Vajpeyi, A. O. Ajagunna, G. Tsiakatouras, A. Adikimenakis, E. Iliopoulos, K. Tsagaraki, M. Androulidaki, and A. Georgakilas, Spontaneous growth of III-nitride nanowires on Si by molecular beam epitaxy, *Microelectron. Eng.* **86**, 812 (2009).

[76] V. Consonni, M. Knelangen, L. Geelhaar, A. Trampert, and H. Riechert, Nucleation mechnisms of epitaxial GaN nanowires: Origin of their self-induced formation and initial radius, *Phys. Rev. B* **81**, 085 310 (2010).

[77] M. Knelangen, V. Consonni, A. Trampert, and H. Riechert, In situ analysis of strain relaxation during catalyst-free nucleation and growth of GaN nanowires., *Nanotechnology* **21**, 245 705 (2010).

[78] R. Songmuang, T. Ben, B. Daudin, D. González, and E. Monroy, Identification of III-N nanowire growth kinetics via a marker technique, *Nanotechnology* **21**, 295 605 (2010).

[79] C. Chèze, L. Geelhaar, A. Trampert, and H. Riechert, In situ investigation of self-induced GaN nanowire nucleation on Si, *Appl. Phys. Lett.* **97**, 043 101 (2010).

[80] O. Landré, Etude de la nucleation et de la croissance de structures filaires GaN et AlN, Ph.D. thesis, Université de Grenoble (2010).

[81] W. P. Mccray, MBE deserves a place in the history books, *Nature Nanotech.* **2**, 259 (2007).

[82] B. A. Joyce and R. R. Bradley, A study of nucleation in chemically grown epitaxial silicon films using molecular beam techniqiques I.-experimental methods, *Philos. Mag.* **14**, 289 (1966).

[83] A. Y. Cho, Film desposition by molecular-beam techniques, *J. Vac. Sci. Technol.* **8**, 531 (1971).

[84] J. R. Arthur, Surface stoichiometry and structure of GaAs, *Surf. Sci.* **43**, 449 (1974).

[85] M. A. Herman and H. Sitter, Molecular beam epitaxy, (Springer-Verlag 1989).

[86] X. Wang and A. Yoshikawa, Molecular beam epitaxy growth of GaN, AlN and InN, *Prog. Cryst. Growth Charact. Mater.* **48/49**, 42 (2004).

[87] B. A. Joyce and T. B. Joyce, Basic studies of molecular beam epitaxy - past, present and some future directions, *J. Cryst. Growth* **264**, 605 (2004).

[88] A. Madhukar, Far from equilibrium vapour phase growth of lattice matched III-V compound semiconductor interfaces: some basic concepts and monte-carlo computer simulations., *Surf. Sci.* **132**, 344 (1983).

[89] B. Heying, A. Averbeck, L. F. Chen, E. Haus, H. Riechert, and J. S. Speck, Control of GaN surface morphology using plasma-assisted molecular beam epitaxy, *J. Appl. Phys.* **88**, 1855 (2000).

[90] M. A. Sanchez-Garcia, F. B. Naranjo, J. L. Pau, A. Jimenez, E. Calleja, E. Munoz, S. I. Molina, A. M. Sanchez, F. J. Pacheco, and R. Garcia, Properties of homoepitaxial and heteroepitaxial GaN layers grown by plasma assisted MBE, *phys. stat. sol. (a)* **176**, 447 (1999).

[91] K. A. Bertness, N. A. Sanford, and A. V. Davydov, GaN nanowires grown by molecular beam epitaxy, *IEEE J. Sel. Topics in Quantum Electron.* **17**, 847 (2011).

[92] H. Morkoc, Handbook of nitride semiconductors and devices. Vol.1, (Wiley 2008).

[93] S. Strite and H. Morkoc, GaN, AlN and InN: a review, *J. Vac. Sci. Technol. B* **10**, 1237 (1992).

[94] C. Y. Yeh, Z. W. Lu, S. Froyen, and A. Zunger, Zinc-blende-wurtzite polytypism in semiconductors, *Phys. Rev. B* **46**, 10 086 (1992).

[95] B. Daudin, G. Feuillet, J. Hübner, Y. Samson, F. Widmann, A. Philippe, C. Bru-Chevallier, G. Guillot, E. Bustarret, G. Bentoumi, and A. Deneuville, How to grow cubic GaN with low hexagonal phase content on (001) SiC by molecular beam epitaxy., *J. Appl. Phys.* **84**, 2295 (1998).

[96] X. L. Sun, Y. T. Wang, H. Yang, L. X. Zheng, D. P. Xu, J. B. Li, and Z. G. Wang, Strain and photoluminescence characterization of cubic (In,Ga)N films grown on GaAs(001) substrates., *J. Appl. Phys.* **87**, 3711 (2000).

[97] A. F. Wright, Basal-plane stacking faults and polymorphism in AlN, GaN, and InN., *J. Appl. Phys.* **82**, 5259 (1997).

[98] J. F. Nye, Physical properties of crystals - their representation by tensors and matrices, (Oxford Science Publications 1985).

[99] A. F. Wright, Elastic properties of zinc-blende and wurtzite AlN, GaN and InN, *J. Appl. Phys.* **82**, 2833 (1997).

[100] K. Kim, W. R. L. Lambrecht, and B. Segall, Elastic constants and related properties of tetrahedrally bonded BN, AlN, GaN, and InN, *Phys. Rev. B* **53**, 16 310 (1996).

[101] A. Polian, M. Grimsditch, and I. Grzegory, Elastic constants of gallium nitride, *J. Appl. Phys.* **79**, 3343 (1996).

[102] M. Yamaguchi, T. Yagi, T. Azuhata, T. Sota, K. Suzuki, S. Chichibu, and S. Nakamura, Brillouin scattering study of gallium nitride: elastic stiffness constants, *J. Phys.:Condens. Matter* **9**, 241 (1997).

[103] R. B. Schwarz, K. Khachaturyan, and E. R. Weber, Elastic moduli of gallium nitride, *Appl. Phys. Lett.* **70**, 1122 (1997).

[104] T. Sugahara, H. Sato, M. Hao, Y. Naoi, S. Kurai, S. Tottori, K. Ymashita, K. Nishimo, L. T. Romano, and S. Sakai, Direct evidence that dislocations are non-radiative recombination centers in GaN, *Jpn. J. Appl. Phys.* **37**, L398 (1998).

[105] J. Wu, When group-III nitrides go infrared: New properties and perspectives, *J. Appl. Phys.* **106**, 011 101 (2009).

[106] G. Steude, D. M. Hofmann, B. K. Meyer, H. Amano, and I. Akasaki, The dependence of the band gap on alloy composition in strained AlGaN on GaN, *phys. stat. sol. (c)* **205**, R7 (1998).

[107] S. R. Lee, A. F. Wright, M. H. Crawford, G. Petersen, J. Han, and R. M. Biefeld, The band-gap bowing of $Al_xGa_{1-x}N$ alloys, *Appl. Phys. Lett.* **74**, 3344 (1999).

[108] J. Wu, W. Walukiewicz, K. M. Yu, J. W. A. III, E. E. Haller, H. Lu, and W. J. Schaff, Small band gap bowing in $In_xGa_{1-x}N$ alloys, *Appl. Phys. Lett.* **80**, 4741 (2002).

[109] V. Y. Davydov, A. A. Klochikin, V. V. Emtsev, S. A. Kurdyukov, S. V. Ivanov, V. A. Vekshin, F. Bechstedt, J. Furthmüller, J. Aderhold, J. Graul, A. V. Mudryi, H. Harima, A. Hashimoto, A. Yamamoto, and E. E. Haller, Band gap of hexagonal InN and InGaN alloys, *phys. stat. sol. (b)* **234**, 787 (2002).

[110] S. T. Liu, X. Q. Wang, G. Chen, Y. W. Zhang, L. Feng, C. C. Huang, F. J. Xu, N. Tang, L. W. Sang, M. Sumiya, and B. Shen, Temperature-controlled epitaxy of $In_xGa_{1-x}N$ alloys and their band gap bowing, *J. Appl. Phys.* **110**, 113 514 (2011).

[111] F. Bernardini, V. Fiorentini, and D. Vanderbilt, Spontaneous polarization and piezoelectric constants of III-V nitrides, *Phys. Rev. B* **56**, R10 024 (1997).

[112] O. Ambacher, B. Foutz, J. SMart, J. R. Shealy, N. G. Weimann, K. Chu, M. Murphy, W. J. S. A. J. Sierakowski, L. F. Eastman, R. Dimitrov, A. Mitchell, and M. Stutzmann, Two dimensionel electron gases induced by spontaneous and piezoelectric polarization in undoped and doped AlGaN/GaN heterostructures, *J. Appl. Phys.* **87**, 334 (2000).

[113] K. Shimada, First-principles determination of piezoelectric stress and strain constants of wurtzite III-V nitrides, *Jpn. J. Appl. Phys.* **45**, L358 (2006).

[114] A. Hangleiter, F. Hitzel, S. Lahmann, and U. Rossow, Composition dependence of polarization fields in GaInN/GaN quantum wells, *Appl. Phys. Lett.* **83**, 1169 (2003).

[115] O. Ambacher, J. Smart, J. R. Shealy, N. G. Weimann, K. Chu, M. Murphy, W. J. Schaff, L. F. Eastman, R. Dimitrov, L. Wittmer, M. Stutzmann, W. Rieger, and J. Hilsenbeck, Two-dimensional electron gases induced by spontaneous and piezoelectric polarization charges in N- and Ga-face AlGaN/GaN heterostructures, *J. Appl. Phys.* **85**, 3222 (1999).

[116] J. Simon, N. T. Pelekanos, C. Adelmann, E. Martinez-Guerrero, R. André, B. Daudin, L. S. Dang, and H. Mariette, Direct comparison of recombination dynamics in cubic and hexagonal GaN/AlN quantum dots, *Phys. Rev. B* **68**, 035 312 (2003).

[117] T. Bretagnon, P. Lefebvre, P. Valvin, R. Bardoux, T. Guillet, T. Taliercio, B. Gil, N. Grandjean, F. Semond, B. Damilano, A. Dussaigne, and J. Massies, Radiative lifetime of a single electron-hole pair in GaN/AlN quantum dots, *Phys. Rev. B* **73**, 113 304 (2006).

[118] J. Renard, R. Songmuang, G. Tourbot, C. Bougerol, B. Daudin, and B. Gayral, Evidence for quantum-confined Stark effect in GaN/AlN quantum dots in nanowires, *Phys. Rev. B* **80**, 121 305 (2009).

[119] C. Adelmann, E. Sarigiannidou, D. Jalabert, Y. Hori, J.-L. Rouvière, B. Daudin, S. Fanget, C. Bru-Chevallier, T. Shibata, and M. Tanaka, Growth and optical properties of GaN/AlN quantum wells, *Appl. Phys. Lett.* **82**, 4154 (2003).

[120] L. Lahourcade, Plasma-assisted molecular beam epitaxy of (11$\bar{2}$2)-oriented III-nitrides, Ph.D. thesis, Institut national polytechnique de Grenoble (2009).

[121] J. M. Cowley, Electron Diffraction Techniques - Volume 1. Chapter 1 - Electron diffraction: an introduction, (Oxford Science Publications 1992).

[122] J. E. Mahan, K. M. Geib, G. Y. Robinson, and R. G. Long, A review of the geometrical fundamentals of reflection high-energy electron diffraction with application to silicon surfaces, *J. Vac. Sci. Technol. A* **8**, 3692 (1990).

[123] L. Daweritz and K. Ploog, Contribution of reflection high-energy electron diffraction to nanometre tailoring of surfaces and interfaces by molecular beam epitaxy, *Semicond. Sci. Technol.* **9**, 123 (1994).

[124] R. Nötzel, L. Däweritz, and K. Ploog, Topography of high- and low-k index GaAs surfaces, *Phys. Rev. B* **46**, 4736 (1992).

[125] P. J. Dobson, B. A. Joyce, and J. H. Neave, Current understanding and applications of the RHEED intensity oscillation technique, *J. Cryst. Growth* **81**, 1 (1987).

[126] B. A. Joyce, P. J. Dobson, J. H. Neave, K. Woodbridge, J. Zhang, P. K. Larsen, and B. Bolger, RHEED studies of heterojunctions and quantum well formation during MBE growth - from multiple scattering to band offsets, *Surf. Sci.* **168**, 423 (1986).

[127] J. Als-Nielsen and D. MacMorrow, Elements of modern X-ray physics, (Wiley 2001).

[128] J.-L. Hodeau, V. Favre-Nicolin, S. Bos, H. Renevier, E. Lorenzo, and J.-F. Bérar, Resonant diffraction, *Chem. Rev.* **101**, 1843 (2001).

[129] H. Renevier, S. Grenier, S. Arnaud, J. F. Bérar, B. Caillot, J. L. Hodeau, A. Letoublon, M. G. proietti, and B. Ravel, Diffraction anomalouus fine-structure at beamline BM2 at the European Synchrotron Radiation Facility, *J. Synchrotron Rad.* **10**, 435 (2003).

[130] F. Boscherini, Characterization of semiconductor heterostructures and nanostructures - Chapter 9 - X-ray absorption fine structure in the study of semiconductor heterostructures and nanostructures, (Elsevier 2008).

[131] T. Metzger, V. favre Nicollin, G. renaud, H. Renevier, and T. Schülli, Characterization of semiconductor heterostructures and nanostructures - Chapter 10 - Nanostructures in the light of synchrotron radiation: surface-sensitive X-ray techniques and anomalous scattering, (Elsevier 2008).

[132] V. Favre-Nicolin, M. G. Proietti, C. Leclere, N. A. Katcho, M.-I. Richard, and H. Renevier, Multiwavelength anomalous diffraction and diffraction anomalous fine structure to study composition and strain of semiconductor nanostructures, *Eur. Phys. J. Special Topics* **208**, 189 (2012).

[133] J. Karle, Some developments in anomalous dispersion for the structural investigation of macromolecular systems in biology, *Internation Journal of Quantum Chemistry, Symposium 7* **18**, 357 (1980).

[134] T. Hahn, International Tables for Crystallography - Vol. A, (Wiley 2006).

[135] G. Salviati, F. Rossi, N. Armani, V. Grillo, and L. Lazzarini, Characterization of semiconductor heterostructures and nanostructures - Chapter 7 - Power-dependent cathodoluminescence in III-nitrides heterostructures: from internal field screening to controlled band-gap modulation, (Elsevier 2008).

[136] S. Sanguinetti, M. Guzzi, and M. Gurioli, Characterization of semiconductor heterostructures and nanostructures - Chapter 6 - Accessing structural and electronic properties of semiconductor nanostructures via photoluminescence, (Elsevier 2008).

[137] L. F. Zagonel, S. Mazzucco, M. Tencé, K. March, R. Bernard, B. Laslier, G. Jacopin, M. Tchernycheva, L. Rigutti, F. H. Julien, R. Songmuang, and M. Kociak, Nanometer scale spectral imaging of quantum emitters in nanowires and its correlation to their atomically resolved structure, *Nano Lett.* **11**, 568 (2011).

[138] L. H. G. Tizei and M. Kociak, Spectrally and spatially resolved cathodoluminescence of nanodiamonds local variations of the NV^0 emission properties, *Nanotechnology* **23**, 175 702 (2012).

[139] R. T. Bondokov, S. G. Mueller, K. E. Morgan, G. A. Slack, S. Schujman, M. C. Wood, J. A. Smart, and L. J. Schowalter, Large-area AlN substrates for electronic applications: an industrial perspective, *J. Cryst. Growth* **310**, 4020 (2008).

[140] R. Dwiliński, R. Doradziński, J. Garczyński, L. P. Sierzputowski, A. Puchalski, Y. Kanbara, K. Yagi, H. Minakuchi, and H. Hayashi, Excellent crystallinity of truly bulk ammonothermal GaN, *J. Cryst. Growth* **310**, 3911 (2008).

[141] R. Dwiliński, T. Doradziński, J. Garczyński, L. Sierzputowski, R. Kucharski, M. Zajac, M. Rudziński, R. Kudrawiec, W. Strupiński, and J. Misiewicz, Ammonothermal GaN substrates: growth accomplishments and applications, *phys. stat. sol. (a)* **208**, 1489 (2011).

[142] R. Kucharski, M. Zajac, R. Doradziński, R. Kudrawiec, and R. Dwiliński, Nonpolar and semi-polar ammonothermal GaN substrates, *Semicond. Sci. Technol.* **27**, 024 007 (2012).

[143] S. Ino, An investigation of the Si(111) 7×7 surface structure by RHEED, *Jpn. J. Appl. Phys.* **19**, 1277 (1980).

[144] P. A. Bennett and M. W. Webb, The Si(111) 7× 7 to "1×1" transition, *Surf. Sci.* **104**, 74 (1981).

[145] G. Binnig, H. Rohrer, C. Gerber, and E. Weibel, 7×7 reconstruction on Si(111) resolved in real space, *Phys. Rev. Lett.* **50**, 120 (1983).

[146] W. Telieps and E. Bauer, The (7×7) ↔ (1×1) phase transition on Si(111), *Surf. Sci.* **162**, 165 (1985).

[147] J. A. Golovchenko, The tunneling microscope: A new look at the atomic world, *Science* **232**, 48 (1986).

[148] C. W. Hu, H. Hibino, and T. O. I. S. T. Tsong, Hysteresis in the (1×1)-(7×7) first-order phase transition on the Si(111) surface, *Surf. Sci.* **487**, 191 (2001).

[149] G. Tourbot, Croissance et propriétés structurales et optiques d'hétérostructures de nanofils InGaN/GaN pour la réalisation de LEDs, Ph.D. thesis, Université de Grenoble (2012).

[150] L. Geelhaar, C. Chèze, B. Jenichen, O. Brandt, C. Pfueller, S. Muench, R. Rothemund, S. Reitzenstein, A. Forchel, T. Kehagias, P. Komninou, G. P. Dimitrakopulos, T. Karakostas, L. Lari, P. R. Chalker, M. H. Gass, and H. Riechert, Properties of GaN nanowires grown by molecular beam epitaxy, *IEEE J. Sel. Topics in Quantum Electron.* **17**, 878 (2011).

[151] F. Furtmayr, M. Vielemeyer, M. Stutzmann, J. Arbiol, S. Estradé, F. Peirò, J. R. Morante, and M. Eickhoff, Nucleation and growth of GaN nanorods on Si (111) surfaces by plasma-assisted molecular beam epitaxy - The influence of Si- and Mg-doping, *J. Appl. Phys.* **104**, 034 309 (2008).

[152] J. R. Heffelfinger, D. L. Medlin, and K. F. McCarty, On the initial stages of AlN thin-film growth onto (0001) oriented Al_2O_3 substrates by molecular beam epitaxy, *J. Appl. Phys.* **85**, 466 (1999).

[153] A. Bourret, A. Barski, J. L. Rouvière, G. Renaud, and A. Barbier, Growth of aluminum nitride on (111) silicon: microstructure and interface structure, *J. Appl. Phys.* **83**, 2003 (1998).

[154] F. Calle, F. J. Sanchez, J. M. G. Tijerot, M. A. Sanchez-Garcia, E. Calleja, and R. Beresford, Exciton and donor-acceptor recombination in undoped GaN on Si(111), *Semicond. Sci. Technol.* **12**, 1396 (1997).

[155] B. Monemar, P. P. Paskov, T. Paskova, J. P. Bergman, G. Pozina, W. M. Chen, P. N. Hai, I. A. B. ad H. Amano, and I. Akasaki, Optical characterization of III-nitrides, *Mat. Sci. Eng. B* **93**, 112 (2002).

[156] F. Furtmayr, M. Vielemeyer, M. Stutzmann, A. Laufer, B. K. Meyer, and M. Eickhoff, Optical properties of Si- and Mg-doped gallium nitride nanowires grown by plasma-assisted molecular beam epitaxy, *J. Appl. Phys.* **104**, 074 309 (2008).

[157] N. Grandjean, J. Massies, M. Leroux, and P. Lorenzini, Ultraviolet GaN light-emitting diodes grown by molecular beam epitaxy using NH_3, *Appl. Phys. Lett.* **72**, 82 (1998).

[158] K. Kornitzer, T. Ebner, K. Thinke, R. Sauer, C. Kirchner, V. Schwegler, M. Kamp, M. Leszczynski, I. Grzegory, and S. Porowski, Photoluminescene and reflectance spectroscopy of excitonic transitions in high-quality homoepitaxial GaN films, *Phys. Rev. B* **60**, 1471 (1999).

[159] J. A. Freitas, Jr., Optical studies of bulk and homoepitaxial films of III-V nitride semiconductors, *J. Cryst. Growth* **281**, 168 (2005).

[160] A. Wysmolek, M. Potemski, R. Stepniewski, J. M. Baranowski, D. C. Look, S. K. Lee, and J. Y. Hu, Resonnant interaction of LO phonons with excited donor states in GaN, *phys. stat. sol. (b)* **235**, 36 (2003).

[161] P. Corfdir, P. Lefebvre, J. Ristic, P. Valvin, E. Calleja, A. Trampert, J. D. Ganière, and B. Deveaud-Plédran, Time-resolved spectroscopy on GaN nanocolumns grown by plasma assisted molecular beam epitaxy on Si substrates, *J. Appl. Phys.* **105**, 013 113 (2009).

[162] M. A. Reshchikov and H. Morkoc, Luminescence properties of defects in GaN, *J. Appl. Phys.* **97**, 061 301 (2005).

[163] V. Consonni, M. Knelangen, A. Trampert, L. Geelhaar, and H. Riechert, Nucleation and coalescence effects on the density of self-induced GaN nanowires grown by molecular beam epitaxy, *Appl. Phys. Lett.* **98**, 071 913 (2011).

[164] E. Galopin, L. Largeau, G. Patriarche, L. Travers, F. Glas, and J. C. Harmand, Morphology of self-catalyzed GaN nanowires and chronology of their formation by molecular beam epitaxy, *Nanotechnology* **22**, 245 606 (2011).

[165] N. Grandjean, J. Massies, F. Semond, S. Y. Karpov, and R. A. Talalaev, GaN evaporation in molecular-beam epitaxy environment, *Appl. Phys. Lett.* **74**, 1854 (1999).

[166] V. Consonni, M. Hanke, M. Knelangen, L. Geelhaar, A. Trampert, and H. Riechert, Nucleation mechanisms of self-induced GaN nanowires grown on an amorphous interlayer, *Phys. Rev. B* **83**, 035 310 (2011).

[167] R. Mata, K. Hestroffer, J. Budagosky, A. Cros, C. Bougerol, H. Renevier, and B. Daudin, Nucleation of GaN nanowires grown by plasma-assisted molecular beam epitaxy: The effect of temperature, *J. Cryst. Growth* **333**, 177 (2011).

[168] V. Consonni, A. Trampert, L. Geelhaar, and H. Riechert, Physical origin of the incubation time of self-induced GaN nanowires, *Appl. Phys. Lett.* **99**, 033 102 (2011).

[169] G. Renaud, M. Ducruet, O. Ulrich, and R. Lazzari., Apparatus for real time in-situ quantitative studies of growing nanoparticles by grazing incidence small angle x-ray scattering and surface differential reflectance spectroscopy, *Nucl. Instr. and Meth. in Phys. Res. B* **222**, 667 (2004).

[170] R. Daudin, Formation and supercooling of AuSi eutectic droplets on Si substrates: an in-situ study using synchrotron radiation, Ph.D. thesis, Université de Grenoble (2012).

[171] V. Cantelli, O. Geaymond, O. Ulrich, T. Zhou, N. Blanc, and G. Renaud, The In situ growth of Nanostructures on Surfaces (INS) end station of the ESRF IF-BM32 beamline: a combined UHV-CVD and MBE reactor for in situ x-ray scattering investigations of growing nanoparticles; especially semiconductor nanowires, *To be submitted to* (2012).

[172] A. G. Schrott and S. C. Fain, Nitridation of Si(111) by nitrogen atoms, *Surf. Sci.* **111**, 39 (1981).

[173] K. Edamoto, S. Tanaka, M. Onchi, and M. NIshijima, Electron Energy-Loss Spectra of Si(111) reacted with nitrogen atoms, *Surf. Sci.* **167**, 285 (1986).

[174] M. Tabe and T. Yamamoto, Initial stages of nitridations of Si(111) surfaces: X-ray photoelectron spectroscopy and scanning tunneling microscopy studies, *Surf. Sci.* **376**, 99 (1997).

[175] C. Maillot, H. Roulet, and G. Dufour, Thermal nitridation of silicon: an XPS and LEED investigation, *J. Vac. Sci. Technol. B* **2**, 316 (1984).

[176] E. Bauer, Y. Wei, T. Müller, A. Pavlovska, and I. S. T. Tsong, Reactive crystal growth in two dimensions: silicon nitride on Si(111), *Phys. Rev. B* **51**, 17 891 (1995).

[177] X.-S. Wang, G. Zhai, J. Yang, L. Wang, Y. Hu, Z. Li, J. C. Tang, X. Wang, K. K. Fung, and N. Cue, Nitridation of Si(111), *Surf. Sci.* **494**, 83 (2001).

[178] C.-L. Wu, J.-L. Hsieh, H.-D. Hsueh, and S. Gwo, Thermal nitridation of the Si(111)-(7×7) surface studied by scanning tunneling micorscopy and spectroscopy, *Phys. Rev. B* **65**, 045 309 (2002).

[179] B. Röttger, R. Kliese, and H. Neddermeyer, Adsorption and reaction of NO on Si(111) studied by scanning tunneling microscopy, *J. Vac. Sci. Technol. B* **14**, 1051 (1996).

[180] Y. Morita and H. Tokumoto, Origin of the $8/3 \times 8/3$ superstructure in STM images of the Si(111)-8×8:N surface, *Surf. Sci.* **443**, L1037 (1999).

[181] J. Falta, T. Schmidt, S. Gangopadhyay, T. Claussen, O. Brunke, J. I. Flege, S. Heun, S. Bernstroff, L. Gregoratti, and M. Kiskinova, Ultra-thin high-quality silicon nitride films on Si(111), *EPL* **94**, 16 003 (2011).

[182] R. Grün, The crystal structure off $\beta - Si_3N_4$; structural and stability considerations between α- and $\beta - Si_3N_4$, *Acta Cryst.* **B35**, 800 (1979).

[183] A. Y. Liu and M. L. Cohen, Structural properties and electronic structure of low-compressibility materials: $\beta - Si_3N_4$ and hypothetical $\beta - C_3N_4$, *Phys. Rev. B* **41**, 10 727 (1990).

[184] O. N. Carlson, The N-Si (Nitrogen-Silicon) system, *Bulletin of Alloy Phase Diagrams* **11**, 569 (1990).

[185] C.-M. Wang, X. Pan, M. Rohle, F. L. Riley, and M. Mitomo, Silicon nitride crystal structure and observations of lattice defects, *J. Mater. Sci.* **30**, 5281 (1996).

[186] H. Ahn, C.-L. Wu, S. Gwo, C. M. Wei, and Y. C. Chou, Structure determination of the $Si_3N_4/Si(111) - (8 \times 8)$ surface: a combined study of Kikuchi electron holography, scanning tunneling micorscopy, and ab inito calculations, *Phys. Rev. Lett.* **86**, 2818 (2001).

[187] C.-L. Wu, J.-C. Wang, M.-H. Chan, T. T. Chen, and S. Gwo, Heteroepitaxy of GaN on Si(111) realized with a coincident-interface AlN/$\beta - Si_3N_4$(0001) double-buffer structure, *Appl. Phys. Lett.* **83**, 4530 (2003).

[188] W. A. Harrison, Electronic structure and the properties of solids - The physics of chemical bond, pp 174-179, (Dover Publications Inc. 1990).

[189] S. A. Nikishin, V. G. Antipov, S. Francoeur, N. N. Faleev, G. A. Seryogin, V. A. Elyukhin, H. Temkin, T. I. Prokofyeva, M. Holtz, A. Konkar, and S. Zollner, High-quality AlN grown on Si(111) by gas-source molecular-beam epitaxy with ammonia, *Appl. Phys. Lett.* **75**, 484 (1999).

[190] S. Vézian, A. Le Louarn, and M. J., Selective epitaxial growth of AlN and GaN nanostructures on Si(111) by using NH_3 as nitrogen source, *J. Cryst. Growth* **303**, 419 (2007).

[191] R. Brener, F. Edelman, and E. Y. Gutmanas, Formation of an interfacial AlN layer in an Al/Si_3N_4 thin-film system, *Appl. Phys. Lett.* **54**, 901 (1989).

[192] D. J. Eaglesham, H.-J. Gossman, and M. Cerullo, Limiting thickness h_{epi} for epitaxial growth and room-temperature Si growth on Si(100), *Phys. Rev. Lett.* **65**, 1227 (1990).

[193] P. J. Desré and A. R. Yavari, Suppression of crystal nucleation in amorphous layers with sharp concentration gradients, *Phys. Rev. Lett.* **64**, 1533 (1990).

[194] W. Bolse, Amorphization and recrystallization of covalent tetrahedral networks, *Nucl. Instr. and Meth. in Phys. Res. B* **148**, 83 (1999).

[195] S. H. Mohamed, M. Raaif, A. M. A. El-Rahman, and E. Shaaban, Properties of RF plasma nitrided silicon thin films at different RF plasma processing powers, *Acta Phys. Pol. A* **120**, 552 (2011).

[196] V. Consonni, V. G. Dubrovskii, A. Trampert, L. Geelhaar, and H. Riechert, Quantitative description for the growth rate of self-induced GaN nanowires, *Phys. Rev. B* **85**, 155 313 (2012).

[197] X. J. Chen, G. Perillat-Merceroz, D. Sam-Giao, C. Durand, and J. Eymery, Homoepitaxial growth of catalyst-free GaN wires on N-polar substrates, *Appl. Phys. Lett.* **97**, 151 909 (2010).

[198] K. A. Bertness, A. W. Sanders, D. M. Rourke, T. E. Harvey, A. Roshko, J. B. Schlager, and N. A. Sanford, Controlled nucleation of GaN nanowires grown with molecular beam epitaxy, *Adv. Funct. Mater.* **20**, 2911 (2010).

[199] L. Largeau, E. Galopin, N. Gogneau, L. Travers, F. Glas, and J.-C. Harmand, N-polar GaN nanowires seeded by Al droplets on Si(111), *Cryst. Growth Des.* **12**, 2724 (2012).

[200] B. Daudin, J. L. Rouvière, and M. Arlery, Polarity determination of GaN films by ion channeling and convergent beam electron diffraction, *Appl. Phys. Lett.* **69**, 2480 (1996).

[201] F. A. Ponce, D. P. Bour, W. T. Young, M. Saunders, and J. W. Steeds, Determination of lattice polarity for growth of GaN bulk single crystals and epitaxial layers, *Appl. Phys. Lett.* **69**, 337 (1996).

[202] B. Daudin, J. L. Rouvière, and M. Arlery, The key role of polarity in the growth process of (0001) nitrides, *Mat. Sci. Eng. B* **43**, 157 (1997).

[203] J. E. Northrup, J. Neugebauer, R. M. Feenstra, and A. R. Smith, Structure of GaN(0001): The latterally contracted Ga bilateral model, *Phys. Rev. B* **61**, 9932 (2000).

[204] Q. Hu, T. Wei, R. Duan, J. Yang, Z. Huo, Y. Zeng, and S. Xu, Polarity dependent structure and optical properties of freestanding GaN layers grown by hydride vapor phase epitaxy, *Materials Science in Semiconductor Processing* **In press**, – (2011).

[205] M. Sumiya, K. Yoshimura, K. Ohtsuka, and S. Fuke, Dependence of impurity incorporation on the polar direction of GaN film growth, *Appl. Phys. Lett.* **76**, 2098 (2000).

[206] N. A. Fichtenbaum, T. E. Mates, S. Keller, S. P. DenBaars, and U. K. Mishra, Impurity incorporation in heteroepitaxial N-face and Ga-face GaN films grown by metalorganic chemical vapor deposition, *J. Cryst. Growth* **310**, 1124 (2008).

[207] A. R. Arehart, T. Homan, M. H. Wong, C. Poblenz, J. S. Speck, and S. A. Ringel, Impact of N- and Ga-face polarity on the incorporation of deep levels in n-type GaN grown by molecular beam epitaxy, *Appl. Phys. Lett.* **96**, 242 112 (2010).

[208] S. F. Chichibu, A. Setoguchi, A. Uedono, K. Yoshimura, and M. Sumiya, Impact of growth polar direction on the optical properties of GaN grown by metalorganic vapor phase epitaxy, *Appl. Phys. Lett.* **78**, 28 (2001).

[209] L. K. Li, M. J. Jurkovic, W. I. Wang, J. M. V. Hove, and P. P. Chow, Surface polarity dependence of Mg doping in GaN grown by molecular-beam epitaxy, *Appl. Phys. Lett.* **76**, 1740 (2000).

[210] H. M. Ng and A. Y. Cho, Investigation of Si doping and impurity incorporation dependence on the polarity of GaN by molecular beam epitaxy, *J. Vac. Sci. Technol. B* **20**, 1217 (2002).

[211] R. Dimitrov, A. Mitchell, L. Wittmer, O. Ambacher, M. Stutzmann, J. Hilsenbeck, and W. Rieger, Comparison of N-face and Ga-face AlGaN/GaN-based high electron mobility transistors grown by plasma-induced molecular beam epitaxy, *Jpn. J. Appl. Phys.* **38**, 4962 (1999).

[212] J. L. Rouviere, J. L. Weyher, M. Seelmann-Eggebert, and S. Porowski, Polarity determination for GaN films grown on (0001) sapphire and high-pressure-grown GaN single crystals, *Appl. Phys. Lett.* **73**, 668 (1998).

[213] M. Seelmann-Eggebert, J. L. Weyher, H. Obloh, H. Zimmermann, A. Rar, and S. Porowski, Polarity of (00.1) GaN epilayers grown on a (00.1) sapphire, *Appl. Phys. Lett.* **71**, 2635 (1997).

[214] A. Kazimirov, G. Scherb, J. Zegenhagen, T. . Lee, M. J. Bedzyk, M. K. Kelly, H. Angerer, and O. Ambacher, Polarity determination of a GaN thin film on sapphire (0001) with x-ray standing waves, *J. Appl. Phys.* **84**, 1703 (1998).

[215] A. R. Smith, R. M. Feenstra, D. W. Greve, J. Neugebauer, and J. E. Northrup, Reconstructions of the GaN(000$\bar{1}$) surface, *Phys. Rev. Lett.* **79**, 3934 (1997).

[216] A. R. Smith, R. M. Feenstra, D. W. Greve, M. . Shin, M. Skowronski, J. Neugebauer, and J. E. Northrup, Determination of wurtzite GaN lattice polarity based on surface reconstruction, *Appl. Phys. Lett.* **72**, 2114 (1998).

[217] J. Wei, R. Neumann, X. Wang, S. Li, S. Fündling, S. Merzsch, M. A. M. Al-Suleiman, U. Sökmen, H.-H. Wehmann, and A. Waag, Polarity analysis of GaN nanorods by photo-assisted Kelvin probe force microscopy, *phys. stat. sol. (c)* **8**, 2157 (2011).

[218] A. Yoshikawa and K. Xu, Polarity selection process and polarity manipulation of GaN in MOVPE and RF-MBE growth, *Thin Solid Films* **412**, 38 (2002).

[219] D. Li, M. Sumiya, K. Yoshimura, Y. Suzuki, Y. Fukuda, and S. Fuke, Characteristics of the GaN polar surface during an etching process in KOH solution, *Physica Status Solidi A* **180**, 357–362 (2000), cited By (since 1996): 13.

[220] D. Li, M. Sumiya, S. Fuke, D. Yang, D. Que, Y. Suzuki, and Y. Fukuda, Selective etching of GaN polar surface in potassium hydroxide solution studied by x-ray photoelectron spectroscopy, *J. Appl. Phys.* **90**, 4219 (2001).

[221] T. Palacios, F. Calle, M. Varela, C. Ballesteros, E. Monroy, F. B. Naranjo, M. A. Sánchez-García, E. Calleja, and E. Muñoz, Wet etching of GaN grown by molecular beam epitaxy on Si(111), *Semicond. Sci. Technol.* **15**, 996 (2000).

[222] M. Sumiya and S. Fuke, Review of polarity determination and control in GaN, *MRS Internet J. Nitride Semicond. Res.* **9**, 1 (2004).

[223] A. Georgakilas, S. Mikroulis, V. Cimalla, M. Zervos, A. Kostopoulos, P. Komninou, T. Kehagias, and T. Karakostas, Effects of the sapphire nitridation on the polarity and structural properties of GaN layers grown by plasma-assisted MBE, *phys. stat. sol. (a)* **188**, 567 (2001).

[224] S. Gangopadhyay, T. Schmidt, and J. Falta, N-plasma assisted MBE grown GaN films on Si(111), *phys. stat. sol. (b)* **243**, 1416 (2006).

[225] Z. T. Wang, Y. Yamada-Takamura, Y. Fujikawa, T. Sakurai, and Q. K. Xue, Atomistic study of GaN surface grown on Si(111), *Appl. Phys. Lett.* **87**, 1 (2005).

[226] B. Alloing, S. Vézian, O. Tottereau, P. Vennéguès, E. Beraudo, and J. Zuniga-Pérez, On the polarity of GaN micro- and nanowires epitaxially grown on sapphire (0001) and Si(111) substrates by metal organic vapor phase epitaxy and ammonia-molecular beam epitaxy, *Appl. Phys. Lett.* **98**, 011 914 (2011).

[227] R. A. Armitage and K. Tsubaki, Multicolour luminescence from InGaN quantum wells grown over GaN nanowire arrays by molecular-beam epitaxy, *Nanotechnology* **21**, 195 202 (2010).

[228] S. Nishikawa and K. Matsukawa, Titre, *Proc. Imp. Acad. Jpn.* **4**, 96 (1928).

[229] D. Coster, K. S. Knol, and J. A. Prins, Unterschiede in der Intensität der Röntgenstrahlen-reflexion an den beiden 111-Flächen der Zinkblende, *Z. Phys.* **63**, 345 (1930).

[230] A. W. Stevenson, S. W. Wilkins, M. S. Kwietniak, and G. N. Pain, Polarity determination of single-crystal epitaxial layers by X-ray diffraction, *J. Appl. Phys.* **66**, 4198 (1989).

[231] R. D. Horning and B. L. Goldenberg, $Al_xGa_{1-x}N$ polarity determination by x-ray diffraction, *Appl. Phys. Lett.* **55**, 1721 (1989).

[232] D. C. Meyer, K. Richter, H.-G. Krane, W. Morgenroth, and P. Paufler, Determination of polarity in noncentrosymmetric layer/substrate systems, *J. Appl. Cryst.* **32**, 854 (1999).

[233] D. Waasmaier and A. Kirfel, New analytical scattering-factor functions for free atoms and ions, *Acta Cryst. A* **51**, 416 (1995).

[234] S. Sasaki, Numerical tables of anomalous scattering factors calculated by the Cromer and Liberman's method, *KEK report* **88-14**, 1–136 (1989).

[235] J. O. Cross, M. Newville, J. J. Rehr, L. B. Sorensen, C. E. Bouldin, G. Watson, T. Gouder, G. H. Lander, and M. I. Bell, Inclusion of local structure effects in theoretical x-ray resonant scattering amplitudes using ab initio x-ray-absorption spectra calculations, *Phys. Rev. B* **58**, 11 215 (1998).

[236] L. Dongsheng, M. Sumiya, K. Yoshimura, Y. Suzuki, Y. Fukuda, and S. Fuke, Characteristics of the GaN polar surface during an etching process in KOH solution, *phys. stat. sol. (a)* **180**, 357 (2000).

[237] L. Dongsheng, M. Sumiya, S. Fuke, D. Yang, D. Que, Y. Suzuki, and Y. Fukuda, Selective etching of GaN polar surface in potassium hydroxide solution studied by x-ray photoelectron spectroscopy, *J. Appl. Phys.* **90**, 4219 (2001).

[238] D. Zhuang and J. H. Edgar, Wet etching of GaN, AlN, and SiC: A review, *Mat. Sci. Eng. R* **48**, 1–46 (2005).

[239] S. C. Han, J. K. Kim, J. Y. Kim, K. K. Kim, H. Tampo, S. Niki, and J. M. Lee, Formation of hexagonal pyramids and pits on V-/VI-polar and III-/II-polar GaN/ZnO surfaces by wet etching, *Journal of the Electrochemical Society* **157**, D60 (2010).

[240] H. M. Ng, N. G. Weimann, and A. Chowdhury, GaN nanotip pyramids formed by anisotropic etching, *J. Appl. Phys.* **94**, 650 (2003).

[241] X. Kong, J. Ristić, M. A. Sanchez-Garcia, E. Calleja, and A. Trampert, Polarity determination by electron energy-loss spectroscopy: application to ultra-small III-nitride semiconductor nanocolumns, *Nanotechnology* **22**, 415 701 (2011).

[242] G. Radtke, M. Couillard, G. A. Botton, D. Zhu, and C. J. Humphreys, Scanning transmission electron microscopy investigation of the Si(111)/AlN interface grown by metalorganic vapor phase epitaxy, *Appl. Phys. Lett.* **97**, 251 901 (2010).

[243] C. T. Foxon, S. V. Novikov, J. L. Hall, R. P. Campion, D. Cherns, I. Griffiths, and S. Khongphetsak, A complementary geometric model for the growth of GaN nanocolumns prepared by plasma-assisted molecular beam epitaxy, *J. Cryst. Growth* **311**, 3423 (2009).

[244] L. Lymperakis and J. Neugebauer, Large anisotropic adatom kinetics on nonpolar GaN surfaces: Consequences for surface morphologies and nanowire growth, *Phys. Rev. B* **79**, 241 308 (2009).

[245] V. Jindal and F. Shahedipour-Sandvik, Density functional theoretical study of surface structure and adatom kinetics for wurtzite AlN, *J. Appl. Phys.* **105**, 084 902 (2009).

[246] N. V. Sibirev, M. Tchernycheva, G. E. Cirlin, G. Patriarche, J. C. Harmand, and V. G. Dubrovskii, Effect of diffusion from a lateral surface n the rate of GaN nanowire growth, *Semiconductors* **46**, 838 (2012).

[247] D. Camacho and Y. M. Niquet, Application of Keating's valence force field model to non-ideal wurtzite materials, *Physica E* **42**, 1361 (2010).

[248] F. Glas, Critical dimensions for the plastic relaxation of strained axial heterostructures in free-standing nanowires, *Phys. Rev. B* **74**, 121 302 (2006).

[249] J. Kioseoglou, E. Kalesaki, L. Lymperakis, G. P. Dimitrakopulos, P. Komninou, and T. Karakostas, Polar AlN/GaN interfaces: structures and energetics, *phys. stat. sol. (a)* **206**, 1892 (2009).

[250] M. J. Hÿtch, E. Snoeck, and R. Kilaas, Quantitative measurement of displacement and strain fields from HREM micrographs, *Ultramicroscopy* **74**, 131 (1998).

[251] S. Raychaudhuri and E. T. Yu, Calculation of critical dimensions for wurtzite and cubic zinc blende coaxial nanowire heterostructures, *Journal of Vacuum Science and Technology B: Microelectronics and Nanometer Structures* **24**, 2053 (2006).

[252] S. Raychaudhuri and E. T. Yu, Critical dimensions in coherently strained coaxial nanowire heterostructures, *J. Appl. Phys.* **99**, 114 308 (2006).

[253] H. L. Zhou, T. B. Hoang, D. L. Dheeraj, A. T. J. Van Helvoort, L. Liu, J. C. Harmand, B. O. Fimland, and H. Weman, Wurtzite GaAs/AlGaAs core-shell nanowires grown by molecular beam epitaxy, *Nanotechnology* **20**, 415 701 (2009).

[254] N. Sköld, L. S. Karlsson, M. W. Larsson, M.-E. Pistol, W. Seifert, J. Tragardh, and L. Samuelson, Growth and optical properties of strained $GaAs-Ga_xIn_{1-x}P$ core-shell nanowires, *Nano Lett.* **5**, 1943 (2005).

[255] M. Montazeri, M. Fickenscher, L. M. Smith, H. E. Jackson, J. Yarrison-Rice, J. H. Kang, Q. Gao, H. Hoe Tan, C. Jagadish, Y. Guo, J. Zou, M.-E. Pistol, and C. E. Pryor, Direct measure of strain and electronic structure in GaAs/GaP core-shell nanowires, *Nano Lett.* **10**, 880 (2010).

[256] Z. Zanolli, M.-E. Pistol, L. E. Froberg, and L. Samuelson, Quantum-confinement effects in InAs-InP core-shell nanowires, *J. Phys.: Condens. Matter* **19**, 295 219 (2007).

[257] L. Rigutti, G. Jacopin, L. Largeau, E. Galopin, A. D. L. Bugallo, F. H. Julien, J.-C. Harmand, F. Glas, and M. Tchernycheva, Correlation of optical and structural properties of GaN/AlN core-shell nanowires, *Phys. Rev. B* **83**, 155 320 (2011).

[258] J. Renard, Optical properties of GaN quantum dots and nanowires, Ph.D. thesis, Université Joseph Fourier (2009).

[259] S. D. Carnevale, J. Yang, P. J. Phillips, M. J. Mills, and R. C. Myers, Three-dimensional GaN/AlN nanowire heterostructures by separating nucleation and growth processes, *Nano Lett.* **11**, 866 (2011).

[260] S. D. Carnevale, C. Marginean, P. J. Phillips, T. F. Kent, A. T. M. G. Sarwar, M. J. Mills, and R. C. Myers, Coaxial nanowire resonant tunneling diodes from non-polar AlN/GaN on silicon, *Appl. Phys. Lett.* **100**, 142 115 (2012).

[261] J. Renard, G. Tourbot, D. Sam-Giao, C. Bougerol, B. Daudin, and B. Gayral, Optical spectroscopy of cubic GaN in nanowires, *Appl. Phys. Lett.* **97**, 081 910 (2010).

[262] G. Tourbot, C. Bougerol, F. Glas, L. F. Zagonel, Z. Mahfoud, S.Meuret, P. Gilet, M. Kociak, B. Gayral, and B. Daudin, Growth mechanism and properties of InGaN insertions in GaN nanowires, *Nanotechnology* **23**, 135 703 (2012).

[263] F. Glas and B. Daudin, Energetics of stress-driven island growth on top of nanowires, *to be submitted to Phys. Rev. B* (2012).

[264] M. Arlery, J. L. Rouvière, F. Widmann, B. Daudin, G. Feuillet, and H. Mariette, Quantitative characterization of GaN quantum-dot structures in AlN by high-resolution transmission electron microscopy, *Appl. Phys. Lett.* **74**, 3287 (1999).

[265] N. Gogneau, D. Jalabert, E. Monroy, E. Sarigiannidou, J. L. Rouvière, T. Shibata, M. Tanaka, J. M. Gérard, and B. Daudin, Influence of AlN overgrowth on structural properties of GaN quantum wells and quantum dots grown by plasma-assisted molecular beam epitaxy, *J. Appl. Phys.* **96**, 1104 (2004).

[266] F. Widmann, B. Daudin, G. Feuillet, Y. Samson, J. L. Rouvière, and N. Pelekanos, Growth kinetics and optical properties of self-organized GaN quantum dots, *J. Appl. Phys.* **83**, 7618 (1998).

[267] F. C. Frank, On Miller-Bravais indices and four-dimensional vectors, *Acta Cryst. A* **18**, 862 (1965).

[268] M. O'Keeffe and B. G. Hyde, Crystal Structures I: Patterns and Symmetry, (Mineralogical society of America 1996).

[269] H. C. Adelmann, Growth and strain relaxation mechanisms of group III nitride heterostructures, Ph.D. thesis, Université Joseph Fourier (2002).

[270] V. K. Gupta, K. L. Averett, M. W. Koch, B. L. Mcintyre, and G. W. Wicks, Selective area growth of GaN using gas source molecular beam epitaxy, *J. Electron. Matter.* **29**, 322 (2000).

[271] K. Kawasaki, I. Nakamatsu, H. Hirayama, K. Tsutsui, and Y. Aoyagi, Formation of GaN nanopillars by selective area growth using ammonia gas source molecular beam epitaxy, *J. Cryst. Growth* **243**, 129 (2002).

[272] K. Kishino, H. Sekiguchi, and A. Kikuchi, Improved Ti-mask selective-area growth (SAG) by rf-plasma-assisted molecular beam epitaxy demonstrating extremely uniform GaN nanocolumn arrays, *J. Cryst. Growth* **311**, 2063 (2009).

[273] K. Kishino, T. Hoshino, S. Ishizawa, and A. Kikuchi, Selective-area growth of GaN nanocolumns on titanium-mask-patterned silicon (111) substrates by RF-plasma-assisted molecular-beam epitaxy, *Electron. Lett.* **44**, 819 (2008).

[274] T. Schumann, T. Gotschke, F. Limbach, T. Stoica, and R. Calarco, Selective-area catalyst-free MBE growth of GaN nanowires using a patterned oxide layer, *Nanotechnology* **22**, 095 603 (2011).

[275] T. Gotschke, T. Schumann, F. Limbach, T. Stoica, and R. Calarco, Influence of the adatom diffusion on selective growth of GaN nanowire regular arrays, *Appl. Phys. Lett.* **98**, 103 102 (2011).

Growth and characterization of GaN nanowires and GaN/AlN nanowire heterostructures

This work focuses on the growth by plasma-assisted molecular beam epitaxy and on the characterization of GaN nanowires (NWs) and of GaN/AlN NW heterostructures.

We first investigate GaN NW morphology (density, mean length, mean diameter, length dispersion) dependence on the growth parameters. Using reflection high energy electron diffraction, GaN NW morphology is correlated to their nucleation dynamics. *In situ* grazing-incidence X-ray diffraction experiments performed at the ESRF allow clarifying GaN NW nucleation processes on bare Si(111) and when using a thin AlN buffer deposited on Si(111).

The use of resonant X-ray diffraction for the determination of GaN NW polarity is then successfully demonstrated. GaN NWs grown on bare Si(111) are shown to be N-polar. Additional KOH selective etching tests reveal that both GaN NWs grown using a thin AlN buffer on Si(111) and when pre-depositing Ga on the Si(111) surface are N-polar, too.

Regarding GaN-AlN NW heterostructures, the growth of an AlN shell around GaN NWs is studied as a function of various growth parameters. The AlN shell aspect ratio is described by a geometrical model. Using a combination of multiwavelength anomalous diffraction, high resolution transmission microscopy and theoretical calculations, GaN core strain state is investigated as a function of the AlN shell thickness. This strain is shown to increase with the shell thickness as long as AlN grows homogeneously around GaN NWs. When the shell is asymmetric, the system relaxes plastically.

Eventually, we study the possibility to fabricate island-like GaN insertions in AlN NWs. We determine the critical AlN NW radius above which GaN undergoes a 2D to 3D shape-transition. Regarding optical properties of these novel structures, the presence of multiple localized states is identified.

Keywords: nanowires, nitrides, molecular beam epitaxy, X-ray diffraction

---

Croissance et caractérisation de nanofils de GaN et d'hétérostructures filaires de GaN/AlN

Ce travail de thèse porte sur la croissance par épitaxie par jets moléculaires assistée plasma et sur la caractérisation de nanofils (NF) de GaN et d'hétérostructures filaires de GaN/AlN.

Dans un premier temps, la morphologie des NFs de GaN (densité, longueur moyenne, diamètre moyen, dispersion de longueurs) est étudiée en fonction des paramètres de croissance. Via la diffraction d'électrons rapides, la morphologie des NFs GaN est corrélée à la dynamique de nucléation de ces derniers. Des expériences de diffraction de rayons X en incidence rasante effectuées à l'ESRF permettent également de clarifier les processus de nucléation des NFs GaN.

Nous démontrons ensuite l'utilisation de la diffraction de rayons X résonnante pour déterminer la polarité des NFs GaN. Nous montrons que ces derniers sont de polarité N lorsque fabriqués sur Si nu. Des tests complémentaires de gravure sélective au KOH révèlent que les NFs GaN fabriqués sur un substrat de Si recouvert d'un fin buffer d'AlN ainsi que ceux dont la fabrication est initiée après pré-déposition de Ga sur la surface du Si, sont aussi de polarité N.

Concernant les hétérostructures filaires GaN-AlN, la croissance d'AlN autour et sur les nanofils de GaN est étudiée en fonction de divers paramètres de croissance. Le rapport d'aspect des coquilles d'AlN (longueur/épaisseur) est décrit par un modèle géométrique. En utilisant une combinaison de diffraction anomale multi-longueurs d'onde, de microscopie en transmission de haute résolution et des calculs théoriques, l'état de contrainte des cœurs de GaN est analysé en fonction de l'épaisseur de la coquille. Cette contrainte augmente avec l'épaisseur de la coquille tant que l'AlN croît de manière homogène autour des NFs de GaN. Dès lors que la coquille est asymétrique, le système relaxe plastiquement.

Nous étudions enfin la possibilité de fabriquer des îlots de GaN dans des NFs AlN. Nous déterminons le rayon critique de NFs AlN au-dessus duquel le GaN déposé subit une transition de forme de 2D à 3D. L'analyse des propriétés optiques de ces nanostructures originales revèle la présence de nombreux états localisés.

Mots clés : nanofils, nitrures, épitaxie par jets moléculaires, diffraction de rayons X